Heavy gas dispersion over complex terrain

Robin K. S. Hankin

Trinity College

A thesis submitted for the degree of Doctor of Philosophy at the University of Cambridge

March 1997

Heavy gas dispersion over complex terrain

Robin Hankin

Abstract

Society benefits considerably from large scale industrial activities. However, these activities can have undesirable side effects which must be adequately controlled and monitored; the motivation for this thesis is risk assessment. Industrial processes often involve large amounts of hazardous, liquified gases, and accidental release of such substances poses a threat to nearby populations.

Accidentally released gases are often denser than air and this thesis addresses the physics of dense gas dispersion. As dense gas clouds tend to adopt low-lying configurations, a shallow layer model (in which physical properties of the cloud are depth averaged) is indicated for simulating dense gas dispersion. This type of model has been comparatively neglected up to the present but is useful because it is capable of simulating the effect of complex terrain such as valleys and mountain ranges.

This thesis presents a computationally validated and physically realistic shallow layer model for dense gas dispersion.

A computational model has been developed to simulate the mathematical model. This model uses the flux correction scheme of Zalesak, generalized to account for complex terrain. The computational model is validated against a number of theoretical results. The model is then compared with a body of experimental data including large scale field trials, laboratory experiments, and established integral models.

A case study, in which the present model was used on a real hazard site, is presented.

To my parents

Abstract

Society benefits considerably from large scale industrial activities. However, these activities can have undesirable side effects which must be adequately controlled and monitored; one motivation for this thesis is risk assessment. Industrial processes often involve large amounts of hazardous, liquified gases. Accidental release of such substances poses a threat to nearby populations and the assessment of this risk is carried out in the UK by the Health and Safety Executive.

Accidentally released gases are often denser than air and this thesis addresses the physics of dense gas dispersion. As dense gas clouds tend to adopt low-lying configurations, a shallow layer model is indicated for simulating dense gas dispersion: a cloud is described in terms of depth averaged quantities such as contaminant concentration. If vertical accelerations are small, a hydrostatic pressure distribution is appropriate and the shallow water equations may be used.

This thesis presents a shallow layer model for dense gas dispersion. The model is time dependent and two dimensional. This type of model has been comparatively neglected up to the present but is useful because it is capable of simulating the effect of complex terrain such as valleys and mountain ranges.

The special physics of the leading edge is handled by augmenting the shallow water equations: extra terms are added that account for the interaction between the ambient fluid and the dense layer. In this manner the front Froude number may be fixed.

The model has a number of free parameters, which have to be empirically determined. The parameters used were either chosen on theoretical grounds, or taken from earlier work.

A computational model has been developed to simulate the mathematical model. This model differs from previous work in being time dependent and fully two dimensional. The model uses the flux correction scheme of Zalesak, generalized to account for complex terrain. The computational model is checked against a number of theoretical results.

The model is then used to simulate the large scale dense gas dispersion field trials carried out at Thorney Island (instantaneous and continuous), and its predictions are compared with the experimental results. In general, there is no evidence to suggest that changing the entrainment parameters would give better agreement. Some assessment of the sensitivity of the model to the free parameters is made.

Model predictions are shown to agree broadly with a number of integral models whose parameters were based on these experiments; cloud averaged concentrations as a function of downwind distance and time were considered.

Model predictions are then compared with laboratory-scale experiments in which dense gas was released over different slopes in a calm ambient. Instantaneous and continuous releases were considered

A case study of a real hazard site, using the present model, is presented.

Keywords

Complex terrain, heavy gas dispersion, density driven flow, depth averaged models, flux corrected transport, risk estimation, shallow layer modelling, shallow water approximations, shallow water equations, stratified shear layers.

Preface

My thanks to Lesley, who has given me the incentive and encouragement needed to finish this project.

Many thanks to my CUED colleagues, for listening to many impromptu talks about dense gas dispersion, and the giving of much-needed practical advice. In particular, Peter Woodburn, Greg Stuart, and Tim Summers have dispensed much wisdom. Dani Gersh has also been of great help.

The Health and Safety Executive have been particularly generous in their support, and my thanks go to both the organisation and its staff. Alf Mercer has been very helpful over the course of my work; also Dr Mary Trainor, and Dr Steve Porter of CHID, have given their unstinting support over a totally unreasonable timescale.

The other members of FLADIS, the European dense gas dispersion syndicate, receive my thanks; my semiannual meetings with this group have enriched my work considerably. In particular, the surgically precise and devastating comments of Dr David Webber have been especially welcome (although not necessarily so at the time).

I should like to make an unorthodox acknowledgment to S. T. Zalesak, author of [200]. It is largely due to his clear writing and vision that this work was possible at all. My understanding of FCT has grown in tandem with my respect for it.

The preparation of this thesis has relied heavily upon public domain- and copyleft- software. My thanks go to all those who contributed to its development, and in particular the linux community.

Thanks are due to my supervisor, Dr Rex Britter, without whom none of this work could have happened. His advice has been invaluable.

Finally, I should like to thank my friend and mentor Dr Nick Hurst. Nick has been of more help to me, both personally and professionally, than is reasonable to expect from anyone.

This dissertation is the result of my own work and includes nothing which is the outcome of work done in collaboration.

Nomenclature

a	primary entrainment paramater
A	cloud area
A^C	antidiffusive flux
b	stratification entrainment parameter
C	Courant number
C_{50}	50th percentile of concentration
C_a	time averaged concentration
C_D	coefficient of surface roughness
C_o	observed peak concentration
C_p	predicted peak concentration
$\overline{C}$	cloud averaged concentration
D	diffusion coefficient in Zalesak's scheme
$\mathcal{D}$	dose
E	entrainment rate
	mechanical energy of a dense layer per unit area
e	ground elevation
FAC2	proportion of statistics correct to within a factor of 2
FB	fractional bias
F^H	high order flux
F^L	low order flux
Fr	Froude number
g	gravitational field strength
g'	reduced gravity $g(\rho - \rho_a)/\rho$
h	depth of a dense layer
k	von Karman's constant
K	kinetic energy of a dense layer per unit area
M	cloud moment
MG	geometric mean
N	cloud non-uniformity
NMSE	normalized mean square error
P	front parameter, one dimension
	potential energy of a dense layer per unit area
	the inverse normal function
$\mathbf{P}$	front parameter, two dimensions
	centroid position
Q	volume flow rate per unit width
	scalar front parameter
R	correlation coefficient
Ri	Richardson number
S_1, S_u, S_{uu}	dimensionless shape parameters

t_a	cloud arrival time
t_d	cloud departure time
t_r	cloud residence time $t_d - t_a$
u_a, v_a	ambient fluid velocity
U_f	front speed relative to ambient flow
u_s	upward velocity of source gas
u, v	two dimensional velocity of dense layer
$\overline{u}, \overline{v}$	depth averaged velocity of dense layer
$u_\star$	friction velocity
v	representative velocity scale
$\mathbf{V}$	turbulent shear force
VG	geometric variance
W	entrainment velocity
$w_\star$	convective velocity
w	generic conserved quantity
w_e	edge entrainment velocity
w_i	a set of generic conserved quantities
w_i^n	a set of discretized generic conserved quantities at timestep n
w_i^{td}	w as calculated by a low order scheme
$w_i^{\max}, w_i^{\min}$	maximum and minimum allowable values for w
w_t	top entrainment velocity
z_0	ground roughness length

α	proportion of dense gas below $z = h$
$\alpha_2 \ldots \alpha_7$,	constants for the entrainment formula
α_E	edge entrainment parameter
Δt_i	i^{th} timestep
Δx_i	size of ith fluid element
$\Delta\rho$	excess density $\rho - \rho_a$
θ	slope of lower boundary
Λ	constant of proportionality for ground level concentration
ρ	density of dense layer
ρ_a	density of ambient fluid
ρ_s	density of source gas
ρ^*	cloud averaged density
$\overline{\rho}$	depth averaged density of dense layer
τ	surface stress

Contents

List of Tables

List of Figures

Chapter 1

Introduction: overview of heavy gas dispersion

Society benefits considerably from large scale industrial activities. However, these activities can have undesirable side effects which must be adequately controlled and monitored. Although the environmental effect of industrial activity is clearly important, the risks to humans from this activity are also important and the motivation for this thesis is risk assessment.

The fundamental purpose of risk assessment is to determine the probabilities and consequences of certain undesirable events, and to judge their acceptability to society. Attention usually focuses on quantifying the human suffering or death caused by a specific activity. As large scale chemical installations have the potential to release large quantities of harmful substances, risk assessment is frequently used to assess the acceptability of such installations.

In the context of risk assessment, 'hazard' is defined as 'the possibility of harm', while 'risk' is defined as 'the chance of bad consequences'. Risk and hazard are thus different concepts: a risk is a hazard with an associated frequency of realization.

Recently, the risk posed to populations living or working near such a 'major hazard site' has become the object of public and legislative concern [93]. This risk is primarily due to the possibility of a release of toxic or flammable material into the atmosphere.

Many industrial processes use liquified gases which are hazardous (that is, potentially harmful). This class of substances is therefore important to a risk assessment as an accidental release may harm large numbers of people.

If the gas is flammable it may ignite immediately after loss of containment, forming a flash fire or vapour cloud explosion. A 'BLEVE' (Boiling Liquid Expanding Vapour Explosion) may form if sufficient heat is supplied to the containing vessel [93]. However, if the gas fails to ignite, either because the gas is of low flammability or there is no source of ignition, a drifting cloud is formed. Such a drifting cloud may cause harm by its toxicity, or by drifting and igniting [91].

Accidentally released gases are often denser than air [25]. This may be due to the high molecular mass of the substance, its low release temperature, the formation of an aerosol, or the condensation of ambient water vapour. Chemical reactions of the released gas with ambient air may also be significant. This thesis will address the problem of the dispersion of dense gas in the context of risk assessment.

Such a dense gas cloud (i.e. one that is denser than air) will remain closer to the ground than a comparable passive cloud, and so the amount inhaled is likely to be larger for a dense gas cloud than an equivalent passive one.

Any risk assessment of a major hazard site will thus have to include a consideration of the consequences of a release of dense gas.

This chapter will begin with a brief outline of risk assessment and justify the study of heavy gas dispersion in that discipline. It will then argue that shallow layer models, although comparatively neglected in this field, may be used to predict heavy gas dispersion over complex terrain. The rest of this thesis will present a new shallow layer model that differs from previous approaches in being time dependent and two-dimensional.

1.1 Risk assessment

Risk assessment consists of two processes: the first is the analysis of the likely human harm incurred by an activity (risk estimation), but risk evaluation—the judgement made on the results of a risk estimation—must also play a part.

Risk assessment is typically carried out when a chemical company seeks permission to build a new site. The surrounding population would thus be subjected to the possibility of a release of hazardous dense gas.

Planning permission for the proposed site will be given (or withheld) as a result of a decision process involving the local planning authority, local pressure groups, the industrial concern itself, and any other interested parties.

Another typical use for risk assessment is the granting of planning permission for buildings close to an existing hazard site. Permission may be refused on the grounds of safety, especially if the proposed occupants are from a sensitive or special group such as children or convalescents.

Risk estimation is thus one input to what must be a political process; thus the results of a risk estimation may be over-ridden by other factors such as the boost given to a local economy by a new development.

It should be noted that heavy gas dispersion models are occasionally used for natural hazards. A famous recent example is that of the Lake Nyos event in which a large volume (estimates range from $3 \times 10^6\,\mathrm{m}^3$ to $6.8 \times 10^{10}\,\mathrm{m}^3$) of a mixture of CO_2 and H_2S was discharged from a lake in Cameroon in 1986 [59, 60]. This event caused over 1700 deaths [8, 9] and is particularly relevant to the present work as the terrain over which the gas spread was very mountainous. Habashi [72] gives a

discussion from a heavy gas dispersion point of view. Despite the importance of such events, attention will focus on the more controllable risk arising from major industrial hazards.

It is the task of a risk estimation to provide a statement of the risks posed to the surrounding population by a hazard. The absolute value of the risk is not as critical as might be imagined: risk assessment can only compare risk estimations to risk criteria which are set politically. Public perception of risk is a complex process [95, 96] but current risk assessment concentrates on providing a consistent, nationwide, approach to the analysis of industrial hazards [94].

This thesis aims to investigate the use of shallow layer models for modelling the effect of terrain on heavy gas dispersion.

This thesis will consider an important source of uncertainty in risk assessment: that of modelling the processes occurring in heavy gas dispersion. It is well known [104, 148] that the heavy gas dispersion model used will influence the outcome of a risk assessment. This thesis will assess a comparatively neglected approach: shallow layer modelling. Its usefulness and physical accuracy will be examined, particularly when non-flat terrain is considered.

1.2 Models of heavy gas dispersion

A working definition of the word 'model' is:

> a mathematical or physical system obeying certain specified conditions whose behaviour is used to understand another physical system to which it is analogous in some way.

Models are frequently simpler, more tractable, or more manageable than the real situation they simulate.

Britter [27] lists five roles for models, the most important being as "a *predictive* tool for various scenarios that have not, themselves, been tested" and it is this role that provides the major motivation for the development of the current model. Britter also mentions the ability of a model to highlight the sensitivity of the output [of the model] to the various input parameters. This is particularly relevant to the present model as it is specifically tailored to investigate the effect on heavy gas dispersion of one set of inputs: local terrain variation. This effect is often ignored in risk assessment and investigation of its importance is one of the main motivations for this work.

1.2.1 Physical accuracy in modelling

Physical accuracy is a requirement for a useful model of heavy gas dispersion, because only a model based on correct physical assumptions can be extrapolated beyond the experiments on which the model was based. The result of any

heavy gas dispersion model is an inductive prediction, and confidence in the induction can only be achieved if the modelling assumptions are based on sound approximations.

Any model must thus have a clear relationship with the situation being modelled. The present work investigates the behaviour of dense gas when released into the atmospheric boundary layer. Such dense gas is influenced by many complex processes: the released gas may be at a low temperature, condense ambient water from the atmosphere, or react chemically with air. Only the much simpler case of inert, single-phase gas at ambient temperature will be considered. This approach clearly involves neglecting many features of a real release and the approximations made are discussed in more detail in chapter 5 and appendix C.

The physical accuracy of modelling this simpler problem is limited by the accuracy of the fluid mechanical modelling assumptions and this is discussed in chapter 4.

Britter [27] points out that even a physically perfect model will have residual uncertainty[1] due to the turbulent nature of the problem; there will also be data errors which arise from measurement errors and uncertainty in the initial conditions.

1.2.2 The needs of the risk assessment community

One of the longer term motivations for this work is the development of a heavy gas dispersion model that can be used by the risk assessment community. Risk assessments must be carried out almost routinely and low computational cost is vital. As will be discussed in the next chapter, there is a clear and recognized need for a computationally cheap model that can handle terrain variations on the same scale as the cloud.

Many hazard sites are situated in areas of considerable topographic complexity. The results of a number of risk assessments have been questioned, by experts and non-specialists, on the grounds that the heavy gas dispersion model assumed the terrain to be flat.

Previous work [25, 30, 41] tends to concentrate on the limiting cases of topographic features which are either very small or very large compared with the horizontal scale of the cloud.

The case of small topographic features has been considered by Britter [25] who observes that the increased levels of turbulence near groups of obstacles will enhance dilution of the cloud. Other effects of obstacles noted by Britter include the alteration of the background flow (and subsequent interaction with the dense

[1] One definition is $\overline{(C_p - C_o)^2}$ where C_p and C_o are the predicted and observed concentrations, and the overbar denotes a generalized ensemble averaging; Hanna [85] presents a detailed discussion. An example of this measure in use is given in chapter 8 of the present work and by Hanna *et al.* [86].

cloud), and a time lag for dispersion of material entering the near-wake of the structures.

Large topographic features reduce to local slopes, and releases of dense gas on slopes have received much attention; references [3, 29, 191] give examples. However, the topography surrounding many real sites is complex on the scale of the cloud and the behaviour of a dense gas cloud released over such topography is not a simple generalization of cloud behaviour on a single slope. In this thesis, 'complex terrain' will mean terrain that varies on the same scale as the cloud.[2]

As current models capable of accounting for complex terrain are generally three-dimensional simulations which use unacceptably large amounts of computer time [26], typical risk assessments ignore the effect of terrain variation. It is clear that there is a need for a heavy gas dispersion model that can account for topographic features between the two extremes of obstacles and slopes.

Many workers have speculated on the effects on a dispersing dense gas cloud of complex topography. Such speculations frequently include the channelling of dense layers into valleys and low-lying areas and the converse 'protection' of higher regions. These effects are the direct result of ground slopes: the dense layer will tend to move down the local slope due to buoyancy effects.

Complex topography may also affect the spread of a dense cloud indirectly, by altering the ambient flow field through which the cloud disperses. Britter and Snyder [32] state that this indirect effect may be more important than the direct effect and this is further discussed in chapter 5.

1.2.3 Common topographic features found near major hazard sites

Many well-known major hazard sites are close to possibly important topographical features. Ellesmere Port, for example, is separated from a nearby housing estate by a steep bank.

Water treatment plants hold large amounts (typically 10^3 kg) of liquid chlorine on site and are generally close to rivers and reservoirs, which can often be topographically complex.

In general, very little analysis of the effects of complex terrain on heavy gas dispersion has been carried out for any existing or proposed major hazard site, although some work by Mercer [133, 134, 135] and the present author [84] has been carried out.

[2]More exactly, complex terrain is terrain such that typical length scales used to describe its elevation are the same order as those used to describe the horizontal extent of the cloud. This definition excludes slopes, rough ground, and valleys.

1.3 Shallow layer models of heavy gas dispersion

As heavy gas dispersion is important to risk assessment, it is necessary to model the process [26]. A number of models, of varying complexity, is available to the risk assessor. At present, one type of model (the integral model) is currently used almost exclusively on account of its low cost.

However, as discussed in chapter 2, integral models cannot account for the effects of complex terrain. Although models do exist that can account for complex terrain (three-dimensional models), this type of model is very rarely used in risk assessment due to its computational cost.

The use of integral models entails the neglect of the effects of complex terrain, a position that is becoming increasingly unacceptable [150]. An accessible model for heavy gas dispersion, capable of accounting for complex terrain, is therefore needed. This thesis presents a type of model that does account for complex terrain but is nevertheless computationally accessible: a shallow layer model.

Dense gas clouds tend to adopt low-lying configurations [25] and this fact suggests a method of modelling known as shallow layer. A shallow *water* model is a particular type of shallow layer model.

Formally, a shallow layer model describes the cloud as a function of time and (two-dimensional) ground position. At any position and time, the cloud is characterized by four variables: cloud depth, two components of velocity, and cloud concentration. Real clouds do not have an exact depth as they have no definite upper surface and so cloud depth has to be defined in terms of the vertical concentration distribution. The other variables are averaged (in a sense to be made precise in chapter 3) over the depth of the cloud. The shallow layer variables are thus often referred to as depth averaged.

Shallow layer models lend themselves particularly well to the adoption of the shallow water approximations. The shallow water approximations state that the pressure distribution is hydrostatic within the main body of the cloud; dispensation is usually made for the special processes occurring at the leading edge.

Many workers have called for a shallow layer model to be developed; at least six review articles [13, 19, 24, 25, 48, 162] specifically state that shallow layer models have been comparatively neglected and would be appropriate for the prediction of heavy gas dispersion. The advent of cheaper computational power has made this practical.

Chapter 2 will review the literature of heavy gas dispersion models and it will be shown that the shallow layer approach has a number of advantages over other methods which make it suitable for heavy gas dispersion.

A detailed account of the physical assumptions made in the shallow layer approach adopted here is found in chapters 3 to 5 and appendix C.

1.4 Thesis overview

This chapter has shown why heavy gas dispersion research is a necessary part of risk estimation, and it will be shown that the effects of complex terrain on a dispersing dense cloud should not be ignored.

This thesis will present a physically realistic model of heavy gas dispersion to be used in the context of risk assessment. This model is specifically designed to simulate the effects of topography and will use a shallow layer approach. It differs from previous shallow layer work in being time dependent and two-dimensional, and thus is capable of accounting for complex terrain.

The overall structure of this thesis is as follows:

- Chapter 1. Introduction and overview of risk assessment.
- Chapter 2. Literature review.
- Chapter 3. Development and generalization of the shallow water equations.
- Chapter 4. Discussion of the circumstances under which the shallow water equations are *not* suitable for heavy gas dispersion; the importance of the leading edge of a dense gas flow and its simulation.
- Chapter 5. The shallow water equations as applied to dense gas flows of industrial interest; the development of the mathematical model used in this thesis.
- Chapter 6. The computational scheme: the shallow water equations are solved numerically using a discretized computational domain. The numerical scheme is outlined.
- Chapter 7. Validation of the computational scheme. The results of the computational model developed in this thesis are compared with known results.
- Chapter 8. Evaluation of the model. The comparison of experimental results to the predictions of the model is discussed and 'good agreement with experiment' quantified.
- Chapter 9. Validation of the model (flat ground). Model predictions are compared with the field data of Thorney Island. Physical interpretation is made where possible and an assessment of the model's sensitivity to its free constants is made.
- Chapter 10. Indirect validation of the model (flat ground). Model predictions are compared with those of established integral models in terms of cloud averaged concentrations.

- Chapter 11. Validation of the model (slopes). The model is compared with several sets of experimental data in which dense gas was released over a slope.
- Chapter 12. Conclusions. An overall view of the model is given, from both a physical- and risk assessment- perspective.

Chapter 2

Previous research

2.1 Outline

This chapter will outline previous work on heavy gas dispersion. The literature splits naturally into four parts:

- small scale laboratory experiments
- wind tunnel and water flume experiments
- field experiments; large scale heavy gas releases
- models of heavy gas dispersion:
  - integral models
  - intermediate models
  - three-dimensional models.

The particular problems encountered when modelling heavy gas dispersion over complex terrain are then discussed in the context of the preceding parts.

2.2 Laboratory investigations

This section will briefly review some of the literature pertinent to heavy gas dispersion and will concentrate on laboratory-scale work. Although it could be argued that wind tunnel and water flume investigations should be classified as laboratory work, there seems to be a reasonably clear division: laboratory work tends to investigate more fundamental issues of fluid mechanics, while wind tunnel or water flume work concentrates on more practical problems which occur in a model of the atmospheric boundary layer.

This section will begin with an overview of some work on stratified shear layers and then review some papers addressing gravity currents.

2.2.1 Stratified shear layers

Stably stratified flows are common in nature and industry and have received much attention in the literature. If a fluid is stably stratified, the stratification may profoundly influence its behaviour and this is particularly relevant to heavy gas dispersion. In particular, if a stably stratified fluid is subject to shearing motion (forming a stratified shear layer) then the resulting fluid mechanics are of direct relevance to the present problem.

It is important to have an understanding of stratified shear layers for two reasons: firstly, to better represent in models the vertical density- and velocity-profiles, and secondly to incorporate only physically realistic entrainment models.

A review article by Fernando [56] written in 1991 considered turbulent mixing in stratified fluids. This paper reported large discrepancies between different workers. Some of the papers considered by Fernando which are of particular relevance to heavy gas dispersion will be discussed below.

An early (1959) paper in this subject, that of Ellison and Turner [52], is one of the most cited papers in the field. This paper discusses an experiment in which a salt water layer flowed down an incline. The authors showed that the Euler equations could be vertically integrated to give depth averaged quantities for the dense layer's density, speed, and depth. The quantities thus defined evolved (in space; the problem considered was steady) according to a set of relationships known as the shallow water equations.

Another much cited paper is that of Turner [180], which discusses the entrainment assumption and its application to geophysical flows. This assumption states that the mean inflow velocity (that is, the entrainment velocity) across the edge of a turbulent flow is proportional to a characteristic velocity of the flow and this idea will be further examined in chapter 5, which develops the model entrainment terms.

Turner [179], considering buoyancy effects in fluids, considers two types of turbulent entrainment:

Externally driven entrainment is entrainment which is caused by turbulence generated externally to the region of strong stratification. In the context of heavy gas dispersion, externally driven entrainment may be caused by turbulence generated at the ground, or turbulence which is present in the atmosphere.

Internally driven entrainment is entrainment caused by turbulence generated by shear across the density interface. That this type of entrainment is important in the present context is clear when considering, for example, a dense layer flowing down a slope.

Externally driven entrainment is typically investigated in the laboratory with the aid of oscillating grids which create turbulence above or below a stable density

interface [5], or by dropping a grid through a quiescent stratified fluid [121]. Interpretation of the results of these experiments is often carried out in terms of the Richardson number Ri:

$$Ri = \frac{\Delta\rho g D}{\rho U^2}, \tag{2.1}$$

where D is a characteristic depth of the system (or mesh length in the case of grid experiments), U is a velocity scale of the turbulence, $\Delta\rho$ is a typical change in density, ρ the density of the fluid and g the gravitational field strength.

The experiments of Kantha *et al.* [109] used a Richardson number as defined above, but taking the friction velocity $u_* = \sqrt{\tau/\rho}$ as the velocity scale. Their experiment investigated the entrainment rate across an initially sharp density interface. The form of the experiment was an annular tank containing, initially, a layer of salt water underneath a layer of fresh water. Turbulence was introduced into the fresh layer by means of a mesh which rotated in the annular tank just beneath the liquid surface. In this way, the stress applied to the liquid could easily be measured and u_* calculated. As the annulus was of finite width, the aspect ratio D/W (where D is the depth and W the width of the channel) was of importance but extrapolation to small D/W was possible. An earlier paper by Kantha [108] gave a different method of extrapolation which gave broadly similar results. One of the consequences of the initial sharp density interface was that the wavenumber vector $\mathbf{k}$ of any internal waves must be horizontal, unlike the earlier experiments of Kato and Phillips [110] that were confined to linear vertical stratification.

A review article (1984) by Wheatley and Webber [194] pointed out that internally generated turbulence is also present in the experiments of Kantha *et al.* [109] and allowance for this was not made in the extrapolation to small D/W. It also suggested that the vertical velocity profile be measured in future experiments. Deardoff [47], in an oceanographical context, considered rotating-screen annulus experiments and reported that "the net entrainment is dominated by that which occurs very near the outer wall of the annulus".

Internally driven entrainment is driven by the turbulence generated at the shear layer between two well mixed layers of different densities. This type of entrainment is frequently seen in geophysical situations such as katabatic winds and internal bores in rivers and oceans [171].

Shear across a density interface is expected to be important in the early stages of dispersion when the dense layer moves at a different velocity from the ambient air. The primary mechanism for internally driven entrainment is the formation and collapse of Kelvin-Helmholtz instabilities [115]. The dimensionless group of interest here is the gradient Richardson number Rg defined as

$$Rg = \frac{g\partial\rho/\partial z}{\rho\left(\partial U/\partial z\right)^2} \tag{2.2}$$

and a flow in which $Rg < 0.25$ may be unstable to the formation of Kelvin-Helmholtz billows [179].

2.2.2 Stratified flows with externally imposed turbulence

This type of flow, using the terminology used above, has both internally- and externally- driven turbulence; both contribute to the entrainment process. Reviews are given by Deardoff [47], Fernando [56], and Sherman *et al.* [170].

These reviews suggest employing an equivalent turbulent velocity u_R to represent the combined effects [56]. This velocity is a weighted sum of ΔU, the difference in velocity between the two layers, and the rms velocity if only diffusion is present.

Other, more complex, approaches are made in papers such as that by Zeman and Tennekes [202], who considered entrainment at the top of atmospheric boundary layer. These workers consider the energy budget at the inversion base and their approach is reviewed in chapter 5.

A detailed justification of the entrainment formula chosen for the current work is deferred to chapter 5, which describes the model under development.

2.2.3 Stratified flows and heavy gas dispersion

Britter, writing in 1988 [23] presented a review of mixing experiments relevant to heavy gas dispersion. Britter was seeking a pragmatically acceptable entrainment correlation and presented a number of useful expressions for the entrainment velocity. These correlations will be further discussed in chapter 5.

2.2.4 Gravity currents

Many workers have investigated buoyancy driven flows and Simpson [171] presented in 1987 a comprehensive review of gravity currents. This work defines gravity currents as "primarily horizontal flows [that] may be generated by density differences of only a few percent". It is the case that accidentally released dense gas will spread out and form a gravity current as it disperses.

The relevance of gravity currents to the current problem is thus clear and Simpson includes a section discussing dense gas dispersion.

Gravity currents on horizontal surfaces

Gravity currents typically take the form of a lengthening shallow layer with a (usually turbulent) leading edge or front. One dimensionless quantity for characterizing the head is the densimetric Froude number $Fr = u/\sqrt{g'h}$, where u is the speed of the front, $g' = (\rho - \rho_a)/\rho_a$ the reduced gravity (ρ and ρ_a are the density of the layer and that of the ambient fluid), and h the depth of the layer. Another

dimensionless parameter encountered is the Reynolds number $Re = U_f h/\nu$, where U_f is the front speed, h the dense layer depth and ν the kinematic viscosity; but this number is immaterial when greater than about 2000: early papers discussing this include Keulegan [111] and Schmidt [168]; Simpson and Britter [172] carried out more recent work. As the range of Reynolds numbers encountered in risk assessment-type problems is typically over 10^6, the influence of the Reynolds number will not be discussed further.

If the gravity current is confined to move between two horizontal planes distance H apart, then the quantity h/H is of interest. Because atmospheric dispersion is considered, there is no firm upper boundary except perhaps for an inversion layer which may be at 0.5 to 1.5 km altitude. Interest here thus centres on small values of h/H; unfortunately, as reported by Britter and Simpson [31], this limit is often difficult to approach experimentally.

In 1989 of Simpson and Linden [173] investigated frontogenesis—that is, the conditions under which a sharp leading edge is formed. Their conclusion was that a horizontal density gradient alone was not sufficient to generate a front; a non-zero second derivative (that is $\partial^2\rho/\partial x^2$) is also needed. As that work considered a lock-exchange type flow (and not the case of small h/H) it does not have direct application here but the ideas provided in that work are relevant.

The leading edge

Many workers have investigated the leading edge of a gravity current. This region has very different properties from the following flow and exhibits many features not seen elsewhere. These include vertical structure unlike that found in the following flow, high levels of turbulence, and strong interaction with the ambient fluid into which the current is intruding [171].

In 1969, Benjamin [10] presented an elegant theory of gravity currents. Although he studied air-filled cavities advancing along the (rigid) upper boundary of a liquid, his study is relevant to the present work. This is because the problem considered by Benjamin is equivalent, subject to certain caveats, to the 'inverted' problem of dense fluid intruding along the lower boundary of an expanse of lighter fluid. That author observed that, because the leading edge did not accelerate, the net hydrostatic force acting horizontally had somehow to be balanced by a deficiency of momentum in the receding flow.

As will be seen in chapter 4, this observation is central to the method of simulating the leading edge used in this thesis.

Many workers have followed Benjamin and further investigated the leading edge of a gravity current. Although detailed simulation of the leading edge is not an objective of this study (chapter 4), a brief synopsis is presented here.

Using an experimental technique that held a gravity current head stationary in laboratory coordinates, Britter and Simpson [31] presented a detailed analysis of the leading edge. They were able to suppress the lobe-and-cleft structure

commonly associated with gravity currents and normally due to over-running of light fluid by the dense one. Those workers were particularly interested in the case of small h/H and expressed surprise that this limit was difficult to approach.

Another conclusion made by Britter and Simpson was that the use of a Froude number defined in terms of a densimetrically weighted dense layer depth lead to accurate and consistent results and this point will be used in this thesis in chapters 4 and 5.

The same workers, in 1979, presented a further analysis of the problem allowing for fluid overrun [172] and again suggested that in the case of small h/H, a densimetrically weighted dense fluid depth could be used.

Gravity currents on slopes

Many gravity currents occur on sloping ground and it is necessary to have a good understanding of their behaviour for the present problem.

Simpson, in his review of gravity currents [171], considered gravity currents on slopes in the context of powder snow avalanches, oceanic turbidity currents, methane streaming in mines, and heavy gas dispersion. Here, attention will be confined to buoyancy conserving flows.

Arguably the most comprehensive paper ever written on this subject is that of Britter and Linden [29] who presented a unified theory of gravity currents on slopes of angle $0.5° \leq \theta \leq 90°$. These workers considered a quiescent fluid of density ρ_a over an inclined plane of angle θ. A fluid of density $\rho > \rho_a$ was introduced at a steady volume flow rate Q per unit width. The front parameter of interest was

$$F = \frac{U_f}{(g_0' Q)^{1/3}} \tag{2.3}$$

where $g_0' = g(\rho - \rho_a)/\rho$ is the initial reduced gravity.

One of the results of Britter and Linden was to show that $F = 1.5 \pm 0.2$ for all slopes in the range $5° \leq \theta \leq 90°$. Although this measure of front speed is not local (that is, the definition includes quantities that are not measured at the front itself), this result will be used in chapter 4, which describes the method used to simulate the leading edge of a dense layer.

2.3 Wind tunnel and water flume investigations

Being intermediate in scale between laboratory work and field trials, wind tunnel investigations are considered in this section.

Heavy gas dispersion has motivated much work in wind tunnels and water flumes, and only a cursory overview is possible here. Wind tunnel work will be considered first, followed by a brief discussion of water flume work.

One of the chief advantages of the wind tunnel approach is that many repeat trials may be conducted at relatively low cost: Hall *et al.* [74] carried out 100 repeats of different instantaneous releases. Although each trial is nominally subject to the same conditions, the turbulent nature of the problem implies that variation between successive experiments will exist. Types of variation typically reported are Eulerian concentration time traces differing from one experiment to the next.

Dynamical similarity between model and full-scale (steady) flows requires that all dimensionless groups that may be obtained from the independent variables be equal at model and full scale. Britter and McQuaid [30] consider this and deduce that, of the many dimensionless groups available, the quantities

$$\frac{U^2}{g'L} \quad \text{and} \quad \frac{\rho q_0^2}{\rho_a U^2 L^4}$$

which represent a densimetric Froude number and a source momentum ratio, should be preserved at the expense of other groups whose invariance is not so crucial. Here, U is the wind speed, $g' = g(\rho - \rho_a)/\rho_a$ the reduced gravity, L a characteristic length scale of the source, and q_0 the volume flow rate.

Many workers stress the practical difficulty of modelling low (full-scale) wind speeds in a wind tunnel. Dense layers may laminarize in low wind speeds, invalidating the experiment [25] because this phenomenon does not occur at large scales. As low wind speeds are generally of great interest to risk assessors, these difficulties can limit the usefulness of physical modelling.

However, as Britter [25] points out, "physical modelling incorporates a model of the fluid mechanics superior to any current mathematical model, provides unequalled spatial and temporal resolution, and is ideally suited to flows influenced by ... variable terrain."

Motivation for the present approach (as opposed to physical modelling) is provided by the need for a tool suitable for use in routine risk assessment; physical modelling is simply too expensive and time consuming for this. Review papers discussing wind tunnel modelling include those by Britter and McQuaid [30] and Meroney [140]; examples of wind tunnel investigations are given by Hall [73, 75, 77]. The series of experiments conducted by Schatzmann [166, 167] will be used as experimental data against which to compare the present model.

Water flume work on heavy gas dispersion is broadly similar to wind tunnel work. Examples of such work include that by Melia [131] and Rottman *et al.* [165].

The use of a 'towing tank' in which (for example) a model of a section of complex terrain is towed through stationary fluid appears to be of limited use for heavy gas dispersion as the uniform approach profile simulated is not equivalent to the velocity profile found in the atmosphere. This technique is more often used for mesoscale problems.

2.4 Field experiments

The difficulties of simulating the atmospheric boundary layer in a laboratory may be overcome by conducting large scale, outdoor experiments.

Britter [26] discusses large scale field trials in the context of provision of data to enable the development of mathematical models (as opposed to being models *per se*). It is in this capacity that large scale experiments will be discussed.

A number of large scale field trials have been conducted and a review of some of the most-cited follows:

Burro and Coyote The Burro [116] and Coyote [53] trials were carried out over a dry lake bed in California, and consisted of releases of LNG (up to 136 kg/s) onto a pool of water. The Burro series concentrated on the dispersion of LNG vapour, while the Coyote series focused on the characteristics of burning clouds and investigation of rapid phase transition events.

One release (Burro 8) is of particular interest to the present study as "the low wind speed permitted the gravity flow of the dense gas to be almost independent of the surrounding atmospheric boundary layer" [116]. This experiment was conducted over ground of slope $\sim 1:25$ and this exerted a clear influence on the behaviour of the dense gas.

Desert Tortoise and Goldfish These trials (references [53] and [11] respectively) were carried out over a desert surface that was covered by a shallow layer of water. Liquid NH_3 (Desert Tortoise) or HF (Goldfish) was released in the form of a flashing two-phase jet. Release rates of up to 130 kg/s and 28 kg/s respectively were maintained. Concentration measurements were taken at distances up to 5.5 km downwind of the source.

Maplin Sands This series of releases [155] involved the release of LNG or LPG onto the surface of the sea at rates up to 44 kg/s.

Thorney Island instantaneous These experiments [128, 130] were carried out on level terrain over close-cropped grass and released, instantaneously, some 2000 m^3 of Freon-12. This sequence of experiments was notable for the extensive characterization of local atmospheric properties, the sophistication of the gas detection equipment used, and the extremely large quantity of gas released.

These experiments stand today (1997) as one of the most useful and complete large scale studies in the field of heavy gas dispersion, and some use will be made of the results in chapter 9.

Thorney Island continuous These experiments involved the release of Freon-12 at rates of up to 10 kg/s. The release site was identical to the instantaneous experiments and much of the instrumentation was common to both.

The Modellers' Data Archive (MDA) arose as a result of heavy gas dispersion model comparison exercises conducted by Hanna *et al.* in 1991 [88] and 1993 [86]. The MDA includes the results of a number of dispersion trials in a common format, and contained enough information to satisfy the input requirements of all the models considered. Some use of the MDA will be made later in this thesis.

2.5 Models for the prediction of heavy gas dispersion

For the purposes of this section, heavy gas dispersion models will mean models that are used for the prediction of heavy gas dispersion in industrially realistic situations.

Previous heavy gas dispersion models fall naturally into three types and in increasing order of complexity they are: integral models, intermediate (SLAB type and shallow layer) models, and three dimensional models.

This thesis will argue that a shallow layer model has a number of advantages over other models; many workers have noted that this approach appears to have been comparatively neglected. There have been repeated calls for such a model to be developed and examples of review articles include [13, 19, 24, 25, 48, 162].

2.5.1 Integral models of heavy gas dispersion

Loss of containment events may discharge hazardous dense gas over widely varying time scales. At one extreme lies catastrophic vessel failure in which the majority of the vessel's contents are released following major mechanical failure; and at the other lie pipework failures which may continue to vent for many minutes. Other releases lie between these two extremes.

As the two limiting cases tend to be very much simpler than intermediate cases, many workers consider only the two extremes and thus some objective criterion is required to place a release in one category or the other; Britter and McQuaid [30] give such a criterion by defining a dimensionless group

$$\frac{U_{\text{ref}} T_0}{x} \tag{2.4}$$

where U_{ref} is the wind speed, T_0 is the duration of release and x is the distance from the source. If this group is greater than 2.5 the release may be viewed as continuous and if it is less than 0.6 the release is to be considered instantaneous. It is usual [25, 30] to refer to the result of an instantaneous release as a 'puff' and that of a continuous release a 'plume' (cloud is the generic term).

A 'box' or 'integral' model of heavy gas dispersion is one that that can be recast to include only functions of one variable (that is, unary functions, or functions

of arity one). For example, if a plume has downwind, cross wind, and vertical dependence then this may be expressed as a combination of several unary functions as in equation 2.5. Usually, vertical or cross-wind variations in cloud or plume properties are averaged over the extent of the cloud, and profiles superimposed. Integral models typically describe a heavy gas release using a small number of degrees of freedom; each one (cloud height, concentration, etc) is given as a unary function of independent variables such as time, downwind distance, or some quotient.

This type of heavy gas dispersion model was developed in response to risk assessors who required a computationally accessible tool. Integral models are used almost exclusively in risk assessment today (1997).

Instantaneous releases will be considered first, followed by the continuous case.

Integral models for instantaneous releases

Integral models typically regard an instantaneously released cloud as a uniform right cylinder; the dependent variables are thus h, the cloud height; R, the cloud radius; and ρ, the cloud density. The independent variables may be the downwind distance x, or the time from release t. Vertical or horizontal profiles are often superimposed on the fundamental model.

Some integral models admit extra degrees of freedom (such as allowing the cloud to become elliptical and introducing a cloud eccentricity) but the underlying idea is unchanged. Integral models have been generalized by Britter *et al.* [28], and Nikmo and Kukkonen [147] to allow for thermodynamic effects and slopes.

However, integral models are limited by their assumption that the cloud remains as a uniform right cylinder or ellipse, possibly with imposed lateral or vertical profiles. This is not true if the cloud is channelled by topographical features into low-lying areas. The model of Webber *et al.* [191] is an exception to this, and is discussed below.

Britter and McQuaid [30], discussing the use of integral models for risk assessment in complex terrain (as defined on page 2) state that, under light wind conditions, "it is unlikely that simple correlations will be available that include topographic effects". This is attributed to the diversity of problems that could arise. These comments do not apply to slopes: integral models for heavy gas dispersion over slopes do exist, such as that of Britter *et al.* [28] and Kukkonen and Nikmo [117].

Integral models for continuous releases

Continuous releases of dense gas occur perhaps an order of magnitude more frequently than instantaneous releases [79]. Although this mode of failure is typically of smaller expected mortality than instantaneous releases, continuous releases must also be modelled in risk assessment.

Webber *et al.*, writing in 1991, present a description of an integral model for continuous releases [187]. The model assumes a steady, time-averaged concentration field $c = c(x, y, z)$ of the form

$$c(x, y, z) = C_m(x)F_v(z/f(x))F_h(y/f'(x)) \tag{2.5}$$

where (x, y, z) are Cartesian coordinates with z vertical and x downwind. The F's are functions that describe the cloud cross section. Equation 2.5 shows the defining feature of integral models: the lack of time dependence implies that the cloud is described using only functions of a single variable (here, the downwind distance x, an altitude parameter $z/f(x)$, and a crosswind parameter $y/f'(x)$), so, for a given release and meteorology, the cloud as modelled may be described in terms of a small number of functions of one variable only.

Wheatley and Webber [194], in a review article, consider integral models for continuous releases and state that it is possible to formulate such a model from an instantaneous model. This is done, in essence, by replacing the independent variable t with x; $\partial/\partial t$ becomes $U\partial/\partial x$, where U is the wind speed. Although this analogy is not perfect (the plume model needs to use a representative wind speed which does not translate simply to the wind speed used in a puff model), this mapping preserves many of the assumptions about the nature of entrainment and leading edge speed made in the corresponding instantaneous model.

Models such as DENS20 [139] and SLAB [145] are considerably more complex than integral models. This is because the cloud is described using functions of two variables (downwind distance and time) rather than the one permitted by integral models.

Many one-dimensional studies of heavy gas dispersion use the shallow water equations, and make the assumption that the vertical density and velocity profiles are uniform within the cloud. As discussed by Mercer and Davies [136], and Mercer and Nussey [138], real releases are not vertically homogeneous and this inhomogeneity should not be ignored: chapter 9 shows how important the vertical structure is, and chapter 3 shows how it may be modelled.

2.5.2 Intermediate models of heavy gas dispersion

Between the simplicity of integral models and the complexity of three-dimensional computational fluid dynamics (CFD) models, there lies an intermediate approach that has met with some success. The advantages and limitations of this type of method are discussed below.

SLAB-type models

The models considered here include cloud descriptions that are functions of two variables. SLAB, for instance, describes a plume as depicted in figure 2.1. At

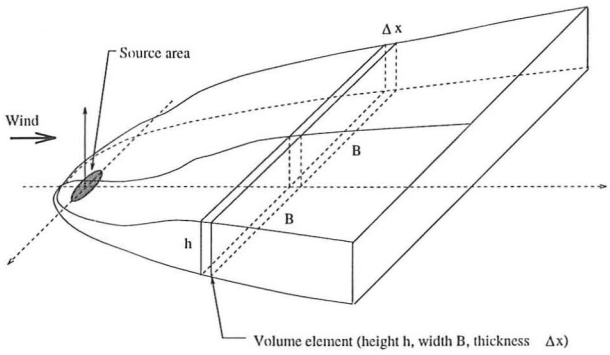

Figure 2.1: Depiction of a dispersing cloud of heavy gas as assumed by SLAB-type models

any downwind distance x and time t, the plume has half-width B, height h, and density ρ (not shown). The model may also account for the temperature of the cloud.

All models of this type have to make some assumptions about the cloud profile at each downwind distance. Typically, the cloud is assumed to have uniform height, concentration and temperature, as in work by Meroney [139] and Morgan *et al.* [145]; although different assumptions have been made in other models such as that of Würtz [198].

However, this type of model is unsuitable for describing the complex shape of clouds generated when large quantities of dense gas are released in light winds over complex terrain. There are two main reasons for this: firstly, the model parameterization is not sufficiently flexible to allow description of complex shapes; and secondly, interactions between terrain, wind, and density effects may disrupt the assumed cross wind profiles.

Two-dimensional time dependent shallow layer models

Two-dimensional time dependent shallow layer models describe a cloud or plume by an array of depth averaged quantities such as cloud density and velocity.[1] As this work argues, a two-dimensional description of dispersing dense gas is indicated on two counts: firstly, the description is natural from a physical viewpoint; and secondly, the needs of the risk assessment community are met.

Two-dimensional shallow layer models for heavy gas dispersion are not unknown: such a model was presented by Meroney [119] in 1988. However, that work does not appear to have been followed up[2] and appears to ignore the special

[1]This type of model includes functions of three variables (two space and one time) which is the reason for their greater complexity.

[2]An extensive on-line literature search conducted at HSL Sheffield in 1992 revealed only one

physics of the leading edge; this region controls the following flow.

This type of model has some advantages over other types. McQuaid [13] stated (in 1989) that they have been "comparatively neglected up to the present", and similar sentiments are expressed by Britter [25]. One reason for this that has been suggested by the present author [83] is the unexpectedly difficult numerical problems that are encountered with this type of model; Foreman [58] and Leonard [120] present some of the difficulties.

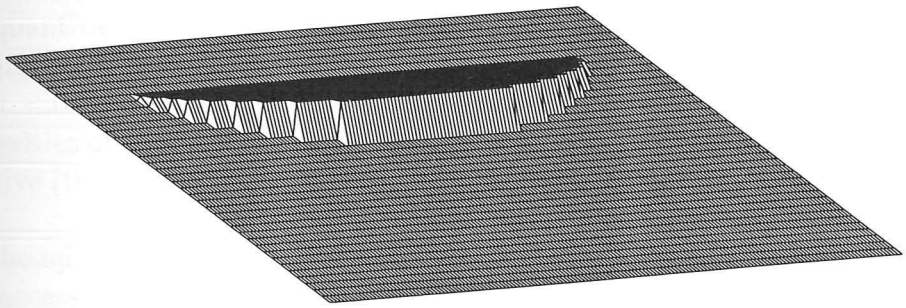

Figure 2.2: Schematic diagram of Webber's 'D' cloud

It could be argued that Webber's 'D' cloud [191] is a two-dimensional shallow layer model; it *is* an analytical solution of the two-dimensional shallow water equations on a slope, albeit with slightly different boundary conditions from those used here; but it is an integral model according to the definition given on page 17. A schematic diagram is given in figure 2.2.

The model of Hepner and Finco [98] was also designed to predict the dispersion of heavy gas over complex terrain. However, their approach was not fluid-mechanical and their impedance surface method has little relation to the model developed here.

2.5.3 Three-dimensional CFD models of heavy gas dispersion

At first sight, a natural method of predicting the behaviour of a dispersing dense cloud is to use a three-dimensional CFD model. Although this is possible, it is (at present) prohibitively expensive for routine use in risk assessment. This section will discuss the use of these sophisticated models for heavy gas dispersion. In the present context, a defining characteristic of this type of model is that it includes functions of four variables (three space and one time).

Dense gas dispersion is, in general, a three-dimensional, turbulent, time dependent process. Direct simulation of this process is generally impossible in

citation, by Britter [25]; and Meroney's work is mentioned there only in the reference list.

practice because the time scale and length scale of the fluctuations (which must be resolved numerically) are too small for any computer to simulate either now or in the foreseeable future.

Conventionally, the equations governing the flow are time-averaged to obtain equations for the mean fields. As these typically vary on much larger time- and length- scales than the instantaneous fields this allows considerable saving of computational power.

However, this approach requires the determination of correlations of fluctuating quantities and these must be determined separately. There is an extensive literature surrounding this topic; Panofsky and Dutton [151] and Rodi [160] present standard works. Any turbulence closure method capable of handling the complexities of a dispersing dense gas cloud will be complex and computationally expensive (that is, too expensive for routine use in risk assessment at the present time).

Although the resolution of the fine spatial and temporal behaviour of the cloud is not necessary if a turbulence closure approach is adopted, there remain regions of a dispersing cloud that still require a relatively fine solution scheme. Following Wheatley and Webber [194], these are:

- the gravity current head
- the shear region between the cloud and the ground
- the density interface between the cloud and the ambient flow above.

Each of these regions exerts a potentially important influence on the development of the cloud. It is therefore necessary to model the cloud behaviour in these regions accurately and this requires a great deal of computer power.

Computational expense is not the only disadvantage of three-dimensional flow solvers. Britter [25] reports that there is evidence to suggest that increasing model sophistication does not necessarily lead to better predictions. With this in mind, many workers use integral models to the exclusion of other types.

2.6 Heavy gas dispersion over complex terrain

Integral models are not intended to account for the effect on a cloud of terrain which varies on the same (horizontal) scale as the cloud.[3] However, the simpler effect of a slope on dispersing dense gas is one which several workers have incorporated into their dispersion models. A critical review of several such works is presented below.

[3] A possible caveat to this is given by Britter [22] in which dense gas flowing down a valley was considered. The model given was formally a integral model but this does not invalidate the above point as the valley had no associated length scales.

Heavy gas dispersion has motivated many one-dimensional studies of the shallow water equations (examples are given in [20, 22, 183, 186, 191]) and results from these works are used in chapter 7.

2.6.1 Integral models simulating dense gas on sloping terrain

As has been mentioned, extension of integral models to complex terrain is not, in general, possible, as the cloud may assume a configuration not capable of description by a small number of independent variables.

However, if the terrain under consideration is a uniform slope, then a dispersing dense gas cloud may well retain the form assumed in an integral model. This possibility has been considered by many workers and a selected review is given below.

The model of Britter *et al.*

Britter *et al.* [28], writing in 1991, presented an integral model for the dispersion of denser-than-air vapour clouds over real terrain. Using entrainment functions derived from two dimensional experiments and analysis, they developed a model capable of simulating heavy gas dispersion over a uniform slope, although they consider more complex topography. The model thus developed was applied to Thorney Island Trial 15 [130] for flat terrain, and a slope of 5° with the wind blowing either directly up or directly down the slope.

Results of maximum concentration versus downwind distance were given. There was a difference of about an order of magnitude between the upslope and the downslope at 100 m downwind, while for distances > 1 km downwind the two slopes gave results agreeing to within a factor of about two; flat terrain interpolated the two sloping results.

The model of Kukkonen and Nikmo

Motivated by risk assessment, Kukkonen and Nikmo presented an integral model for use on uniform slopes [117]. The model neglected the influence of sloping ground on the spreading and dilution of the gas cloud, and considered only its effect on the transport of the cloud. The model assumed that the released gas remained in the form of a uniform right cylinder. This assumption is questioned in the work of Webber *et al.* [191] which is discussed below.

The 'D' model of Webber *et al.* [191]

In an ingenious analysis, Webber *et al.* [191] presented an analytical solution of the resisted shallow water equations on a slope. The leading edge condition used

by Webber *et al.* was different from that used here.

The leading edge conditions used in both the present model and that of Webber *et al.* are discussed in detail in chapter 4. This model neglects air entrainment, although subsequent work [189] addresses this.

2.7 Summary

This chapter has discussed some literature relevant to the present work. Discussion of the computational fluid dynamics literature is deferred to chapter 6 which introduces the computational model developed here. This chapter has considered physical- and mathematical- modelling of heavy gas dispersion and each is summarized below:

Physical modelling

A natural, though not perfect, division of experimental work into laboratory-, wind tunnel/water flume- and large scale- experiments has been made.

The laboratory work is itself split into investigations of stratified shear layers and entrainment, and gravity currents. A large amount of work on stratified shear layers exists; discussion of the entrainment model adopted in this work is given in chapter 5. Several of the gravity current investigations cited present ideas that will be used throughout this thesis.

Wind tunnel work, concentrating on scaled-down simulations of real hazard situations, was discussed and one strength of this technique is the ability to conduct large numbers of nominally identical trials, giving data from which to estimate ensemble statistics. Difficulties with the technique include the practical difficulties of simulating the atmospheric boundary layer in the important case of low wind speeds.

Four series of large scale field trials have been chosen for comment, but there is little large-scale work investigating the effect of sloping terrain or complex terrain on heavy gas dispersion. Some of the results from the Thorney Island trials will be used in chapter 9 of the present work.

Mathematical models of heavy gas dispersion

Models for the prediction of heavy gas dispersion fall into several main classes: integral models, intermediate (SLAB-type) models, shallow layer models, and three-dimensional CFD models.

Integral models, describing a dispersing dense gas cloud in terms of a small number of parameters as functions of one variable, do not have the flexibility to characterize a cloud influenced by complex terrain.

Intermediate, SLAB-type, models use functions of two variables but also suffer from similar drawbacks, although they admit more complex cloud geometries than integral models.

Shallow layer models, using functions of three variables, describe a dispersing dense gas cloud in terms of cloud depth, density, and two components of velocity. These four quantities are functions of two dimensional ground position and time.

Three-dimensional models, solving the Reynolds averaged Navier Stokes equations over a three-dimensional computational lattice, tend to be expensive to develop and run. They include functions of four variables (three space and one time).

The model presented in this thesis is intermediate in complexity between three-dimensional models and SLAB-type models as it includes functions of three variables (two spatial variables and time). It will be shown that this approach retains many of the advantages of each type of model, yet remains computationally cheap and sufficiently flexible to incorporate future work on stratified shear layers.

It is hoped that the model presented here will be of use to the risk assessment community and will allow the accurate assessment of the effects of complex terrain on dispersing dense gas.

Chapter 3

The generalized shallow water equations

3.1 Outline

This chapter will give an overview of the shallow water assumptions. The shallow water equations will be developed and generalized to include the effects of non-uniform density, such as in dispersing dense gas. It will be shown that extension of the generalized shallow water equations to two dimensions is not trivial due to the large number of dimensionless shape parameters required to describe the flow.

The generalized shallow water equations as developed in this chapter will be used throughout the remainder of this thesis for heavy gas dispersion.

3.2 The shallow water equations

The shallow water equations have been used in the fields of oceanography [64, 141, 142], meteorology [64, 171], glaciology [101, 102], and civil engineering [97, 182]. Many fluid systems are composed of a layer of dense fluid under an expanse of lighter fluid, and if typical depth scales are small compared to typical horizontal scales the fluid is known as shallow. This section will begin with a statement of the shallow water equations and will progress to the full case of the generalized shallow water equations over non-uniform terrain. In all the following, the Reynolds number will be assumed to be sufficiently high to allow the direct effects of viscosity to be neglected.

If fluid of constant density ρ and depth $h = h(x, y, t)$ moves with velocity $\mathbf{u}(x, y, t) = (u, v)$ over a rigid horizontal surface and under ambient fluid of density ρ_a, the equations of motion are well-known [194]. If surface stresses are neglected

they are:

$$\frac{\partial h}{\partial t} + \nabla \cdot (h\mathbf{u}) = 0 \tag{3.1}$$

$$\frac{\partial h\rho u}{\partial t} + \frac{\partial h\rho u^2}{\partial x} + \frac{\partial h\rho uv}{\partial y} + \frac{\partial}{\partial x}(\frac{1}{2}g(\rho - \rho_a)h^2) = 0 \tag{3.2}$$

$$\frac{\partial h\rho v}{\partial t} + \frac{\partial h\rho uv}{\partial x} + \frac{\partial h\rho v^2}{\partial y} + \frac{\partial}{\partial y}(\frac{1}{2}g(\rho - \rho_a)h^2) = 0, \tag{3.3}$$

where $\nabla = (\partial_x, \partial_y)$ is the differential operator nabla in two dimensions. Equation 3.1 expresses conservation of volume of dense fluid (or mass, as the density is constant); equations 3.2 and 3.3 are the vertically integrated Euler equations under the assumption of a hydrostatic pressure distribution. An extra equation is required (expressing conservation of mass) if the density ρ is also allowed to be a function of space and time:

$$\frac{\partial h\rho}{\partial t} + \nabla \cdot (h\rho\mathbf{u}) = 0. \tag{3.4}$$

Note that equations 3.2 and 3.3 are still true when the restriction of constant ρ is relaxed. Equations 3.1 to 3.4 will be referred to as the shallow water equations. They may be combined to give equation 3.5:

$$\frac{\partial \rho}{\partial t} + (\mathbf{u} \cdot \nabla)\rho = 0, \tag{3.5}$$

which states that density ρ is *advected* in contrast to quantities such as h and $h(\rho - \rho_a)$ which evolve according to conservation equations.[1] Because equations 3.1 to 3.4 relate to the non-entraining case, equation 3.5 explicitly shows that any shallow water system in which the density is uniform must remain so for all time. This is an important point: if $\nabla \cdot (\mathbf{u}(\mathbf{x})) < 0$ then there is a *mass* flux into an infinitesimal control volume at point $\mathbf{x}$. It is clear that the effect of this mass flux will not be to increase the density of the fluid in the volume, but rather to increase the height. This is related to the 'anelastic' approximations made in some three-dimensional models such as that of Chan *et al.* [36, 37].

3.2.1 The shallow water equations with entrainment

Equations 3.1 to 3.4 may easily be modified to account for entrainment of the ambient fluid. This was done by Wheatley and Webber [194], although the approach used here differs slightly.

The right hand sides of equations 3.1 to 3.4 must account for the volume, mass, and momentum of the entrained fluid. If the entrainment rate is W, which may

[1] As discussed in chapter 6, a quantity Q is said to be conserved if it satisfies the conservation equation $\partial Q/\partial t + \nabla \cdot (\mathbf{u}Q) = 0$, where $\mathbf{u}$ is the velocity field in which Q moves.

be a function of time and space, the shallow water equations for an entraining system are

$$\frac{\partial h}{\partial t} + \nabla \cdot (h\mathbf{u}) = W \tag{3.6}$$

$$\frac{\partial h\rho}{\partial t} + \nabla \cdot (h\rho\mathbf{u}) = W\rho_a \tag{3.7}$$

$$\frac{\partial h\rho u}{\partial t} + \frac{\partial h\rho u^2}{\partial x} + \frac{\partial h\rho uv}{\partial y} + \frac{\partial}{\partial x}(\frac{1}{2}g(\rho - \rho_a)h^2) = W\rho_a u_a \tag{3.8}$$

$$\frac{\partial h\rho v}{\partial t} + \frac{\partial h\rho uv}{\partial x} + \frac{\partial h\rho v^2}{\partial y} + \frac{\partial}{\partial y}(\frac{1}{2}g(\rho - \rho_a)h^2) = W\rho_a v_a \tag{3.9}$$

where $\mathbf{u}_a = (u_a, v_a)$ is the velocity of the ambient fluid.

3.3 The generalized shallow water equations in one dimension

The previous derivations assumed a uniform velocity profile and constant density. If the dense layer flow considered is not uniform, this introduces a number of complications. It is necessary to consider these factors, as gravity currents have complex density- and velocity- profiles and, for example, have no unique 'height'; it is clearly necessary to use some type of depth averaging.

The following analysis is due to Ellison and Turner [52], who considered a release of salt water into an expanse of fresh water. The lower surface of the flow was a smooth plane at inclination θ. They proceeded to present analysis and experimental work on steady, two-dimensional density currents. Take the x-axis along the current, and the y- axis perpendicular to it. Let $v(x, y)$ be the mean velocity relative to the ambient fluid, and let $V(x)$, $h(x)$ and $\Delta(x)/g$ be the velocity, length and density scales in the cross section. Also let A be the flux of density difference. If A is independent of x, then V, h, A, and Δ may be *defined* as functions of x by the following equations:

$$Vh = \int_{y=0}^{\infty} v \, dy \tag{3.10}$$

$$V^2 h = \int_{y=0}^{\infty} v^2 \, dy \tag{3.11}$$

$$A = \int_{y=0}^{\infty} (\rho - \rho_a).g.(v + V_a) \, dy \tag{3.12}$$

$$= (V + V_a)h\Delta. \tag{3.13}$$

The subscript 'a' refers to the ambient fluid. The definition of the entrainment constant E is given as

$$\frac{d\,h(V+V_a)}{dx} = E|V| \tag{3.14}$$

These definitions are a very natural way of describing dense layers using depth averaged quantities; they are of especial use to the dense layer modeller as vertically integrating the Euler equations gives relations that may be expressed in terms of the quantities defined above. Here, these three quantities are functions of x alone.

Again following [52] the three equations linking the three flow quantities are:

$$Vh\Delta = A \tag{3.15}$$

$$\frac{d(Vh)}{dx} = EV \tag{3.16}$$

$$\frac{d(V^2h)}{dx} = -CV^2 - \frac{1}{2}\frac{d(S_1\Delta h^2\cos\theta)}{dx} + S_2\Delta h\sin\theta \tag{3.17}$$

where

$$S_1\Delta\rho_a h^2 = 2\int_{y=0}^{\infty} g(\rho-\rho_a)y\,dy \tag{3.18}$$

and

$$S_2\Delta\rho_a h = \int_{y=0}^{\infty} g(\rho-\rho_a)\,dy. \tag{3.19}$$

In equations 3.15 to 3.19, θ is the slope of the lower boundary; the Boussinesq approximation has been invoked. Equation 3.17 is the momentum equation for the fluid bounded by x, $x+\delta x$, and the lower boundary. These equations are relevant to any steady flow with negligible vertical acceleration. The first term on the right hand side of equation 3.17 is a drag term that accounts for the surface friction at the lower boundary; C is assumed to be independent of Reynolds number.

Such a vertical averaging process is clearly necessary in situations where the exact vertical density (or velocity) profile is not available, as here. The value of this type of analysis is that it allows the reduction, in an objective manner, of a complex flow (a stratified shear layer) to a small number of meaningful variables. These variables may be shown to behave in an easily predicted way.

3.4 The generalized shallow water equations in two dimensions

Extension of the time-dependent generalized shallow water equations to two dimensions is not straightforward. It is made difficult by the surprisingly large number of shape parameters required. The derivation given below includes seven dimensionless parameters.

When considering dense flows whose vertical structure may be ignored, four quantities are needed for shallow water modelling. These are: the depth averaged density $\overline{\rho}$; two components of depth averaged velocity, $\overline{u}$ and $\overline{v}$; and the depth of the layer, h.

The approach adopted here is to define the four depth averaged quantities in such a way as to make the treatment of buoyancy simple. The buoyancy b per unit volume of fluid of density ρ is $g(\rho - \rho_a)$; the total buoyancy B of the fluid within a volume V may be defined as

$$B = \int_{\mathbf{x}\in V} g(\rho - \rho_a)\, d^3\mathbf{x} \tag{3.20}$$

and it is well-known [179] that the continuity equation $\partial b/\partial t + \nabla \cdot (b\mathbf{u}) = 0$ (or equivalently $\partial B/\partial t + \int_{\partial V} b\mathbf{u} \cdot d\mathbf{S} = 0$) is satisfied in a uniform gravitational field.

With these comments in mind, it is convenient to use the following relations for definition of the four depth averaged quantities h, $\overline{\rho}$, $\overline{u}$, and $\overline{v}$:

$$h(\overline{\rho} - \rho_a) = \int_{z=0}^{\infty} (\rho(z) - \rho_a)\, dz \tag{3.21}$$

$$h(\overline{\rho} - \rho_a)\overline{u} = \int_{z=0}^{\infty} (\rho(z) - \rho_a)u(z)\, dz \tag{3.22}$$

$$h(\overline{\rho} - \rho_a)\overline{v} = \int_{z=0}^{\infty} (\rho(z) - \rho_a)v(z)\, dz \tag{3.23}$$

where $\rho = \rho(z)$ is the density of the layer at height z and $u(z), v(z)$ are the two components of velocity. This set of definitions requires another relation to close the system. A consistent way is

$$h(\overline{\rho} - \rho_a)(\overline{u}^2 + \overline{v}^2) = \int_{z=0}^{\infty} (\rho(z) - \rho_a)[u(z)^2 + v(z)^2]\, dz \tag{3.24}$$

or

$$h(\overline{\rho} - \rho_a)U = \int_{z=0}^{\infty} (\rho(z) - \rho_a)\sqrt{u(z)^2 + v(z)^2}\, dz, \tag{3.25}$$

where $U = \sqrt{\overline{u}^2 + \overline{v}^2}$ is the mean layer speed. It is possible to construct other definitions along similar lines following Ellison and Turner [52], or Liu *et al.* [125]; but all share with 3.24 and 3.25 the lack of simple incorporation into the desired end equations.

The approach adopted here is partially in response to risk assessors who require a definition of cloud height h related in a simple and direct way to the vertical density profile; the use of equations such as 3.24 or 3.25 precludes this desirable property.[2] The definition for h that will be used is that h is the height

[2]This is because the calculation of h requires the simultaneous solution of four equations. Interpretation of h is therefore not straightforward. It is also the case that any integral definition of h renders derivation of the volume conservation equation 3.29 (or, equivalently, a concentration advection equation such as 3.5) extremely complex.

below which some fraction α of the buoyancy is located:

$$\int_{z=0}^{h} (\rho(z) - \rho_a)\, dz = \alpha \int_{z=0}^{\infty} (\rho(z) - \rho_a)\, dz. \tag{3.26}$$

The choice of α is clearly arbitrary, but necessary. Useful values for α might be 0.90 or 0.95 ($\alpha = 1$ is only meaningful if there exists a height $z_{\max}$ such that $z > z_{\max}$ implies $\rho(z) = \rho_a$). The utility of this approach will become clear in chapter 4.

The generalized shallow water equations with no entrainment

It is convenient to derive the generalized shallow water equations for the case of zero entrainment, and account for entrainment at a later stage.

The generalized shallow water equations with zero entrainment in two dimensions may now be derived. If an infinitesimal control volume of infinite height is considered, in which there is no source or sink of buoyancy, equations 3.21 to 3.23 give

$$\frac{\partial h(\overline{\rho} - \rho_a)}{\partial t} + \frac{\partial h(\overline{\rho} - \rho_a)\overline{u}}{\partial x} + \frac{\partial h(\overline{\rho} - \rho_a)\overline{v}}{\partial y} = 0 \tag{3.27}$$

directly. This equation is an immediate consequence of conservation of buoyancy and the definitions 3.21 to 3.23.

A two-dimensional analogue of equation 3.1 is now required. If an infinitesimal volume bound by the ground and of height z is considered, the total volume flux into it will be zero. If $w = w(x, y, t; z)$ is the vertical component of velocity, then

$$w + \frac{\partial}{\partial x}\left[\int_{z'=0}^{z} u(x, y, t; z')\, dz'\right] + \frac{\partial}{\partial y}\left[\int_{z'=0}^{z} v(x, y, t; z')\, dz'\right] = 0. \tag{3.28}$$

If the case of $z = h$ is considered, then it is clear that $\partial h/\partial t = w(x, y, t; h)$ if there is no buoyancy flux normal to the instantaneous streamline passing through the top of the control volume.[3] Writing $\int_{z=0}^{h} u\, dz = k_u h\overline{u}$ and $\int_{z=0}^{h} v\, dz = k_v h\overline{v}$, and assuming that $k_u = k_v = k$, then

$$\frac{\partial h}{\partial t} + k\frac{\partial h\overline{u}}{\partial x} + k\frac{\partial h\overline{v}}{\partial y} = 0. \tag{3.29}$$

This equation is the volume conservation equation. This equation is independent of the choice of α, upon which h depends.

The derivation of the remaining two conservation equations is not straightforward. If it is assumed that there is no stress across the plane $z = h$, then the

[3]The above argument is also true for non-zero entrainment if the reasonable assumption that the divergence of the horizontal buoyancy flux below $z = h$ is α times the total: $\nabla \cdot (\mathbf{B}'_x) = \alpha\nabla \cdot (\mathbf{B}_x)$, where $\mathbf{B}_x$ is the horizontal component of buoyancy flux, and $\mathbf{B}'_x$ is the horizontal component of buoyancy flux above $z = h$.

momentum equations for an infinitesimal control volume bounded by the ground and $z = h$ are

$$\frac{\partial}{\partial t}\left[\int_{z=0}^{h} \rho(z)u(z)\,dz\right] + \frac{\partial}{\partial x}\left[\int_{z=0}^{h} \rho(z)u(z)u(z)\,dz\right] + \frac{\partial}{\partial y}\left[\int_{z=0}^{h} \rho(z)u(z)v(z)\,dz\right] = -\frac{\partial}{\partial x}\left[\left(\int_{z=0}^{h} gz[\rho(z)-\rho_a]\,dz\right) + h\int_{z=h}^{\infty} g(\rho(z)-\rho_a)\,dz\right] \tag{3.30}$$

and

$$\frac{\partial}{\partial t}\left[\int_{z=0}^{h} \rho(z)v(z)\,dz\right] + \frac{\partial}{\partial x}\left[\int_{z=0}^{h} \rho(z)u(z)v(z)\,dz\right] + \frac{\partial}{\partial y}\left[\int_{z=0}^{h} \rho(z)u(z)v(z)\,dz\right] = -\frac{\partial}{\partial y}\left[\left(\int_{z=0}^{h} gz[\rho(z)-\rho_a]\,dz\right) + h\int_{z=h}^{\infty} g(\rho(z)-\rho_a)\,dz\right]. \tag{3.31}$$

The left hand side of equations 3.30 and 3.31 use integrals which run from zero to h, not infinity. This is so because only finite quantities may be manipulated here. Also, the assumption of zero stress across the plane $z = h$ allows the use of a simpler hydrostatic forcing term on the right hand side.

A number of shape parameters is now required to link equations 3.30 and 3.31 with the volume conservation equation 3.29 and the buoyancy conservation 3.27. The spirit of these shape parameters follows the work of Ellison and Turner [52].

$$\int_{z=0}^{h} g[\rho(z)-\rho_a]z\,dz + h\int_{z=h}^{\infty} g(\rho(z)-\rho_a)\,dz = S_1.\frac{1}{2}gh^2(\overline{\rho}-\rho_a) \tag{3.32}$$

$$\int_{z=0}^{h} \rho(z)u(z)\,dz = S_u h\overline{\rho}\,\overline{u} \tag{3.33}$$

$$\int_{z=0}^{h} \rho(z)v(z)\,dz = S_v h\overline{\rho}\,\overline{v} \tag{3.34}$$

$$\int_{z=0}^{h} \rho(z)u(z)u(z)\,dz = S_{uu} h\overline{\rho}\,\overline{u}^2 \tag{3.35}$$

$$\int_{z=0}^{h} \rho(z)u(z)v(z)\,dz = S_{uv} h\overline{\rho}\,\overline{u}\,\overline{v} \tag{3.36}$$

$$\int_{z=0}^{h} \rho(z)v(z)v(z)\,dz = S_{vv} h\overline{\rho}\,\overline{v}^2 \tag{3.37}$$

Equations 3.32 to 3.37 are defined so that a uniform dense layer (that is, one in which the vertical concentration- and velocity- profiles are uniform) has all shape

parameters equal to unity. These parameters will be assumed to be constant and may thus commute past differentiation. The momentum equations for flow with no ground stress may now be recast:

$$S_u \frac{\partial h\overline{\rho}\,\overline{u}}{\partial t} + S_{uu}\frac{\partial h\overline{\rho}\,\overline{u}^2}{\partial x} + S_{uv}\frac{\partial h\overline{\rho}\,\overline{u}\,\overline{v}}{\partial y} + S_1\frac{\partial \frac{1}{2}g(\overline{\rho}-\rho_a)h^2}{\partial x} = 0 \quad (3.38)$$

$$S_v \frac{\partial h\overline{\rho}\,\overline{v}}{\partial t} + S_{uv}\frac{\partial h\overline{\rho}\,\overline{u}\,\overline{v}}{\partial x} + S_{vv}\frac{\partial h\overline{\rho}\,\overline{v}^2}{\partial y} + S_1\frac{\partial \frac{1}{2}g(\overline{\rho}-\rho_a)h^2}{\partial y} = 0 \quad (3.39)$$

These equations, together with the buoyancy conservation equation 3.27 and the volume equation 3.29, constitute the generalized shallow water equations with zero entrainment. The case of non-zero entrainment is considered below.

The generalized shallow water equations with source terms and entrainment

The generalized shallow water equations may easily account for a source of buoyancy; the paradigm is a pool of evaporating liquified gas, but the formulation presented here is applicable to any source of buoyancy. Here, the upward speed of the source gas (of density ρ_s) is u_s; it is assumed to have no horizontal momentum.

The right hand sides of equations 3.38 and 3.39 are zero: no momentum from the ambient fluid enters the dense layer. If entrainment occurs, the entrained fluid carries with it momentum. If the entrainment rate is W and the ambient fluid moves at speed $\mathbf{u}_a = (u_a, v_a)$, then:

$$\frac{\partial h}{\partial t} + k\frac{\partial h\overline{u}}{\partial x} + k\frac{\partial h\overline{v}}{\partial y} = W + u_s \quad (3.40)$$

$$\frac{\partial h(\overline{\rho}-\rho_a)}{\partial t} + \frac{\partial h(\overline{\rho}-\rho_a)\overline{u}}{\partial x} + \frac{\partial h(\overline{\rho}-\rho_a)\overline{v}}{\partial y} = u_s(\rho_s-\rho_a) \quad (3.41)$$

$$S_u \frac{\partial h\overline{\rho}\,\overline{u}}{\partial t} + S_{uu}\frac{\partial h\overline{\rho}\,\overline{u}^2}{\partial x} + S_{uv}\frac{\partial h\overline{\rho}\,\overline{u}\,\overline{v}}{\partial y} + S_1\frac{\partial \frac{1}{2}g(\overline{\rho}-\rho_a)h^2}{\partial x} = W\rho_a u_a \quad (3.42)$$

$$S_v \frac{\partial h\overline{\rho}\,\overline{v}}{\partial t} + S_{uv}\frac{\partial h\overline{\rho}\,\overline{u}\,\overline{v}}{\partial x} + S_{vv}\frac{\partial h\overline{\rho}\,\overline{v}^2}{\partial y} + S_1\frac{\partial \frac{1}{2}g(\overline{\rho}-\rho_a)h^2}{\partial y} = W\rho_a v_a \quad (3.43)$$

which are in conservation form. All seven shape parameters are here assumed to vary slowly with time and distance and thus may be taken outside or inside the differentiation.

3.5 Surface stress

Typical dense gas releases travel over rough ground, and it is clear that a drag on the dense layer will be exerted. Britter and McQuaid ([30], chapter 4) consider

the effect of ground roughness to be 'peripheral' and the simple approach adopted here reflects this.

Although the surface shear stress is a function of the stratification of the dense layer as reported by Kantha *et al.* [109], this effect will be ignored.

The ground stress $\boldsymbol{\tau}$ used is a standard model:

$$\boldsymbol{\tau} = -\frac{1}{2}\overline{\rho} C_D \boldsymbol{u}|\boldsymbol{u}| \tag{3.44}$$

where C_D is a constant. Here, C_D may be a function of position, thus allowing some account of the effect of surface roughness variations to be made.

3.6 The generalized shallow water equations over complex terrain

The momentum equations may easily be generalized to account for non-horizontal lower boundaries and are stated with no derivation:

$$\begin{aligned} S_u \frac{\partial h\overline{\rho}\,\overline{u}}{\partial t} + S_{uu}\frac{\partial h\overline{\rho}\,\overline{u}^2}{\partial x} + S_{uv}\frac{\partial h\overline{\rho}\,\overline{u}\,\overline{v}}{\partial y} \\ + S_1\left[\frac{\partial \frac{1}{2}g(\overline{\rho}-\rho_a)h^2}{\partial x} + g(\overline{\rho}-\rho_a)h\frac{\partial(e)}{\partial x}\right] = W\rho_a u_a - \frac{1}{2}C_D\overline{u}|\boldsymbol{u}| \end{aligned} \tag{3.45}$$

and

$$\begin{aligned} S_v \frac{\partial h\overline{\rho}\,\overline{v}}{\partial t} + S_{uv}\frac{\partial h\overline{\rho}\,\overline{u}\,\overline{v}}{\partial x} + S_{vv}\frac{\partial h\overline{\rho}\,\overline{v}^2}{\partial y} \\ + S_1\left[\frac{\partial \frac{1}{2}g(\overline{\rho}-\rho_a)h^2}{\partial y} + g(\overline{\rho}-\rho_a)h\frac{\partial(e)}{\partial y}\right] = W\rho_a v_a - \frac{1}{2}C_D\overline{v}|\boldsymbol{u}| \end{aligned} \tag{3.46}$$

where $e = e(x, y)$, the ground elevation, is now a function of x and y. Here, $\mathbf{u} = (u, v)$ is the horizontal component of velocity. The buoyancy generated force acting on the dense layer is zero if $\overline{\rho}$ and $e + h$ are constant; this corresponds to a dense fluid of uniform density with a horizontal free surface.

3.7 Discussion

The volume conservation equation 3.40 and the buoyancy conservation equation 3.41 together imply, for the non-entraining case with no source,

$$\frac{\partial h\overline{\rho}}{\partial t} + \frac{\partial h\overline{\rho}\,\overline{u}}{\partial x} + \frac{\partial h\overline{\rho}\,\overline{v}}{\partial y} = \rho_a(1-k)\left[\frac{\partial h\overline{u}}{\partial x} + \frac{\partial h\overline{v}}{\partial y}\right] \tag{3.47}$$

and it is clear that the right hand side of equation 3.47 is zero for the non-generalized shallow water equations, as k is equal to one. However, equation 3.47 must not be regarded as a mass flux equation: the mass flux of the cloud in terms of the shallow water variables introduced above is not well-defined. This may be seen by considering a vertical density profile of the form $\rho(z) = \rho_a + \rho_0 \exp(z/h_0)$, where h_0 is a depth scale of the cloud.[4] Now the *buoyancy* flux $g \int_0^\infty (\rho(z) - \rho_a).\mathbf{u}\, dz$ is clearly almost unaffected by the fluid speed $\mathbf{u}$ changing at heights $\gg h_0$; but the mass flux $\int_0^\infty \overline{\rho}\mathbf{u}\, dz$ is strongly dependent upon the speed of fluid at any height. The mass flux is thus seen to be of limited relevance to a dense layer whose properties (such as depth and speed) should be functions only of fluid at heights $\sim h$. One possibility is to define a quantity $M = h\overline{\rho}$ and then identify M with mass per unit area; the mass flux is then $M\mathbf{u}$. However, equation 3.47 shows that M is not conserved so M is not a useful quantity.

Webber [184] points out that the shallow water variables as defined above lack Galilean invariance.[5] Although the physical system considered here clearly exhibits Galilean invariance, the dimensionless shape parameters are dependent on the coordinate system in which they are evaluated. This dependence is assumed to be weak. The special case of 'top hat' profiles (that is, uniform density- and velocity- profiles both of the same height) implies that all the shape parameters are unity, for all observers.

As reported by Jirka and Arita [106], density currents brought to rest by an oncoming boundary layer can assume the form of a density wedge, a configuration not well modelled by the present approach because of the mismatch between the buoyancy- and volume- fluxes.

3.8 Summary

This chapter has shown that the shallow water equations 3.1 to 3.3 may be generalized to include the effects of non-uniform density- and velocity- profiles, and ground slope. This requires the introduction of a large number of dimensionless shape parameters, and essentially follows the work of Ellison and Turner [52].

[4]The length scale h_0 is distinct from the cloud depth h: with this density profile, equation 3.26 implies that $h = -h_0 \log(1 - \alpha)$.

[5]True coordinate independence may be obtained by definition of a momentum vector $P_i = hS_{(i)}\overline{\rho}u_i$, and a momentum flux tensor $M_{ij} = S_{(ij)}h\overline{\rho}u_iu_j$ (not summed over bracketed indices), giving the expressions

$$\partial_t h + k(hu_j)_{;j} = W + u_s \tag{3.48}$$

$$\partial_t B + (Bu_j)_{;j} = u_s(\rho_s - \rho_a) \tag{3.49}$$

$$\partial_t P_i + (M_{ij})_{;j} + G_{;i} + [S_1 B](e_{;i}) = W\rho_a(\mathbf{u}_a)_i \tag{3.50}$$

where a subscript of '$;j$' is interpreted as (covariant) differentiation with respect to x_j. Here, $B = h(\overline{\rho} - \rho_a)g$ is the buoyancy, and $G = S_1 \frac{1}{2} g(\overline{\rho} - \rho_a)h^2$ the potential energy, per unit area.

This work differs from previous approaches in defining h as that height above which a certain, fixed proportion of the buoyancy of the dense layer lies. This approach allows h to be meaningfully defined in the context of two dimensional shallow flow. The generalized shallow water equations 3.40 to 3.46 will be used in the remainder of this work to investigate the behaviour of accidentally released dense gas clouds.

Chapter 4

The shallow water equations and heavy gas dispersion

4.1 Outline

This chapter will consider the physical basis for assuming that the shallow water approximations accurately describe a dense gas release, and under what circumstances they break down.

The shallow water approximations are useful for describing systems of small aspect ratio (that is, average depth over horizontal extent) which have Lagrangian vertical accelerations that are small compared to g'.

A hydraulic jump is not a solution to the shallow water equations [171]. As hydraulic jumps (and the closely related phenomenon of bores) are known to occur, the shallow water equations must be modified to simulate them. The modification required is an additional term that models the loss of mechanical energy associated with a hydraulic jump.

It is clear that the shallow water approximations are incorrect at the leading edge of a gravity current. The method developed in this chapter to account for the leading edge will be used throughout the rest of this thesis.

These points are discussed in turn below, followed by an account of the method used to simulate the leading edge.

4.2 The aspect ratio of heavy gas releases

Dense gas, on release into the atmosphere, tends to slump to the ground due to its negative buoyancy, and simultaneously tends to spread outwards as a gravity current is generated. These processes tend to decrease the aspect ratio of the cloud and it is not until dilution of the cloud by the ambient fluid becomes important that the aspect ratio will start to increase again.

The first and second Thorney Island series of experiments [129, 130], in general, support this view.

Dense gas releases over complex terrain have received relatively little attention [25] and any conclusions must therefore be more tentative, but several workers such as Brighton *et al.* [20] and Webber *et al.* [191] have used the shallow water equations in this context and this work will follow them.

This work will consider only dense gas flows of low aspect ratio. This restriction implies that the earliest stages of some accidental releases of dense gas cannot be simulated.

4.3 Vertical acceleration in heavy gas releases

As the shallow water approximations require a hydrostatic pressure distribution ($\partial p/\partial z = -\rho g$) within the dense layer it is clear that any fluid with significant vertical Lagrangian acceleration will invalidate the approximation.

The shallow water equations as derived in chapter 3 are applicable only to a fluid within which vertical acceleration is zero. Formally, the hydrostatic forcing term F (the right hand sides of equations 3.30 and 3.31) in one dimension is

$$F = \frac{\partial}{\partial x} \int_{z=0}^{h} p \, dz, \tag{4.1}$$

where p is the pressure at any point. For F to be significantly different from that calculated on the basis of a hydrostatic pressure distribution, there must be systematic deviations of pressure from hydrostatic. Any deviations must be caused by vertical acceleration of dense fluid. To be significant, they must be of vertical and horizontal length scale $\gtrsim h$; and they must persist for times $\gtrsim (h/g')^{1/2}$. As system-averaged vertical accelerations $\sim g'(h/L)^2$, where L is the horizontal length scale, this approximation is well suited to systems of low aspect ratio, as here.[1] However, vertical acceleration occurs locally and is associated with three phenomena:

1. turbulent (three-dimensional) eddies within the cloud,
2. the bulk motion of dense fluid over a sudden slope change, and
3. dense flow phenomena such as leading edges or hydraulic jumps.

The first cause of vertical acceleration, turbulent eddies in the dense layer, has been the subject of much study including work by Georgiev [63], Mercer and Davies [136], and Bo Pedersen [12]. In general, the stable stratification found in

[1] Baines [6] shows that the hydrostatic approximation is valid if $Fr.\frac{h}{L} \ll 1$. Here $Fr = u/\sqrt{g'h}$ is a typical Froude number.

dispersing dense gas clouds inhibits vertical motion and therefore forces the pressure distribution to be more nearly hydrostatic. It is common practice to consider these turbulent eddies as random perturbations superimposed on the background (gravity driven) flow, as done by Brandeis and Ermak [17] and Brandeis and Kansa [18]. These workers implicitly assumed that the timescales associated with such random perturbations were small compared with those of interest. This approach will be adopted here.

The second cause, dense fluid flowing over a sudden change of ground slope, may be viewed as a situation in which body forces are generated on the dense fluid. These forces are not important in practice because they act only on the dense fluid near a change in ground slope; and in the case of steady flow, they do no work. The physical accuracy of the shallow water equations is recovered by defining a region W outside of which the pressure distribution is hydrostatic[2] and ignoring the detailed structure of the flow within W.

The third cause of non-hydrostatic pressure distributions is the existence of dense layer flow features such as bores and the leading edge. It is well known [69, 70] that it is important to simulate these features accurately as they may exert a profound effect on the structure of the flow (unlike the effects of changes of ground slope considered above).

A bore is equivalent to a hydraulic jump for the case when the density of the upper fluid is small compared to that of the lower; a bore is a hydraulic jump moving with respect to the coordinate system chosen. The equivalence is lost when the two densities are comparable, as then the upper fluid, if moving relative to the jump, may exert a significant net force on the fluid of the jump by virtue of its velocity.

It is convenient to define a hydraulic jump as a special case of a bore in which the relative speed of jump and upper fluid is zero. A leading edge is thus a special case of a bore in which the upstream fluid depth is zero.

As the pressure distribution within a hydraulic jump is not hydrostatic,[3] the shallow water equations may not be used to simulate the detailed structure of such a region.

These flow features are particularly important to the shallow water modeller. The leading edge, in particular, may control the flow behind it and thus may exert an important effect on the global flow structure; also, bores may control regions of the flow, as reported by Wood and Simpson [196].

The next section presents a unified method by which both these phenomena may be simulated in a shallow water model.

[2]The size of this region W may be determined for a one-dimensional steady flow by comparing body forces to buoyancy forces. If the change in ground slope within W is $\Delta\theta$, and the change in Richardson number Ri based on speed and fluid depth above some datum is ΔRi, then W will be sufficiently large if $\Delta\theta \ll \Delta Ri$.

[3]Unless it is very weak, in which case the flow near the jump is not steady because waves are generated.

4.4 Hydraulic jumps

One of the validation exercises carried out in chapter 7 is the simulation of a hydraulic jump. Although motivation for this exercise is given there, it is noted here that hydraulic jumps are anticipated in dense gas dispersion by Webber *et al.* [191] (although this study was confined to the non-entraining case) and must therefore be simulated accurately.

It is clear that the velocity of fluid in a dense layer varies from the depth averaged velocity by a fluctuating amount. These fluctuations are potentially important in regions of large (depth averaged) velocity gradients as turbulent shear stresses are generated.

Several workers consider this problem [54, 55, 57] in the context of tidal flow fields in estuaries. Although the turbulence in tidal flows is different from that in density currents (stable density gradients are absent in these flows [113]), it is reasonable to adopt a similar term to model the turbulent shear stress, with different constants.

If the dense layer moves with depth averaged velocity $\boldsymbol{u} = (\overline{u}, \overline{v})$, the result of turbulent shear stress is to exert a force $\boldsymbol{V} = (V_x, V_y)$ per unit area on the dense fluid, where

$$\boldsymbol{V} = \zeta h \overline{\rho} \nabla \cdot (\lambda \nabla \boldsymbol{u}) . \tag{4.2}$$

Here ζ is a small constant of proportionality and λ is a quantity that measures turbulent interaction between adjacent fluid elements. Dimensionally, λ must be of the form m^2/s in SI and a common choice is $\lambda = h|\boldsymbol{u}|$. This choice will be used for the remainder of this thesis, and the importance of ζ will be discussed further in chapter 7. Equation 4.2 is more readily expressed in index form:

$$V_i = \zeta h \overline{\rho} \frac{\partial}{\partial x_j} \left(\lambda \frac{\partial u_i}{\partial x_j} \right) . \tag{4.3}$$

The effects of a non-zero ζ are mostly apparent at hydraulic jumps because only there do the second derivatives used to calculate $\boldsymbol{V}$ become large. Turbulent shear does not strongly affect the leading edge under the depth averaged approach adopted here, because the (depth averaged) velocity of dense fluid near a leading edge is quite uniform.

Equation 4.3 is not in conservation form (chapter 7 discusses conservation forms for differential equations). Roache [158] considers a term of the same form as equation 4.3 in the related field of compressible gas flow. He gives two examples of cases in which the conservation form for terms like those in equation 4.3 are more accurately modelled using non-conservation forms.

4.5 The effect of the ambient fluid on a dense layer

The shallow water equations as developed in chapter 3 assume that the ambient fluid has a pressure distribution that is hydrostatic. It is clear that this is not true for the ambient fluid close to the leading edge, as this fluid undergoes considerable vertical acceleration as it is displaced by the oncoming dense current. This behaviour also occurs elsewhere and is discussed below.

The central tenet of this thesis is that a gravity current such as a dense gas release may be modelled as a shallow water flow, with additional terms that are applied close to the leading edge. These additional terms encompass the strong interaction between dense fluid of the leading edge and the ambient fluid. For the purposes of identifying closeness to the leading edge, a 'front parameter' will be defined that is large close to a leading edge and small everywhere else. These comments may apply equally to a bore as a bore can control the flow behind it [196].

4.5.1 The leading edge of a gravity current

Gravity currents consist of two major regions, the leading edge and the following flow. These regions exhibit very different behaviour and Simpson [171] reports:

> The leading edge of a gravity current forms a typical frontal zone, i.e. although intense mixing is present, a sharp dividing line is maintained between the two fluids. A characteristic 'head' which is deeper than the following flow is usually formed at the front. This raised head is a zone of breaking waves and intense mixing and plays an important part in the control of the current which follows. In a gravity current moving horizontally the head remains steady but in one flowing down an incline the relative size of the head increases with the angle of the slope.

The leading edge of a gravity current, being so qualitatively and quantitatively different from the rest of the flow, has prompted many workers to deal with it as a control for the following flow [69, 163, 164].

Nondimensionalisation of the front speed may be carried out in a number of ways. Although considering steady buoyancy release on slopes, Britter and Linden [29] gave evidence that nondimensionalising U_f with the cube root of buoyancy flux $(g_0'Q)^{1/3}$ gave consistent and accurate results.

This approach requires knowledge of the flow far from the leading edge. As the present work treats unsteady flows over two-dimensional topography, such information is not available and another dimensionless group, using only 'local'

information, must be used. Use will be made of the term 'local variable', which is defined as a function of the flow close to the region of interest.

The dimensionless parameter used here to describe gravity current fronts is the Froude number $Fr = U_f/\sqrt{g'h}$ where U_f is the speed of advance of the current into the ambient fluid, $g' = g(\rho - \rho_a)/\rho_a$ is the reduced gravity of the layer, and h is the depth of the gravity current head. Note that the front speed is relative to the ambient flow and so $U_f = \overline{u} - u_a$.

Many experimental investigations of gravity current fronts indicate that the front Froude number is of order one [31, 10, 168] and many numerical investigations [69, 70, 186, 191] simulate gravity currents as shallow water flows controlled by a discontinuity whose speed is set to maintain a constant Froude number.

This approach is commonly used amongst one-dimensional simulations [69, 163, 164] as the position of the front is described by a single number: the distance from some reference point of the discontinuity of the front. Axisymmetric flows are considered to be one-dimensional because the flow is described in terms of the real variable r, the radius. This type of flow also has a front that may be completely described by one real variable.

A diagrammatic illustration of a one-dimensional flow is given is figure 4.1. It can be seen that all the structure of the leading edge is neglected and the leading edge is used solely to control the following flow by way of fixing the front Froude number.

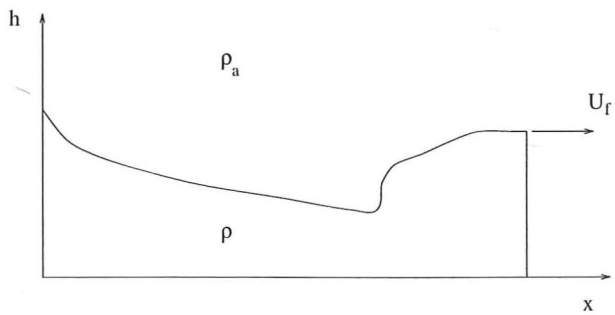

Figure 4.1: A one-dimensional model of shallow water flow (diagrammatic)

As simulations of this type adopt the shallow water approximations simulation of the detailed structure of the leading edge is not possible. Nor is it an objective: description of the leading edge necessarily requires information not included in the shallow layer variables.

Extension of the ideas presented above to two dimensions is not trivial. The present author [83] investigated two-dimensional analogues of the techniques described above and concluded that the generalization was impractical. One of the

most difficult problems encountered was that of keeping track of the discontinuity that marked the leading edge of the flow. When simulating one-dimensional gravity currents, the position of the discontinuity is completely described by a single real variable. This variable represents the distance of the leading edge from some datum point and there exist well established methods [43, 203] for simulating one-dimensional gravity current leading edges travelling at fixed front Froude numbers.

In two space dimensions this discontinuity is a *line* rather than (as in one-dimensional simulations) a point. However, the line which marks the position of the leading edge in a two-dimensional flow is capable of exhibiting much more complex behaviour.

For example, figure 4.2 shows a plan view of a horseshoe-shaped dense gas cloud flowing around a region of high elevation.[4] It is seen that, although there is actually little difference between the two clouds, there is a great difference between their boundaries. In the first case, the boundary is one continuous line; but in the second, there are two distinct lines, each one of which is a boundary. Any computational scheme has to check for this type of behaviour and this is complex, potentially unreliable, and costly in terms of computer processing time. Other problems encountered in this type of simulation are detailed by Hankin and

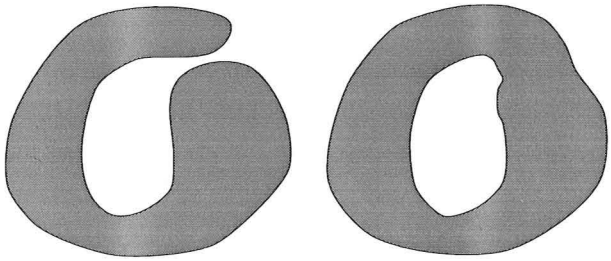

Figure 4.2: Plan view of dense gas cloud changing genus. The shaded area represents ground covered by the cloud

Britter [83].

The alternative method of simulation, known as 'shock smearing' [158, 174] involves modelling a discontinuity as being spread over a small number of computational elements. The structure of the flow in this region is subsequently ignored. As discussed in chapter 7, there is a close correspondence between the shallow water equations and the Euler equations for compressible gas flow. Computational problems in compressible gas dynamics have many features in common with shallow water problems and shock smearing techniques developed for compressible gas flow have precise analogues in the present problem. In particular, a shock in

[4]Such flow is observed in practical dense gas dispersion predictions [84] and an example is shown in appendix F.

compressible gas flow is entirely analogous to a hydraulic jump in shallow water flow, discussed from an experimental viewpoint by Gilmore *et al.* [66].

The computational model used in this thesis uses a shock smearing method, detailed in chapter 6. The implementation of this method requires some knowledge of the processes affecting fluid at the leading edge, and in particular an understanding of the agency by which the hydrostatic force tending to accelerate the flow forward is balanced to give a quasi-steady front.

4.5.2 The leading edge in a two-dimensional gravity current

Figure 4.3 shows a schematic cross section of a gravity current advancing along a horizontal lower boundary into an expanse of lighter fluid. This type of flow is known as two-dimensional as the vertical structure is also important. The depth averaged density of the current is ρ and that of the ambient fluid ρ_a. The leading edge is viewed in a coordinate system that brings it to rest.

Motion will be assumed to be steady, following Britter and Simpson[5] [31] and the Reynolds number Re will be assumed to be sufficiently large to be immaterial [171, 172, 168].

Schmidt number, Sc, effects will also be ignored, following Kantha *et al.* [109]. Crapper and Linden [44], however, investigating turbulent density interfaces, argue that the Péclet number $Pe = Re/Sc$ is important, but only for $Pe \leq 200$. As Pe typically exceeds 10^5 in cases of interest, these effects may safely be ignored.

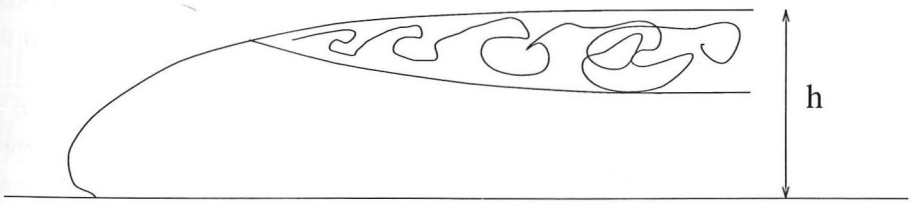

Figure 4.3: Schematic view of a one-dimensional gravity current

In figure 4.3, h is the height of the current. Head height was defined by Simpson and Britter [172] as "the height from the ground to the top of the billows forming on the head before they began to break up and lose a clear outline" and is mentioned here to show that the unsteady nature of the flow does not preclude the use of a unique height.

[5]The assumption of steady flow was examined by Simpson and Britter [172], who discussed the unsteady three-dimensional flow near the head. These workers proposed that the ensemble-averaged flow field relative to the gravity current head was sufficient to describe the flow and this is done here.

The velocity U_f of the gravity current is determined by the quantities ρ, ρ_a, h, and g; thus $U_f = f(\rho, \rho_a, h, g)$. Introduction of the Boussinesq approximation reduces the independent variables to h and the reduced gravity $g' = g(\rho - \rho_a)/\rho_a$. A simple dimensional analysis [169] shows that the densimetric Froude number $Fr = U_f/\sqrt{g'h}$ is constant; several workers [69, 70, 186, 191] have carried out simulations on the supposition of constant densimetric front Froude numbers, and this work follows those cited.

A slight rearrangement of the equation expressing the fact that the densimetric front Froude number is constant gives

$$\frac{1}{2}S_1 g(\rho - \rho_a)h^2 = kh\rho_a(U_f)^2, \tag{4.4}$$

where S_1 is the shape parameter introduced on page 32, and k is another constant.

The generalized shallow water equations derived in chapter 3 will not simulate the behaviour of a gravity current, because they predict that a net force acts on the dense fluid of the leading edge, thereby accelerating it. This is clearly not the case, as gravity currents such as illustrated in figure 4.3 are known to advance at a constant speed over level ground, if the buoyancy flux at the head is constant.

The shallow water equations give erroneous results for the leading edge of a dense layer as they assume that the pressure distribution at $z = h$ is hydrostatic; this is untrue in the vicinity of a leading edge as the ambient fluid has a stagnation point close to the frontmost part of the head. The pressure there thus exceeds that far upstream at the same level by $\frac{1}{2}\rho_a U_f^2$.

Equation 4.4 suggests a simple method by which the leading edge of a gravity current may control the following flow in a depth averaged model:

1. Firstly, the shallow water equations will be applied to the whole of the dense layer, including the leading edge where they are not applicable. The shallow water equations show that a net force is exerted on the fluid of the leading edge and its magnitude per unit width is readily calculated to be the left hand side of equation 4.4.

2. A force equal to the right hand side of equation 4.4 will be applied to the fluid of the leading edge, accounting for the non-hydrostatic pressure distribution found at $z = h$.

The result of steps 1 and 2 above is to simulate the leading edge insofar as it controls the following flow, although the detailed structure of the leading edge is not simulated. This must be the case as the shallow water approximations are violated in this region.

Forces of the same form as the right hand side of equation 4.4 are commonly encountered when considering the form drag exerted on bluff bodies moving through

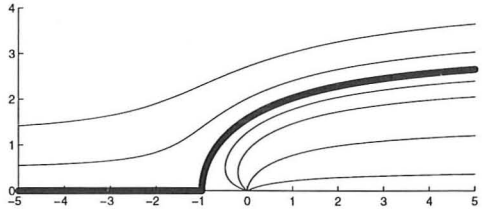

Figure 4.4: Source at $(0,0)$ of unit strength in inviscid fluid moving with unit speed from left to right; dividing streamline ($\psi = 0$) shown in bold

a fluid[6] [7]. Rearranging equation 4.4 gives

$$k = 2/(S_1.Fr^2). \tag{4.5}$$

This relation furnishes (by virtue of defining k) a shock-smearing method for simulating a leading edge with a fixed front Froude number.

The force corresponding to the right hand side of equation 4.4 affects the dense layer at the leading edge. However, this force acts upon an extended region of the dense layer and methods of accounting for this force are discussed below.

Because shock-smearing techniques are constrained to use only shallow water variables (that is, the depth, density, and speed of the flow) some way must be found to distribute the force $F = k\rho_a h(U_f)^2$ amongst the dense fluid 'near' the front and this is done by isolating a parameter P of the flow which is large near the front and small everywhere else. The resisting force F may then be applied to the fluid in proportion to P and as long as $\int_{x=0}^{\infty} P\,dx = F$, the total resistive force applied will be as indicated in equation 4.4. This scheme allows the simulation of a gravity current front moving at a constant front Froude number.

It remains to isolate a suitable front parameter P and show that it has the required properties. Because internal bores and hydraulic jumps are closely related to leading edges, the choice of P will have to account for these in addition to

[6]There is an inviscid solution of a source in a uniform stream, as shown in figure 4.4, and the part of this flow field above the dividing streamline is identical to fluid flowing over an infinitely long body of a similar shape to the foremost part of a gravity current. It can be shown that the horizontal force exerted on such a body by the fluid is $hP_0 + \frac{1}{2}g\rho h^2$ per unit width where h is the (asymptotic) height of the body and P_0 is the free stream pressure at elevation h; Batchelor [7], page 461, gives an analogous result for the axisymmetric case. This force is independent of the free stream fluid speed. This apparent paradox may be resolved by comparing the flow outside a gravity current instead to that found in the theory of Helmholtz motions [144]. If a body bound by the $x-$ axis, a straight lamina extending from the origin to $(0,h)$ and the streamline touching the lamina is considered, then the horizontal force on the body is $hP_0 + \frac{1}{2}g\rho h^2 + h\pi/(\pi+4)\rho u^2$ per unit width, where u is the free stream fluid speed. The body so described is a Riabouchinksy solid.

leading edges; this type of flow feature is commonly encountered in shallow water models of dense gas dispersion—for example, those of Webber *et al.* [190, 191]. Hydraulic jumps are considered below.

4.5.3 Hydraulic jumps in a one-dimensional gravity current

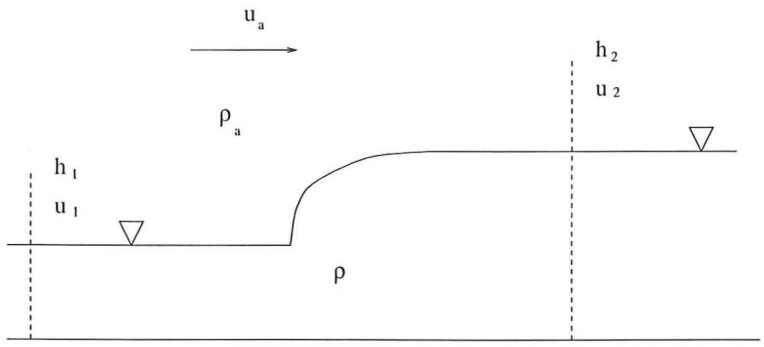

Figure 4.5: Hydraulic jump at rest in ambient fluid of speed u_a

Figure 4.5 shows a steady hydraulic jump at rest in an ambient fluid of density ρ_a moving at speed u_a, but the case of $u_a = 0$ is considered first as it is simpler. It is known [97, 171] that the shallow water equations as described in chapter 3, together with the stress given in equation 4.2, are adequate to describe the behaviour of the dense fluid. This is because the ambient fluid is at rest and the pressure distribution within it (and therefore at $z = h$) will be hydrostatic.

In the case of non-zero u_a, ambient fluid is forced over the jump and correct simulation of this system requires additional terms to be added to the shallow water equations to account for the non-hydrostatic pressure distribution at the boundary.

If the situation shown in figure 4.5, with $u_a > 0$ is viewed from a frame in which the ambient fluid is at rest, the system is more commonly described as a 'bore' [171, 196]. The shallow water equations, as they assume the pressure distribution at $z = h$ to be hydrostatic, predict that bores accelerate. However, bores are known to advance at a constant Froude number so the shallow water equations are not capable of describing their behaviour.

Wood and Simpson [196] consider bores in a flume of finite depth D. Their results were dependent upon the ratios y_1/D and y_2/D where y_1 and y_2 were the dense layer depths upstream and downstream of the bore respectively. However, they concluded that strong bores (that is bores with large y_2/y_1) behaved as though they were gravity currents and the results of Simpson and Britter [172] were approximately correct (Baines [6] reports that "jumps behave essentially as

gravity currents when breaking occurs."). This characterization became inaccurate only for cases where the ratio of upstream depth to downstream depth was small and the bore became undular.

It is thus reasonable to consider a bore as though it were a front of height $h_2 - h_1$ advancing at speed u_a into the ambient fluid.

If this is the case, then the correct behaviour of a bore may again be simulated by accounting for the non-hydrostatic pressure distribution at $z = h$. This may be carried out by generalizing the method described above for leading edges.

Bores will thus be simulated correctly by application of the shallow water equations, with an additional force accounting for the non-hydrostatic pressure distribution at $z = h$. This force will be of magnitude $k.(h_2 - h_1)\rho_a u_a^2$ per unit width. This will ensure that bores are simulated correctly.

Note that u_a is the speed of the ambient fluid relative to the *jump,* and not the speed of the fluid of the dense layer; the jump itself may be at rest, although the fluid of which it is comprised is moving.

4.5.4 Choice of P

The choice of P will have to account for the situations described above. Also, to preserve the shallow water equations' accuracy, P must be small everywhere except close to a leading edge or a bore.

There is only one simple choice of P that is Galilean invariant, and correctly predicts the force exerted by moving ambient fluid on a dense layer in the cases considered above. This is

$$P = -k\rho_a \left[\frac{\partial h(u - u_a)}{\partial t} + u_a \frac{\partial h(u - u_a)}{\partial x} \right] \tag{4.6}$$

which is Galilean invariant. Equation 4.6 may be rewritten as

$$P = -k\rho_a \left(\frac{\partial}{\partial t} + u_a \frac{\partial}{\partial x} \right) [h(u - u_a)].$$

The right hand side is a Galilean invariant operator acting on a Galilean invariant quantity. Here, u_a is the wind speed *relative to the coordinate system.* One interpretation of P is the volume rate of displacement of ambient fluid per unit area, as measured by an observer at rest relative to the ambient fluid.

The force on a dense layer predicted by P is evaluated for three simple cases below.

1. P at a hydraulic jump at rest relative to the ambient fluid

   The suitability of formula 4.6 for P may be seen by considering the hydraulic jump shown in figure 4.5 with $u_a = 0$. In this case, the force exerted by the ambient fluid on the dense layer is purely hydrostatic (i.e. $P = 0$) as the

ambient fluid is at rest relative to the jump and consequently the pressure therein (and in particular at $z = h$) is hydrostatic. This is anticipated in equation 4.6, which correctly shows that P is zero.

2. P at a leading edge

   It may seen that formula 4.6 integrates to the correct value for a leading edge by transforming to a frame in which the speed of the dense fluid of the head is zero (this is often done in experiments in which the head is brought to rest with respect to the laboratory). If this is done, $P = k\rho_a(u_a)^2\partial h/\partial x$ is obtained and $F(= \int_{x=0}^{\infty} P\,dx) = k\rho_a h(u_a)^2$, as required. This illustration also shows that the 'front parameter' is proportional to the gradient of dense layer depth in the case of a gravity current front, which is reasonable; also, P is small everywhere except near a leading edge, as required. However, the generality of equation 4.6 precludes such simple characterizations as may be seen by considering P at hydraulic jumps.

3. P at a hydraulic jump moving at speed u_a relative to the ambient fluid

   Here, it is convenient to transform to a coordinate system in which the hydraulic jump is at rest; thus $\partial(hu)/\partial x = 0$, and $\partial/\partial t$ is equal to the zero operator. Thus $P = k\rho_a(u_a)^2\partial h/\partial x$ which correctly integrates to give $F = k\rho_a(\Delta h)(u_a)^2$, where $\Delta h = h_2 - h_1$ is the depth change across the jump.

It is seen that the formula for P accurately accounts for the situations discussed above. This is strong evidence that P is an appropriate front parameter.

There is one rare case that is not covered here: that of a retreating dense layer.[7] If, for example, a moving layer with a sharp trailing edge is considered, then equation 4.6 predicts that a net force acts on the trailing edge in the direction of its motion. This is clearly incorrect and this is dealt with in chapter 5 along with the edge entrainment.

If the speed of the approaching ambient fluid is dependent upon height, then u_a is taken as $u_a(h) = u_a(h(x))$, where $h(x)$ is the depth of the dense layer at point x.

4.5.5 Generalization of P to two dimensions

There is only one simple generalization of equation 4.6 to two dimensions: the front parameter becomes the vector quantity $\boldsymbol{P}$, where

$$\boldsymbol{P} = -k\rho_a \left[\frac{\partial[h(\boldsymbol{u} - \boldsymbol{u}_a)]}{\partial t} + (\boldsymbol{u}_a \cdot \nabla)\,[h(\boldsymbol{u} - \boldsymbol{u}_a)] \right]. \tag{4.7}$$

[7] This is rare because the hydrostatic term usually forces a dense layer with sharp depth gradient to intrude into the ambient fluid; this case must nevertheless be covered as incorrect modelling could lead to unphysical simulations.

This formula for the front resistance term is the one used throughout this thesis. The quantity $\boldsymbol{P}$ is now the force exerted by the ambient fluid on the dense layer per unit area and is thus a stress.

The generalization shown in equation 4.7 has some consequences that are perhaps unexpected, particularly in the case of gravity current fronts that are not perpendicular to the oncoming flow. In such cases, equation 4.7 predicts that a force parallel to the leading edge (a lateral force) acts on the dense fluid. Experimental work on such flows does exist for instantaneous buoyancy releases on slopes [2, 126, 167] but deductions about the lateral force are not possible from these works. Kneller *et al.* [112] consider oblique reflection of turbidity currents from ramps, but present their results in terms of downslope solitary waves, which are reported to move normal to the ramp.

The following discussion is in a frame in which the depth averaged velocity of the fluid of the leading edge is zero; the oncoming ambient fluid thus meets the leading edge at an angle. If the leading edge in question entrains ambient fluid, the lateral force is not zero because the entrained fluid has lateral momentum (that is, momentum parallel to the front) which could then be transferred to the dense layer.

However, equation 4.7 refers to the non-entraining case and here less is known about the behaviour of such a flow. Several mechanisms have been proposed to account for a lateral force, including the generation of laterally-moving waves. It is also the case that the leading edge of a real gravity current consists of lobes split by deep clefts [171]; and laterally moving ambient fluid impinging on the leading edge could quite easily generate pressure differences between either side of a lobe.[8]

The work of Webber *et al.* [191] implicitly assumes the lateral force to be zero. If the height of the leading edge is h, and unit vector $\hat{\boldsymbol{n}}$ is normal to the leading edge (write $\boldsymbol{n} = \hat{\boldsymbol{n}}h$), then the total force $\boldsymbol{F}$ exerted by the ambient fluid on the dense layer per unit width of front is

$$\boldsymbol{F} = \begin{cases} k\rho_a \boldsymbol{u}_a(\boldsymbol{u}_a \cdot \boldsymbol{n}) & \text{This work} \\ k\rho_a(\boldsymbol{u}_a \cdot \boldsymbol{u}_a)\boldsymbol{n} & \text{Webber } et\ al. \text{ [191]} \end{cases} \tag{4.8}$$

The work done per unit time and per unit width of front by the dense layer $(\boldsymbol{F} \cdot \boldsymbol{u}_a)$ on the ambient fluid is identical in each case; the forces differ by $k\rho_a \boldsymbol{u}_a \times (\boldsymbol{u}_a \times \boldsymbol{n})$ per unit width.

In the absence of experimental evidence confirming the presence or absence of the lateral force, equation 4.7 will be used as it represents all known forces on a gravity current and, unlike the force calculated by Webber *et al.* [191], is usable in a shock smearing scheme such as used here. Both approaches are reasonable methods of simulating leading edges.

[8] If a frame in which the front is at rest is chosen, the region of the flow where lateral momentum is transferred to the fluid will be moving backwards (left to right in figure 4.3). Further work would be required to determine whether this fact is relevant to the above discussion.

4.6 Accelerating gravity currents

Because gravity currents may not be in the equilibrium of forces indicated in equation 4.4, it is possible to have a leading edge that accelerates. For example, in the experiments of Spicer and Havens [175], a cylinder of dense gas was released from rest over a smooth horizontal plane. The leading edge thus initially had zero speed and the front resistance force provided by the ambient fluid (air) was zero. The leading edge therefore accelerated until the balance indicated in equation 4.4 was attained. Some of this behaviour will be simulated, but a gravity current may have very different structure in its accelerating phase from that in quasi-steady flow (a quantity Q is quasi-steady if $Q(\dot{Q})^{-1}$ is large compared to the timescales of interest). For this type of release it is clear that the front speed U_f is quasi-steady after this accelerating phase, and the method developed here simulates this second regime.

The subsequent deceleration of the leading edge is here associated with the decreasing depth of frontal fluid; an example of the current model simulating such a release is given in chapter 7.

Gravity current fronts tend to achieve equilibrium speeds quickly; the relevant timescale is $(h/g')^{1/2}$. In any case, these early stages are not well described by the shallow water approximations as vertical accelerations are not negligible, and concentration profiles are strongly influenced by the circumstances of the release mechanism. Such considerations are beyond the scope of this thesis and attention will be restricted to the behaviour of dense gas away from the source.

4.7 Gravity currents on slopes

If the lower surface over which a gravity current advances is inclined, a new dimensionless parameter, the angle of the slope θ, is introduced. Britter and Linden [29] considered this problem and conducted theoretical and experimental studies of continuous buoyancy sources that produced gravity currents travelling down an incline. They concluded that the front velocity U_f, when nondimensionalised by the cube root of the buoyancy flux $g_0'Q$, is independent of the slope angle for $5° \leq \theta \leq 90°$.

These workers presented theoretical arguments that led to the expression

$$\frac{U_f}{(g_0'Q)^{\frac{1}{3}}} = S_2^{\frac{1}{3}} \left(\frac{\cos\theta}{\alpha} + \frac{\alpha \sin\theta}{2(E + C_D)} \right) \left(\frac{\sin\theta}{E + C_D} \right)^{-\frac{2}{3}} \tag{4.9}$$

where E was the entrainment coefficient and S_2 was as defined in Ellison and Turner [52] (see chapter 3). Britter and Linden went on to demonstrate that equation 4.9 was consistent with $U_f/(g_0'Q)^{1/3} = 1.5 \pm 0.2$. As discussed above, this approach is not open to the present study.

The derivation of equation 4.9 used the fact that the buoyancy flux was conserved in the flow behind the head, but not in the flow up to the leading edge. As the head accumulates buoyancy this work is not of direct relevance to the present study as there is no direct relationship between the Froude number as defined in [29] and that used here. If it is assumed that buoyancy is conserved from source to leading edge, following Hay [90], equation 4.9 implies that the Froude number as defined here is also approximately constant.

At least one numerical study of gravity currents on inclines has been undertaken [191] in which the Froude number based on head height was assumed to be constant. This approach is adopted here. Although the modelling assumptions developed in this chapter become more complex if sloping lower boundaries are considered, it may be shown that they imply a fixed front Froude number for motion over a slope.

Gravity currents on slopes of angle less than 5° behave differently from those on steeper inclines. Britter and Linden [29] indicate that this is because of the importance of skin friction at the lower boundary; and for slopes of angle less than 0.5°, this friction is of such a magnitude as to preclude a steady flow. Chapter 3 showed how present approach simulates this friction.

4.7.1 Gravity currents travelling up slopes

If a gravity current encounters an upslope (such that the dense fluid rises as it travels), then its behaviour close to the leading edge may be profoundly altered. Brown [33] and Edwards *et al.* [49] describe some of the processes that occur under these circumstances in a quiescent ambient. Of particular importance to the present approach is the creation of a two-layer system: the lower layer has dense fluid flowing down the slope, while the upper, less dense, layer remains roughly at rest. Multi-layer systems are not easily simulated in the present approach, as the approximation that the dimensionless shape parameters defined on page 32 are unity becomes increasingly inaccurate. Some of the consequences of this are described on page 124 in chapter 9.

The present model captures only part of the behaviour of a gravity current travelling up a slope. If entrainment is ignored, then the depth of the leading edge decreases with time; a momentary equilibrium is reached when the buoyancy flux reaches zero; then the current reverses and a trailing edge is produced. The model simulation of trailing edges is described on page 59.

A gravity current may also arise from a continuous upward buoyancy flux from a sloping lower boundary in an opposing wind. The dense fluid will travel down the slope before reversing its direction. Although an opposing wind is known [124] to flatten the current, questions such as the strength of the wind required to reverse the downslope flow are unanswered [122]. The two-layer system generated by such

a source term is not simulated well by the present model;[9] but in practice the flow is not strictly two dimensional and a lateral buoyancy flux occurs.

4.8 Summary

This chapter has developed the resisted shallow water equations in two dimensions, and given some justification for the method chosen to simulate the leading edge, where the shallow water approximations are not accurate. Fundamentally, a dense layer will be simulated by applying the generalized shallow water equations, with an additional force. This additional force simulates the backward (left to right in figure 4.3) force exerted on the dense layer by the ambient fluid by virtue of its motion. The force is small everywhere except near a leading edge or hydraulic jump, and is of the correct magnitude to ensure that a leading edge advances at a constant (given) front Froude number.

The front resistance force is calculated as a stress $\boldsymbol{P}$, where

$$\boldsymbol{P} = -k\rho_a \left[\frac{\partial[h(\boldsymbol{u} - \boldsymbol{u}_a)]}{\partial t} + (\boldsymbol{u}_a \cdot \nabla)\,[h(\boldsymbol{u} - \boldsymbol{u}_a)] \right]$$

per unit area.

The equations may be expressed in indexed form:

$$\frac{\partial h}{\partial t} + k\frac{\partial h u_j}{\partial x_j} = W + u_s \tag{4.10}$$

$$\frac{\partial h(\overline{\rho} - \rho_a)}{\partial t} + \frac{\partial h(\overline{\rho} - \rho_a)u_j}{\partial x_j} = u_s(\rho_s - \rho_a) \tag{4.11}$$

$$\begin{aligned} S_{(i)}\frac{\partial(h\overline{\rho}u_i)}{\partial t} + S_{(ij)}\frac{\partial(h\overline{\rho}u_i u_j)}{\partial x_j} + \frac{\partial}{\partial x_i}\left[\frac{1}{2}g(\overline{\rho} - \rho_a)h^2\right] & \\ + k\rho_a\left(\frac{\partial}{\partial t} + (u_a)_j\frac{\partial}{\partial x_j}\right).[h(u_i - (u_a)_i] &= \\ W\rho_a(u_a)_i + V_i - \frac{1}{2}C_D|\boldsymbol{u}|u_i & \end{aligned} \tag{4.12}$$

Here bracketed subscripts are not summed and all terms correspond to those in equations 3.40 to 3.43. The two equations 4.12 now include the interaction between dense layer and ambient flow as introduced earlier in this chapter.

[9]This discrepancy is not Galilean invariant: there is a privileged reference frame, that in which the ground (equivalent in this case to the gravity current head) is at rest, and that in which the ambient fluid at $z = h$ is at rest. Although the depth-averaged quantities (depth, density and two components of velocity) used in the model are Galilean independent, the discrepancy in volume flux between reality and that calculated by the model ($h\boldsymbol{u}$) is not Galilean independent because of the role these privileged reference frames play in determining the flow patterns in a gravity current.

A discussion of the behaviour of dense layers on slopes was given, and it was shown that flows in which two layer systems are generated (such as gravity currents travelling up slopes) are not well simulated by the present model.

The resisted generalized shallow water equations as derived above will be used throughout this thesis to model the behaviour of dense gas accidentally released over complex terrain.

Chapter 5

The model

5.1 Outline

Dispersing dense gas clouds are subject to dilution, and the depth averaged variables developed in chapter 3 are sufficiently general to incorporate this process. The entrainment of ambient fluid into a dense cloud will be modelled using a standard approach, generalized for use in the present context.

5.2 Overview of the model

A dense gas release is modelled here in three main stages as follows:

1. Because aspect ratios are low and the pressure distribution in the vertical approximately hydrostatic in a dense gas release, the shallow water approximations are valid. The shallow water equations (which describe this type of fluid flow) will be used for the cloud with the exception of the leading edge, where the shallow water equations do not govern the depth averaged properties of the cloud.

2. The leading edge of the cloud, as it interacts strongly with the ambient flow, has a pressure distribution that is not hydrostatic and the shallow water equations are not applicable. Depth averaged properties of the cloud are simulated at the leading edge by the addition of new terms in the shallow water equations. Simulation of the leading edge is important as it controls the following flow.

3. Cloud dilution is modelled by empirical entrainment formulæ of similar form to those used in integral models.

The shallow water equations were developed in chapter 3, and the method of simulating the leading edge was developed in chapter 4. The remainder of this chapter presents the entrainment routine used.

5.3 The model: a detailed description of the entrainment algorithm

Although not directly applicable to the present model, ambient fluid entrainment as implemented by integral models has some desirable features that inspired the present approach. A brief overview of the entrainment formulæ used in integral models follows.

5.3.1 Entrainment in integral models: dense phase

Integral models typically distinguish between gravity-dominated and passive dispersion. The following discussion refers to the gravity-dominated phase; passive dispersion is considered separately.

Integral models for instantaneous releases, describing a cloud in terms of a cylinder of radius R and height h, typically divide entrainment into two distinct processes: top and edge entrainment. The volume rate of change $\dot{V}$ is modelled using an entrainment velocity approach [25] such that

$$\dot{V} = w_e A_e + w_t A_t, \tag{5.1}$$

where w_e and w_t are edge and top entrainment velocities respectively, and $A_e = 2\pi Rh$ and $A_t = \pi R^2$ are the edge and top areas respectively. This approach is stated to be universal amongst integral models for dense gas dispersion in the dense phase by Simpson [171] and Wheatley and Webber [194].

There are several motivations for treating entrainment in this way. Dimensional considerations show that

$$\dot{V} = \sum_{n=-\infty}^{\infty} u_n [h^n R^{2-n}] \tag{5.2}$$

where the u_n are velocities. Only the terms with $n = 0$ or 1 have any clear physical meaning: $n = 0$ corresponds to top entrainment and $n = 1$ is edge entrainment (no feature of a dense gas cloud as described by an integral model has area $\propto h^2$).

For the term with $n = 0$, the stratified layer discussion on page 10 is relevant because the entrainment considered takes place across a stratified shear layer. Britter [25] states that the correlations that have been used are generally of the form

$$\frac{w_t}{u_*} = \frac{a}{1 + b\left(\frac{g'h}{u_*^2}\right)}. \tag{5.3}$$

Integral models account for cloud dilution as modelled in equation 5.3 by use of a cloud-averaged entrainment rate. The volume rate of entrainment clearly scales with cloud top area. A non-averaged formula is required for the present approach; the top entrainment model of Eidsvik [51] appears to be especially suitable for

this purpose and will be used for the present model and this is discussed in section 5.3.3

The leading edge requires separate treatment as this part of the flow is strongly atypical of the rest of the cloud; chapter 3 discusses the leading edge more fully. Edge entrainment corresponds to $n = 1$. Most integral models use a velocity that is proportional to the rate of increase of the radius of the cloud, U_f. If a factor of 2π is introduced, the first term on the right hand side of equation 5.1 is recovered. This formulation of the edge entrainment will be generalized to shallow water models of dense gas dispersion below.

Concepts such as edge area have no clear counterpart in the present approach, and it would appear that this division of entrainment is not possible in a shallow water context. This is not so, as will be shown below.

5.3.2 Edge entrainment in a shallow water model

The edge entrainment formula introduced above for integral models is equivalent to the statement that the volume rate of entrainment at the leading edge of a gravity current is proportional to $h(U_f - u_a)$ per unit width of curved surface, using the notation of chapter 3. This is most easily seen by considering the case of zero wind, $u_a = 0$, and noting that the curved surface area of the cloud as described in an integral model is $2\pi Rh$. The volume rate of entrainment in both cases is then proportional to $2\pi RhU_f$, as required.[1]

Consideration of an integral model in zero wind shows that a constant of proportionality greater than unity gives unreasonable results, and in particular mechanical energy would increase with time.

An entrainment term corresponding to this physically reasonable formula is now sought for the present, shallow water, model. As the entrainment rate must be calculated locally (that is, the entrainment rate at a location is a function only of depth averaged variables close to the point in question), some generalization of the integral model formulation is required.

This will be carried out by identifying some parameter of the flow which is a function of local, depth averaged variables, that is large close to a front and small everywhere else. Edge entrainment will then be taken to be proportional to this parameter.

It is convenient to use the terminology of chapter 4 which described the momentum transfer between the leading edge of the dense layer and the ambient flow. A leading edge was characterized as a region of flow that displaced a large amount of ambient fluid. A vector quantity **P** was defined whose magnitude was small everywhere except close to a leading edge (or bore).

An analogous procedure is desirable for volume entrainment, although this is

[1] An alternative interpretation is that, of the ambient fluid displaced by a gravity current, a fixed proportion is entrained.

a scalar quantity and the momentum transfer is a vector. A *scalar* quantity Q is required, small everywhere except close to a leading edge. Edge entrainment per unit area will then be taken to be proportional to Q. A suitable definition of Q is

$$Q = \max\left[\left(\frac{\partial h}{\partial t} + (\mathbf{u}_a \cdot \nabla)\, h\right), 0\right], \tag{5.4}$$

where h is the cloud height and $\mathbf{u}_a$ the ambient wind speed. This quantity Q has all the properties required of a scalar front parameter: it is Galilean invariant, and refers to features of the flow rather than the speed of fluid within the dense layer. Note that Q is not permitted to become negative, as this would give unacceptable results if $[\partial/\partial t + (\mathbf{u}_a \cdot \nabla)]h < 0$. This approach is a generalization of that used in integral models, as may be seen from the following argument.

An edge entrainment proportional to Q gives, for a gravity current of unit width, a volume entrainment rate of khU_f, where k is the constant of proportionality. A circular cloud of radius R, height h and front speed U_f thus gives a volume entrainment rate of $k.2\pi RhU_f$. This is the curved surface area of the cloud multiplied by the frontal speed and a dimensionless constant; identical formulations are used in integral models.

Although the terms edge and top entrainment are suggestive of entrainment through the cloud edge and top, this twofold characterization cannot provide any direct insight into where the entrainment actually takes place. Wheatley and Webber [194] consider this and state that

> The edge entrainment term does not necessarily correspond to entrainment through the edge ...it may occur over the whole top area of the cloud.

It is clearly necessary to address this problem in the present model, as the density is here allowed to vary over the extent of the cloud. Note that integral models implicitly assume edge entrainment occurs over the whole of the cloud, as the frontal speed is independent of the edge entrainment rate. Characterization of edge entrainment as entrainment that occurs close to the leading edge is thus not necessarily consistent.

With the more sophisticated simulation allowed by a shallow layer approach, entrained air may be incorporated into the dense gas cloud at a precisely controlled location. Several methods of entrainment were investigated with the overall conclusion that localizing edge entrainment (that is, entrainment rates per unit area proportional to Q) resulted in unrealistic behaviour. Because the entrained air entered the cloud at the leading edge, the volume of gas increased there. This volume increase was manifested either as an increased leading edge depth, or an increased leading edge speed. Both these led to an increased entrainment rate and such simulations entrained air at an exponential rate. This behaviour was

clearly unacceptable and was not alleviated by spreading the entrainment over a region closer than a few cloud depths to the leading edge.

In summary, localizing edge entrainment to the leading edge resulted in simulations that entrained at exponentially growing rates.

One solution to this problem was to delocalize edge entrainment over the whole upper surface of the cloud. This method is consistent with the integral model approach and has physical precedent in the work of Webber and Wheatley [192, 194].

However, this approach has the unreasonable consequence that locality is lost: conditions at one position may strongly affect distant parts of the cloud. This is inconsistent with a shallow water model.

Not all integral models use edge entrainment: the default parameters of the DENZ model [61] set edge entrainment terms to zero.

Edge entrainment and the leading edge condition

In chapter 4 it was stated that the present model simulated a leading edge as a force balance between a hydrostatic pressure pushing the leading edge forward, and an analogue of form drag that prevented the leading edge from accelerating. This resisting force was proportional to a front parameter P, or $\mathbf{P}$ in two dimensions. It was also stated that formula 4.6 was incomplete as it gives erroneous results for receding dense layers.

It is now clear how to handle such cases: simply set P or $\mathbf{P}$ to zero if $[\partial/\partial t + (\mathbf{u}_a.\nabla)]h < 0$. With this condition, a receding dense layer (a 'trailing edge') is modelled as though hydrostatic forces alone influence this region; this is reasonable if the edge is sharp. The argument on page 46 is not strictly relevant is it requires a particular form for the fluid depth behind the front; it implies a front Froude number of $\sqrt{2(\pi+4)/\pi} \simeq 2.13$.

5.3.3 Top entrainment in a shallow layer model

Top entrainment is defined here by analogy with the corresponding terms used in integral models: a volume rate of entrainment that is proportional to the upper surface area of the cloud and some entrainment velocity that is a function of the local turbulence.

Top entrainment is a process that dilutes the cloud by incorporating eddies of ambient fluid into the body of the cloud. As well as affecting the depth averaged velocity of the cloud, dilution also occurs. It is thus important to understand the mechanisms by which these processes occur and to model them accurately.

This type of entrainment is driven by three primary sources of turbulent energy: ambient turbulence present in the atmosphere, turbulence generated by the shearing motion between air and dense layer, and turbulence generated at the ground by the passage of dense gas across the rough lower boundary of the fluid.

Chapter 2 described some of the previous work that has been done on the problem of stratified shear flow and concluded that a wide range of opinion exists. Fernando, in a review of turbulent mixing in stratified fluids [56], emphasizes the lack of consensus in this field.

The various entrainment formulations developed for integral models are of relevance to the present study, but all are necessarily averaged over the extent of the cloud, and not expressible in terms of the shallow water variables at a given point, as is required here. This thesis addresses this problem by using an entrainment formula similar to those used in integral models, but without cloud wide integration.

The shallow water approach to dense gas dispersion is sufficiently flexible to allow the use of any model of entrainment capable of expression in terms of depth averaged quantities. This is one of the strengths of the present approach: for example, future research on entrainment in the lee of buildings or trees, if capable of expression in terms of a changed entrainment rate, may be incorporated into the present model and used directly. Such extensions to the present work would require little additional computational expense.

Motivated by the need to express the rate of entrainment across the top of the cloud, the work of Eidsvik [51] will be used. Eidsvik presented an integral model of dense gas dispersion with a top entrainment term that was capable of use in a shallow layer model. A brief summary of Eidsvik's entrainment model is given here.

Eidsvik required, as here, a simple model for top entrainment that had only a small number of experimental coefficients. His model incorporated a commonly used [25, 110, 202] relation

$$w_t = \frac{a}{1 + b.Ri} v \tag{5.5}$$

where w_t was the top entrainment velocity, a and b experimental coefficients, v a representative velocity scale, and $Ri = g'h/v^2$ the Richardson number.

Eidsvik noted that as $Ri \longrightarrow 0$, equation 5.5 reduced to $w_t = a.v$, which describes the entrainment rate into a passive contaminant in a neutral boundary layer; Tennekes and Lumley [178] and Turner [180] discuss the problem of passive dispersion in this context.

The best definition of v, the representative velocity, was argued by Eidsvik to be a weighted sum of the friction velocity u_* and the convective velocity w_*, and was defined as

$$v^2 = (\alpha_2 w_*)^2 + (\alpha_3 u_*)^2. \tag{5.6}$$

Here $w_* = \left(\overline{(\theta w)}_0 gH/T\right)^{1/3}$; $\overline{(\theta w)}_0$ is the surface heat flux at the ground, H the height of the convective boundary layer, and T the temperature. Inclusion of the effects of convective velocity is not a thermal effect in the sense of section C.5 in which the effects of cloud temperature were discussed. Here, convective velocity will be treated solely insofar as it affects the fluid mechanics of the dense layer.

Eidsvik was able, because he was working with an integral model, to use a cloud averaged value for v. Here, because of the shallow layer approach, a local value of v must be used. It is logical and convenient to use a weighted quadratic sum for v. It is clear that v, being a representative fluid speed, will have contributions from three distinct sources:

- internally generated turbulence arising from the shear caused by the cloud having a different velocity from the ambient flow;
- externally generated turbulence arising from the dense layer moving over the ground; and
- externally generated turbulence present in the planetary boundary layer.

Although these three sources of turbulent energy contribute to v, the relative importance of each term is not clear and the model follows Eidsvik and others in the use of empirically determined constants. Thus

$$v^2 = k_1^2 u_*^2 + k_2^2 w_*^2 + k_3^2 |\mathbf{u}|^2 + k_4^2 |\mathbf{u} - \mathbf{u}_a|^2,$$

where $\mathbf{u}$ is the velocity of the cloud and $\mathbf{u}_a$ the ambient flow speed at the height of the cloud; the k_i are dimensionless constants.

Both to maintain consistency with Eidsvik, and to reflect the source of the turbulent energy, the k_i will be rewritten: $k_1 = 1$, $k_2 = \alpha_2$, $k_3 = \alpha_3\sqrt{\frac{1}{2}C_D}$, and $k_4 = \alpha_7$. Combining the above arguments gives

$$v^2 = u_*^2 + (\alpha_2 w_*)^2 + \frac{1}{2}C_D\alpha_3^2\mathbf{u}^2 + \alpha_7^2|\mathbf{u} - \mathbf{u}_a|^2. \tag{5.7}$$

This is used in the present model. Both the friction velocity u_* and the ambient air velocity $\mathbf{u}_a$ may be obtained either by use of analytical results (such as using the logarithmic velocity profile seen over level terrain), or by some numerical atmospheric flow field predictor. The latter approach is preferable, as then it is possible to account for the complex flow seen near variable terrain such as recirculation zones.

The parameters above must be set to particular values in order to use the present model. Each parameter is discussed in turn below.

- a, the primary entrainment coefficient. In this model, a is the passive entrainment coefficient. It is possible to determine a from passive experiments as equation 5.5 reduces to $w_t = av$ if $Ri = 0$.

  Pasquill and Smith [152] state that identification of a with von Karman's constant k may be made on the assumption that the vertical spread of neutrally-buoyant particles is described by the gradient-transfer relation with a diffusivity equal to the eddy viscosity, $K = ku_*z$. The identity follows from the assumption of a self-similar profile (as here).

Britter [23] states that where equation 5.5 is used, $a = 0.4$ (=von Karman's constant) and $b = 0.125$ are used; these values have been deduced from experimental work. Here, u_* is the friction velocity and $Ri = g'h/u_*^2$ is the Richardson number.

The exact value of von Karman's constant is uncertain. A range of 0.33 to 0.41 for k is offered by Pasquill and Smith [152]. This work will follow Britter and use $a = 0.4$.

- b, a parameter that is large if the inhibition of entrainment by stable stratification is small. This work follows Britter and others in using $b = 0.125$; Eidsvik chose $b = 0.28$.

- α_2, the relative importance of a convective atmosphere. Atmospheric stability is considered by Britter and McQuaid [30] to be a 'peripheral variable' and this work will follow Eidsvik and use a value of $\alpha_2 = 0.7$.

- α_3 and C_D; classed as peripheral variables by Britter and McQuaid. In calm conditions (such as in the experiments of Schatzmann [167]), the turbulence generated at ground level is comparable to that generated by the upper shear layer of the cloud. A reasonable value for α_3 is 1.3 (following Eidsvik) and this will be used here. The value of C_D may be estimated either from a knowledge of u and u_*, or of local ground characteristics.

- α_7, the relative importance of shear. Values of $\mathcal{O}(1)$ are indicated and this study will follow Eidsvik and use $\alpha_7 = 1$.

The other free parameters in the model, which are not directly relevant to the top entrainment modelling, are:

- α_E, the edge entrainment coefficient. As discussed above, theoretical reasons suggest a value of zero for α_E in the present model.

- Fr, the front Froude number. It is convenient and conventional [25, 69, 194] to take $Fr = 1$ and this will be carried out here.

- S_1, the hydrostatic dimensionless shape parameter. Following Ellison and Turner [52], $S_1 = 0.5$ will be used.

- $S_{\mathbf{u}}$ and $S_{\mathbf{uu}}$, the other dimensionless parameters introduced for the generalized shallow water equations in chapter 3. These nondimensional shape parameters will be assumed to be unity.

5.4 Passive cloud spread

Integral models typically consider dense gas clouds by analysing them in terms of a number of regimes. After initial momentum-dominated and buoyancy-dominated phases, a cloud is usually assumed to be passive; some models ensure a smooth transition from one regime to the next. Models typically [187] follow Britter [25] in comparing u_* with $\sqrt{g'h}$ to determine which regime is in force.

In the case of integral models for continuous releases, Webber *et al.* [188] consider the concentration field to be

$$c(x, y, z) = C_m(x) \exp\left(-(z/a)^s\right) \exp\left(-|y/b|^w\right). \tag{5.8}$$

Here, x, y, and z are the standard coordinates, a and b functions of x, and s and w dimensionless parameters that express the sharpness of the cloud edge.

In the passive regime, w approaches 2, giving a Gaussian profile. Horizontal diffusion is essentially modelled by $db/dt = ku_*/U$, where k is a constant and U the windspeed at a height related to the cloud at that point. Passive vertical diffusion is modelled by a top entrainment similar to equation 5.3, which has an appropriate passive limit; instantaneous releases have a longitudinal dispersion which is modelled similarly.

The present model does not account for the horizontal component of diffusion in the passive limit and one consequence of this might be overprediction at large distances. It is not clear how this phenomenon could be modelled in a shallow layer simulation. This is because shallow layer models have both depth and concentration as variables, and it is difficult to see how both could be diffused in a manner consistent with the passive case but preserving the shallow water solutions of the model in the early buoyancy dominated regime. The difficulties of such an approach are exacerbated by the fact that some parts of a cloud may be passive and some not; any scheme would have to carry out diffusion in such a way as to approach a Gaussian cross-wind profile on flat ground. There is no obvious method that has all the required properties, although future work may yield a workable solution.

Some estimation of the importance of horizontal diffusion in the passive limit to the present model is made in chapter 11.

5.5 Further processes occurring in dense gas releases considered in risk assessment

One of the aims of this thesis is to have a physically realistic model of dense gas dispersion over complex terrain to be used in risk assessment. Ambient flow will be treated as given, and a depth averaged approach has been chosen for further study. Several phenomena occur in accidental dense gas releases that the present model ignores; each of these caveats will be discussed in appendix C.

5.6 Summary

The shallow water equations developed in this thesis include the effects of entrainment. Empirical correlations are required to determine the entrainment rate and a suitable method is presented in this chapter. A set of standard values has been given.

The mathematical model has now been fully detailed. The rest of this thesis will describe and use the computational model that implements the mathematical model.

Chapter 6

The computational scheme

6.1 Outline

Now that the mathematical model that will be used has been developed a computational scheme that simulates the mathematical model is now required. Any computational simulation is only an approximation to the mathematical model because further simplifications have to be made; at the very least, some discretization is required.

This chapter will outline the computational scheme used in this thesis. Firstly, computational schemes in general will be discussed. An outline of the conservation equations (of which the shallow water equations are one example) and their importance in the field of computational fluid dynamics follows. Next, some difficulties encountered when solving the conservation equations are noted and the flux correction scheme of Zalesak [200] will be shown to overcome them.

The chapter then discusses the problems that non-uniform terrain presents to computational solutions of the conservation equations. The extensions to Zalesak's methods that have been implemented in order to accommodate non-uniform terrain are given in appendix A.

6.2 Computational schemes and their use

The mathematical model developed in chapters 3 to 5 consists of a set of equations; a computational scheme is required to solve the discretized version of these equations. The result of applying a computational scheme to a mathematical model is known as a computational model.

Fundamentally, the use of computational models involves three steps:

1. A domain is chosen and divided into computational elements. The elements are sufficiently small so that variations in fluid properties across an element

may be neglected. In the present case, the domain is a two-dimensional area of ground as the mathematical model uses depth averaged variables.

2. The equations to be solved (in this case, equations 4.10 to 4.12, representing the shallow water equations with a fixed front Froude number at the leading edge) are discretized. This discretization shows how the depth averaged fluid properties within each computational element evolve with time.

3. A computational method is used to implement the discretized equations that describe the evolution of the the fluid properties within each computational element.

The field of computational fluid dynamics has generated a large volume of literature and reviews are given by Roache [158] and Sod [174]. Many of the arguments presented later in this chapter, and the development of the numerical scheme, have been strongly influenced by Roache in particular.

6.3 Conservation form for differential equations

Many partial differential equations in the field of fluid dynamics (including the shallow water equations) may be expressed in 'conservation form'. This format is necessary for a number of numerical solution techniques including the method used here.

Formally, if $w = w(x, y, z; t)$ is a variable, dependent upon space and time, and the quantities f, g, and h are functions of position and possibly w, then the equation

$$\frac{\partial w}{\partial t} + \frac{\partial f}{\partial x} + \frac{\partial g}{\partial y} + \frac{\partial h}{\partial z} = 0 \tag{6.1}$$

is in *conservation form.*

For example, if a scalar quantity w is advected in a known velocity field $\mathbf{U} = (u_x, u_y, u_z)$ and conserved, then the equation

$$\frac{\partial w}{\partial t} + \nabla \cdot (w\mathbf{U}) = 0 \tag{6.2}$$

expresses this fact. Equation 6.2 is in conservation form because it is a special case of equation 6.1. That this terminology is appropriate may be seen by applying Gauss' theorem to 6.2 over a region R:

$$\frac{\partial}{\partial t} \int_{\mathbf{x} \in R} w \, d^3\mathbf{x} + \int_{\partial R} w\mathbf{U} \cdot d\mathbf{S} = 0; \tag{6.3}$$

the right hand side being zero expresses the fact that the quantity w is conserved.[1]

[1]Note that if $\nabla \cdot \mathbf{U} = 0$ (as for an incompressible fluid) then equation 6.2 may be written as

$$\frac{\partial w}{\partial t} + (\mathbf{U} \cdot \nabla) w = 0$$

The concept of conservation form may be extended to simultaneous partial differential equations. If $w_1, w_2, \ldots w_n$ are all conserved scalar quantities advected in a velocity field $\mathbf{U}$ then the system of equations

$$\frac{\partial w_i}{\partial t} + \nabla \cdot (w_i \mathbf{U}) = 0 \tag{6.4}$$

is also said to be in conservation form.

With some abuse of notation, a system of equations may still be in conservation form when some of the w_i are components of a vector such as the velocity field $\mathbf{U}$ itself.

Equation 6.4 may be recast in Cartesian form as:

$$\frac{\partial w_i}{\partial t} + \frac{\partial f_i}{\partial x} + \frac{\partial g_i}{\partial y} + \frac{\partial h_i}{\partial z} = 0, \tag{6.5}$$

where $f_i = w_i u_x$, etc. Conservation equations, in their most general form, allow the f_i, g_i, and h_i to be of a different form [158]; the next section gives an example.

6.4 Numerical solution of equations in conservation form

For simplicity, the one-dimensional system of equations

$$\frac{\partial w}{\partial t} + \frac{\partial f}{\partial x} = 0 \tag{6.6}$$

is considered, where w and f are vector functions of position and time; the subscript 'i' has been dropped for clarity. If, for example, the following choice is made:

$$w = \begin{pmatrix} h \\ h(\rho - \rho_a) \\ h\rho u \end{pmatrix} \qquad f = \begin{pmatrix} hu \\ h(\rho - \rho_a)u \\ h\rho u^2 + \frac{1}{2}g(\rho - \rho_a)h^2 \end{pmatrix} \tag{6.7}$$

then this is the shallow water equations in one dimension. Other choices for w and f give other systems such as the Euler equations.

Numerical solution of this system of equations is not simple and many numerical schemes have been devised; review articles are given by Chock [39] and Woodward [197]. However, only one scheme will be considered here: that of Zalesak [200]. This scheme presented the earlier work of Boris and Book [14, 15] and Boris *et al.* [16] in a generalized, simplified, and improved format.

which is not in conservation form. If w is interpreted as 'depth of fluid' in the shallow water equations then this form of expressing conservation of fluid volume is frequently used, for example by Wheatley and Webber [194] or Grundy and Rottman [69].

Finite difference solution schemes for equation 6.6 must make some type of approximation to $w = w(x,t)$, which is a function of both space and time. This is done by discretizing space and time and considering only $w(x_i, t_n)$, where x_i is the ith grid point and t_n the nth timestep. It is standard practice to write $w(x_i, t_n) = w_i^n$. Note that, for fixed i and n, w_i^n is here a vector. If $\Delta x_i = (x_{i+1} - x_i)$ is the grid size, then the fluid from $x_i - \frac{1}{2}\Delta x_{i-1}$ to $x_i + \frac{1}{2}\Delta x_i$ ('cell i') is assumed to have sufficiently constant properties for w_i to be representative of the whole of cell i.

The concept of a numerical solution scheme being in conservation form is now introduced. A finite difference approximation to equation 6.14 is in conservation form if it may be written in the form

$$w_i^{n+1} = w_i^n - \Delta x_i^{-1} \left[F_{i+(1/2)} - F_{i-(1/2)} \right] \Delta t \tag{6.8}$$

where $\Delta t = t_{n+1} - t_n$ is the time step. The $F_{i\pm(1/2)}$ are called the transportive fluxes and are functions of the f of equation 6.6 at times t_m where $m \leq n$. This notation emphasizes that the $F_{i\pm(1/2)}$ model transport into and out of cell i.

In the context of numerical solution of this type of differential equation, the relationship between the f and F defines the type of advection scheme; examples include upwind donor-cell schemes and the Lax-Wendroff method described by Roache [158]. Recent reviews, such as that by Sod [174], list many different types. High order schemes for calculating F from f are known [174, 200] to suffer from certain deficiencies, particularly in regions close to sharp gradients in one or more elements of w.

High order advection schemes[2] often suffer from the generation, by the numerical scheme, of oscillations or 'wiggles' in the solution which may become sufficiently large to interfere with the numerical integration. These numerical oscillations often have no physical meaning and are a result of the advection scheme used. This is particularly relevant to the present computational model because the shallow water equations tend to give solutions with ever-steepening depth gradients.[3] The unacceptability of even very slight numerical oscillations for the present problem is discussed on page 75.

Although numerical ripples may be avoided by the use of a low order scheme (first order or less) such as the donor-cell, low order schemes tend to suffer from excessive 'numerical diffusion'. Numerical diffusion is another undesirable feature of advection schemes; it has no physical meaning. Schemes suffering from this

[2]Numerical schemes solving the equation $\partial Q/\partial t + \partial(uQ)/\partial x = 0$ with grid spacing Δx and time steps of Δt usually expand (locally) up to a given order in the parameters $\delta = \Delta t\, uQ^{-1}\partial Q/\partial x$ and $\epsilon = u\Delta t/\Delta x$. The order of this expansion is known as the *order* of the scheme. The order in ϵ is usually unimportant as ϵ (the Courant number) is often constrained to be of $\mathcal{O}(1)$.

[3]Solutions of both the shallow water equations and the Euler equations exhibit similar behaviour in this respect: compression waves tend to steepen while expansion waves tend to flatten. This is ultimately due to the fact that the adiabatic index γ is positive.

Finite difference solution schemes for equation 6.6 must make some type of approximation to $w = w(x,t)$, which is a function of both space and time. This is done by discretizing space and time and considering only $w(x_i, t_n)$, where x_i is the ith grid point and t_n the nth timestep. It is standard practice to write $w(x_i, t_n) = w_i^n$. Note that, for fixed i and n, w_i^n is here a vector. If $\Delta x_i = (x_{i+1} - x_i)$ is the grid size, then the fluid from $x_i - \frac{1}{2}\Delta x_{i-1}$ to $x_i + \frac{1}{2}\Delta x_i$ ('cell i') is assumed to have sufficiently constant properties for w_i to be representative of the whole of cell i.

The concept of a numerical solution scheme being in conservation form is now introduced. A finite difference approximation to equation 6.14 is in conservation form if it may be written in the form

$$w_i^{n+1} = w_i^n - \Delta x_i^{-1} \left[F_{i+(1/2)} - F_{i-(1/2)} \right] \Delta t \tag{6.8}$$

where $\Delta t = t_{n+1} - t_n$ is the time step. The $F_{i\pm(1/2)}$ are called the transportive fluxes and are functions of the f of equation 6.6 at times t_m where $m \leq n$. This notation emphasizes that the $F_{i\pm(1/2)}$ model transport into and out of cell i.

In the context of numerical solution of this type of differential equation, the relationship between the f and F defines the type of advection scheme; examples include upwind donor-cell schemes and the Lax-Wendroff method described by Roache [158]. Recent reviews, such as that by Sod [174], list many different types. High order schemes for calculating F from f are known [174, 200] to suffer from certain deficiencies, particularly in regions close to sharp gradients in one or more elements of w.

High order advection schemes[2] often suffer from the generation, by the numerical scheme, of oscillations or 'wiggles' in the solution which may become sufficiently large to interfere with the numerical integration. These numerical oscillations often have no physical meaning and are a result of the advection scheme used. This is particularly relevant to the present computational model because the shallow water equations tend to give solutions with ever-steepening depth gradients.[3] The unacceptability of even very slight numerical oscillations for the present problem is discussed on page 75.

Although numerical ripples may be avoided by the use of a low order scheme (first order or less) such as the donor-cell, low order schemes tend to suffer from excessive 'numerical diffusion'. Numerical diffusion is another undesirable feature of advection schemes; it has no physical meaning. Schemes suffering from this

[2]Numerical schemes solving the equation $\partial Q/\partial t + \partial(uQ)/\partial x = 0$ with grid spacing Δx and time steps of Δt usually expand (locally) up to a given order in the parameters $\delta = \Delta t\, uQ^{-1}\partial Q/\partial x$ and $\epsilon = u\Delta t/\Delta x$. The order of this expansion is known as the *order* of the scheme. The order in ϵ is usually unimportant as ϵ (the Courant number) is often constrained to be of $\mathcal{O}(1)$.

[3]Solutions of both the shallow water equations and the Euler equations exhibit similar behaviour in this respect: compression waves tend to steepen while expansion waves tend to flatten. This is ultimately due to the fact that the adiabatic index γ is positive.

phenomenon may be unable to reproduce the sharp gradients often seen in shallow water flow.

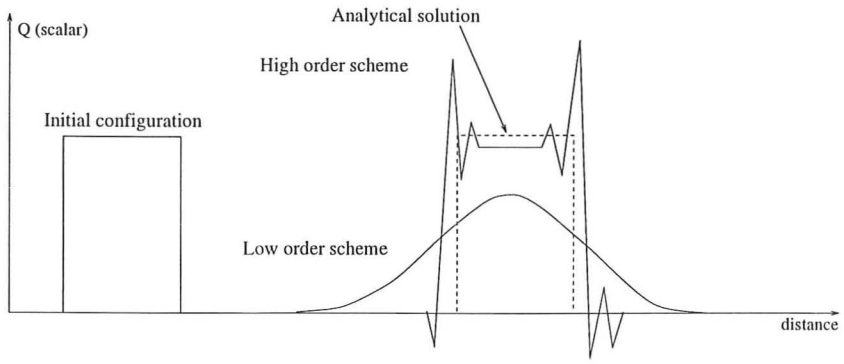

Figure 6.1: Schematic view of a low order- and a high-order advection scheme in a uniform velocity field

The diverse problems besetting low- and high- order schemes are shown diagrammatically in figure 6.1, following Sod [174]. It may be seen that the high order scheme exhibits short wavelength numerical oscillations and the low order scheme exhibits numerical diffusion.

One solution to these problems is to use the flux correction scheme of Zalesak [200] and this scheme is considered in the next section. Motivation for the use of this scheme over alternatives is provided in chapter 7.

6.5 The flux correction scheme of Zalesak

In a frequently cited paper, Zalesak [200] presented an advection scheme that combined the low numerical diffusion of high order schemes with the absence of numerical oscillations typical of low order schemes. This advection scheme was based on the earlier work of Boris and Book [14, 15] and Boris *et al.* [16] but improved upon those works by extending their ideas to multiple spatial dimensions. Many workers in the field of computational fluid dynamics have used his ideas [174, 197]. Although the original application of Zalesak's scheme was a problem in plasma physics, the ideas presented by Zalesak have been used in such diverse fields as meteorology, compressible gas flow, and the simulation of environmental pollution. The following paragraph paraphrases Zalesak:

> Flux corrected transport [FCT] is a technique that embodies the advantages of both low- and high- order schemes. Fundamentally, FCT calculates the fluxes F_i by taking a weighted average of a flux as computed by a low order scheme and the flux as computed by a high order

scheme. The weighting is done in such a manner as to use the high order scheme unless to do so would result in the creation of overshoots (that is, new extrema in w) not predicted by the low order scheme. The assumption is therefore that any new extrema predicted by the low order scheme are genuine.

The method given by Zalesak by which extrema were avoided was to limit w above and below by $w_i^{\max}$ and $w_i^{\min}$. Briefly, $w_i^{\max}$ is the maximum value that w_i may assume without causing an unacceptable (numerical) overshoot; $w_i^{\min}$ is likewise the minimum allowable value of w_i. Here, w is a vector and the above characterizations of $w_i^{\max}$ and $w_i^{\min}$ apply for each value of the index i; so, for example, $(w_i)_1 = h_i$ is the depth of the current at grid point i and $(w_i)_2 = h(\rho - \rho_a)$ is the buoyancy per unit area divided by the gravitational field strength. Each component of w_i is thus constrained by the vectors $w_i^{\max}$ and $w_i^{\min}$. A complete description of the method is given in Appendix A.

6.6 The two-dimensional shallow water equations in conservation form

For convenience the two-dimensional, non-entraining shallow water equations are restated here. For simplicity, only the case of level ground is considered, viscous forces are neglected, and ground drag assumed to be negligible. All dimensionless constants identified in chapter 3 are taken to be unity:

$$\frac{\partial h}{\partial t} + \frac{\partial hu}{\partial x} + \frac{\partial hv}{\partial y} = 0 \tag{6.9}$$

$$\frac{\partial h(\rho - \rho_a)}{\partial t} + \frac{\partial h(\rho - \rho_a)u}{\partial x} + \frac{\partial h(\rho - \rho_a)v}{\partial y} = 0 \tag{6.10}$$

$$\frac{\partial h\rho u}{\partial t} + \frac{\partial [h\rho u^2 + \frac{1}{2}g(\rho - \rho_a)h^2]}{\partial x} + \frac{\partial h\rho uv}{\partial y} = 0 \tag{6.11}$$

$$\frac{\partial h\rho v}{\partial t} + \frac{\partial h\rho uv}{\partial x} + \frac{\partial [h\rho v^2 + \frac{1}{2}g(\rho - \rho_a)h^2]}{\partial y} = 0 \tag{6.12}$$

where equation 6.9 expresses conservation of dense current volume, equation 6.10 expresses conservation of buoyancy, and equations 6.11 and 6.12 are the momentum equations in the $x-$ and $y-$ directions.

Equations 6.9 to 6.12 are in conservation form. Defining

$$w = \begin{pmatrix} h \\ h(\Delta\rho) \\ h\rho u \\ h\rho v \end{pmatrix}, f = \begin{pmatrix} hu \\ h(\Delta\rho)u \\ h\rho u^2 + \frac{1}{2}g(\Delta\rho)h^2 \\ h\rho uv \end{pmatrix} \text{ and } g = \begin{pmatrix} hv \\ h(\Delta\rho)v \\ h\rho uv \\ h\rho v^2 + \frac{1}{2}g(\Delta\rho)h^2 \end{pmatrix} \tag{6.13}$$

where $\Delta\rho = \rho - \rho_a$ is the density difference between the dense layer and that of the ambient fluid, implies

$$\frac{\partial w}{\partial t} + \frac{\partial f}{\partial x} + \frac{\partial g}{\partial y} = 0 \tag{6.14}$$

is the two-dimensional shallow water equations in conservation form.

These equations are well suited to solution using Zalesak's method. At least one other study, by Webber [183], has used this method for the shallow water equations. That work considered only one-dimensional motion of a non-entraining flow.

6.7 Varying ground elevation and flux correction

Numerical solution of the shallow water equations must account for varying ground elevations—considerations not part of a compressible gas flow calculation. The introduction of ground elevation requires generalizations to be made to Zalesak's original scheme and these changes are discussed in Appendix A.

6.8 Summary

This chapter has discussed the numerical solution of the shallow water equations. Because the shallow water equations may be expressed in conservation form, a number of numerical methods are available.

Although all numerical schemes have disadvantages, the flux correction method of Zalesak [200] is well suited to the present problem, but requires generalization for non-flat ground.

Chapter 7

Validation of the computational scheme

7.1 Outline

This chapter will show that the computational scheme described in chapter 6 accurately simulates the physical model developed in chapters 3 to 5.

Only the idealized case of zero entrainment will be considered in this chapter, as several analytical results exist for this case against which the results of the code may be compared. The effects of top- and edge- entrainment may be accounted for separately.

The validation exercises will follow a logical order, first testing the most basic feature of the computational model (the advection scheme) in one dimension and then two dimensions. Next, the gravitational forcing terms will be tested by verifying that the momentum and energy of a dense layer behave as expected.

Physical phenomena are independent of the coordinate system used to describe them, and this fact is known as invariance. Invariance under those coordinate transforms allowed by the computational scheme is then demonstrated.

Finally, the code is then tested against a number of exact, analytical solutions, as recommended by Roache [158].

7.2 Introduction

It is necessary to show that the non-entraining case is correctly modelled, as confidence in the full (entraining) case rests firmly upon the simpler non-entraining problem. Further, the non-entraining case is open to analytical investigation, unlike the full problem. Webber *et al.* [191] state:

> Credible hazard analysis can only come about using models which are well validated... and incorporate sound physical assumptions (and

accurate calculational methods) in extrapolating their predictions to larger scales.

It is the intention of this chapter to justify the accuracy of the computational scheme in the light of Webber's observations.

The computational scheme described is capable of simulating two-dimensional shallow water flow with a specified densimetric front Froude number. This capability allows the simulation of dense gas dispersion in two dimensions by a shallow water model.

7.3 The advection equation

The code under development incorporates several novel features (mostly generalizations and extensions of the flux correction scheme of Zalesak [200] which are detailed in appendix A), and several checks on this new scheme will be presented.

7.3.1 The one-dimensional advection equation

The advection equation governs the transport of a conserved scalar quantity (cloud height in this case) when the velocity field is specified. The velocity field transports the scalar quantity from place to place. Any numerical scheme must solve the advection equation accurately as this underpins the more general case. That the advection equation is solved accurately is shown below; the one-dimensional case is addressed in this section, and the two-dimensional case is presented next.

The advection equation is found in many systems. For example, if h is the fluid depth at any point and u is the fluid velocity, then the advection equation for h in one dimension is

$$\frac{\partial h}{\partial t} + \frac{\partial hu}{\partial x} = 0, \tag{7.1}$$

which is the mathematical statement of conservation of fluid volume. This equation is written in conservation form. Numerical solution of the advection equation is not trivial and many review articles [39, 143, 174, 197] discuss different numerical schemes together with the problems they encounter.

It is necessary to eliminate numerical overshoot near sharp gradients of fluid depth, such as shown in figure 6.1. The shallow water equations are equivalent to the Euler equations for compressible gas flow[1] with $\gamma = 2$, and thus many of the techniques used for compressible gas simulation are applicable to the present case, as discussed by Courant and Friedrichs [43].

[1]The depth h of a shallow flow is analogous to the density ρ of a compressible gas and the speed $u = \sqrt{g'h}$ of gravity waves translates to the speed of sound.

The test involves fixing the speed u at a constant value and setting h to be zero everywhere except for a finite region in which it is constant. In this case, the fluid depth h is 4.44 m over a width of 11 m and the speed u is fixed at 1 m/s; the Courant number[2] used was 0.1. Workers such as Chock [39] and Woodward and Colella [197] use tests of this type as they check that the advection solver can handle both leading- and trailing- discontinuities, which are known to cause problems for many solvers.

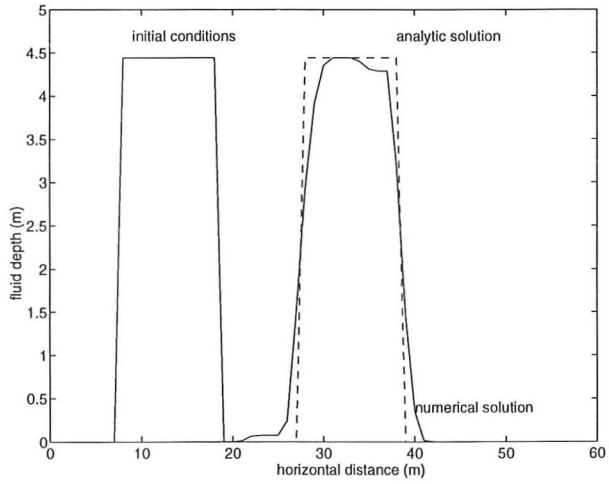

Figure 7.1: Standard uniform motion test for numerical advection schemes: initial, final, and analytical depth profiles

Figure 7.1 shows the result of such a test on the present scheme. It is seen that the initial maximally sharp depth distribution has suffered some degradation as the discontinuity is spread over about three computational elements. These results compare favourably with those of Sod [174] and Würtz [198]. Further, if the simulation illustrated in figure 7.1 is allowed to proceed, the form of the numerical solution remains identical; that is, there is no further degradation. One implication of this is that the differences between the computed and exact solutions are scaled with the gridsize used: in this case, the width of the smearing is about three computational elements wide. Thus, the width of the smearing is proportional to the gridsize used.

One interpretation of these results is that if the initial conditions were the final numerical solution shown in figure 7.1, then there would be no numerical diffusion

[2] A working definition of the Courant number C is $C = \max(|\mathbf{v}|)\Delta t/\Delta x$, where $\mathbf{v} = (v_x, v_y)$ is the depth averaged velocity of the fluid, Δt is the timestep, and Δx is the gridsize. The timestep is adjusted at each iteration to maintain the Courant number at a constant. A formal definition is given in chapter 6 on page 68.

at all.

The advection equations—as they stand—admit negative fluid depths but physical considerations show that this is unrealistic. In the same way, the advection scheme does not explicitly forbid negative depths as artificial extrema are suppressed. This is important: slight numerical oscillations near the leading edge could cause negative fluid depths which can lead to severe numerical problems.[3]

The present approach thus does not require an artificially imposed minimum fluid depth of zero; rather, negative fluid depths are implicitly forbidden by the nature of the problem. This is a desirable feature of any advection solver, both on the grounds of computational efficiency and physical accuracy.

7.3.2 The two-dimensional advection equation

It is necessary to test that the *two-* dimensional advection equation is correctly solved because two-dimensional velocity fields may exhibit behaviour such as steady stagnation points that are not seen in the one-dimensional case.

The advection equation in conservation form is readily extended to two dimensions:

$$\frac{\partial C}{\partial t} + \frac{\partial Cu}{\partial x} + \frac{\partial Cv}{\partial y} = 0.$$

Here, $\mathbf{u} = (u, v)$ is the two-dimensional velocity decomposed into its $x-$ and $y-$ components. Here C is the scalar quantity that is being transported and may be thought of as contaminant concentration or (in the case of shallow water modelling) the depth of fluid.

In 1983, Chock and Dunker [40] presented a comparison of several methods of solving the two-dimensional advection equation. These workers used a standard test for advection schemes, following Sod [174] and this test will be carried out on the present scheme.

The test presented by Chock and Dunker [40] was that of solid body rotation. In this case the velocity field was specified to be

$$\begin{aligned} u &= -\Omega(y - y_0) \\ v &= +\Omega(x - x_0) \end{aligned} \tag{7.2}$$

[3] As discussed above, the shallow water equations are closely related to the Euler equations: the depth of fluid in a shallow water simulation is analogous to the density of fluid in a compressible flow and a hydraulic jump is analogous to a shock front. The phenomenon of depth (density) oscillations near a hydraulic jump (shock front) is not as critical in a compressible flow simulation as a slight amount of numerical oscillation near a shock front will not result in negative densities, because the fluid on the upstream side of a shock has a positive density and can thus 'tolerate' a small amount of oscillation without assuming a negative density anywhere. In contrast, because the fluid depth is *zero* in front of a leading edge, even very small numerical oscillations may stop the simulation due to negative fluid depths.

where Ω is the constant angular velocity in radians per second, and (x_0, y_0) is the axis of rotation. This is shown schematically in figure 7.2. Here, $R = 10\,\mathrm{m}$. The test is to advect the initial fluid distribution through one or more rotations; here, the initial scalar distribution is a cosine-hill:

$$C(x,y) = \begin{cases} 50\left[1 + \cos\left(\frac{\pi R}{4}\right)\right] & \text{for } R \leq 4, \\ 0 & \text{otherwise.} \end{cases} \tag{7.3}$$

Figure 7.3 shows the initial configuration and results of applying a standard test to the code under development. Note that the test illustrated has a different initial configuration from that discussed in the text. This is because the test used for the present code appears virtually identical before and after the rotation. The vertical axis is to be interpreted as the value of the scalar C at each point.

The following four quantities allow the accuracy of an advection algorithm to be assessed:

$$\text{Mass conservation ratio (MCR)} = \sum_{i,j} C_{i,j}(t) \,/\, \sum_{i,j} C_{i,j}(0) \tag{7.4}$$

$$\text{Mass distribution ratio (MDR)} = \sum_{i,j} C^2_{i,j}(t) \,/\, \sum_{i,j} C^2_{i,j}(0) \tag{7.5}$$

$$\text{Average absolute error (AAE)} = \sum_{i,j} \left|C_{i,j}(t) - C^e_{i,j}(t)\right| / (33 \times 33) \tag{7.6}$$

$$\text{Maximum absolute error (MAE)} = \max_{i,j} \left|C_{i,j}(t) - C^e_{i,j}(t)\right|. \tag{7.7}$$

In the above, $C_{i,j}(t)$ is to be interpreted as the concentration at grid point (i,j) at time t. The superscript 'e' corresponds to the exact solution; the factor of 33×33 was used as the computational domain used by Chock and Dunker was 33 elements square.

Table 7.1 shows the four measures above along with the best, worst, and median of those tested by Chock and Dunker. The table refers to the case where the fluid underwent two full revolutions. Table 7.1 omits the mass conservation ratio (MCR) because the values of this quantity were not given by Chock and Dunker [40]. That work regarded it as immaterial because the MCR was within 2.2% of the correct value for each of the nine schemes considered. The present code has an MCR ratio that is within 0.02% of the correct value, some two orders of magnitude smaller than Chock and Dunker regarded as sufficiently accurate.

The advection scheme recommended by Chock and Dunker was a 'Chapeau function' method (Pepper *et al.* [153] outline this scheme) and the second choice was that of Zalesak [200]. However, Chock and Dunker warned that "... a severe problem with [the Chapeau function method] is the presence of ripples with negative concentrations". This warning renders that particular method of no use for the present problem (see the footnote on page 75).

measure ideal value	MDR 1	AAE 0	MAE 0
Present code	0.6	0.7	45
Best of [40]	1.0	0.3	10
Worst of [40]	0.1	3.2	75
Median of [40]	0.6	0.7	40

Table 7.1: Comparison of present scheme's performance against those tested by Chock and Dunker [40]

It is concluded that the best method available for the problem under investigation is the multidimensional flux correction scheme of Zalesak, which is the scheme used here. The present scheme's performance was indistinguishable from that of Zalesak's scheme as implemented by Chock and Dunker.

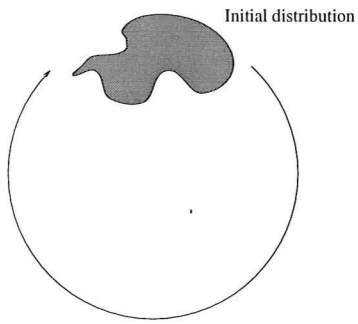

Figure 7.2: Standard solid-body rotation test for numerical advection schemes: schematic diagram of configuration

7.3.3 The advection equation with two scalar quantities

The problem under investigation is actually more complex than stated above, as both cloud density ρ and height h are advected by the velocity field:

$$\frac{\partial h}{\partial t} + \frac{\partial hu}{\partial x} + \frac{\partial hv}{\partial y} = 0 \tag{7.8}$$

$$\frac{\partial h\rho}{\partial t} + \frac{\partial h\rho u}{\partial x} + \frac{\partial h\rho v}{\partial y} = 0. \tag{7.9}$$

If the density of the layer is initially uniform, and the entrainment is set to zero, then the density should remain constant as shown in equation 3.5. This

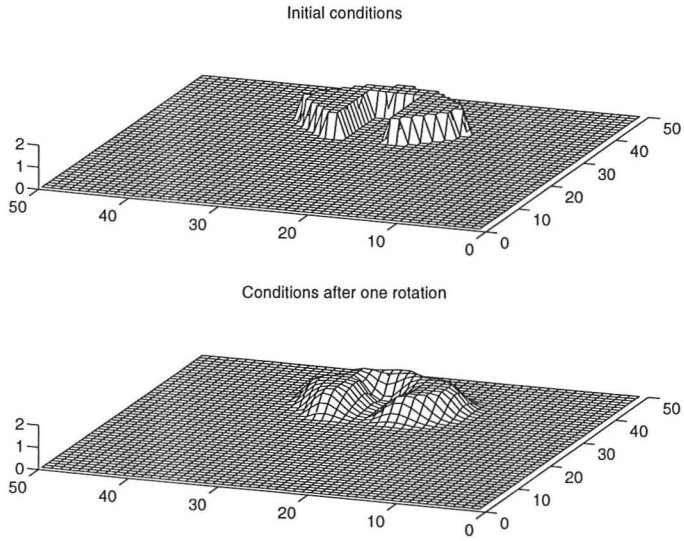

Figure 7.3: Standard solid-body rotation test for numerical advection schemes: initial and final configurations

is, however, not explicitly stated in the problem (although it is trivially obtained from the advection equations) and the density is actually free to assume any value. If the test presented in the previous subsection is carried out with the extended advection equations 7.8 and 7.9, then this furnishes a further test of the advection scheme: a perfect scheme will yield no variation in density. In practice, there was a slight variation in density ($\Delta\rho = \rho - \rho_a$ varies by about one part in 10^4 over a typical run) but the numerical diffusion for density was effectively zero.

This result may be interpreted as further evidence that the advection scheme used here is suitable for the current problem and is correctly implemented.

7.4 The momentum equation

The shallow water equations have four unknowns: cloud depth h, cloud density ρ, and two components of cloud velocity, u and v. The advection equations 7.8 and 7.9 provide two equations; the system is closed by applying the momentum equations to an infinitesimal control volume:

$$\frac{\partial h\rho u}{\partial t} + \frac{\partial h\rho u^2}{\partial x} + \frac{\partial h\rho uv}{\partial y} + \frac{\partial\left[\frac{1}{2}g(\rho-\rho_a)h^2\right]}{\partial x} = 0 \tag{7.10}$$

$$\frac{\partial h\rho v}{\partial t} + \frac{\partial h\rho uv}{\partial x} + \frac{\partial h\rho v^2}{\partial y} + \frac{\partial\left[\frac{1}{2}g(\rho-\rho_a)h^2\right]}{\partial y} = 0. \tag{7.11}$$

The numerical scheme under development incorporates several non-standard features (described in appendix A) mainly in order to handle the sharp depth gradients found at the leading edge. It is possible that some interaction between Zalesak's scheme and the hydrostatic forcing terms used in the present model could cause unacceptable behaviour such as incorrect solution of the momentum equations 7.10 and 7.11.

This possibility is examined below in a test case and it is shown that this test case is simulated accurately. The test case has been chosen as it isolates the quantity of interest (the $x-$ momentum) but allows the simulation to proceed freely.

Here, only the $x-$ component of the momentum is considered; however, the accurately isotropic behaviour of the scheme (shown in section 7.7.2) shows that any component of the (vector) momentum is also correctly simulated.

The test scenario shown in figure 7.4 is a simulation of a non-resisted dense layer current.[4] The volume flow rate Q is $1.6\,\mathrm{m}^3/\mathrm{s}$ per unit width and $g' = 3.45\,\mathrm{m/s}^2$ which give a time scale $(Q/g'^2)^{1/3} \simeq 0.5\,\mathrm{s}$ and a length scale $(Q^2/g')^{1/3} \simeq 0.9\,\mathrm{m}$.

If a control volume as shown in figure 7.5 is considered, then the total amount of $x-$ momentum within this volume is just the $x-$ momentum of the dense layer. This is because equations 7.10 and 7.11 assume that there is no stress between the dense layer and the ambient fluid.

If the motion is steady except for a lengthening front, and of depth h_{in} over the region of fluid source (the paradigm is an evaporating pool of liquified gas), then it can be shown that $h_{\mathrm{in}} = 2(Q^2/g')^{1/3}$. This result is only approximately true because the fluid depth varies slightly over the region.

The momentum equation shows that the fluid within the volume receives a force of magnitude $\frac{1}{2}g(\rho - \rho_a)h^2$ per unit width to the right, which in this case implies that the total force on the dense fluid is 485 N as the equilibrium fluid depth at $x = 0$ was 2.15 m, the dense fluid density $1.85\,\mathrm{kg/m}^3$ and the width of the channel 33 m. The ambient fluid has density $1.26\,\mathrm{kg/m}^3$. Figure 7.6 shows nondimensionalised time versus the difference between the $x-$ momentum per unit width of the dense fluid as calculated by the numerical code under development, and that calculated analytically (the momentum deficit). The momentum deficit per unit width is nondimensionalised with $\rho Q^{5/3} g'^{-1/3}$. Figure 7.6 shows three distinct phases: a rising phase, due to the fluid depth at the wall increasing; a plateau phase, when the system is steadily lengthening; and a decreasing phase, following the dense layer hitting the downstream wall. It is not possible to test the present scheme's performance against theoretical solutions as the system considered here has transients that are not simple to solve analytically. The present scheme is compared to other theoretical results in sections 7.6.1 and 7.6.2 (one dimensional), and section 7.8 (two dimensional).

[4]Here, 'non-resisted' means that the shallow water equations 7.8 to 7.11 are solved.

The plateau phase is constant to within less than 2% and it is concluded that the computational scheme correctly predicts the momentum of the dense layer.[5] This is true even in the presence of sharp gradients which are strongly influenced by the flux correction scheme of Zalesak.

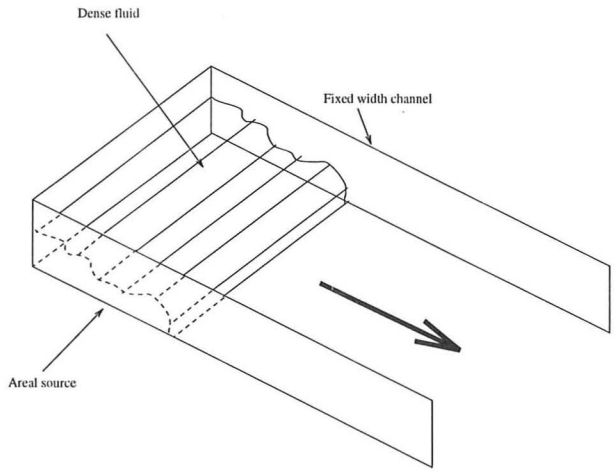

Figure 7.4: Constant width channel for testing momentum equation

[5] A small jump is seen at $t/(Q/g'^2)^{1/3} \simeq 20$. This jump is less than 1% of the total momentum of the layer and is possibly a result of the changing fluid depth at the downstream wall.

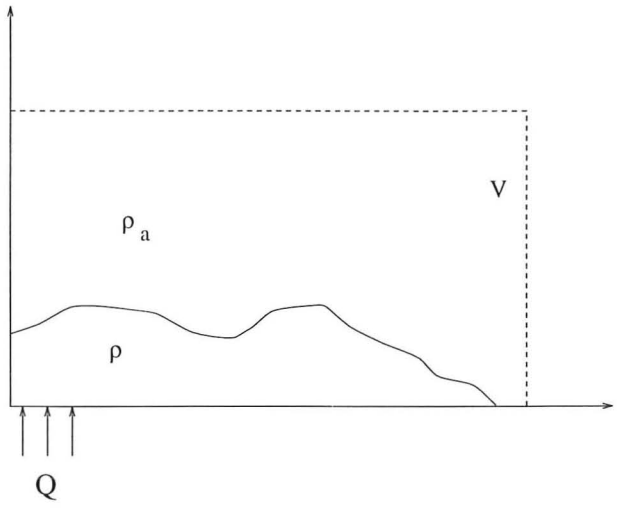

Figure 7.5: Cross sectional view of one-dimensional unresisted shallow water flow

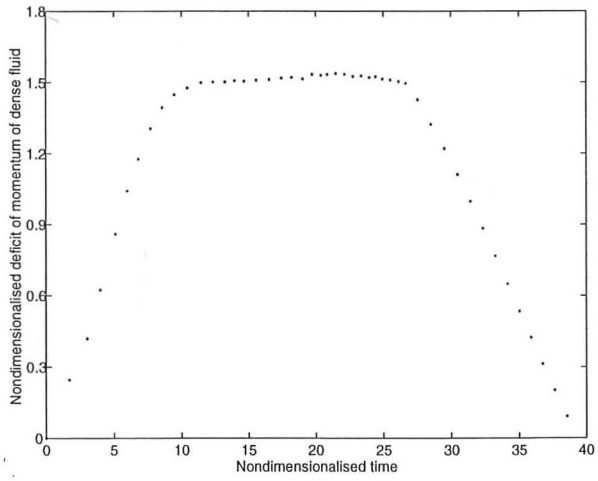

Figure 7.6: Nondimensionalised momentum deficit of dense layer in a constant width channel against time

7.5 Energy conservation

The present formulation of the shallow water equations includes no statement of conservation of energy: rather, energy conservation arises as a consequence of the four shallow water equations used.

It is important to show that energy is conserved in the simulations for much the same reasons as those given above for momentum. It is shown below that energy is conserved to an acceptable degree of accuracy.

The shallow water equations conserve energy:

$$\frac{\partial E}{\partial t} + \nabla \cdot (\mathbf{u}E) + \nabla \cdot (\mathbf{u}P) = 0, \tag{7.12}$$

where $K = \frac{1}{2}\rho h u^2$ is the kinetic energy per unit area, $P = \frac{1}{2}(\rho - \rho_a)gh^2$ is the potential energy per unit area and $E = P + K$ is the total mechanical energy per unit area. This equation is proved and generalized to the entraining case in appendix D.

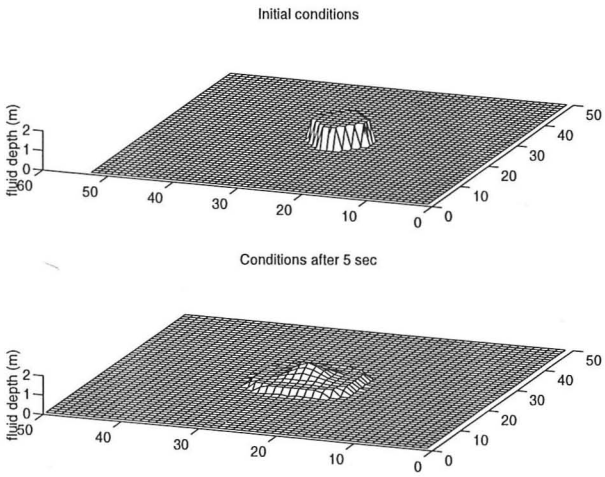

Figure 7.7: Non-entraining axisymmetric release; initial conditions and depth at $t_0 = 4$

Figure 7.7 shows the simulation of an unresisted dense layer spreading over level smooth ground and figure 7.8 shows the energy of the layer against time. In figures 7.7 and 7.8, $t_0 = r_0/\sqrt{g'_0 h_0}$ and $E_0 = V(g'_0 h_0)\rho_0/2$ where V is the cloud volume and a subscript zero denotes initial values. Although there is a small amount of energy change, this is small compared to the energy exchange involved in such processes as entrainment, viscous interaction, and ground drag. The fluxes between adjacent fluid elements in this case are strongly limited by flux-correction and thus quantities such as energy may not be precisely conserved.

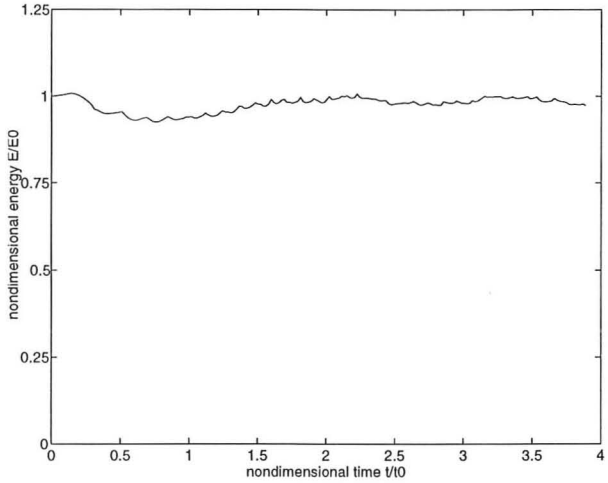

Figure 7.8: Non-entraining axisymmetric instantaneous release: energy as a function of time after release

However, the energy loss is some 10^3 times less than the work done against the ambient fluid in a resisted dense layer leading edge. It is thus the case that the total mechanical energy of a dense fluid layer is conserved to an acceptable degree of accuracy.

7.6 The leading edge

As discussed in chapter 4, the leading edge is modelled in such a way as to represent the hydrostatic force pushing the current forward and the drag offered by the ambient fluid.

Although this method ignores the structure of the leading edge, it will be simulated in such a way as to control the following flow in the same way as a real current.

7.6.1 The leading edge in equilibrium with the following flow

The approximation of a constant front Froude number implies that the hydrostatic (forward) force is balanced by a momentum deficiency in the following flow of ambient fluid, following Benjamin [10]. It is important to show that the momentum interaction between dense layer and ambient fluid is simulated correctly as the method used (introduced in chapter 4) is novel.

Figure 7.9 shows a schematic view of a resisted dense layer moving from left

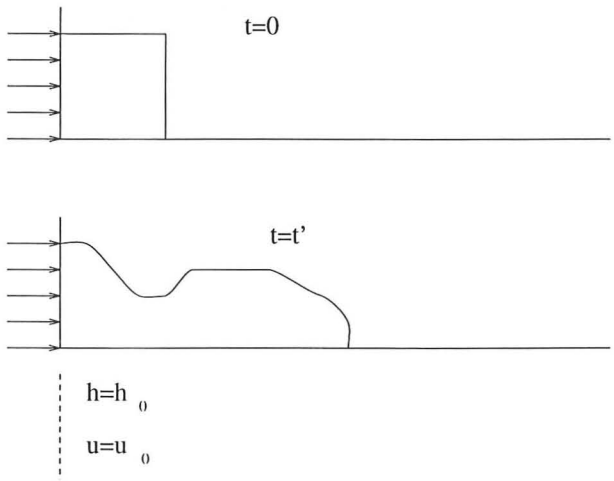

Figure 7.9: Non-entraining one-dimensional gravity current: schematic view

to right. Dense fluid is forced in at the left hand side in such a way as to maintain a densimetric Froude number of unity at the point of entry. This should result in a current of uniform depth moving in solid body motion away from the source of fluid; at the front the hydrostatic force pushing the current forward is matched by the drag afforded by the ambient fluid through which the dense layer is intruding.

Figure 7.10 thus shows an accurate simulation, with the exception of a slight numerical wiggle at the leading edge which appears to be a characteristic of FCT at a severe discontinuity. In view of the smallness of this oscillation (it persists but does not grow) and the fact that detailed simulation of the leading edge is not an objective, this behaviour is acceptable: the model is accurately simulating the leading edge as discussed in chapter 3.

7.6.2 The leading edge controlling the following flow

If there is a mismatch between the inflow conditions and the front condition, then the leading edge will exert an influence on the rest of the current; the leading edge is said to 'control' the following flow. It is necessary for such behaviour to be reproducible as the influence of the leading edge may be considerable.

That the front can control the following flow is seen in figure 7.11 in which the leading edge condition is incompatible with the source on the left hand side. This has been done by changing the speed of the ambient fluid: the dense layer is now advancing into a headwind moving at half the speed of the inflow. As the front densimetric Froude number is defined relative to the ambient fluid and not the ground the headwind is expected to force the current back, and eventually a new equilibrium flow will be reached. There is an incompatibility between the

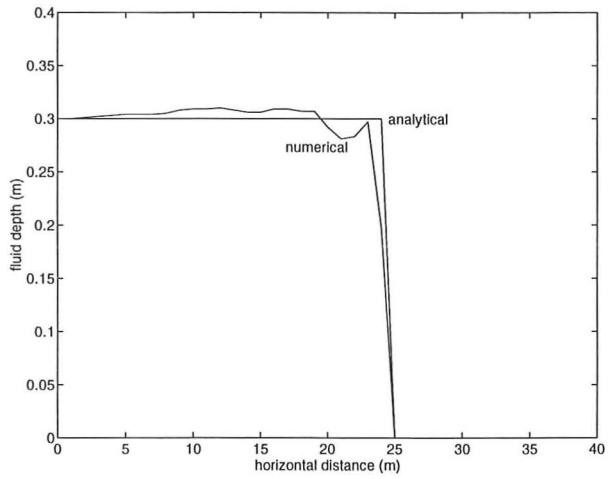

Figure 7.10: Non-entraining one-dimensional gravity current: analytical and numerical predictions for stationary ambient fluid

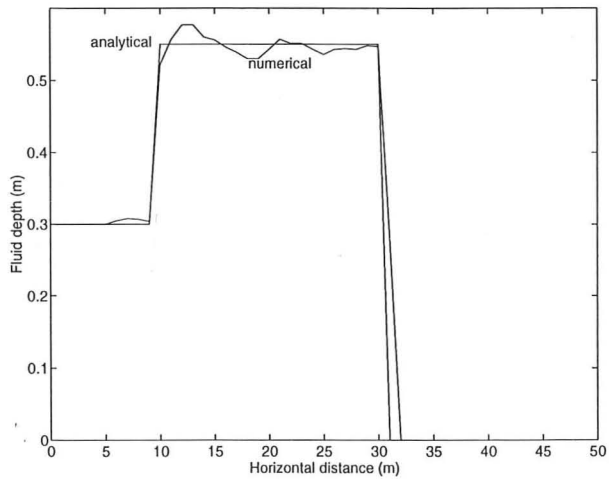

Figure 7.11: Non-entraining one-dimensional gravity current in headwind: analytical and numerical predictions

inflow conditions and the leading edge.

The incompatibility causes a hydraulic jump which is close to the analytical prediction[6] also shown on the figure. The slight oscillations are due to transient waves that take a finite time to decay. A hydraulic jump is not a solution of the shallow water equations as they conserve energy (appendix D) and a jump converts directed mechanical energy into random turbulent energy. In a hydraulic jump, therefore, some energy has to be dissipated and this occurs in nature by turbulent dissipation or waves. A term corresponding to the dissipation has been added to this model (see chapter 4) and it is seen to perform satisfactorily. In the absence of this dissipative term, energy which would dissipate in a real hydraulic jump is carried away by waves that grow and eventually stop the simulation.

7.7 Computational mesh independence

The results of a computer simulation of a dispersing dense gas cloud must be independent of the coordinate scheme used to describe the problem.

Because the problem is solved using a uniform array of squares, the only possible coordinate transformations must be composed of the following elementary operations:

1. a spatial translation
2. a rotation
3. a scaling (that is, multiplying both $x-$ and $y-$ axes by the same quantity);
4. a Galilean transformation.

The $x-$ and $y-$ axes have to remain identically scaled. That the results of the code under development are not affected by the four coordinate transformations shown above will be shown below.

7.7.1 Spatial translation

The coordinate transformation considered is:

$$\begin{aligned} x' &= x + k_x \\ y' &= y + k_y, \end{aligned} \tag{7.13}$$

[6]The analytical prediction uses the hydraulic jump relation [171] and volume conservation on either side of the jump. If $R = y_2/y_1$ is the ratio of downstream to upstream fluid depth, F and F_{IN} the densimetric Froude numbers at the front and inflow point respectively, and $X = w/v_1$ the windspeed nondimensionalised with the inflow speed, then it can be shown that $R^4 - 2R^3 + 2R^2 - 2R(1 + F_{IN}(X - 1 + F/F_{IN})^2 + 1 = 0$. This system has one meaningful root with the specified parameters: $R \simeq 1.82$, which generated the analytical result.

where (k_x, k_y) is a constant vector.

That the code under development is invariant under spatial translation may be seen from inspection of figure 7.12. Any dependence of the cloud's behaviour on position would destroy the axisymmetry of the cloud and this is not seen.

Other diagrams in this chapter also serve as sensitive indicators of spatial inhomogeneity but a close scrutiny of these shows no dependence of cloud behaviour on location. It may be concluded that the code is invariant under spatial translation.

7.7.2 Rotational invariance

As the present simulation is two-dimensional, the coordinate transformation considered is

$$\begin{pmatrix} x' \\ y' \end{pmatrix} = \begin{pmatrix} \cos\theta & \sin\theta \\ -\sin\theta & \cos\theta \end{pmatrix} \begin{pmatrix} x \\ y \end{pmatrix}. \tag{7.14}$$

It is clear that an axisymmetrical cloud should remain so for all time. This is shown in figure 7.12, in which an initially square (diamond-shaped) cloud is allowed to spread. The initial non-axisymmetry decays leaving a round cloud. This shows that the model is correctly isotropic: the code is directionally independent. The slight asymmetry seen in figure 7.12 is due to the graphical routine used. In the case of a release such as this, the time scales with $t_0 = r_0/\sqrt{g'h_0}$, where r_0 is the initial cloud radius and h_0 the initial cloud depth. In this case, the 40 s of simulation time is equal to approximately $12t_0$.

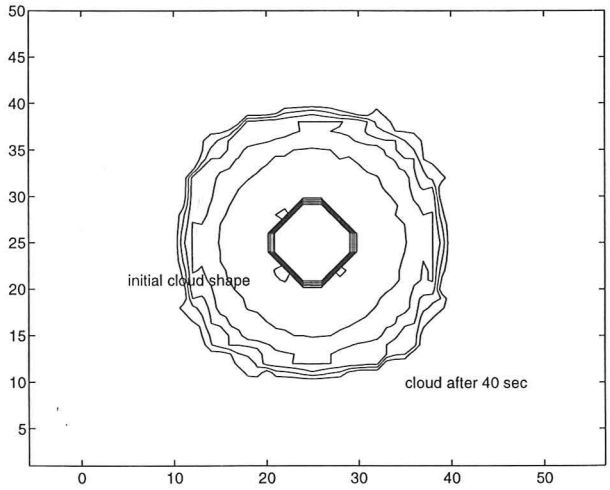

Figure 7.12: Non-entraining axisymmetric instantaneous release: initial cloud shape and shape after 40 s

7.7.3 Scaling independence

Scaling independence considers whether the grid size chosen to describe the problem affects the subsequent behaviour of the cloud. The transformation considered is

$$\begin{aligned} x' - x_0 &= S.(x - x_0) \\ y' - y_0 &= S.(y - y_0) \end{aligned} \tag{7.15}$$

where S is a constant scalar and (x_0, y_0) is the fixed point, taken to be the centre of the computational domain. The grid size chosen should have no effect on the behaviour of the cloud. Equations 7.15 suppose that $\Delta x = \Delta x'$, or that the numerical value of the grid size is unchanged by the transformation.

The measures of performance given on page 76 are not appropriate for verifying the scale independence of the present code. This is because two simulations (one with a fine grid and one with a coarser grid) could yield clouds of similar shape and appearance but differ in detail because of the different grid sized used.

A better way of comparing two simulations is to identify physically meaningful parameters such as cloud radius and compare these. A tentative set of comparative measures is shown below.

1. cloud area: $A = \int I(h_t(x,t))\, dx\, dy$
2. cloud centroid position $(c_x, c_y) = \left(\frac{\int x h_t(x,y)\, dx\, dy}{\int h_t(x,y)\, dx\, dy}, \frac{\int y h_t(x,y)\, dx\, dy}{\int h_t(x,y)\, dx\, dy} \right)$
3. cloud moment $M = \frac{\int r h_t(x,y)\, dx\, dy}{\int h_t(x,y)\, dx\, dy}$
4. cloud non-uniformity: $N = \frac{A \int (h_t(x,y))^2\, dx\, dy}{\left(\int h_t(x,y)\, dx\, dy\right)^2}$

where $h_t(x,y)$ is the fluid height at point (x,y) at time t, $I(x)$ is the indicator function ($I(x) = 1$ if $|x| > 0$ and zero otherwise) and $r = \sqrt{(x - c_x)^2 + (y - c_y)^2}$ is the distance from the centroid. All integrations are carried out over the computational domain. Cloud non-uniformity N is a natural measure of the deviation of a cloud from uniform height; N is bounded below by unity for a uniform cloud but any other configuration will have $N > 1$.

All the measures shown above will be nondimensionalised with respect to their values at $t = 0$, except cloud non-uniformity which is already dimensionless.

The test case chosen for study is an instantaneous release of density $\rho = 1.44\,\mathrm{kg/m^3}$. The dense gas initially has height 1.11 m and is 3 m square. These values are suitable for a gridsize of 1 metre as the cloud has time to become independent of the initial conditions before encountering the edge of the computational domain.

The simulations proceed for 5 seconds, which corresponds to a nondimensional time of $\hat{t} = 4.5$. Two sets of comparisons will be presented, the first in zero wind speed and the second in a wind speed of 1.5 m/s. The grid sizes chosen for the simulation span an order of magnitude.

Zero wind speed releases

Table 7.2 shows the cloud parameters for the zero wind case. It may be seen that the parameters are in close agreement (the differences are in each case less than 6%) for the two smallest gridsizes, and show some deviation for the largest size chosen. The gridsize is nondimensionalised with the diameter of the cloud.

nondimensional gridsize	0.1	0.04	0.02	0.01
cloud area A/A_0	9.90	8.98	8.81	8.83
moment M/M_0	2.58	2.87	3.04	3.06
non-uniformity N	1.15	1.30	1.21	1.15

Table 7.2: Cloud parameters in zero wind speed for simulations with different gridsizes

The relatively large discrepancies seen for a gridsize of 0.1 are due to the initial cloud covering only a small number of fluid elements. As the advection scheme updates the properties of fluid element (i, j) using fluid elements such as $(i+3, j)$, these discrepancies are to be expected for large nondimensionalised grid sizes. Nevertheless, they are well within the tolerances accepted by Chock [39] for the majority of schemes tested.

The practical simulations presented in chapters 9 to 11 use nondimensional gridsizes of the order of 0.01-0.05.

7.7.4 Galilean invariance

Here coordinate transformations of the type

$$\begin{pmatrix} x' \\ y' \\ t' \end{pmatrix} = \begin{pmatrix} x + ut \\ y + vt \\ t \end{pmatrix} \tag{7.16}$$

are considered. These are known as the Galilean transformations.

Exact Galilean invariance is known to be difficult to approach for Eulerian-based methods [120, 174, 197], especially for systems solving the advection equation with large spatial scalar gradients (as here). Chock [39], discussing the Galilean invariance properties of numerical schemes, states that "the difficulty... lies in minimizing both artificial diffusion and the occurrence of spurious ripples."

Although the mechanism for simulating the leading edge in one dimension has been shown to be Galilean invariant (on page 85), this section will show the Galilean invariance of the whole model. This will be done by simulating an instantaneous release the same size and density as described on page 88.

The test case has zero wind and the dense fluid initially at rest. The Galilean transformations 7.16 will be executed by setting the wind speed and the initial fluid velocity to the same value. As the simulation is known to be accurately isotropic, the direction of the velocity is unimportant. The speeds chosen will be 0.5, 1.0, and 2.0 m/s.

The physical system to which this corresponds is invariant under the Galilean transformations and the cloud should look the same for each case, except that the cloud will be advected in the direction (u, v).

Table 7.3 shows the cloud parameters identified on page 88 for the base case and the Galilean-transformed clouds. The cloud parameters in table 7.3 show a variability of $\simeq 10\%$. In view of the harsh nature of this test, this result may be taken to indicate acceptable Galilean invariance.

wind speed (m/s)	0.0	0.5	1.0	2.0
cloud area A/A_0	8.83	9.47	8.72	10.00
moment M/M_0	3.06	2.92	2.91	2.81
non-uniformity N	1.15	1.08	1.05	1.33

Table 7.3: Cloud parameters for Galilean-transformed clouds

7.7.5 Courant number (timestep) independence

The Courant number, defined on page 68 (chapter 6) and discussed from a practical viewpoint on page 74, is a nondimensionalised timestep. It has been fixed at 0.1 throughout the whole of this chapter, with the exception of the two-dimensional test of the advection scheme where the Courant number was specified to be 0.2. The effect of varying this parameter will now be investigated.

The standard case (defined on page 88) will be used, but with an ambient fluid speed of 1.5 m/s. The method of solution requires two dimensionless numerical parameters, the Courant number C and a diffusion coefficient D for Zalesak's scheme. These quantities are discussed in chapter 6 and appendix A.

It is necessary for D to be the same order of magnitude as C. Here C and D will be identical and range from 0.05 to 0.5.

Table 7.4 shows the three cloud parameters for varying Courant numbers. The parameters for $C = 0.05$ and $C = 0.1$ are very similar, with a slight change as $C = 0.5$ is approached. The use of $C = 0.1$ is thus justified, as is the claim that the simulation is independent of Courant number for $C \approx 0.1$.

C, D	0.05	0.1	0.2	0.5
cloud area A/A_0	8.73	8.83	9.50	10.85
moment M/M_0	2.94	3.06	3.08	2.48
non-uniformity N	1.25	1.15	1.35	1.54

Table 7.4: Cloud parameters for varying values of the Courant number C and diffusion coefficient D

7.8 Comparison of current code with analytical results

The above confirmations of the behaviour of the present numerical scheme are not enough, alone, to give confidence that the scheme is accurately solving the resisted shallow water equations. For example, some numerical (and unphysical) instability could prevent accurate shallow water simulation.

If, however, the numerical scheme compares favourably with known analytical solutions, then this can be taken as further evidence that the code is behaving as required. Roache [158] makes the recommendation that, if exact solutions are available, they should be compared against the output of a code and this is done here. The present code is now compared with analytical solutions from the literature.

The present approach differs from that of Rottman and Simpson [164] who solve the shallow water equations with zero interaction with the ambient fluid everywhere except near the leading edge. Because the present work defines 'leading edge' as 'region of dense fluid which displaces a large amount of ambient fluid', ambient fluid exerts a force on the dense layer at, for example, a bore which is predicted to move at constant Froude number [196]. The two approaches agree in the cases simulated as $[\partial/\partial t + \mathbf{u}_a \cdot \nabla]h < 0$ away from the front.

7.8.1 Comparison of the present model with that of Rottman and Simpson [164]

In 1983, Rottman and Simpson [164] presented a series of analytical results of finite-volume releases of dense fluid in a one-dimensional channel. As they considered lock-exchange flows, only the case of a very deep upper layer will be used here. One of the results of Rottman and Simpson was to show that such one-dimensional shallow water flows approach a self-similar solution, that is a flow which may be described using a small number of variables. In their case, the configuration shown in figure 7.13 has a similarity solution, previously presented in the context of oil slicks [103] moving with a front Froude number of β:

$$h(x,t) = \frac{1}{9g'}\alpha^2 t^{-2/3}\left[\eta^2 + \frac{4-\beta^2}{\beta^2}\right] \tag{7.17}$$

$$u(x,t) = \frac{2}{3}\alpha t^{-1/3}\eta, \tag{7.18}$$

where

$$\alpha^3 = \left[\frac{27\beta^2 g' x_0 h_0}{12-2\beta^2}\right], \qquad \eta = \frac{x}{x_f(t)} \tag{7.19}$$

and $x_f = x_f(t) = \alpha t^{2/3}$ is the front position at time t.

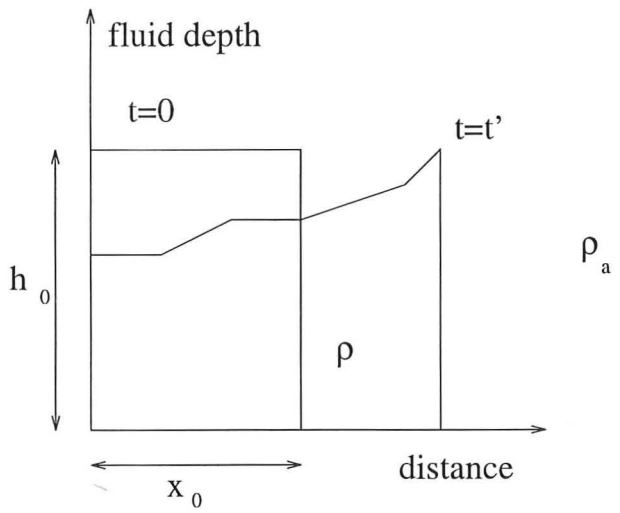

Figure 7.13: Configuration for one-dimensional tests of computational scheme at $t = 0$ and $t = t'$

The nondimensional results shown here were obtained with an initial configuration as shown in figure 7.13. The initial fluid depth h_0 was 1 m and the horizontal extent x_0 was 5 m; the reduced gravity g' was 4.85 m/s^2. The results shown here (after nondimensionalisation) are only a weak function of the initial aspect ratio of the dense fluid.

Another difference between the two approaches is that here an initially stationary dense fluid accelerates in a finite time until the specified front Froude number is approached; Rottman and Simpson assumed that the front speed instantaneously adjusted to maintain the leading edge Froude number. The time scale for this adjustment is of order $t_0 = \sqrt{h_0/g'}$.

Figures 7.14 to 7.16 show a comparison between the present code and the similarity solutions of Rottman and Simpson [164] for dimensionless times t/t_0 of 2, 3, and 6. In this case, the analytical curve is a simple configuration to which the

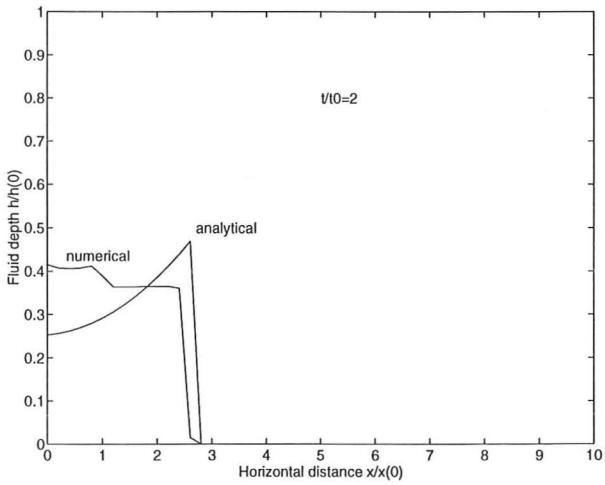

Figure 7.14: Non-entraining release of a finite volume of dense fluid in a one-dimensional channel. Numerical and similarity solutions after $2t_0$

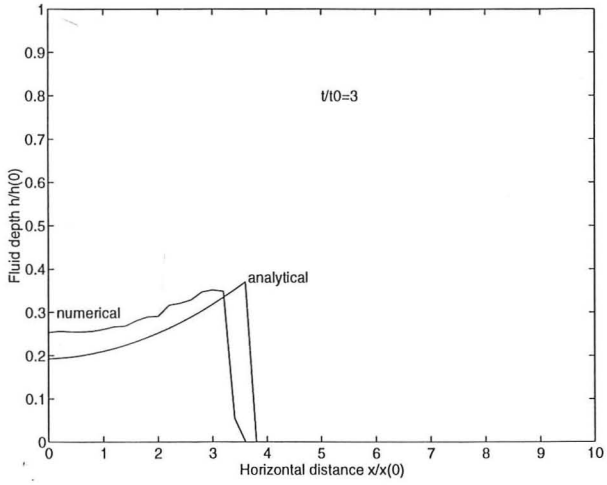

Figure 7.15: Non-entraining release of a finite volume of dense fluid in a one-dimensional channel. Numerical and similarity solutions after $3t_0$

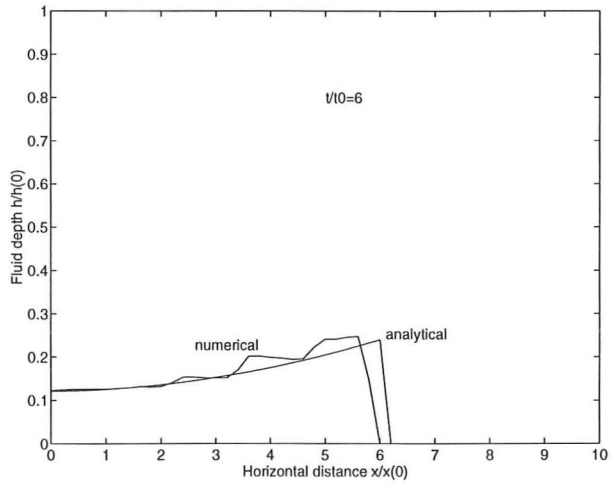

Figure 7.16: Non-entraining release of a finite volume of dense fluid in a one-dimensional channel. Numerical and similarity solutions after $6t_0$

numerical solutions tend. The long time intervals (up to $6t_0$) should have ensured that any transients have decayed and the similarity solution should be close to the actual solution. However, there are certain differences between the two curves and these differences appear to persist. Notably, the current is shorter than the similarity solution and for later times, the leading edge is slightly deeper.

The differences in leading edge position are ascribed to the acceleration time which is not accounted for in the equations leading to the similarity solution. This difference in position of leading edge also accounts for the slight difference in leading edge depth.

The numerical solutions presented by Rottman and Simpson appear to be slightly higher near the front than the similarity solutions, as here. The small difference between the two front positions, seen on figures 7.14 to 7.16, is possibly due to the time taken for the initially stationary fluid to accelerate toward the speed of the similarity solution.

7.8.2 Comparison of the present model with the analytical results of Grundy and Rottman [69] and Britter [21]

This section will compare the results of the present model with the analytical solutions given by Grundy and Rottman [69] and Britter [21].

These workers presented the radius of an axisymmetric dense current as a function of time, but here the area covered will be considered instead. This is because the radius of a dense current is not well defined in the present simulation

but the area is exactly calculable, using the area equation on page 88.

The problem considered was that of the present study (that is, the shallow water equations 3.40 to 3.43 together with a fixed, specified front Froude number β for the leading edge); entrainment was neglected.

Constant volume axisymmetric dense currents

In 1985, Grundy and Rottman [69] presented an analysis of planar and axisymmetric gravity currents. The axisymmetric results from that paper will be compared to those of the present code.

If a volume V of dense fluid of density ρ is released onto an infinite, smooth horizontal plane, then providing $\rho - \rho_a \ll \rho_a$ (where ρ_a is the ambient fluid density), Grundy and Rottman [69] argued that the radius r_m of the dense layer at large times t will be asymptotic to

$$r_m = \left(\frac{16}{\pi}\right)^{1/4} \left\{\frac{\beta^2}{4-\beta^2}\right\}^{1/4} (Vg')^{1/4} t^{1/2}, \tag{7.20}$$

where g' is the reduced gravity $g(\rho - \rho_a)/\rho_a$ and β is the front Froude number. Here, t must be large compared to $x_0^2/(g'V)^{1/2}$ where x_0 is the initial radius of the dense fluid; the Reynolds number of the flow is assumed to be sufficiently high to be immaterial.

The test case chosen for comparison is the same as used on page 88. The area of the dense layer as predicted by the present code and that predicted by equation 7.20 are shown in figure 7.17 to agree closely.

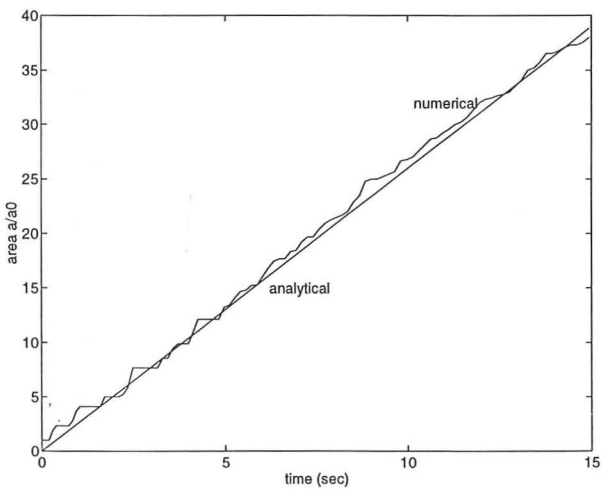

Figure 7.17: Comparison of axisymmetric dense current areas: present work and Grundy and Rottman [69]

Constant flux axisymmetric dense currents

If the volume of the dense layer increases linearly with time, the system is said to be 'constant flux'. Britter [21] considered this problem and in an intuitively appealing argument gave the layer radius as:

$$r_m = \left(\frac{3}{4}\right)^{-3/4} \left(\frac{\alpha}{2\pi}\right)^{1/4} \beta^{1/2}(g'Q)^{1/4}t^{3/4} \tag{7.21}$$

where Q is the volume flow rate and α is an empirically determined dimensionless number. Britter then gave arguments to suggest that $\alpha = 1$.

Figure 7.18 shows that the area of the dense layer as predicted by the current numerical scheme agrees closely with equation 7.21. The step-like appearance of the numerical curve is due to the computational discretization: the area increases discontinuously when a new fluid element has non-zero depth (the model's independence of gridsize was demonstrated in section 7.7.3). The magnitude of the jumps is proportional to the gridsize used.

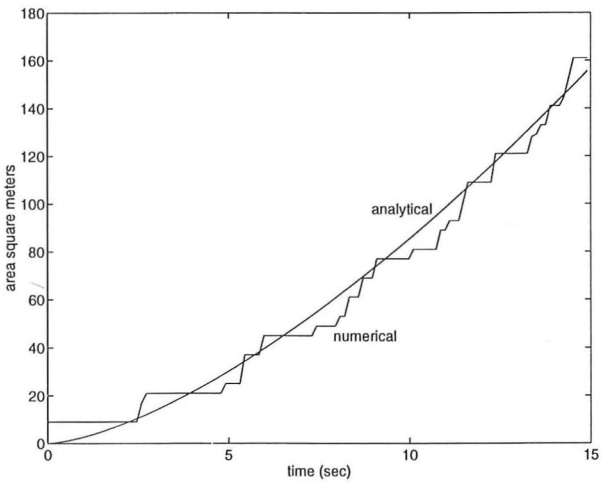

Figure 7.18: Comparison of axisymmetric dense current areas: present work and Britter [21]

7.9 Summary

The numerical scheme under development has been checked in a number of ways in this chapter. The advection scheme, being required to eliminate numerical overshoot completely, performs adequately. Quantities such as mechanical energy and momentum have been shown to behave as expected when integrated over the dense layer; the scheme has been shown to be homogeneous and isotropic. The

code is invariant under all the coordinate transforms allowed by the numerical scheme. A number of analytical results have been simulated accurately.

There is thus confidence that the computational model solves the discretized shallow water equations accurately.

Chapter 8

Model evaluation and optimization

8.1 Outline

Chapters 1 to 7 of this thesis have presented a mathematical model for the simulation of dense gas dispersion over complex terrain. Evaluation of this model may be carried out by comparison with experimental results. Such comparison may take the form of either physical interpretation or statistical analysis. These types of comparison are complementary and both must be used in model assessment.

Experimental data from dense gas dispersion experiments is typically of the form of a number of Eulerian concentration traces. Comparison of such data with predictions tends to be difficult due to the large amount of data generated by experiment (and in this case by the model). In order to make meaningful comparisons, therefore, some sort of data reduction is necessary.

This chapter thus defines several physically meaningful quantities that may be evaluated for either experimental traces or predicted traces. Their comparison provides an objective measure of the adequacy of the model's predictions.

This chapter will discuss assessment of the model's performance against a number of experimental results. Next, several objective 'goodness of fit' quantities, expressing how well a model fits experimental data, will be reviewed. The quantities so defined will be referred to as 'Goodness-of-fit measures' or GFMs, following Wheatley *et al.* [193] and others.

A discussion of repeat- and atmospheric- variability follows.

8.2 Extraction of useful information from experimental results

Any dense gas dispersion experiment generates a large amount of data, which must be reduced in some way to meaningful quantities. Examples of such quantities include peak concentration and dose; while not losing sight of the physical

significance of these quantities, their relevance to the risk assessment community must not be forgotten. The term 'statistic' will be used in its original sense of a partition of possible datasets.

A typical concentration trace for a continuous release and an instantaneous release is shown in figure 8.1, taken from Schatzmann [167]. Both traces rise sharply from 'noise' levels, but after the rise the instantaneous trace decays, while the continuous trace remains at an approximately steady value.

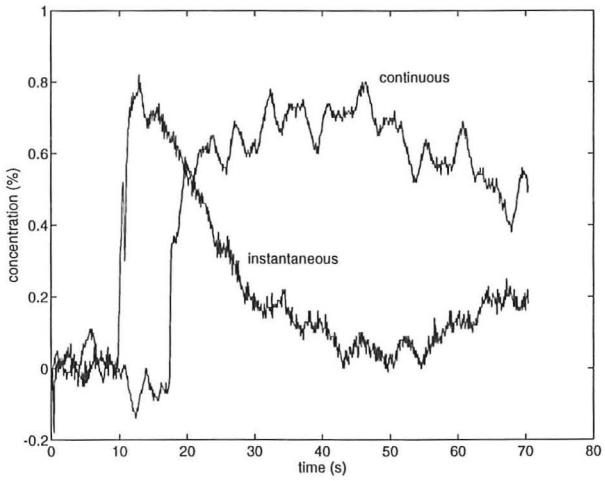

Figure 8.1: Typical concentration-time traces from the Schatzmann experiments [167] for instantaneous and continuous releases

It is clear that the two types of concentration traces are so different in nature that different data reduction techniques will be necessary, and the reduction techniques are discussed separately below.

8.2.1 Statistics for instantaneous releases

The typical trace for an instantaneous release, shown in figure 8.1, suggests several statistics that may be obtained from such concentration traces. Five potential quantities are discussed below; their relevance to risk assessment is self-evident.

Schatzmann carried out five repeat trials for each release under nominally identical conditions. The statistics defined below should be calculated for each of the five trials.

Although the repeated trials allow some estimation of ensemble statistics to be made this will not be done here; this point is discussed later in this thesis, in chapter 9. It is possible to apply GFMs to any quantity that is predicted and measurable, and several candidate quantities are discussed below.

Average concentration This quantity is well defined for continuous releases, but not for instantaneous releases where the concentration traces do not suggest a unique time over which to average. The concept of 'average concentration' for an instantaneous release is therefore not pursued.

Cloud arrival time Most concentration traces in the experiments show an almost instantaneous increase from zero to a large value, but some traces do not exhibit such clear-cut behaviour and an objective definition is required. These problems become more acute when considering the far field sensors that gave output that was only marginally distinguishable from noise.

Cloud arrival time t_a will be defined as the first time at which the cloud concentration exceeds half the maximum concentration of the trace. This definition is insensitive to the considerations below, as the concentration trace usually increases sharply around $t = t_a$.

Cloud residence time Intuitively, the cloud residence time should reflect the length of time for which the concentration trace remains appreciably greater than background. The cloud residence time clearly requires objective definition. Determination of cloud departure time can be difficult as the concentration tends to decrease very slowly after an initial sharp rise.

Here, a cloud departure time t_d is defined as the last time at which the cloud concentration exceeds half the maximum concentration. Although this time is usually well-defined, some traces exhibit slowly-decaying concentrations around $t = t_d$.

Cloud residence time t_r is defined as $t_r = t_d - d_a$.

Peak concentration This quantity is clearly defined as the maximal concentration experienced at a given sensor. However, real sensors have a finite averaging time and the peak concentration as recorded by a real instrument is a strong function of the averaging time used. These considerations are independent of those considered in appendix C, where the model's ability to reproduce short time-scale concentrations is discussed.

Peak concentration is the only quantity used for calculation of GFMs (for instantaneous dense releases) by Hanna *et al.* [86]. It is convenient, unambiguous, and important in risk assessment. An incorrect prediction of peak concentration usually has a clear interpretation when examining the present model.

For the Thorney Island releases [130], sensor drift was removed in such a way as to preserve peak concentration at the expense of other statistics [46].

Dose The dose $\mathcal{D}$ is important to risk estimations as it used to link an Eulerian concentration trace to a probability of death. It is defined as $\mathcal{D} = \int_t C(t)\,dt$,

where $C(t)$ is the concentration at time t. Toxic load $\mathcal{L}$ is a generalization of dose with

$$\mathcal{L} = \int_t [C(t)/C_0]^n \, dt \tag{8.1}$$

where n is dependent on the substance released and C_0 is a reference concentration (usually either the initial concentration of a release, or a relevant biologically determined concentration). Here, n will be taken to be unity so the dose is the area under a concentration-time trace (it only by this token that mean concentration is meaningful).

Of the four statistical measures of concentration data detailed above, only , peak concentration time will be used for the objective optimization exercise. Dose, and cloud residence time (being of order $\mathcal{D}/C_{\text{peak}}$) will be reserved for the subjective process of physical interpretation.

8.2.2 Statistics for continuous releases

Continuous releases are, in general, simpler than instantaneous releases because the source term becomes steady.[1]

The limited number of relevant statistics is discussed below.

Cloud arrival time Cloud arrival time t_a is similarly defined as in the instantaneous case: t_a is the first time at which the cloud concentration exceeds half the peak concentration of the trace. In the case of the continuous experiments, the peak concentration is well defined for all the traces examined. Cloud residence time is not meaningful for a continuous release.

Average cloud concentration The continuous trace on figure 8.1 shows that 'average' concentration is not a clear concept. In the absence of a detailed statistical study of the experiments of Schatzmann [167], the cloud concentration that will be used will be the time-averaged concentration C_a for times $t > t_a$, where the system appears to have reached a steady state.

Concentration variability If the nth concentration percentile is C_n, the continuous phase of the trace will have $C(t) < C_n$ for $n\%$ of the times considered and $C(t) > C$ for the remainder. The interquartile range $R = C_{75} - C_{25}$ (or R/C_{50}) gives a measure of concentration variability.

The primary statistic used in chapters 9 and 11 will be C_a, although some use will be made of t_a and the concentration percentiles.

[1] Equivalent experiments for outdoor releases are not so simple: a dense plume tends to meander in response to changing wind direction. The process of cloud meander is closely related to the concentration fluctuations discussed in appendix C, although occurring on longer timescales. Also, because of the nature of the present model, a 'continuous release' is defined as one that starts at a particular time but continues indefinitely.

8.3 Model quality and model evaluation

The determination of the best free parameters to use in the present model should be part of the wider activity of model quality improvement. The quality (defined as 'fitness for purpose') of dense gas dispersion models is discussed by Britter [26], who considers features of models such as computational expense and ease of use in addition to physical accuracy. Here, attention will be confined to scientific assessment, and this will be achieved by analysing the discrepancies between prediction and experiment.

8.4 Goodness-of-fit measures (GFMs)

Large scale dense gas dispersion experiments typically generate a large amount of data, as reported by McQuaid and Roebuck [130]. This renders direct comparison of predicted concentrations to measured concentrations very difficult.

Choosing a small number of concentration time traces for detailed comparison with model predictions as a sole method of model assessment is unacceptable for two reasons. Firstly, this is sensitive to the (subjective) choice of traces to be used; and secondly, such comparison yields little, if any, information about systematic model errors.

With these comments in mind, it is clearly necessary to define objective measures of how closely experimental results are predicted by a model; the term 'GFM' (goodness-of-fit) will be used to cover all such quantities. In addition to meeting the comments above, the definition of a GFM elucidates precisely what features of the experimental results the model is attempting to reproduce.

In general, GFMs are interpreted as the 'distance' of the model predictions from the data; thus a smaller GFM indicates a better fit (except for the nonparametric FAC2). Different GFMs highlight different aspects of a model's predictions.

It is the case that a small GFM can obscure serious shortcomings in a model. This may be mitigated by the use of a large number of GFMs and optimizing with respect to some overall quantity, but even this approach has disadvantages that are discussed below. Physical interpretation of a model's results must also be made, even though such considerations cannot be objective. Several GFMs have been defined in the literature and a critical review follows.

8.4.1 The GFMs of Wheatley *et al.* 1986 [193]

Following the Thorney Island series of experiments [130], Wheatley *et al.* [193] considered how results from an integral model could be compared to the fluctuating concentration traces made by the many instrument masts at the experimental site.

These workers defined, for each time t_i, a 'cloud averaged' concentration $\overline{C_i}$ that was the arithmetic mean of all sensors that detected gas at time t_i; a variance σ_i^2 was defined analogously. Several GFMs were defined, the first of which was

$$S_1 = \frac{\sum_i a_i n_i (\overline{C_i} - C_i^\lambda)^2}{\sum_i a_i n_i}, \tag{8.2}$$

where n_i was the number of sensors in the cloud at time t_i, and a_i was the time averaging period used. The predicted concentration at time t_i was C_i^λ and was a function of a vector of model parameters λ.

This GFM is well suited to integral models; the model discussed by Wheatley *et al.* predicted one concentration for the whole cloud. Although further GFMs were defined that essentially weighted the terms in equation 8.2 according to the size of σ_i^2, this class of GFMs is unsuitable for use here as the present model does not carry out cloud-wide averaging. This and other GFMs were used to estimate the top entrainment parameter α_T, and it was observed that

> It is tempting to think that a GFM could be defined for the trials as a whole and a single overall optimum value found for α_T ... This approach would, however, be misleading for a number of reasons. Firstly, if an overall value of α_T is defined, then differences that occur between the [model] fit and data are not entirely random; there is also a systematic component, according to the choice made for the entrainment model. Secondly, the accuracy to within which the optimum value of α_T for a given trial is determined is not commensurate with the minimum size of the GFM; ... this could lead to unjustified biasing in favour of a few trials merely because they show less scatter.

Wheatley *et al.* determined a value of α_T for each of the Thorney Island instantaneous releases.

The use of such GFMs appeals to the central limit theorem to assure the normality of the random variables considered. However, the central limit theorem only applies to large numbers of uncorrelated random variables.[2] Thus, the formal application of the central limit theorem requires that the measured concentrations within a dense gas cloud be independent.

The model optimization process carried out by Wheatley *et al.* [193] was made very much simpler by the fact that only one parameter, the top entrainment α_T, was being varied, unlike the present analysis.

[2]Tapia and Thompson [177] discuss the central limit theorem in the context of maximum likelihood estimation and state that "maximum likelihood estimators frequently ... behave poorly for small samples." These workers do not consider correlated random variables.

8.4.2 The GFMs of Hanna *et al.* 1991 [87] and Hanna *et al.* 1993 [86]

Following earlier work on the evaluation of (passive) air quality models [85], Hanna *et al.* considered dense gas dispersion [87]. Although the material discussed was hydrogen fluoride, and thus not part of the present study (appendix C discusses this further), the GFMs presented will be considered here. Hanna *et al.* defined the fractional bias (FB), the normalized mean square error (NMSE), and the fraction within a factor of two (FAC2), as follows:

$$\text{FB} = (\overline{C_o} - \overline{C_p})/0.5(\overline{C_o} + \overline{C_p}) \tag{8.3}$$

$$\text{NMSE} = \overline{(C_o - C_p)^2}/\overline{C_o}.\overline{C_p} \tag{8.4}$$

$$\text{FAC2} = \text{Fraction of } C_p \text{ within a factor of 2 of } C_o, \tag{8.5}$$

where C_o and C_p are the observed and predicted concentrations, and an overbar indicates an average over one particular group of concentration measurements. Hanna *et al.* thus calculated the three GFMs above for a number of datasets and took a weighted mean of these to be representative of the model as a whole. They were thus able to assess the goodness of fit of fourteen dense gas dispersion models to the 'Goldfish' experiments [11] and models were represented on a plane as points, the $x-$ and $y-$ coordinates being the FB and the NMSE score of that model. Models with small NMSE and FB scores were thus represented as points close to the origin.

Subsequent related work [86] defined the geometric mean bias MG, the geometric variance VG, and the correlation coefficient R as follows:

$$\text{MG} = \exp\left[\overline{\ln(C_o/C_p)}\right] \tag{8.6}$$

$$\text{VG} = \exp\left[\overline{\ln(C_o/C_p)^2}\right] \tag{8.7}$$

$$\text{R} = \overline{(\ln C_o - \overline{\ln C_o})(\ln C_p - \overline{\ln C_p})}/(\sigma_{\ln C_p}.\sigma_{\ln C_o}) \tag{8.8}$$

with the same definition of FAC2. This set of GFMs implicitly uses the more realistic lognormal distribution of concentration and will be used throughout the remainder of this chapter. Note that MG corresponds to FB, and VG to NMSE, but assuming that the *logarithms* of the concentrations are drawn from a symmetric distribution. Hanna *et al.* set C_p to sensor noise level if $C_p = 0$ and this device will be used in this thesis.

Hanna used resampling methods [50] to calculate the variances of the three GFMs above and then applied Student's t- test to assess whether differences in the GFMs were significant in a statistical sense. The t- test will not be used here as there is no assurance that the GFMs are normally distributed.[3]

Britter [26] points out that the NMSE (and by extension VG) is bounded below by stochastic uncertainty and data errors and notes that

[3]If the central limit theorem is applicable, then VG and NMSE are theoretically of equal

> ...even if the model physics error was zero there is an underlying or inherent uncertainty due to the stochastic nature of the problem and to data errors

and goes on to discuss GFMs in the context of model evaluation. Davies [45], commenting on Hanna *et al.* [86], presents statistical arguments to support Britter's statements. Here, attention will be confined to assessment of the present model's physical accuracy and its ability to predict experimental data.

8.5 GFMs and shallow water models

Unlike integral models, whose output is a small number of variables as functions of one variable, the present model records Eulerian concentration timetraces for any of the large number of computational elements. It is therefore necessary to approach the problem of parameter evaluation in a very different way from that used with integral models, even though the number of free parameters in both approaches is very similar at $\mathcal{O}(10)$. This is the case even for continuous release experiments as the present model gives Eulerian concentration profiles.

It is also the case that the present shallow water model requires perhaps three orders of magnitude more computer processing power than the models considered by Wheatley *et al.* [193] and Hanna *et al.* [86], and such considerations will clearly restrict the procedures available for use.

8.6 Experimental data for evaluation of GFMs

No large scale experimental data concerning dense gas dispersion on slopes has been located. However, large scale trials have been conducted over level ground, and smaller-scale experiments have been carried out over a variety of lower surfaces. These two classes of experimental data are considered below.

8.6.1 Large scale field trials and the Modellers' Data Archive

Large scale dense gas dispersion experiments, all of which took place on level or near-level ground, have been summarised by Hanna *et al.* [86] in the Modellers' Data Archive (MDA). The MDA was originally created in order to compare the results of a number of dispersion models with experiment. This was done by

validity. However, in practice, normality is approached much faster if more nearly normally distributed variables are summed, which is of particular relevance to the work in [86] as there ~ 5 variables were summed.

placing the results of a number of dispersion trials in a common format; the format included sufficient information to run the dispersion models, and a condensed subset of the experimental results. Hanna *et al.* went on to develop a method by which the dispersion models could be compared, both to one another and to the experimental data and this is described here under GFMs.

A brief description of nine dispersion trials was given by Hanna *et al.* [86]. Two of these were passive experiments and six measured the dispersion of substances whose behaviour was strongly influenced by thermodynamic effects such as phase changes[4] and thus not considered here. This leaves two experiments: the instantaneous and continuous Thorney Island trials reported by McQuaid and Roebuck [130], and use will be made of those Thorney Island trials that appear in the MDA.

8.6.2 The experiments of Schatzmann [167]

Several workers have released small ($\sim 0.04\text{m}^3$) releases of dense gas over a range of sloping lower surfaces. This thesis will use the data of Schatzmann [114, 167] which is uniquely suitable in several respects.

In 1991, Schatzmann [167] investigated the behaviour of dense gas flowing over a slope as part of the CEC's Major Technological Hazard Programme. This study was motivated, as here, by risk assessment and split into continuous releases and instantaneous releases. These two classes will be described below.

Schatzmann released gas (SF_6) over three different smooth slopes: 11.63%, 8.6%, and 4.0%. The results used here took place in calm conditions.

The concentration sensors used were artificially aspirated hot-film anemometers that provided a frequency response of about 50 Hz. Schatzmann reported that gas concentrations could be detected down to about 0.1% by volume [114]. The data analysed here were sampled at either 80 or 100 millisecond intervals. No further data manipulation was carried out after the translation of the probe response to percentage gas concentration; thus all interpretation in this thesis is carried out on raw data.

The experiments considered here split into instantaneous and continuous releases. Each class is considered below.

Instantaneous releases

For each of the three slopes, Schatzmann released either $125\,\text{cm}^3$ or $450\,\text{cm}^3$ of SF_6 from a cylinder of aspect ratio of approximately unity. Each experiment was repeated five times under nominally identical conditions and concentration traces from each of eight sensors was recorded. There are thus $3 \times 5 \times 8 = 120$ traces.

[4]The substances released were liquified natural gas, ammonia, and hydrogen fluoride—all of which have lower molecular masses than air and must therefore be dense either because of the low temperature of release or the presence of liquid.

Each trace continued for 70 or 80 seconds. The concentrations recorded were a volume percentage given to two decimal places.

Continuous releases

For continuous releases, Schatzmann released SF_6 over each of the three slopes. The release lasted for over 70 s and the volume release rate was 100 ℓ per hour. The continuous release experiments were carried out once for each slope.

8.6.3 Statistics and heavy gas dispersion modelling

The statistics defined above are such that they may be calculated for both experimental and predicted concentration traces. If the statistics are calculated in the same manner for each, a consistent method of comparing the predictions of a model to experimental data is achieved.

In general, nonparametric methods are preferable [177] as the underlying distribution is not known and the central limit theorem is of limited applicability.

8.7 Repeat- and atmospheric- variability

As discussed in chapter 2, each Thorney Island release was performed only once: results are therefore one realisation from an ensemble.

Puttock and Colenbrander considered ensemble statistics in the context of risk assessment [156] and concluded that a useful model of dense gas dispersion should produce a typical member of the ensemble as output (and not ensemble averaged values). Carn *et al.* [35], discussing variability, stated that prior agreement on criteria for typicality should be adopted; and Chatwin [38] emphasised the importance of clear definition of the underlying ensemble. Carn *et al.*, commenting on Puttock and Colenbrander's work, stressed that judicious choice of ensemble would reduce the discrepancies between useful model predictions and ensemble average traces discussed by Puttock and Colenbrander.

The comments of Carn *et al.* [35] are accounted for in this work by using statistics from each of Schatzmann's experiments; and by using a large number of datapoints from the Thorney Island releases.

Hall [74] has investigated the repeat variability of instantaneously released dense gas clouds. He used a scale model of the release mechanism used at Thorney Island [130] and carried out either 50 or 100 repeats. Hall reported that

> ...the ratio of the 10th to the 90th percentile is typically of order 2, with occasional larger excursions which do not exceed an order of magnitude...this is the component of the variability due to a combination of variations in the self-driven flow within the gas cloud and

of small scale atmospheric turbulence of the sort reproduced in wind tunnel models.

Hall went on to discuss the additional variability occurring in practical situations as a result of larger-scale meteorological variations not reproduced in wind tunnels.

Wilson [195], considering concentration fluctuations in hazard assessment, states that "The peak concentration observed during any one [dense gas] release event can vary by a factor of 10 among the members of an ensemble of identical releases into the same atmospheric conditions."

The greater variability reported by Wilson was due to atmospheric phenomena such as wind direction swings that are not reproduced in wind tunnels. Wilson stated that dense releases would meander as they entrain air with crosswind velocity fluctuations.

Wilson went on to compare dense plume variability with the passive case, and reported that "fluctuations caused by inhomogeneous mixing, excluding meandering, are as strong in dense plumes as they are in neutrally buoyant releases."

Thus agreement with Thorney Island data to within a factor of about 3 is the best that could reasonably be expected. Variability is one reason why comparison of a large number of datapoints is required, as then underlying systematic trends may be distinguished through the scatter.

8.8 Summary

Experimental data must be reduced in some way before comparison with the present model. This can be done by defining a number of statistics that are functions of the Eulerian concentration traces measured. These statistics are defined in an objective manner and are physically meaningful. There are statistics for continuous releases and instantaneous releases:

continuous releases cloud arrival time t_a and time-averaged concentration C_a.

instantaneous releases cloud arrival time t_a and cloud departure time t_d; cloud residence time $t_r = t_d - t_a$; peak concentration C_{peak} and dose $\mathcal{D}$.

The goodness-of-fit measures MG, VG, R, and FAC2, originally defined by Hanna *et al.*, may be applied to all the above statistics to give overall performance measures that may be evaluated objectively. Trends in these statistics may be identified and physical explanations given.

Webber *et al.* consider statistical evaluation of heavy gas dispersion models and conclude that optimization of a model's parameters to best fit experimental data is neither possible nor necessarily desirable.

For the Thorney Island releases, atmospheric- and repeat- variability means that agreement to within a factor of about 3 is the best that could be expected.

Chapter 9

Model validation: Thorney Island

9.1 Outline

In this chapter, the present model is evaluated by comparing its predictions with field data from the Thorney Island experiments [130]. The main form of analysis is the comparison of peak concentrations. The evaluation method used will be the investigation of systematic mispredictions (trends); any such trends would be indicative of problems either in the physical assumptions made in the model, or the choice of free parameters. Additional benefits from this analysis will include estimating the likely errors made by the model, and the sensitivity of the model to the variation of the free parameters.

9.2 Overview of methodology

Given that no overall 'best' model may be found (Wheatley's comments [193] reproduced on page 103 discuss this) it is neither possible nor desirable to 'optimize' the constants in the present model to the Thorney Island dataset. The general approach will be as follows:

1. A reasonable set of constants will be chosen for the model. These constants will either be generally accepted values, or values taken from other dense gas dispersion models. The parameters thus obtained are independent of the Thorney Island experiments as they were determined before 1982.

2. For certain of the Thorney Island Instantaneous Trials (restricted to those included in the MDA), the model will be run with the same source and meteorology. The results will be compared using both GFMs and physical reasoning.

3. The constants used will be altered if necessary to obtain better agreement.

The comparison method chosen uses all sensors detecting gas. This gives an objective comparison (there is no subjective choice of which sensor data to use). Although Thorney Island data has been used for model comparison before, by Hanna *et al.* [86], that comparison used only centreline concentrations. The present model is being used here to predict peak concentrations in three dimensional space, and it is thus reasonable to expect higher MG- and VG- scores.

Following the discussion on page 99, peak concentration will be used as the primary comparison statistic. However, peak concentration depends on the averaging time used and this is discussed below.

9.3 Peak concentration and averaging time

Nussey *et al.* [149] consider measured peak concentration as a function of time averaging period used. They consider that averaging times need to be between 0.3 s and 1 s and concluded that "...0.6 s represents an averaging time that is reasonably consistent with the criterion that [instrument] noise should be suppressed."

Peak concentrations calculated on a 0.6 s (moving-point) averaging time basis have been used here, following Hanna *et al.* [86].

This system filters out high-frequency fluctuations which are not simulated with the present shallow layer model, which cannot resolve phenomena on timescales $\leq (h/g')^{1/2}$. A 0.6 s averaging time is thus appropriate for any model not simulating the fine-scale structure of the cloud, as here.

The present model describes a spreading dense gas cloud as a function of ground position and time; it is thus possible to compare very much more than peak concentrations against downwind distance. This study will therefore consider the response of every sensor that detects gas, using the full three-dimensional coordinates of the point (downwind distance, cross-wind distance, and altitude). This will allow investigation of such aspects of the cloud as its width, and height.

The ratio of observed to predicted concentrations may be plotted as functions of downwind distance, cross wind distance, or sensor altitude. Examination of these residual plots would show any systematic error that would indicate incorrect entrainment parameters.

9.4 Ensemble variation and model predictions

The present model does not include the random effects of turbulence: it is deterministic. Model predictions are therefore interpreted as representative measures of the relevant ensemble. The method of comparison used compares large numbers of peak concentrations in one realisation to the predictions of the present model on a logarithmic scale.

As discussed in chapter 8, peak concentrations in an ensemble of Thorney-type releases have a range of about an order of magnitude. This variability is one reason why large numbers of peak concentrations are compared: any trends that are coherent over an experiment can reasonably be attributed to physical causes (and not random variation).

9.5 Code comparison

The Thorney Island Phase One instantaneous release experiments comprised sixteen releases [130]; the series is discussed here in chapter 2. Of the sixteen releases, seven are not suitable for use here: one was a test run, the release mechanism failed for one, the wind changed in two, and air contaminated the gas bag to an unknown extent in three. The nine remaining Trials constitute the Modellers' Data Archive (MDA, discussed in chapter 8).

Each of these nine successful Trials generated a considerable amount of experimental data. An average of some 56 sensors detected gas (506 in total); the trace left by each of these sensors was a series of some 20 000 concentrations; after the 0.6 second averaging process discussed above, each trace was constituted about 1 800 numbers.

For the purposes outlined above, a detailed discussion of three experiments will be made; the other six will be briefly discussed using goodness-of-fit measures.

The experiments chosen are numbers 08, 09, and 13. These Trials were chosen as they spanned the full range of windspeeds (Trial 09 had the slowest windspeed and Trial 13 the fastest); Trial 08 was included as it had the greatest number of useful sensor records. Each of the nine Trials included in the MDA was matched against the present model by the present author [81]; the Trials chosen here were not exceptional in terms of GFMs in any way, although each Trial was different.

Each of the chosen Trials is described in turn.

9.6 Thorney Trial 08

9.6.1 Outline

Thorney Island Trial number 08 was a particularly successful one: a large proportion of the sensors operated satisfactorily, and the wind direction almost bisected the sensor array; for this reason more analysis has been carried out on this Trial than the others. A number of workers have used results from this Trial for analysis of models, particularly three dimensional CFD models [99].

In particular, the present model has been tested with different entrainment parameters against the experimental results from this Trial. Several methods of analysis will be presented.

- The vertical concentration profile to be used will be investigated. Three different assumed vertical concentration profiles (exponential, Gaussian, and uniform) will be used and their results compared.
- Differing values of the entrainment parameters will be used and the results compared with experiment. The 'base case' used takes values from theoretical studies and previous dense gas dispersion models. It is shown that there is no basis for using entrainment parameters that differ from these default values.
- Residual analyses are presented and where severe over- or under- prediction occurs, a physical explanation is sought (for example, many underpredictions are due to the sensor in question lying outside the predicted plume path).
- A number of severe over- and under- predictions are discussed on an individual basis.
- The model is run using a smaller gridsize to further investigate the properties of the near-source flow field.

9.6.2 Vertical concentration profiles

One of the aims of this analysis was to investigate the suitability of different vertical concentration profiles. Appendix B shows how vertical concentration profiles may be represented in a shallow layer model; the equation of state may be used to link the concentration C to the density ρ. Appendix B shows that

$$\rho(z) = \begin{cases} \rho_a + (\overline{\rho} - \rho_a).\frac{4}{\pi S_1} \exp\left[-\left(\frac{2z}{S_1 h\sqrt{\pi}}\right)^2\right] & \text{Gaussian distribution} \\ \rho_a + (\overline{\rho} - \rho_a).\frac{2}{S_1} \exp\left[-\frac{2z}{h}\right] & \text{Exponential distribution} \\ \rho_a + (\overline{\rho} - \rho_a).\frac{1}{S_1} \mathrm{H}\left[z - h\right] & \text{Uniform distribution.} \end{cases} \tag{9.1}$$

where H is the Heaviside operator with $\mathrm{H}(x) = 0$ if $x < 0$ and unity otherwise; S_1 is the dimensionless shape parameter defined in chapter 3.

The approach used here is to use each of the three distributions described in equations 9.1 and assess the performance of the model under each one (the model, giving only depth averaged density $\overline{\rho}$ and cloud depth h, needs to be run only once; vertical profiles are imposed after a computational run).

Melia [131] and Stretch [176] investigated the vertical concentration profile in dense gas dispersion experiments using a water flume to simulate the atmospheric boundary layer and salt water to represent dense gas. These workers considered profiles of the form $C(z) = C(0)\exp\left[-(z/h_0)^\beta\right]$ but used $\beta = 1$. Britter [23], however, reviewing a number of experimental results, reported that "...all [these

workers] find a value of $\beta \simeq 1.5$ in the laboratory... [f]ield data are not inconsistent with these estimates. There is little evidence to support a value of β as low as 1.2.". For the purposes of the present work, a value of β other than 1 or 2 is practically intractable: the analogue to formulae 9.1 includes the incomplete gamma function;[1] standard numerical packages such as `calc` [65] do not have robust methods for inverting this function and in addition such solution is often time-consuming [154]. The requirement of having a usable model essentially forbids the use of non-integral values for β. As no residual analysis shows opposite trends with altitude for $\beta = 1$ and $\beta = 2$, this problem is not one that affects the present study.

Vertical profiles may be assessed by plotting the residuals C_o/C_p for each sensor as function of altitude. Figures 9.1 to 9.3 show the residual analysis for Thorney Trial 08 using exponential, Gaussian, and uniform vertical profiles respectively.

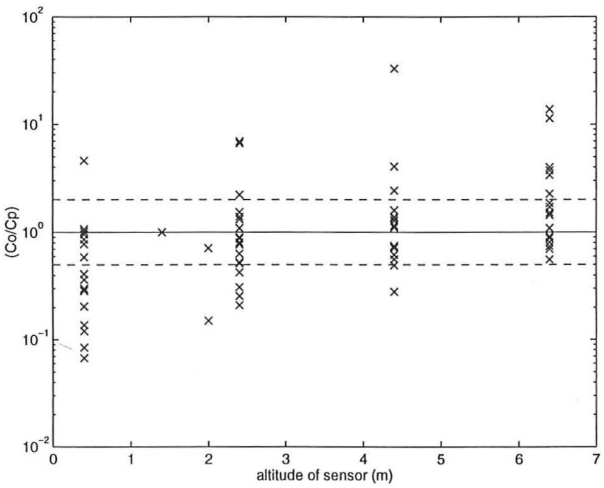

Figure 9.1: Thorney Island Trial 08: C_o/C_p as a function of the altitude of the sensor. Exponential vertical concentration distribution.

These graphs show that there is a slight tendency to overprediction (see table 9.1 for a precise statement) and a slight systematic trend for the lowest sensors to be overpredicted and the highest sensors to be underpredicted. These

[1]Standard textbooks [1] define the incomplete gamma function $P = P(a, x)$ using $P(a, x) = \frac{1}{\Gamma(a)} \int_{t=0}^{t=x} e^{-t} t^{a-1}\, dt$. The equation to be solved (appendix B) for h/h_0 when the vertical concentration profile follows $C(z) = C(0) \exp\left[-(z/h_0)^\beta\right]$ is $\alpha = P\left(\beta^{-1}, (h/h_0)^\beta\right)$; an explicit solution is required for the determination of ground level density ρ_0 in terms of $\overline{\rho}$. This equation has no analytical solution for most values of β, so must be solved by numerical means such as Newton's method or bisection. Neither method is robust as the gradient at the root is small.

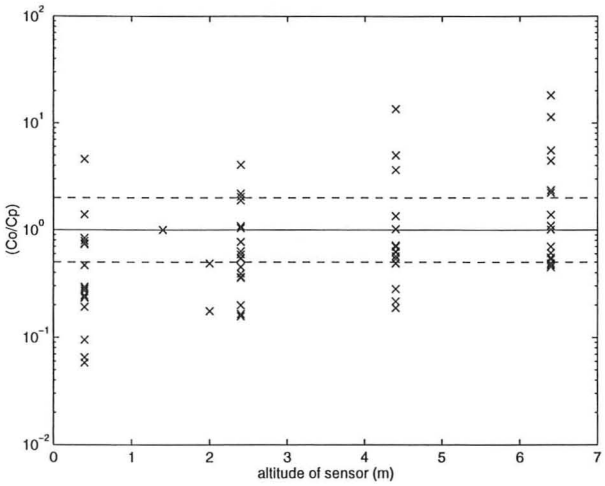

Figure 9.2: Thorney Island Trial 08: C_o/C_p as a function of the altitude of the sensor. Gaussian vertical concentration distribution.

	GFM (rank)			
distribution	MG	VG	R	FAC2
exponential	0.80(1)	3.85(1)	0.52(2)	0.52(1)
top hat	0.51(3)	7.10(3)	0.49(3)	0.30(3)
Gaussian	0.70(2)	4.10(2)	0.53(1)	0.41(2)

Table 9.1: GFMs for three vertical concentration distributions (bracketed figures show rank—1, 2, and 3 for first, second, or third respectively); Thorney Island Trial 08

trends are, however, not statistically significant, even at a 50% level of confidence (formally: if no trend were present, statistical fluctuations would result in a more pronounced trend more than half the time).

The GFMs defined by Hanna *et al.* for the present model with each of the three vertical concentration profiles are now analysed. Table 9.1 shows the four GFM scores defined by Hanna *et al.* calculated using the 73 sensors detecting gas at Trial 08. It is clear that the exponential fit is the best, followed by Gaussian, and the top hat is the worst. Exponential concentration distributions will therefore be used for this report, although different distributions may be considered if a residual analysis against sensor altitude shows any trend.

An exponential vertical concentration distribution appears to be the most appropriate. Only this distribution will be used for the remaining Trials, but a significant systematic trend for over- (or under-) prediction with increasing altitude might suggest that another distribution would fit the data better.

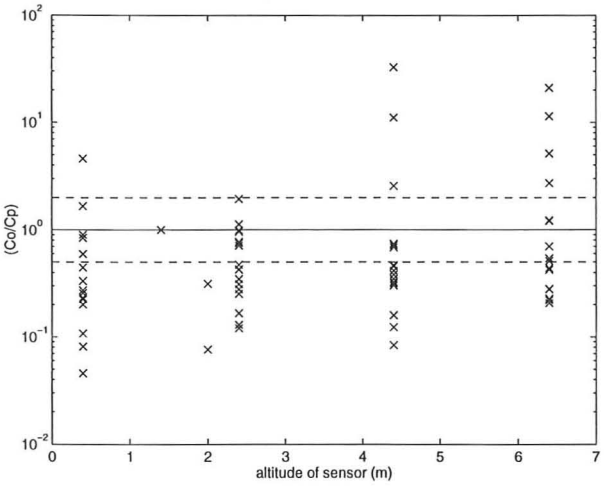

Figure 9.3: Thorney Island Trial 08: C_o/C_p as a function of the altitude of the sensor. Uniform vertical concentration distribution.

9.6.3 Variation of a

As discussed in section 9.2, the base case model uses entrainment parameters that are set to standard values obtained from the literature. Here, the the effect of changing them is investigated.

These values for a and b were used as a 'base case'. The existence of any significant trends would then used as case for alteration of either a or b in equation 5.5 (page 60, chapter 5).

Figures 9.4 to 9.9 show C_o/C_p as a function of distance with a equal to 0.1, 0.2, 0.3, 0.4 (von Karman's constant), 0.5 and 0.7. The purpose of this exercise was twofold: first to ascertain the sensitivity of the model to a, and second to determine whether the experimental data warrant a value for a other than the preferred and theoretically supportable value of 0.4. This method of analysis also allows some estimation of the errors likely to be made when using the present model to estimate peak concentration as a function of position.

As the value of a increases, more entrainment occurs through the cloud top, with consequent faster dilution (both in space and time; the windspeed is held constant). For large values of a, therefore, it would be expected for large distances to be underpredicted compared to small distances; the opposite effect should be evident for small values of a. This exercise will not result in a 'best' value for a; the purpose is to assess whether there are grounds for changing the parameters used.

Figures 9.4 to 9.9, taken together, are more similar to one another than might be expected; each exhibits about the same magnitude of scatter; and each has

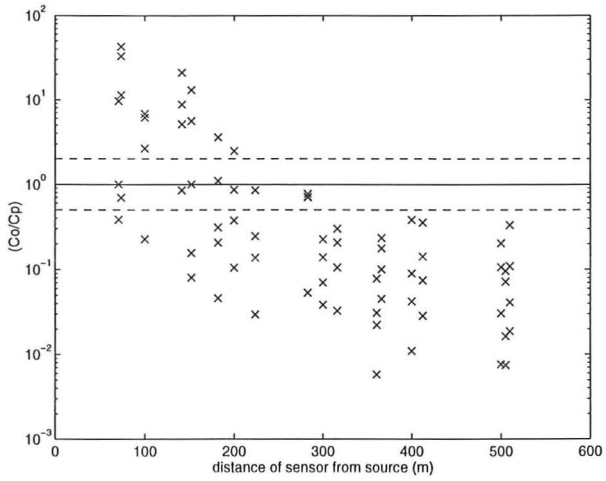

Figure 9.4: Thorney Island Trial 08: C_o/C_p as a function of the distance of the sensor from the source. Model using $a = 0.1$

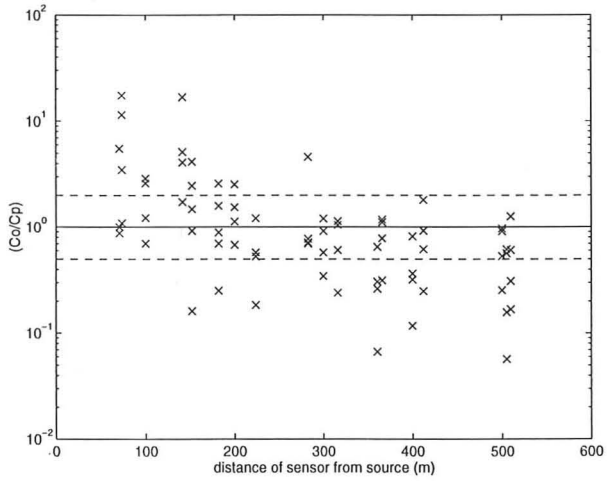

Figure 9.5: Thorney Island Trial 08: C_o/C_p as a function of distance from source. Model using $a = 0.2$

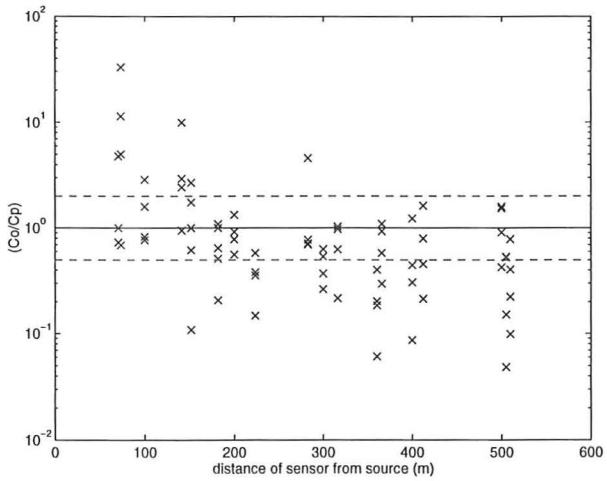

Figure 9.6: Thorney Island Trial 08: C_o/C_p as a function of distance from source. Model using $a = 0.3$

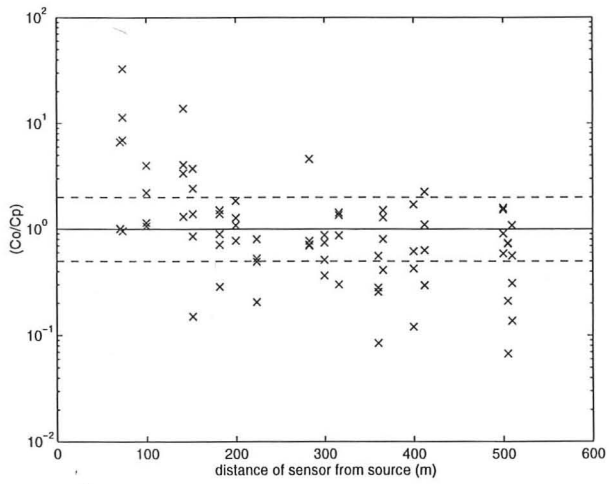

Figure 9.7: Thorney Island Trial 08: C_o/C_p as a function of the distance of the sensor from the source. Model using $a = 0.4$

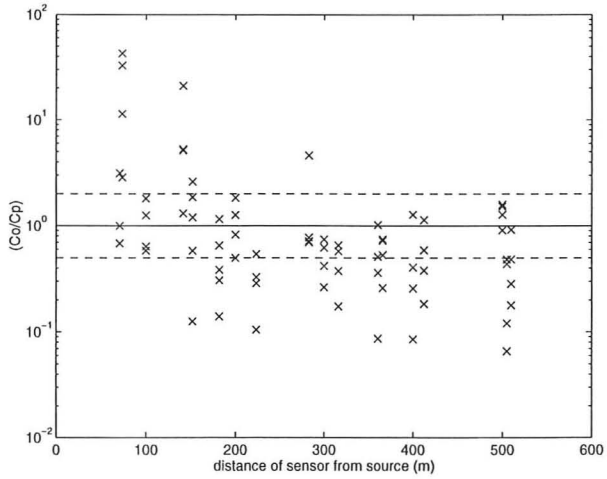

Figure 9.8: Thorney Island Trial 08: C_o/C_p as a function of the distance of the sensor from the source. Model using $a = 0.5$

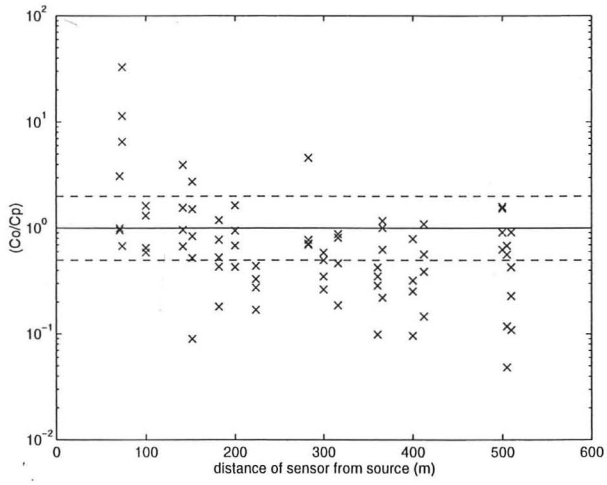

Figure 9.9: Thorney Island Trial 08: C_o/C_p as a function of the distance of the sensor from the source. Model using $a = 0.7$

severe underpredictions at small distances (the behaviour of the model close to the source is further discussed below); and each exhibits a tendency to overprediction for distances larger than $\simeq 100\,\mathrm{m}$. Only figure 9.4 ($a = 0.1$) exhibits a systematic trend: overprediction tends to increase with distance, as would be expected for such a small value of a.

Each of figures 9.4 to 9.9 exhibit large scatter. This could be due to several factors, discussed on page 107. If residual analyses are presented for all meaningful variables and no trends found, then the remaining 'unexplained' mispredictions may be interpreted as manifestations of the random nature of the turbulent dispersion occurring at Thorney Island, together with random noise imposed on the sensor records.

The uniformity of scatter between figures 9.4 to 9.9 shows that the model is not very sensitive to the value of a. This is encouraging from a pragmatic viewpoint because the model does not appear to depend on the exact value used for a, and indeed these figures appear to suggest that the model performance is not significantly affected by changing a within the range 0.2-0.7.

Because the vertical height of the cloud is affected by the choice of a (large values of a give higher predicted cloud heights), it is worth investigating the residual analysis for C_o/C_p as a function of sensor altitude. These residual plots will be presented for the extreme values of a used (figures 9.10 and 9.11 for $a = 0.1$ and 0.7 respectively). It is seen that both figures exhibit a slight trend for high sensors to be underpredicted relative to lower sensors. These figures show that any differences in predicted cloud height exert little effect on C_o/C_p vs altitude residual analysis.

9.6.4 Variation of b

Here, b will be varied from its default value of 0.125. Figure 9.12 shows the residual analysis for C_o/C_p with b set to 0.0625, half the default value; figure 9.13 shows the case with $b = 0.25$, double the default.

When $b = 0.0625$, results are broadly similar to the default (the GFMs are marginally worse); when $b = 0.25$, the scatter is definitely increased.

9.6.5 Results of varying a and b

The values for a and b suggested by Britter [25] and others [161] will be used for simulating the remaining Trials, because other values did not perform better against experiment. However, this work is not conclusive: if any significant trend is found, one of the investigative tools available is to change these entrainment parameters and analyse the results.

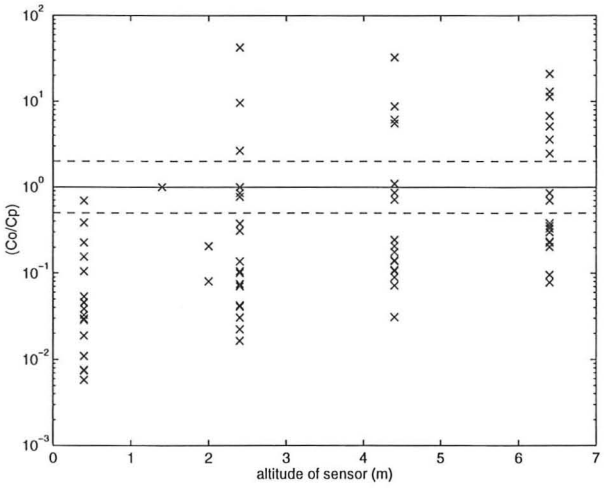

Figure 9.10: Thorney Island Trial 08: C_o/C_p as a function of the altitude of the sensor. Model using $a = 0.1$

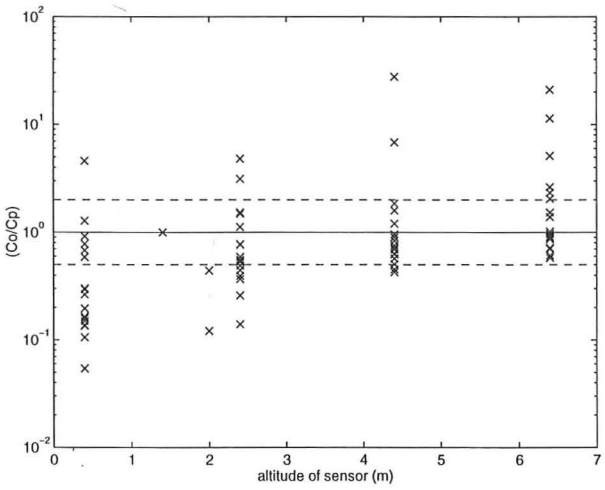

Figure 9.11: Thorney Island Trial 08: C_o/C_p as a function of the altitude of the sensor. Model using $a = 0.7$

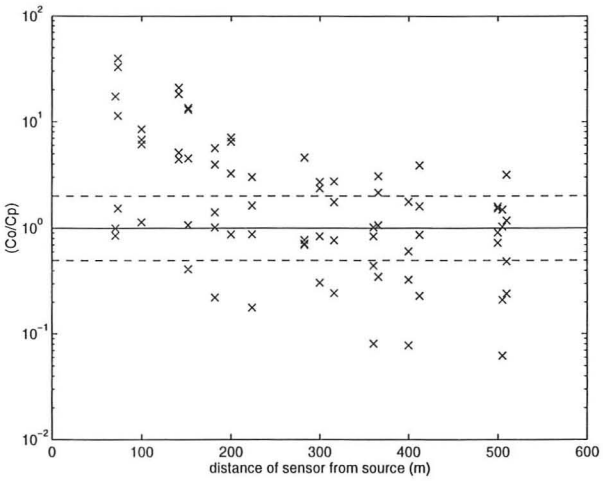

Figure 9.12: Thorney Island Trial 08: C_o/C_p as a function of the distance of the sensor from the source. Model using $b = 0.0625$

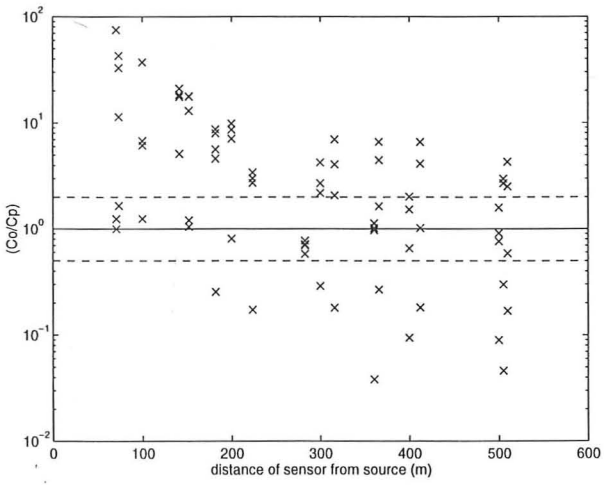

Figure 9.13: Thorney Island Trial 08: C_o/C_p as a function of the distance of the sensor from the source. Model using $b = 0.25$

9.6.6 The model using the default values for a and b

The possibility that the mispredictions above are systematically linked to cross wind distance or sensor altitude is now investigated using the default values of a and b. Residual analyses for C_o/C_p as functions of distance from source, crosswind distance and sensor altitude are presented. However, a discussion of the predicted cloud footprint is presented first to place the more formal analysis in context.

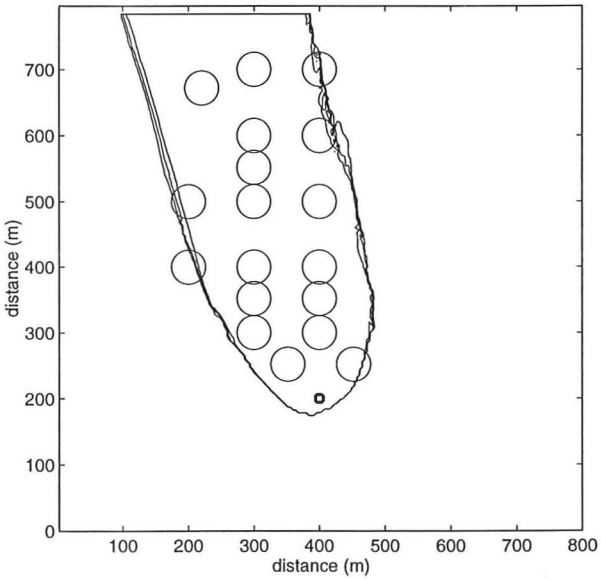

Figure 9.14: Thorney Island Trial 08: contours of predicted dose (irregular lines; values 10^4, 10^5, and 10^6 ppm^{2}min) and sensors detecting gas (circles). Small square at (400, 200) is the source.

Figure 9.14 shows a plan view of the site. Each sensor detecting gas is seen as a circle, the source is the small square at (400, 200), and the irregular lines are the contours of predicted dose.

With the exception of the sensor mast at (200, 400), only sensors detecting gas were predicted to do so. This is evidence that the cloud width is correctly modelled, although this should be interpreted with the residual analysis.

Residual cross wind analysis for the default case

Figure 9.15 shows the crosswind residual analysis for Thorney Trial 08. No trend is visible, although three extreme underpredictions may be seen at a crosswind distance of about +75 m (they are the sensors at (450, 250) and are discussed below).

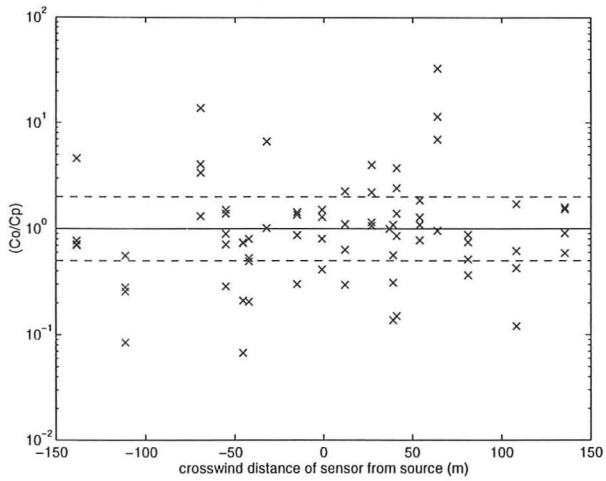

Figure 9.15: Thorney Island Trial 08: C_o/C_p as a function of crosswind distance

The lack of systematic crosswind dependence of C_o/C_p is further evidence that the plume width is correctly modelled: if (for example) the predicted plume were too narrow, points at high absolute crosswind distance would be underpredicted and the residual analysis graph would be a U shape.

9.6.7 Individual sensor records

The residual plots presented include some severe over- and under- predictions. These outliers (only two sensors positions were overpredicted by more than a factor of ten) are now analysed in terms of their Eulerian concentration traces. Many of the underpredictions are caused by the predicted plume lying outside the sensor mast in question and are thus largely independent of the entrainment parameters used; but the overpredictions require a different analysis. It is found that many of the overpredictions discussed here are intimately connected with the vertical concentration profile that is fitted to the model at the post-processing stage; thus any sensor record should be viewed in the context of the other sensors on the same mast.

The four most severe overpredictions are discussed below.

Sensor position (450, 250)

The mast at (450, 250) was one of the closest to the source; underpredictions of up to a factor of about 30 are recorded there. Four sensors were on this mast; only the uppermost two were underpredicted by more than a factor of ten. Table 9.2

height (m)	C_{peak} (obs, %)	C_{peak} (pred %)
0.4	8.97	9.35
2.4	4.27	0.61
4.4	3.28	0.10
6.4	1.14	0.10

Table 9.2: Observed and predicted peak concentrations at (450, 250, 0.4) for Thorney Island Trial 08

shows the observed and predicted peak concentrations. It may be seen that the concentration at 0.4 m is almost correct, but the predicted height is too small.[2]

Figure 9.16 shows the predicted and experimental concentration history at (450, 250, 0.4). It is seen that although the peak concentration is accurately predicted, the cloud arrival time is later in the simulation than measured. This is consistent with the reported toroidal vortex that occurred in the early stages of the release (which is not part of the present simulation) that is able to transport contaminant gas quickly outwards.

The simulation is clearly limited by the fact that it uses depth averaged values for velocity. Thus, a gravity current at rest in the laboratory frame cannot be simulated: such a flow is essentially two layered (the lower layer transports buoyancy upstream to the leading edge; the upper, more dilute, layer flows downstream maintaining the steady state). This is discussed in chapter 4, page 52.

The maximum upwind spread for the dense cloud as determined from aerial video recordings made at Thorney Island is about 1.5 source diameters. The present model predicts a maximum upwind spread of about one source diameter.

The plan view shown in figure 9.14 shows that the sensor at (450, 250) was close to the edge of the predicted plume. The height of the cloud ($\sim$ 10 m) was comparable to the distance from the plume edge to the sensor; and shallow layer modelling explicitly ignores phenomena occurring on these or smaller horizontal length scales. A simulation with a smaller grid size is thus indicated and results are presented below on page 127.

Sensor position (200, 400)

Figure 9.14 shows that this sensor mast, although detecting gas, was not within the predicted plume. Peak concentrations on this mast were therefore set to the sensor noise level of 0.1%. Peak concentrations for this mast were generally below

[2]If the height of the cloud is h and the depth averaged density $\overline{\rho}$, then the concentration at height z is $\frac{2}{S_1}(\overline{\rho}/\rho - 1)\exp[\frac{-2z}{S_1 h}]/\,(M/M_a - 1)$, where $S_1 \simeq 0.5$ is the shape parameter and M and M_a are the molecular masses of contaminant gas and air respectively. The argument of the exponential term is thus $\frac{z}{h}(-2/S_1)$, so small h implies that concentration decays rapidly with altitude z.

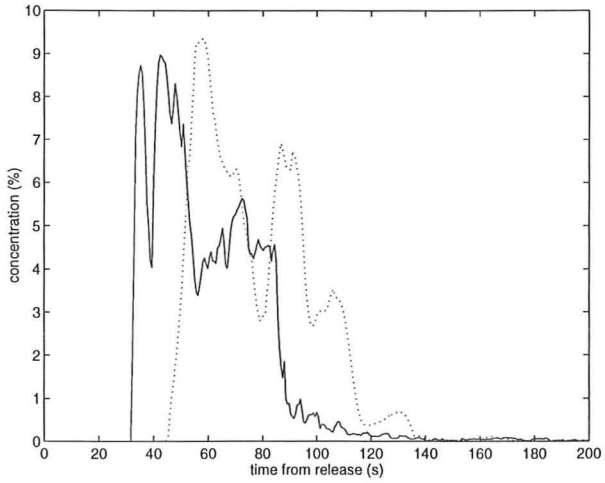

Figure 9.16: Thorney Island Trial 08: observed (—) and predicted (...) concentrations at (450, 250, 0.4) as a function of time

height (m)	C_{peak} (obs, %)	C_{peak} (pred %)
0.4	0.11	1.24
2.4	0.17	0.65
4.4	0.10	0.35
6.4	0.10	0.18

Table 9.3: Observed and predicted peak concentrations at (200, 500) for Thorney Island Trial 08

the nominal threshold although it is possible to discern the presence of gas at this position.

Sensor position (200, 500)

There were four sensors on the sensor mast at (200, 500), at the standard altitudes of 0.4 m, 2,4 m, 4 m, and 6.4 m. The predicted and observed peak concentrations are given in table 9.3.

The observed peak concentrations all occur almost simultaneously; so do the predicted peak concentrations. As the observed peaks are independent of height, a comparison of depth averaged concentrations is indicated. The inference is that this mast detected a vertically homogeneous and almost passive puff.[3]

[3]Cloud residence times appear to be of order 20 s; compare times of 200 s for the mast at (300, 500). The present model could not be expected to simulate this type of flow well, as the shallow water timescales ($\sim$ 100 s) are much larger than the cloud residence time.

height (m)	C_{peak} (obs, %)	C_{peak} (pred %)
0.4	0.15	2.26
2.4	0.17	0.83
4.4	0.24	0.53
6.4	0.21	0.36

Table 9.4: Observed and predicted peak concentrations at (220, 670) for Thorney Island Trial 08

The depth averaged peak concentration at this sensor is about 0.31%; so in terms of depth averaged values, the model is correct to within a factor of three.

Sensor position (220, 670, 0.4)

This sensor was overpredicted by a factor of about 15. Table 9.4 shows the other sensors on the same mast. The cloud height appears to be underpredicted, but as the observed peak concentrations do not decrease with altitude this mast clearly experienced an atypical vertical profile.

9.6.8 Individual sensor records: discussion

In summary, the closest sensors to the source in Trial 08 were underpredicted as a result of cloud upwind travel being poorly modelled, and the vertical profile being incorrect. For the simulation discussed above, three main reasons are evident:

1. Poor modelling of the earliest stages of the release. That these initial process are poorly modelled was anticipated in chapters 3 and 4. Fundamentally, the first few seconds of the release violate the modelling assumptions used in the present model: vertical accelerations are not negligible; the aspect ratio of the system is not small; and the vertical concentration profile of the gas at this point is atypical of that further away from the source.

2. Poor modelling of the upwind spread of the dense fluid. This is discussed in chapter 4 on page 52.

3. The shape of the source is poorly modelled. In order to simulate the cloud at the distance of the furthest sensors, a grid size of 4 m was indicated. At this scale, the Thorney Island source was nine computational elements in area, and these were arranged in a 3×3 square. Work by Hall [76] shows that an initially square dense gas cloud released in calm conditions does not approach circular symmetry for some considerable time. The model was run with a smaller gridsize (1 m) to allow a 'more circular' initial configuration, and these results are discussed in section 9.6.9 below.

4. The windfield around the source is assumed to be unperturbed by the presence of the gas bag before release. This is not the case, as argued by Rottman *et al.* [163], who consider the motion of a cylinder of dense fluid released over a horizontal surface in a cross flow. These workers were interested in the effect of the containment structure on the ambient flow and stated that "... the vorticity shed from the structure and the ground before the collapse [of the source container] generates a flow that continues after the collapse", although they pointed out that this effect was most important for low initial Richardson numbers.

   The inclusion of such effects is not part of the present model, which assumes that the ambient flow is unperturbed by the cloud. In any case, this effect varies on timescales shorter than $\sqrt{l/g'}$ and is therefore beyond the modelling abilities of the present approach.

The items above have shown that a number of assumptions that have to be made for a shallow layer model are incompatible with the earliest stages of the Thorney releases.

9.6.9 Thorney Island Trial 08 using a smaller gridsize

As discussed above, certain results from the 'standard' simulation above are not reliable because they vary on length scales comparable to the computational grid size used. In the case discussed, this spatial variation was due to the sensor being close to the edge of the plume.

A simulation using the same source terms but with a smaller grid size is therefore indicated. A grid size of 1 m was chosen for this exercise as the computational domain so specified included four sensor mast positions. Such a grid size allowed a reasonably accurate source term to be constructed, shown in figure 9.17. This source term was closer in both geometry and area to experiment than was possible with the larger grid size used for the main study. A 1 m grid size was not used for the main study as such a simulation cannot track the cloud to the further sensors (a 200×200 grid was considered to be as large as consistent with reasonable run times; a 1 m grid would reduce the size of the computational domain to 200 m).

Figure 9.18 shows the predicted and observed concentration traces at (450, 250, 0.4). This figure is very similar to figure 9.2, except for some short time scale features. This would be expected because the Courant number was fixed.

It is clear that contaminant gas reaches this point, and the predicted peak concentration is close to the experimental (the model is correct to within 10%).

The main discrepancy is that the predicted cloud arrival time is in each case later than the experimental. This misprediction is not a function of the higher resolution of the system (both grid sizes have approximately the same predicted cloud arrival time) but is due to a limitation of the shallow water methodology adopted in the current model. The definitions of cloud depth, velocity and density

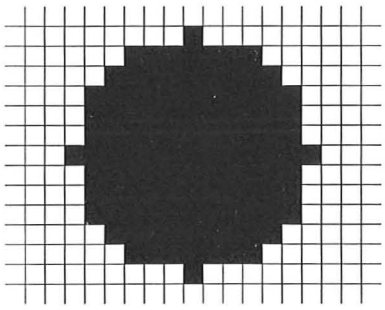

Figure 9.17: Thorney Island Trial 08: source term used with 1 m grid size

are such that buoyancy transport is modelled[4] at the expense of fluxes such as volume flux and momentum flux. It is clear that in the case of the initial motion of the Thorney Island Trial 08 dense cloud, that strong vertical velocity gradients exist [78, 31] which prevent correct simultaneous simulation of volume flux and buoyancy flux.

9.6.10 Conclusions from Trial 08

In this section, Thorney Island Trial 08 has been simulated with the present model. This Trial, being particularly successful, contains more analysis than the other Trial comparisons.

There was no evidence to suggest that changing the default entrainment parameters used in the model would give better agreement with experimentally determined peak concentrations. Since there is a body of theoretical and other evidence supporting the use of this choice of entrainment parameters, these will be used. However, if any other Trials display any systematic trend, then one analytical tool available would be to vary the default parameters.

One of the outcomes of varying a and b was to show that the model is relatively insensitive to the exact values used. This is encouraging as it suggests that precise determination of a and b is unnecessary for risk assessment purposes.

Using the default values of a and b, three vertical concentration profiles were examined. The model predictions remained largely insensitive to changing the assumed profile, but an exponential profile gave the best agreement with experiment.

Several experimental traces were selected for more detailed study. These

[4]The relationships between the depth-averaged quantities used in the present model and the real cloud are such that the actual buoyancy flux equals the modelled buoyancy flux. Quantities such as volume flux require multiplication by an indeterminate dimensionless shape parameter (S_v for volume, for example) for correct modelling.

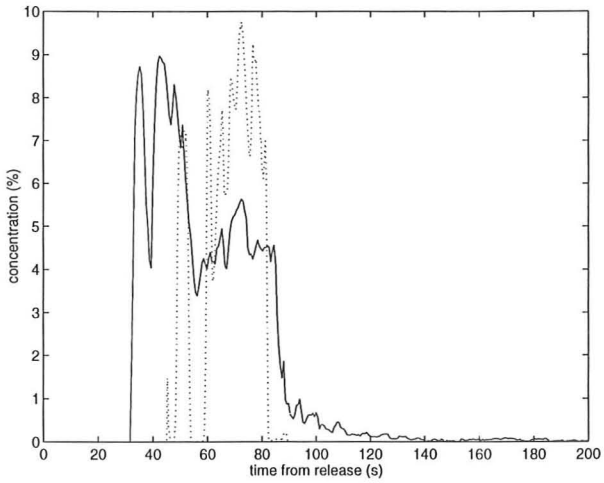

Figure 9.18: Thorney Island Trial 08: predicted (...) and experimental (—) Eulerian concentration traces at (450, 250, 0.4). Model using a 1 m gridsize.

points were either severely over- or under- predicted and physical explanations sought or discussed. Much of the apparent under prediction is due to the predicted plume lying outside the sensor location in question; and much of the over prediction is due to the assumed vertical profiles.

The work in this section suggests that, for the remaining Trials considered, the following protocol is appropriate:

- The three residual plots (C_o/C_p as a function of distance from source, altitude, and cross wind distance) are produced
- Any trends found investigated from a physical viewpoint including change of the entrainment parameters a and b
- Any outlying points further investigated and any physical explanation for the misprediction given.

9.7 Thorney Trial 09

Thorney Trial number 09 was conducted at the lowest windspeed of all the Phase 1 Trials (1.7 m/s). A total of 56 sensors detected gas; the mean wind direction was 26.9° to the right of the sensor array centreline.

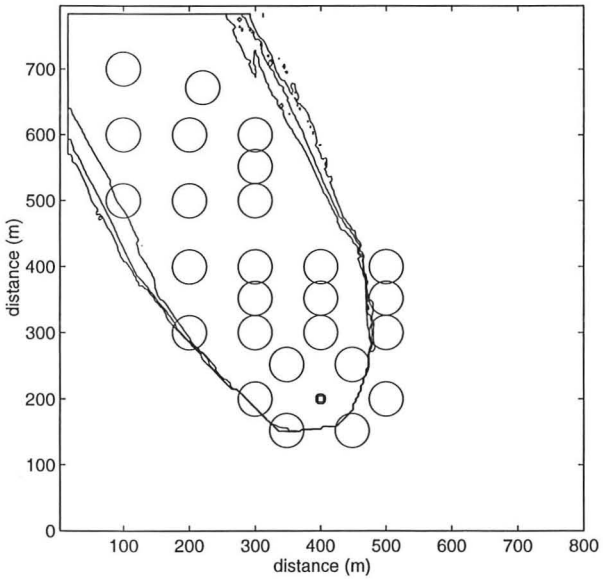

Figure 9.19: Thorney Island Trial 09: contours of predicted dose (irregular lines; values 10^4, 10^5, and 10^6 ppm^{2}min) and sensors detecting gas (circles). Small square at (400,200) is the source.

Figure 9.19 shows the positions of the sensors detecting gas and the outline of the predicted plume as determined by the dose experienced at ground level. It is clear that a number of sensors that detected gas in the experiment are outside the plume as predicted by the present model.[5] That the predicted plume does not include these sensors is clearly due to the modelling of the earliest phases of the release, during which the upwind spread of the cloud is determined (at no other time does the cloud have enough potential energy to travel against the wind).

Nine sensors that were deemed to have detected gas had predicted peak concentrations of zero—or sensor noise level. However, peak concentration data should be interpreted in context. The five ground positions of these sensors are visible as the rightmost four sensors in figure 9.19 with an extra location at

[5]The predicted gas concentration is defined in these circumstances to be the noise level of the sensors. That the model correctly predicted *absence* of gas for the remaining sensors with the exception of the sensor at (400, 500) is encouraging.

(450, 150). Table 9.5 shows the peak concentration measured at these locations. Although in each case, the peak concentration is well above the nominal sensitivity, each trace (figure 9.20, showing two traces at (500, 300), is a typical example) reveals that the upper sensor, at an altitude of either 2.4 m or 1.4 m, detected gas but only transiently (the timescale for judging transience is $\sqrt{h/g'} \sim 1\,\mathrm{s}$). It is reasonable to say that the cloud is $\lesssim 1.4\,\mathrm{m}$ high in this region; such formations are poorly handled by the present model, as discussed on page 52.

position	peak conc (expt)
(500, 400, 0.4)	0.22%
(500, 400, 2.4)	0.22%
(500, 350, 0.4)	0.76%
(500, 350, 2.4)	0.20%
(500, 300, 0.4)	1.02%
(500, 300, 2.4)	0.14%
(500, 200, 0.4)	1.82%
(450, 150, 0.4)	6.62%
(450, 150, 1.4)	0.71%

Table 9.5: Locations of sensors detecting gas but predicted to be outside the plume

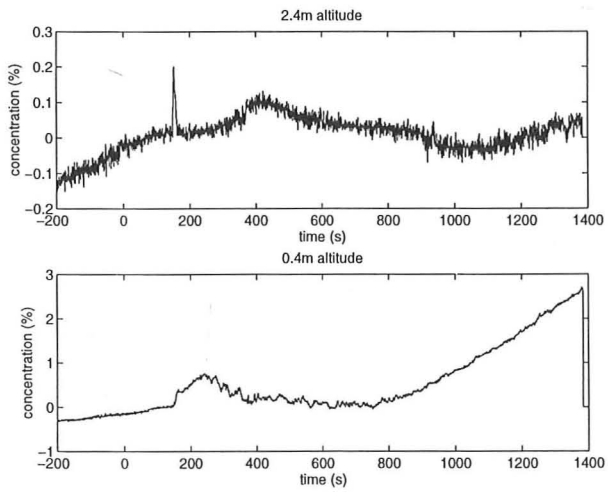

Figure 9.20: Thorney Island Trial 09: concentration at (500, 350) as a function of time from release. Altitudes: 2.4 m (top graph), 0.4 m (lower graph)

Figures 9.21 and 9.22 show C_o/C_p versus altitude and cross wind distance respectively. No systematic trends are seen, except for a cluster of underpredictions

at small altitudes in figure 9.21. This is discussed with reference to distance from source below.

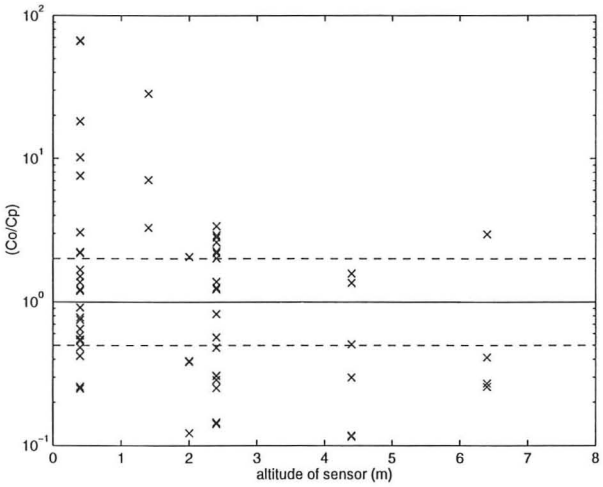

Figure 9.21: Thorney Island Trial 09: C_o/C_p as a function of the altitude of the sensor

Figure 9.23 shows the residuals plotted against distance from source. This graph shows no distinct trends (apart from the near sensors to be underpredicted because they are outside the predicted plume), again indicating that the model with default parameters entrainment parameters gives no systematic trends. The general underprediction at small distances seen in figure 9.23 is due to the five sensor positions which experienced gas but were not inside the predicted plume. Given that only transient exposure to gas was experienced at these masts at altitudes $\geq 1.4\,\mathrm{m}$ at these points, it is clear that closer inspection of the cloud's behaviour at these points is required. This is most easily achieved by using a smaller grid size in order to represent the source term better than is possible with a 4 m grid. However, changing the gridsize does not allow the simulation to discern phenomena happening on timescales less than $(h/g')^{1/2}$, even though the numerical timestep is smaller (the Courant number is fixed); the purpose of this simulation is to use a better representation of the source.

A 1 m grid will be used. This finer simulation will differ from the main, long-range simulation on length scales close to the grid size; but in this case, such differences are likely to be important as the sensors of interest were $\sim 4\,\mathrm{m}$ from the plume edge.

Figure 9.24 shows a plan of the region close to the source and confirms that the code is independent of grid size.[6] However, this figure shows that three of the

[6]The upwind spread in each case is about 30 m; and the sensor at (350, 150) is close to the plume edge.

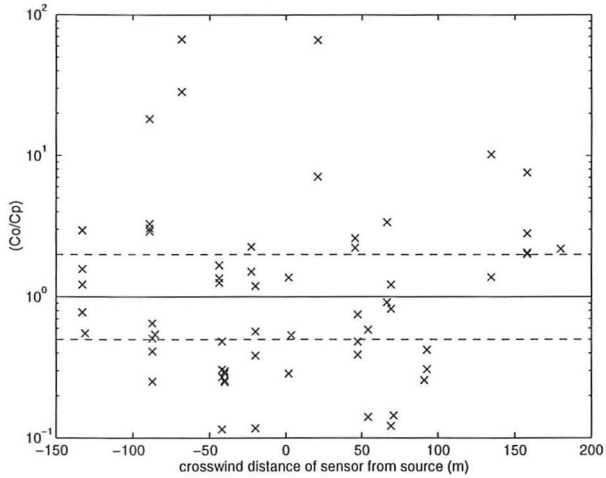

Figure 9.22: Thorney Island Trial 09: C_o/C_p as a function of crosswind distance

sensors detecting gas are not within the predicted cloud path (compare Thorney 08: there these sensors were at a considerable distance from the predicted cloud edge). This figure shows that the present model is poor at modelling upwind spread close to the source. The reason for the poor modelling is that the shallow water assumptions made in the mathematical model are not correct for near-source behaviour; and in particular do not allow for the recirculation experienced close to a gravity current head, whereby the current front is supplied with dense gas by a low-lying current which reverses (at the head) and is blown downwind, diluted, by the ambient flow. The model cannot handle this type of behaviour because it assumes that a single depth averaged velocity is appropriate for the flow at any point; clearly incorrect here.

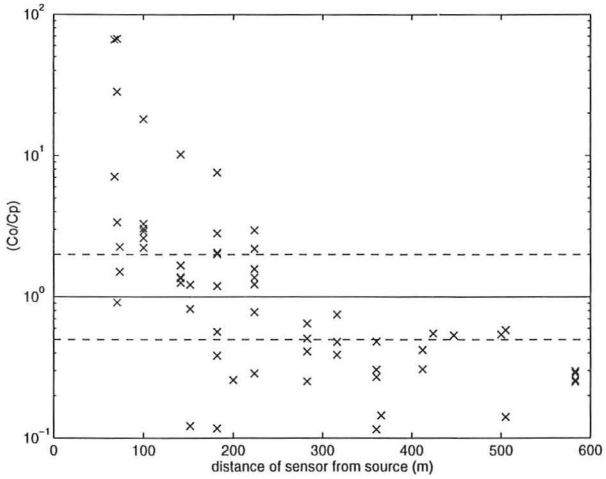

Figure 9.23: Thorney Island Trial 09: C_o/C_p as a function of distance from source

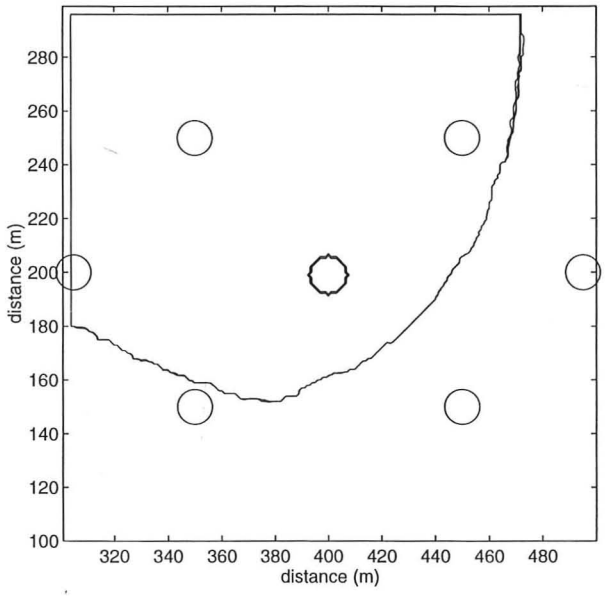

Figure 9.24: Thorney Island Trial 09: contours of predicted dose (irregular lines) and sensors detecting gas (circles). Simulation using a 1 m grid size. Circle at (400, 200) is the source

9.8 Thorney Trial 13

Thorney Trial number 13 was conducted at the highest windspeed of the programme, 7.1 m/s at the reference height of 10 m. Although some buffeting of the gas bag was observed at this high windspeed, the release was judged to be successful.

Figure 9.25 shows the path of the predicted plume, together with the locations of the sensors that detected gas. It is evident that the sensor at (500, 600), while detecting gas, is outside the predicted plume, leading to an overprediction factor of ~ 7. As no sensors to the right of those shown were deployed at the site, it is reasonable to conclude that the plume width is being simulated approximately correctly, but at an incorrect bearing. The wind direction used in the present simulation was taken directly from databook 19 [92].

Evidence for the hypothesis that an inappropriate wind direction was used is provided by figure 9.26, in which the C_o/C_p values alternate between over- and under- prediction from about 300 m from the source. This is due to the coincidence that the sensors at successively larger distances from the source alternate between underprediction (lying outside the predicted plume but inside the experimental plume) and overprediction (lying close to the centre of the predicted plume but at the edge of the experimental plume). Successive points alternate between being closer to the predicted plume centreline than the real plume centreline, and being further away.

Figures 9.26 to 9.28 show the standard residual analyses of C_o/C_p against distance, altitude, and crosswind distance respectively. Only figure 9.28 shows a trend; the sensors at the most negative crosswind distances were underpredicted as the simulated plume did not pass over them.

It is logical to investigate the nature of the experimental concentration trace at the leftmost gas detector seeing gas (the gas signal could have been transient or registered only at one height). Figure 9.29 shows that there was gas at (500, 600) and that the signal was not limited to the lowest sensor. Each trace shows that gas was present for some time and not just a single datum. It is interesting to observe that gas was present at 0.4 m both before and after the presence of gas at 6.4 m. It is also the case that the peak concentration at this level was almost independent of height for the sensors at this mast.

In the light of these observations it is reasonable to conclude that the wind bearing of 30.8° given in the databook is not an absolute figure and should be viewed in the context of both the experimental concentration traces and the environmental history at the site. This may be tested by running the present model with a different wind direction, and results are presented below.

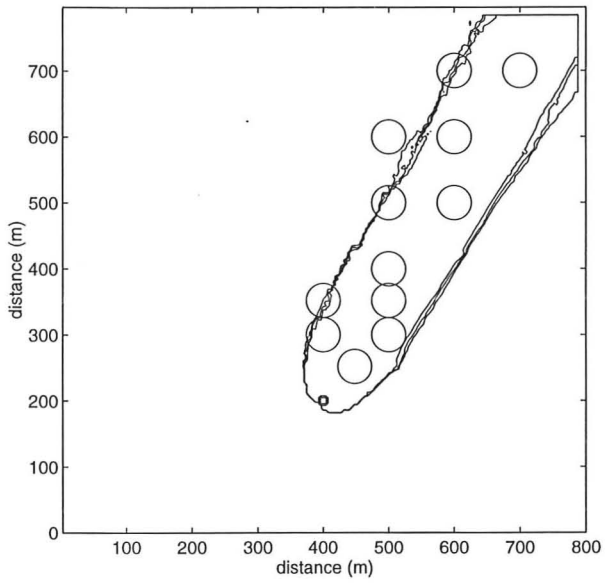

Figure 9.25: Thorney Island Trial 13: contours of predicted dose (irregular lines; values 10^4, 10^5, and 10^6 ppm^{2}min) and sensors detecting gas (circles). Small square at (400,200) is the source.

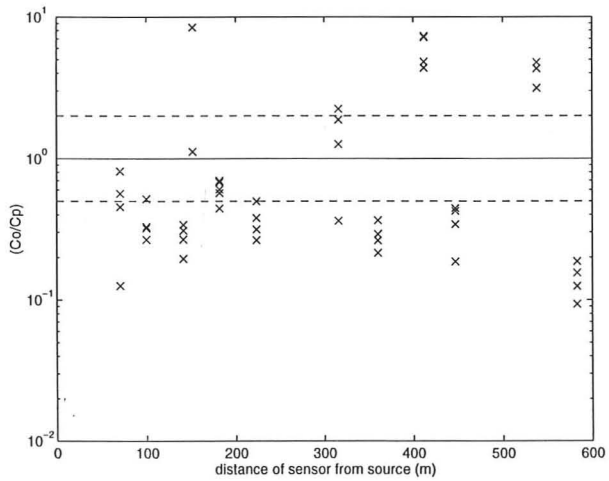

Figure 9.26: Thorney Island Trial 13: C_o/C_p as a function of distance from source

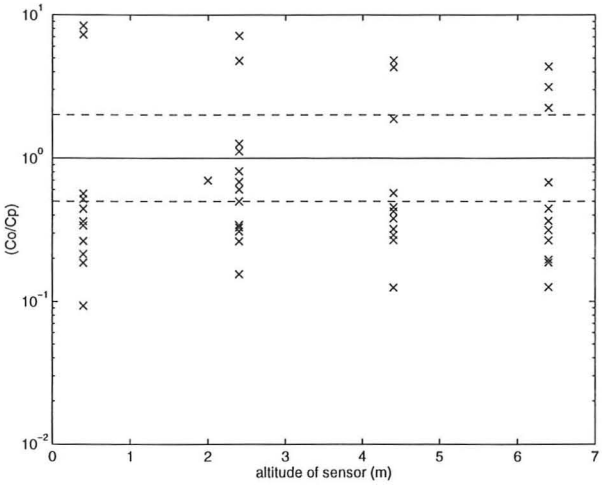

Figure 9.27: Thorney Island Trial 13: C_o/C_p as a function of the altitude of the sensor

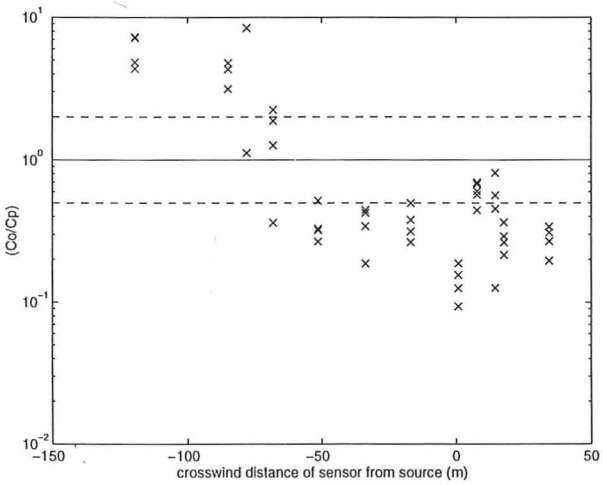

Figure 9.28: Thorney Island Trial 13: C_o/C_p as a function of crosswind distance

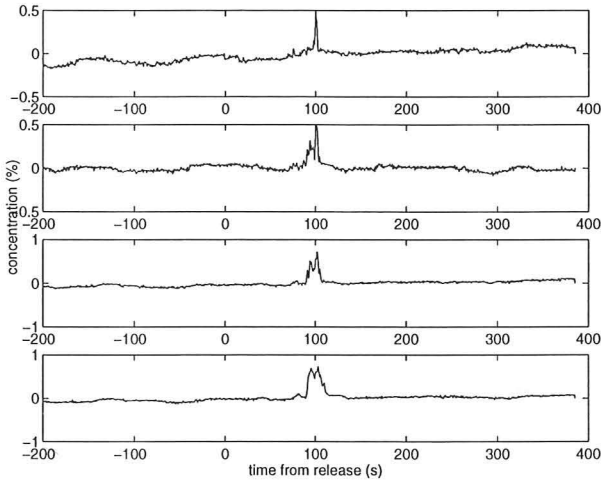

Figure 9.29: Thorney Island Trial 13: concentration (%) as a function of time at (500, 600). Altitudes (from bottom up): 0.4 m, 2.4 m, 4.4 m, 6.4 m

9.9 Thorney Trial 13: wind direction change

As discussed above, the sensor records at Trial 13 are to some extent inconsistent with the reported wind direction. In this section, the present model will be used to simulate Trial 13, but with a different wind direction.

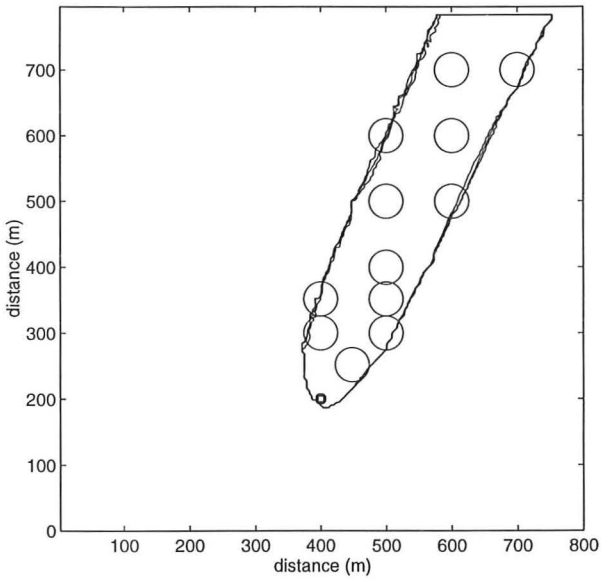

Figure 9.30: Thorney Island Trial 13: contours of predicted dose (irregular lines; values 10^4, 10^5, and 10^6 ppm^{2}min) and sensors detecting gas (circles); simulation using a wind bearing of 25°. Small square at (400,200) is the source.

Figure 9.30 shows a plan view of the site. The cloud path, as illustrated by time-integrated dose contours, may be seen to be at an angle of 25° from the array centreline; this more accurately tracks the positions of the sensors that detected gas. Figure 9.31 shows the crosswind distance residual analysis. No trend is seen; compare figure 9.28 in which negative crosswind distances were overpredicted and vice versa.

9.10 Thorney Trials 45 and 47

The Thorney Island continuous releases 45 and 47 [130] are now considered briefly, using a different analysis method which is more compatible with previous ap-

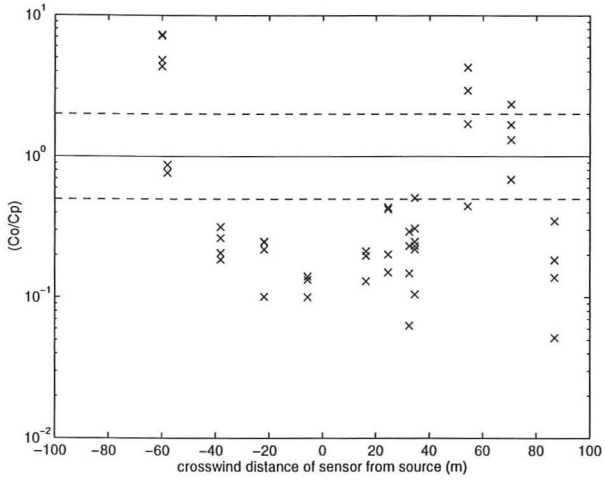

Figure 9.31: Thorney Island Trial 13: C_o/C_p as a function of crosswind distance; simulation using a wind bearing of 25°.

proaches. Figures 9.32 and 9.33 show observed[7] and predicted concentrations against downwind distance for Trials 45 and 47 respectively. The predicted concentrations were obtained from the model by running the simulation and taking an instantaneous recording of concentration as a function of position. The predicted figures are not a single valued function of distance as the present model is two-dimensional.

The agreement between observed and predicted concentrations is seen to be reasonable for the smaller distances. The predicted concentrations for the larger distances exhibits structure on account of waves propagating downwind, causing cross-wind and downwind variations in concentration. The experimental data considered do not indicate whether this phenomenon really occurs in the large scale experiments.

9.11 Summary

This chapter has compared the present model with the experimental results from Thorney Island [130], mainly using peak concentrations for comparison. Scatterplots of C_o/C_p against altitude, cross wind distance, and distance from source were presented; no significant trends were found. Significantly better agreement was not obtained by varying the default parameters in the model.

[7]The observed concentrations are taken from the Modellers' Data Archive [86] and correspond to peak measured concentrations after 0.6 s averaging.

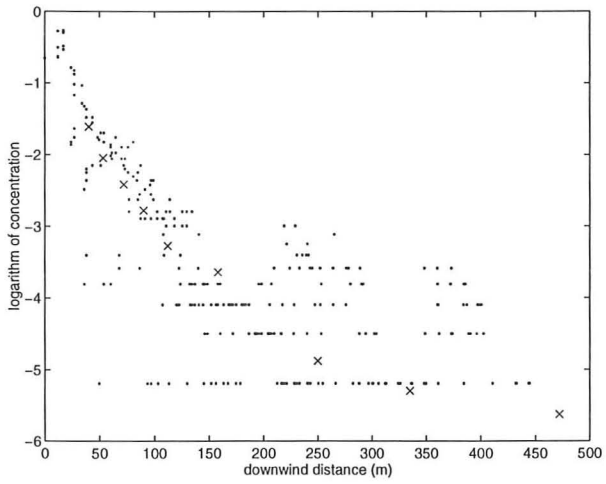

Figure 9.32: Distance against $\log(C/C_0)$ for the Thorney Island continuous release number 45; ×—experiment, ·—predicted

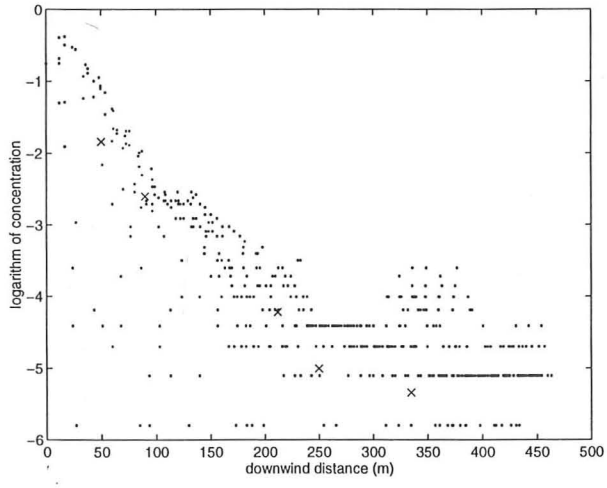

Figure 9.33: Distance against $\log(C/C_0)$ for the Thorney Island continuous release number 47; ×—experiment, ·—predicted

The continuous release Trials 45 and 47 were also simulated, with reasonably accurate results.

In general, about half the predicted peak concentrations were correct to within a factor of two, and almost all correct to within an order of magnitude.

Chapter 10

Model validation: comparison with integral models

10.1 Outline

This chapter will compare the results of the present model with those of existing, commonly used, integral models. This is to investigate if the present model differs from integral models and, if it does, why. The present model's predictions may thus be assessed in a broader context.

It is desirable to choose source terms that have previously been used in a model comparison. The code comparison exercise of Mercer [132], in which standard dispersion models were compared, will be used. Predictions of the present model are placed in this context: because integral models were used by Mercer, cloud averaged concentrations are considered.

The main finding of this chapter is that the present model gives cloud averaged concentrations, for a number of scenarios, that are within the range given by Mercer.

10.2 Cloud averaged concentrations

Chapter 9 compared field data against the present model's predictions. That comparison exercise considered primarily peak concentrations, essentially following Hanna *et al.* [86]. Here, cloud averaging will be used, allowing direct comparison with integral models. The methodology adopted will be to consider cloud averaged concentrations as functions of distance from release point.

10.3 The code comparison exercise of Mercer

Although comparison with a single integral model would yield useful information, this would give no indication of the range of predictions existing in the field of integral modelling; comparison with a number of models is therefore desirable.

In 1991, Mercer compared a number of dense gas dispersion models against one another [132]; this work was carried out as a result of the development of a number of new dispersion codes and an abbreviated account was published in 1994 [137].

The development of these codes followed the Second Symposium on Heavy Gas Dispersion Trials at Thorney Island [89]; it had become clear that significant differences in the results of codes existed, even for simulations within the scope of the trial conditions. Mercer attributed these differences to the different ways of optimizing the parameters in the models and went on to state that "these differences may well be magnified when the models are extrapolated to different conditions."

Twenty five cases were considered: five different releases under five meteorological conditions (table 10.1). The comparison exercise did not involve any direct use of the Thorney Island data. Mercer's results were made publicly available and are used here.

volume (m^3)	radius (m)	z_0 (m)	windspeed (m/s) at 10 m and stability class				
			1; D	1; F	2; D	4; D	8; D
2×10^3	7	0.01	A	B	C	D	E
2×10^3	7	0.3	F	G	H	I	J
2×10^3	24	0.01	K	L	M	N	O
2.5×10^5	120	0.05	P	Q	R	S	T
2.5×10^5	120	1.5	U	V	W	X	Y

Table 10.1: The 25 cases considered by Mercer

The majority of results presented by Mercer were in the form of cloud averaged concentration vs distance (of cloud centroid) from release, although some additional results were given such as cloud width and height.

Each of the cases A to Y have been considered by the present author [80] and four are selected for presentation here: cases A, E, P, and T. These cases span the range of windspeeds considered, involve only neutral stability, and had a value of z_0 compatible with the present approach.

Mercer's methodology was dictated by the nature of the models available; all the models considered were integral. The present model, being a shallow layer simulation, differs considerably from the models considered by Mercer. A review of the methodology used follows.

10.4 Methodology of including the present model in Mercer's code comparison

Mercer's work was driven by the integral model paradigm, in which cloud-wide averaging takes place at the modelling stage. Shallow layer simulations, not being uniform in height or density, render the concepts of 'cloud radius' and 'cloud height' not directly meaningful.

However, a reasonable method by which simulations may yield a 'cloud averaged concentration' as a function of 'downwind distance' follows.

10.4.1 Definitions of cloud centroid and cloud averaged concentration

Shallow layer simulation results are in the form of functions of two spatial dimensions and time; here the outputs of interest are the depth averaged quantities $h = h(\mathbf{x}, t)$ and $\overline{\rho} = \overline{\rho}(\mathbf{x}, t)$. Here, $\mathbf{x}$ is the ground position relative to the release point and t is the time from release. It is not clear that 'cloud averaged concentration as a function of downwind distance' is meaningful in this more general context. However, it is possible to proceed by defining a buoyancy-weighted cloud centroid position vector $\mathbf{P} = \mathbf{P}(t)$ as follows:

$$\mathbf{P} \int_{\mathbf{x}:\,\overline{\rho}(\mathbf{x},t)>\rho_a} h(\overline{\rho} - \rho_a) d^2\mathbf{x} \quad = \quad \int_{\mathbf{x}:\,\overline{\rho}(\mathbf{x},t)>\rho_a} h(\overline{\rho} - \rho_a)\mathbf{x} d^2\mathbf{x}, \tag{10.1}$$

and the cloud averaged density ρ^* satisfies

$$\rho^* \int_{\mathbf{x}:\,\overline{\rho}(\mathbf{x},t)>\rho_a} h\, d^2\mathbf{x} \quad = \quad \int_{\mathbf{x}:\,\overline{\rho}(\mathbf{x},t)>\rho_a} h\overline{\rho}\, d^2\mathbf{x}. \tag{10.2}$$

The definitions of h and $\overline{\rho}$ imply that ρ^* is the average density of the cloud at time t over points where $\overline{\rho} > \rho_a$. From $\overline{\rho}$, the cloud averaged concentration may be obtained using the equation of state: $C = (\rho^* - \rho_a)/(\rho_a\,[M/M_a - 1])$, where M and M_a are the molecular masses of the dense gas and air respectively, and ρ_a the density of air.

Now, $P = |\mathbf{P}|$ is the distance of the centroid from the release point, and $\overline{C} = \overline{C}(t)$ is the cloud averaged concentration, at time t. It is now possible to use a sequence of simulation results to give a series of Ps and $\overline{C}$s, yielding $\overline{C} = \overline{C}(P)$, as required. Quantities such as cloud width or radius are not so easy to define as they are used only in integral models.[1]

[1] One example of a cloud with no clear radius is reproduced in figure F.3 on page 204. This shows the difficulties that may be encountered in transferring apparently clear notions such as cloud width from integral models to the present model.

Summary of methodology

Cloud averaged concentration $\overline{C}$ is calculated as a function of downwind distance P as discussed above. The methodology of integral models uses downwind distance (or time from release) and cloud averaged concentration as starting points for the rest of the model; these quantities are not used in shallow layer modelling. Here $\overline{C}$ and P are *calculated* from simulation outputs and this methodology is used here to include the present model in Mercer's code comparison exercise.

10.5 Results

10.5.1 Overview

The results that follow show predictions from the present model alongside the models considered by Mercer. Concentrations are calculated as a function of distance, and time from release. Eight graphs are shown, two for each of the chosen cases; the present model is shown in bold. A short line indicates that the relevant code did not give a result for all distances for that case.

The lines in each figure were calculated by linear interpolation between the points provided by Mercer (typically results from four distances or times were considered). Results from the present model are calculated in the same way, giving rise to the abrupt changes of slope[2]

10.5.2 Large values of z_0

Mercer's cases U to Y used a roughness length z_0 of 1.5 m; this corresponds to "centres of cities with very tall buildings" on flat ground [151]. For each of these cases, most of the integral models did not give results because the cloud height gets close to the roughness length.[3] The present model did not return useful output for these cases.

As the logarithmic velocity profile from which z_0 is determined is valid only if $z \geq 10z_0$ [62] the use of z_0 for describing atmospheric flow at heights $\sim z_0$ is not appropriate: roughness length is meaningful only to describe flow at heights $\gg z_0$. The reference height used for specification of the windspeed, 10 m, would be below the largest roughness elements of a large city and the logarithmic profile not applicable at these altitudes.

[2]This is unrelated to the sudden change of slope seen in the predictions of integral models caused by the assumption of instantaneous changes between regimes. For example, `crunch` [105] assumes a that the cloud becomes passive instantaneously and this causes the abrupt changes in slope.

[3]The initial cloud height for cases U to Y is about 5 m. One code [34] gave a minimum cloud height of about 2 m for case U.

Roberts *et al.* [159] consider large values of z_0 and state that, for roughness lengths $> 0.6\,\mathrm{m}$, "the size and shape of the roughness elements and the manner in which they are arranged affects dispersion." For cases U to Y this implies that ground roughness cannot be characterized by z_0 alone, even for altitudes $z \gg z_0$.

Because of these restrictions the present model treats any parts of a dense layer with height less than z_0 as being insignificant. Cases U to Y give clouds with substantial parts having heights $h < z_0$ and the model gave no useful output.

10.5.3 Case A

volume (m^3): 2×10^3
radius (m): 7
z_0 (m): 0.01
windspeed (m/s): 1

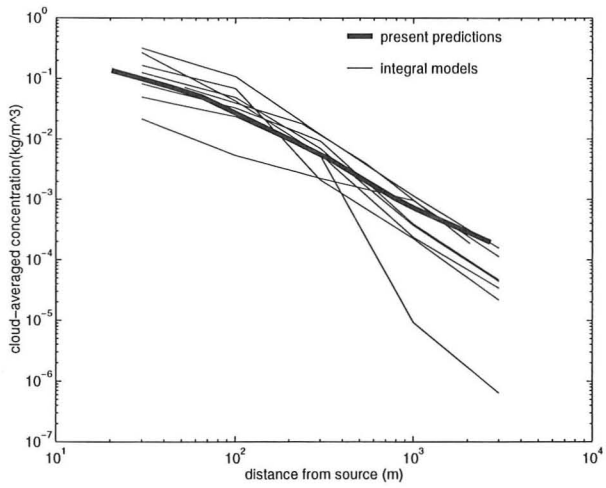

Figure 10.1: Cloud averaged concentration vs downwind distance, case A

Figure 10.1 shows the present model's predictions for case A against downwind distance from release point to cloud centroid. For distances up to $\sim 10^3$ m, the present model gives predictions that lie within the range. At larger distances, the present model's predictions lie at the upper end of the spectrum.

Figure 10.1 includes one model with predictions for 3000 m an order of magnitude lower than any other model. Even without this model, however, there is a spread of a factor of $\simeq 10$ at this distance.

Figure 10.2 shows the equivalent graph using time from release as the independent variable; the present model lies within the range, again at the upper end of the range. This figure illustrates Mercer's finding that differences between models were generally smaller when results were expressed against time; Mercer interpreted this in terms of differing cloud advection speeds used in the models. Such arguments are difficult to apply to the present model, as cloud centroid has only a restricted meaning.

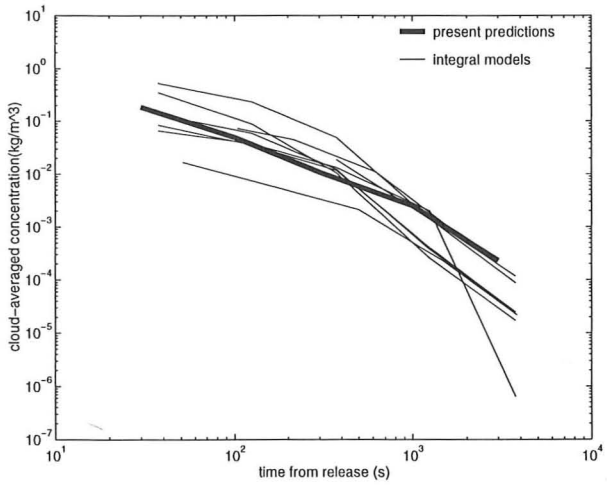

Figure 10.2: Cloud averaged concentration vs time from release, case A

10.5.4 Case E

volume (m^3): 2×10^3
radius (m): 7
z_0 (m): 0.01
windspeed (m/s): 8

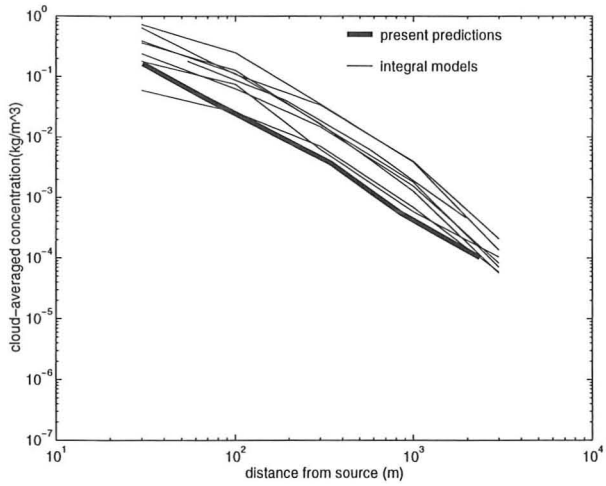

Figure 10.3: Cloud averaged concentration vs downwind distance, case E

Figure 10.3 shows the present model's predictions against downwind distance for case E. Here, the present model's predictions lie at the lower end of the spectrum. Figure 10.4 shows the equivalent graph against time from release.

Integral models for case E agree more closely at a given distance than those for case A; this is also true for predictions at a given time. Case E, however, contradicts Mercer's general rule that the differences between models were more pronounced when the independent variable was distance from release.

Figure 10.3 and 10.4 exhibit a range of about an order of magnitude.

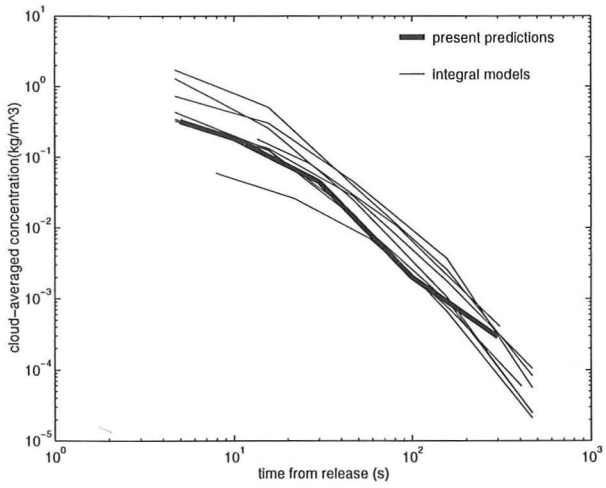

Figure 10.4: Cloud averaged concentration vs time from release, case E

10.5.5 Case P

volume (m^3): 2.5×10^5
radius (m): 24
z_0 (m): 0.05
windspeed (m/s): 1

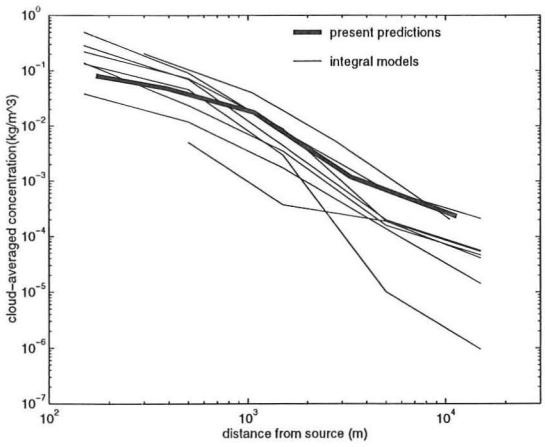

Figure 10.5: Cloud averaged concentration vs downwind distance, case P

Figure 10.5 shows the present model's predictions against downwind distance for case P; figure 10.6 shows predictions against time. Here, the present model's predictions lie at the upper end of the spectrum, but again within the range.

As for case A, a large spread of concentrations is evident, especially for larger distances, in line with Mercer's observation that low wind speeds gave rise to a greater range of predictions than high wind speeds.

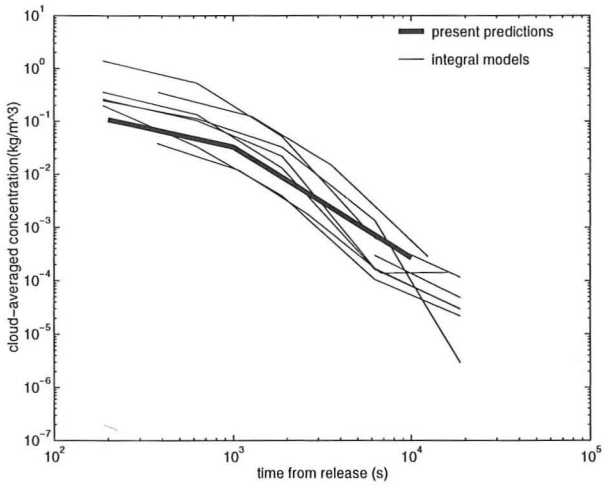

Figure 10.6: Cloud averaged concentration vs time from release, case P

10.5.6 Case T

volume (m^3): 2.5×10^5
radius (m): 24
z_0 (m): 0.05
windspeed (m/s): 8

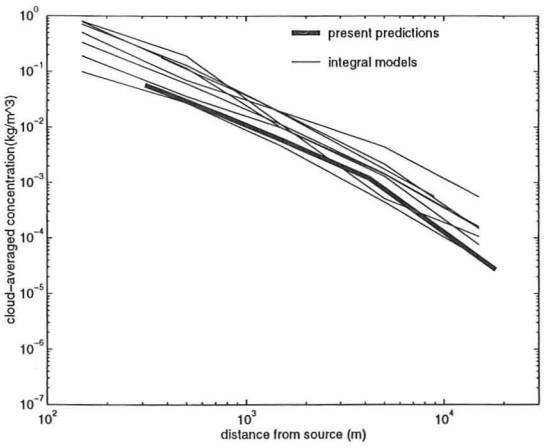

Figure 10.7: Cloud averaged concentration vs downwind distance, case T

Figure 10.7 and 10.8 shows the present model's predictions against downwind distance and time for case T. Here, the present model lies at the lower end of the spectrum but it is consistent with those of the integral models.

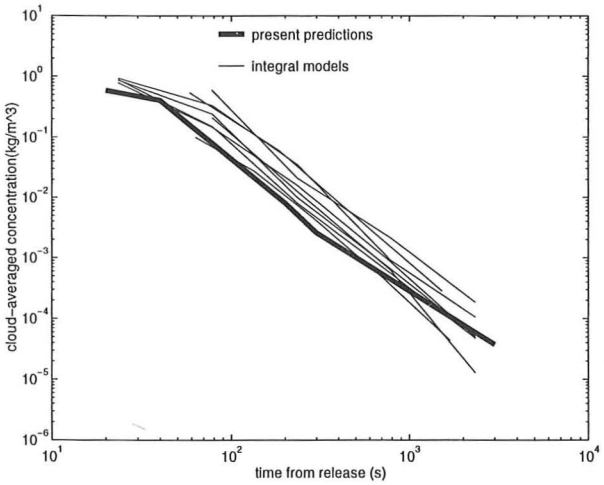

Figure 10.8: Cloud averaged concentration vs time from release, case T

10.6 Discussion

The primary conclusion of the code comparison presented above is that the present model gives predictions that are consistent with the integral models considered by Mercer. Predicted cloud averaged concentrations agree broadly with the consensus.

Overprediction at large distances was anticipated in chapter 5 on page 63, where passive cloud behaviour was discussed. However, this is not observed.

Although the present model accounts for vertical diffusion (the entrainment rate being von Karman's constant times the friction velocity u_*), the model does not incorporate horizontal diffusion. The model nevertheless agrees with the consensus given by Mercer.

Further interpretation of these findings is difficult in the absence of a detailed analysis of the integral models considered by Mercer.

Integral models usually account for horizontal diffusion; a profile is superimposed on the cloud's nominally uniform lateral form. The effects of turbulent diffusion are usually represented in terms of Gaussian half-widths as in equation 5.8 on page 63.

The ability to account for phenomena such as lateral diffusion is one reason for the almost exclusive use of integral models in risk assessment today. The present model gives predictions that fall within the range presented by Mercer.

10.7 Summary

The present model has been used to simulate four representative cases considered by Mercer [132]. In terms of cloud averaged concentration vs centroid position and time, the present model gave predictions that were consistent with the integral models used by Mercer.

As the model neglects horizontal diffusion for passive clouds, overprediction at large downwind distances was expected, but not generally observed.

In common with most of the models considered by Mercer, the present model did not return useful output for the five cases with a surface roughness of 1.5 m.

Chapter 11

Dense gas dispersion on a slope

11.1 Outline

The model developed in chapters 3 to 7 will now be used with a sloping lower surface. Model predictions will be compared with the experimental results of Schatzmann [167], in which dense gas was released over three different slopes in a calm ambient. Continuous and instantaneous releases will be considered in turn; the same model is used for both.

Physical reasoning will be used to discuss the model's performance.

11.2 Introduction

The model developed in chapters 2 to 7 of this thesis will now be used to simulate the experiments of Schatzmann. The computational grid will be 200×200. This size of grid was used to give reasonable spatial (and temporal) resolution without excessive run times. The gridsize used was 2 cm square. One iteration took about 1 s on a 200 MHz P6; 80 s of simulation time typically required ~ 1500 iterations.

The experiments of Schatzmann were discussed in chapter 8, on page 106. Briefly, dense gas was released both instantaneously and continuously over three different slopes in calm surroundings; the instantaneous releases were repeated five times. Each experiment deployed eight sensors, mounted flush with the smooth lower surface. The positions of the sensors varied from release to release but were typically 1 or 2 m from the source. Quantities released were $\mathcal{O}(1\ell)$.

11.3 Continuous releases

The three continuous release experiments conducted by Schatzmann were simulated using the present model. As for the Thorney Island comparison exercise, formal statistical methods are supplemented by analysis of individual traces.

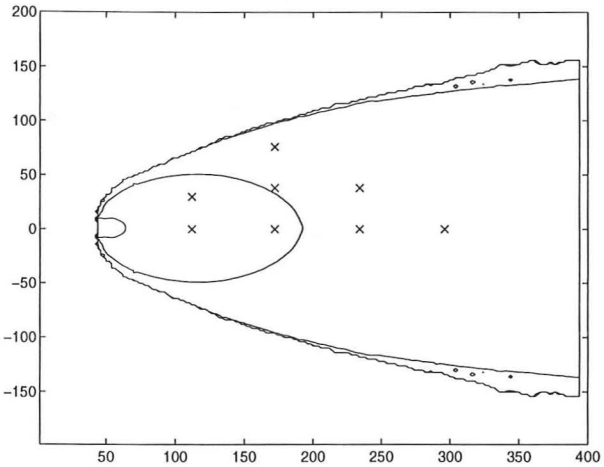

Figure 11.1: Contour plot of predicted concentration (values 1%, 0.5% and 0.1%) for a continuous release on an 8.6% slope, source at (50, 0). Crosses mark sensor positions; current flows down from left to right

Figure 11.1 shows a plan view of the predicted flow over the 8.6% slope. The positions of the sensors are shown as crosses. It may be seen that the flow widens as it descends the slope.

Tables of results are now given that indicate the model's performance against the continuous experimental dataset in terms of mean concentration (after the transient concentration increase given in the simulation) and cloud arrival time.

Table 11.1 shows predicted and observed concentrations, at each sensor position. A tendency to underprediction is seen, in general, by a factor of about 3. This is in contrast to the overprediction seen in chapter 9, where the Thorney Island releases, both instantaneous and continuous, were considered. This discrepancy is possibly a result of the different mechanisms of turbulent entrainment at the outdoor clouds at Thorney Island and the calm-ambient releases of Schatzmann (page 10, chapter 2). This table shows that, for each centreline sensor, increasing slope gives monotonically increasing experimental concentrations, but monotonically decreasing predictions. Possible reasons for this reverse trend are discussed below.

The decreased concentration at ground level for steeper slopes is related to the widening flow pattern. If a one-dimensional flow, such as that considered by Ellison and Turner [52] is considered, the depth averaged concentration is inversely proportional to the entrainment coefficient E. Ellison and Turner, although employing slightly different depth averaging techniques and concentrating on slopes $> 10°$, present evidence to suggest that $E \propto \theta$, where θ is the slope. This implies

	concs, % (obs vs. pred)		
coords/slope (%)	4	8.6	11.63
(61, 0)	$5.49 > 2.71$	$6.04 > 2.21$	$6.91 > 2.10$
(61, 31)	$2.09 \lesssim 2.50$	$1.21 \lesssim 1.90$	$0.77 < 1.60$
(123, 0)	$2.58 \gtrsim 1.43$	$3.17 > 1.03$	$3.67 > 0.92$
(123, 23)	n/a	n/a	$2.02 > 0.88$
(123, 38)	$1.10 \lesssim 1.35$	$0.90 \lesssim 0.94$	$0.66 \lesssim 0.77$
(123, 77)	$0.43 < 1.15$	$0.18 < 0.67$	n/a
(184, 0)	$1.62 \gtrsim 0.93$	$1.93 > 0.64$	$2.22 > 0.56$
(184, 38)	$1.02 \gtrsim 0.92$	$0.99 \gtrsim 0.61$	$1.02 > 0.50$
(245, 0)	$1.39 \gtrsim 0.72$	$1.44 > 0.47$	$1.71 > 0.39$

Table 11.1: Coordinates, and observed and predicted concentrations for all eight sensors in each of the three Schatzmann continuous release experiments; measurements in centimetres, source at (0, 0). Here, $\lesssim$ and $\gtrsim$ mean 'correct to within a factor of two'. For example '$2.09 \lesssim 2.50$' means that the observed concentration of 2.09% is less the predicted 2.50% but correct to within a factor of two.

that the depth averaged concentration decreases with increasing slope.

This line of argument must be erroneous, as the opposite trend is observed. Two reasons for this might be:

1. The shape parameter S_1 is a function of slope and, while this does not affect the depth averaged concentration of the flow, the ground level concentration is inversely proportional to S_1.

2. Steep slopes, having an increased downslope component of buoyancy force, affect the two-dimensional structure of the flow and in particular inhibit the outward spread of fluid from the source.

Both these phenomena occur to some extent, but neither is directly detected in the experiments.

Figure 11.2 shows the Eulerian concentration trace for each slope at the point $(184, 0)$. If the intermittent noise on the 4% trace is ignored,[1] it may be seen that an increase in slope is associated with a higher average concentration. Although the trace for the 11.63% slope appears to increase less abruptly than the shallower slopes, this is not necessarily significant as this feature is not seen elsewhere.

Table 11.2 shows predicted and observed cloud arrival times. It may be seen that arrival time is quite well predicted on the centreline, for each sensor position. Off axis sensors are less well predicted, and are typically early. This is because the simulated cloud front is too broad, unlike the more rounded shape indicated by experiment. As indicated in section 4.5.5, further work on oblique gravity current

[1]This noise appears on each of the continuous traces for the 4% slope and nowhere else.

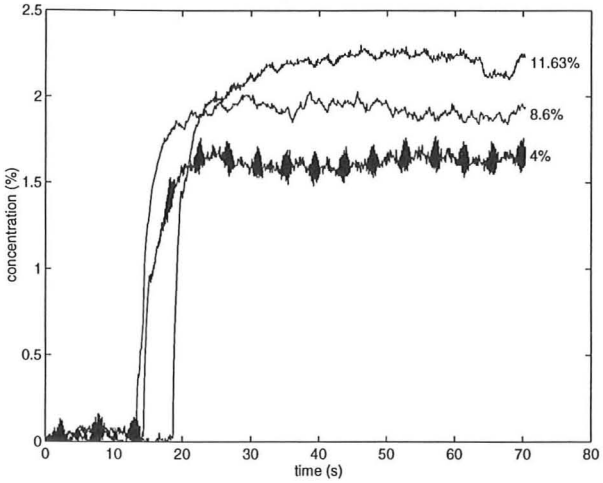

Figure 11.2: Eulerian concentration traces for the sensor at $(184, 0)$ for each slope

fronts on slopes would be needed to assess the leading edge condition used in this thesis, although it could be argued that the experimentally determined cloud arrival times support the view of Webber, also discussed in section 4.5.5.

	arrival time (s) (obs vs. pred)		
coords/slope (%)	4	8.6	11.63
(61, 0)	$9.9 > 7.5$	$6.0 < 6.1$	$9.8 > 5.8$
(61, 31)	$12.9 > 9.5$	$9.0 > 8.4$	$13.3 > 7.7$
(123, 0)	$20.4 > 15.6$	$12.1 < 12.2$	$14.2 > 11.3$
(123, 23)	n/a	n/a	$15.8 > 11.6$
(123, 38)	$24.4 > 17.2$	$14.6 > 13.9$	$18.8 > 13.1$
(123, 77)	$34.2 > 23.4$	$35.8 > 21.0$	n/a
(184, 0)	$28.2 > 24.2$	$18.1 < 18.6$	$19.4 > 17.1$
(184, 38)	$34.3 > 24.6$	$20.7 > 19.2$	$23.7 > 18.0$
(245, 0)	$35.5 > 33.2$	$24.0 < 25.3$	$25.7 > 23.0$

Table 11.2: Coordinates, and observed and predicted arrival times for all eight sensors in each of the three Schatzmann continuous release experiments; measurements in centimetres, source at (0, 0)

Figure 11.3 shows the predicted and observed Eulerian concentration trace at $(61, 0)$. This figure is typical in several respects:

- Cloud arrival time is well predicted on the centreline.

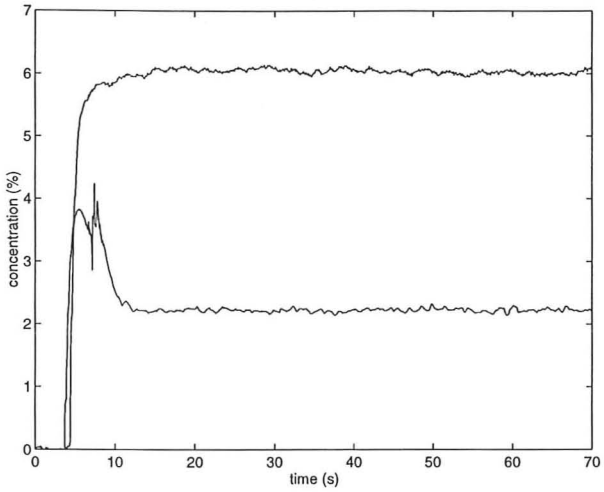

Figure 11.3: Predicted (lower) and experimental (upper) Eulerian concentration traces for the sensor at $(61, 0)$ on the 8.6% slope

That these cloud arrival time are well predicted is evidence that the boundary conditions discussed in chapter 3 are appropriate. However, the late arrival time generally seen for off-axis sensors may be due to the three dimensional flow behind the leading edge being poorly simulated.

- The mean concentration is underpredicted by a factor of about 3.

  Underprediction of the mean concentration is associated with the vertical profile used. Here, an exponential profile is used but alternative profiles will give different results (appendix B).

- Unlike the experimental trace, the predicted trace rises to a maximum before stabilising.

  This phenomenon occurs nowhere in the experimental results and is a result of the non-steady flow immediately after starting (the present model, being time varying, has to simulate this non-steady starting phase). The magnitude of the peak decreases with increasing distance from source; no similar peak is observed at the furthest points.

  Interpretation of this result is difficult. It appears to be due to a mismatch between the leading edge and the following flow, suggesting an inappropriatley small front Froude number; but as cloud arrival times are quite accurately predicted, this would not seem to be the case. This result could be because the present model is not able to include edge entrainment.

Examination of ongoing simulations suggests that the initial high concentration is associated with a localised region of low cloud height and relatively high concentration. This region is created immediately after the buoyancy flux starts, and travels in front of the leading edge. Although this dense fluid disperses slowly (the following flow gradually overtakes and merges with it), Eulerian concentration histories show its presence.

It is reasonable to conjecture that the quasi-equilibrium analysis presented in chapter 4 is being used for a situation in which the experimental flow adjusts faster than the simulation; this might be expected on the grounds that depth averaged quantities are used in the present model, while the experimental flow generally has a multi-layer structure that allows faster adjustment to a state of quasi-equilibrium.

- Neither trace is steady;[2]in each case the interquartile range is about 2% of the mean.

  These oscillations are not dependent on the details of the numerical scheme: the present model, when run with a gridsize an order of magnitude smaller, gave statistically similar results (the frequency of oscillation is $\sim (h/g')^{1/2}$, independent of the numerical timescales involved). Appendix E shows that the shallow water equations have no steady stable solution on a slope in one dimensional flow, and suggests reasons why this may be the case for two dimensional flow.

  Linden and Simpson, considering buoyancy driven flow into a room through an open door [123], present experiments that clearly show oscillations travelling away from the source of buoyancy. Simpson [171], commenting on this work, observes that

  > A gravity current which is spreading out ...often shows periodic oscillations in the form of the head. These oscillations have been seen in environmental flows and examples have been observed in laboratory experiments.

  These oscillations, although affecting the depth averaged variables used in the present model, do not necessarily penetrate to the ground.

[2]Previous versions of the present model exhibited much more severe oscillations. It has been established that this is due to a different definition of g'; in the present model, $g' = g\Delta\rho/\rho$; the previous model used $g' = g\Delta\rho/\rho_a$ (the change was made to avoid the possibility of $g' > g$, considered unrealistic by many workers [68]. A convenient notation is to use g' and g'' respectively). In the case of industrially relevant flow, this makes little difference as the majority of the cloud has $\Delta\rho/\rho_a \ll 1$; and this affects the simulation only weakly as shown in equation 5.5. However, in the present case, $\rho_0 = 6.16\,\mathrm{kg/m^3}$, giving $g'' \simeq 4g$.

The use of g' alleviates the instabilities detailed in appendix E because it reduces the inhibitory effect of density difference on entrainment. Small perturbations on the background flow (for example, transient features at small t) are more effectively smoothed out using g' than g''.

If gravity waves do form in this release, then the relationship between depth averaged densities and ground level concentration becomes more complex than indicated in appendix B. This is because a shallow layer model of dense gas dispersion implicitly assumes that entrained air, although entering the cloud from the top down, mixes sufficiently quickly so as to maintain the assumed vertical structure. The presence of gravity waves prevents this from happening as fluid properties then vary on relatively short timescales.

The preceding discussion has presented some of the difficulties that the present model has when predicting continuous flow.

At Thorney Island, the main source of turbulent kinetic energy was that present in the atmosphere, and characterized in the present model as the friction velocity u_* (this was described by Turner [179] as externally generated turbulence).

In the indoor experiments of Schatzmann, the ambient fluid was at rest, so turbulence was generated internally, at the shear layer.

The present model required a combined velocity scale (equation 5.5, page 60) that was a weighted quadratic sum of u_* and the relative layer speed $|\mathbf{u} - \mathbf{u}_a|$; other minor terms were also added. The weight applied to the relative layer speed (α_7 in equation 5.7, page 61) was unity, following Eidsvik; this has little impact on outdoor simulations because $|\mathbf{u} - \mathbf{u}_a|$ is small if cloud height $h \gg z_0$.

One interpretation of the results of table 11.1 is that a case could be made to reduce the relative layer speed weight. However, results for the instantaneous case would appear to indicate that this may not be appropriate.

11.4 Instantaneous releases

The instantaneous releases of Schatzmann are now considered. The model is unchanged from the above cases, but the source terms used are different. Here, the aspect ratio of the release is set to unity but, as for the Thorney Island simulations, the shape of the cloud at $t = 0$ is approximately a cube.

As for the previous section, a table detailing all sensors will be presented and discussed, followed by a more detailed discussion of a selection of sensor traces.

Tables 11.3 and 11.4 show the present model's performance against the instantaneous experimental results.

Table 11.3 shows predicted and observed peak concentrations. No readily observable trend for either over- or under- prediction is seen; all but one sensor is correctly predicted to within a factor of two, and 25% of the predicted peaks are within the experimental range.

Table 11.4 shows that cloud arrival time is generally well predicted for the 4% slope. This is in contrast with the continuous flow results, in which cloud arrival times were generally reasonably well predicted.

	concs, %: obs [min, max] vs. pred		
coords/slope (%)	4	8.6	11.63
(61, 0)	$[4.7, 7.2] \gtrsim 3.1$	$[6.6, 10.1] \approx 7.5$	$[6.7, 9.4] \approx 6.8$
(61, 23)	n/a	n/a	$[6.2, 7.9] \approx 7.2$
(61, 46)	$[1.9, 2.2] \lesssim 2.4$	$[2.3, 2.6] \gtrsim 1.5$	$[1.8, 2.4] > 0.6$
(61, 77)	$[0.3, 0.7] \lesssim 1.0$	$[0.3, 0.4] \lesssim 0.5$	n/a
(123, 0)	$[1.5, 1.8] \gtrsim 1.0$	$[2.8, 3.5] \lesssim 1.4$	$[2.7, 4.0] \gtrsim 2.1$
(123, 23)	n/a	n/a	$[2.6, 3.3] \lesssim 4.9$
(123, 38)	$[0.8, 1.1] \approx 0.8$	$[1.5, 1.8] \approx 1.7$	$[1.3, 1.6] \lesssim 2.1$
(123, 77)	$[0.3, 0.5] \lesssim 0.8$	$[0.3, 0.7] \lesssim 1.0$	n/a
(184, 0)	$[0.9, 1.1] \gtrsim 0.6$	$[1.4, 1.7] \gtrsim 1.0$	$[1.2, 1.8] \gtrsim 0.9$
(184, 38)	$[0.5, 0.7] \approx 0.5$	$[0.7, 1.1] \lesssim 1.5$	$[0.8, 1.1] \gtrsim 0.5$

Table 11.3: Coordinates, and observed and predicted peak concentrations for all eight sensors in each of the three Schatzmann instantaneous release experiments; measurements in centimetres, source at (0, 0). Here, $\approx$ means 'includes' and $\lesssim$, $\gtrsim$ mean 'correct to within a factor of two'. For example, '$[4.7, 7.2] \gtrsim 3.1$' means that the observed range of peak concentrations, 4.7% to 7.2%, is greater than the predicted peak of 3.1%, but $4.7\% \leq 2 \times 3.1\%$.

The two larger slopes generally have late predicted arrival times, especially for the off-axis sensors. In contrast to the continuous case, this result is consistent with the leading edge of the simulated current being more pointed than experiment.

Figures 11.4 and 11.5 show Eulerian concentration traces at $(61, 0)$ and $(284, 0)$ respectively. The only difference between the three parts of each figure is the slope over which the gas was released. Several differences between the traces are apparent:

- The time of arrival decreases with increasing slope for the sensor at $(184, 0)$; no trend is discernible at $(61, 0)$. This would be expected with a constant front Froude number because steeper slopes give taller leading edges and $u_f \propto h_f^{1/2}$.
- Peak concentration increases with increasing slope, although not significantly between the 8.6% slope and the 11.63% slope (either in experiment or simulation). As discussed above, this is possibly connected to the narrower cloud width on steeper slopes.
- Residence time decreases with increasing slope. This would be expected as clouds on steeper slopes move faster.

Figures 11.4 and 11.5 generally show that cloud residence time is underpredicted. This is possibly due to the $(h/g')^{1/2}$ timescale resolution limit of the present

	arrival time (s): obs [min, max] vs. pred		
coords/slope (%)	4	8.6	11.63
(61, 0)	$[2.3, 2.6] > 1.8$	$[1.4, 1.5] > 1.2$	$[1.6, 1.8] > 1.1$
(61, 23)	n/a	n/a	$[2.1, 2.3] < 5.2$
(61, 46)	$[4.0, 4.3] < 6.0$	$[2.6, 2.9] < 5.8$	$[2.8, 3.2] < 9.4$
(61, 77)	$[10.1, 11.6] \approx 10.4$	$[7.4, 8.3] < 10.6$	n/a
(123, 0)	$[10.0, 11.4] \approx 10.1$	$[4.4, 4.9] < 6.7$	$[4.4, 5.2] < 5.7$
(123, 23)	n/a	n/a	$[4.6, 5.5] < 12.7$
(123, 38)	$[11.9, 13.4] \approx 12.0$	$[5.6, 6.1] < 10.0$	$[5.6, 6.1] < 8.9$
(123, 77)	$[18.7, 21.4] < 16.9$	$[4.6, 6.5] < 15.0$	n/a
(184, 0)	$[17.8, 20.1] < 20.5$	$[8.6, 9.6] < 15.5$	$[7.8, 9.0] < 12.6$
(184, 38)	$[21.5, 24.7] > 21.4$	$[9.4, 11.0] < 16.4$	$[9.4, 11.8] < 14.2$

Table 11.4: Coordinates, and observed and predicted cloud arrival times for all eight sensors in each of the three Schatzmann instantaneous release experiments; measurements in centimetres, source at (0, 0). Here, $\approx$ means 'includes'

work. When the cloud becomes very dilute, this timescale becomes large and model predictions begin to degrade.

In each case, cloud residence time as defined on page 100 is too small; the simulated cloud passes over the sensor too quickly. This is possibly due, as for the Thorney Island simulations, to the inability of the present model to simulate the behaviour of the releasant at early times.

Figures 11.6, 11.7, and 11.8 show, for the three slopes, the results of the simulation after 20 seconds. In each figure the intensity of the plot shows the concentration, and the height of the plot is the depth of the dense layer.

If these figures are compared and contrasted, common features include:

- In each case the leading edge is more dilute than the following flow; this is so even though the edge entrainment is set to zero.
- A region of high concentration is left behind, close to the release point. This region moves only slowly and is of low depth.
- The leading edge is deeper than the following flow.

However, there are many features that differ between the slopes:

- The flow over steeper slopes was narrower. Cloud width rises from 2.1 m for the 4% slope through 2.3 m for 8.6%, to 2.6 m for 11.63%.
- The flow for the steeper slopes advanced further (at $t = 20\,\mathrm{s}$) than for the shallower slopes (consistent with the traces shown in figure 11.5 and 11.4).

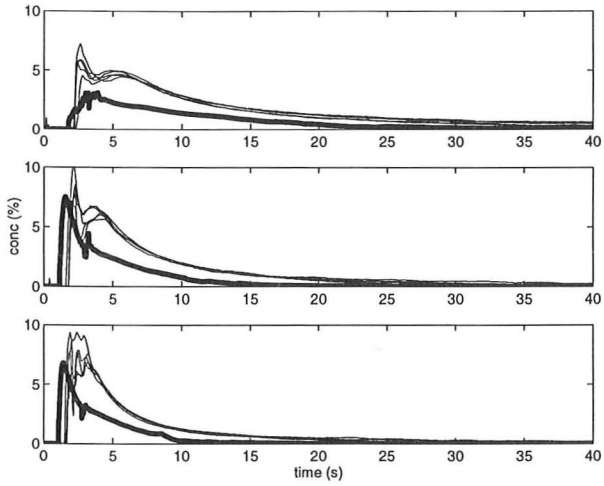

Figure 11.4: Eulerian concentration traces at $(61, 0)$ for each slope. From top to bottom: 4%, 8.6%, and 11.63%

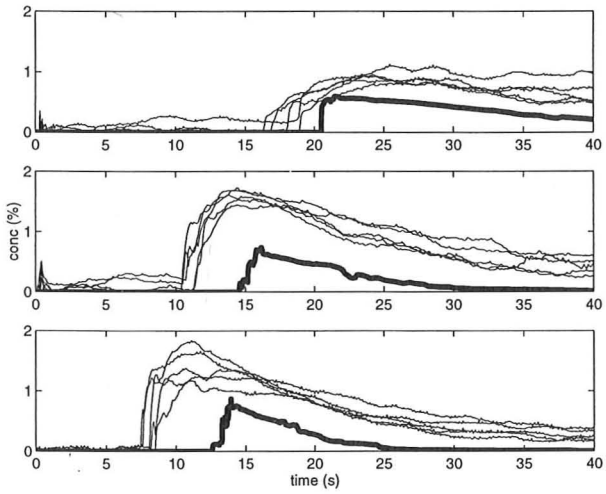

Figure 11.5: Eulerian concentration traces at $(184, 0)$ for each slope. From top to bottom: 4%, 8.6%, and 11.63%

- The flow over the shallower slopes is very much smoother (in terms of low cloud non-uniformity).
- The region, behind the leading edge, of dilute flow is larger for the steeper slopes.

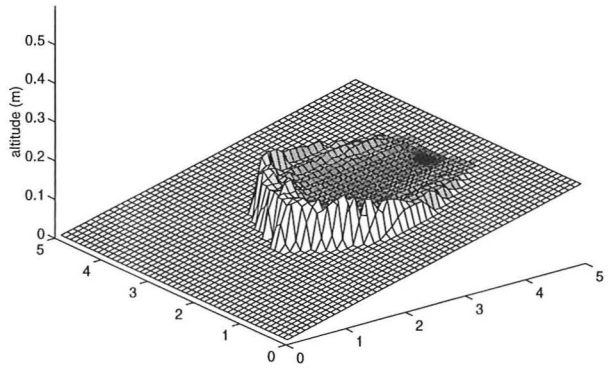

Figure 11.6: Base case simulation for the 4% slope after 20 seconds; height of a point is the depth of the cloud (multiplied by a factor of 5 for clarity); shading of a point proportional to the contaminant concentration. Note vertical scale differs from horizontal scales

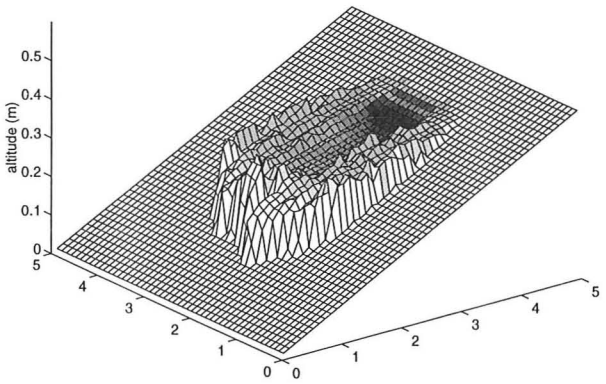

Figure 11.7: Base case simulation for the 8.6% slope after 20 seconds; height of a point is the depth of the cloud (multiplied by a factor of 5 for clarity); shading of a point proportional to the contaminant concentration. Note vertical scale differs from horizontal scales

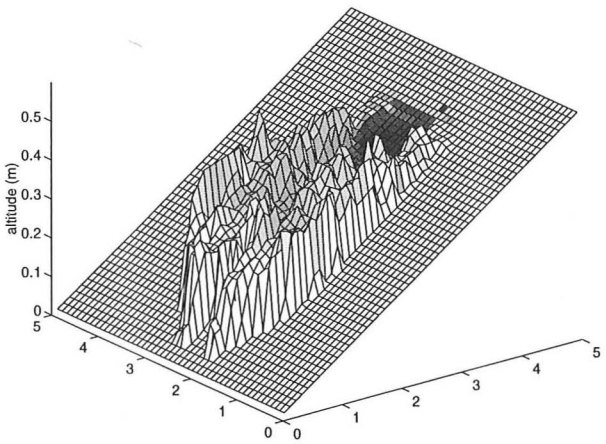

Figure 11.8: Base case simulation for the 11.63% slope after 20 seconds; height of a point is the depth of the cloud (multiplied by a factor of 5 for clarity); shading of a point proportional to the contaminant concentration. Note vertical scale differs from horizontal scales

11.5 Summary

In this chapter, the results of Schatzmann [167] were analysed; both continuous and instantaneous releases were considered.

The present model simulated both experiments and gave useful output. Predicted concentrations were generally underpredicted for the continuous releases, but were mostly correct to within a factor of two for the instantaneous releases.

For continuous releases, cloud arrival times were quite accurate for centreline sensors and late for off-axis sensors. For instantaneous releases arrival times tended to be late, especially for off-axis sensors. Cloud residence time was underpredicted for the instantaneous releases. Where predictions differed from experiment, physical explanations were given where possible.

This chapter has shown that the present model can simulate the flows investigated by Schatzmann, subject to the caveats discussed in chapters 1 to 7.

Chapter 12

Conclusions

The objective of this thesis was to investigate the use of shallow layer models in heavy gas dispersion. A shallow layer model describes a dispersing dense gas cloud as a function of ground position and time: vertical properties of the cloud are integrated out. Shallow layer models are appropriate for a dispersing dense gas cloud as the system is usually of low aspect ratio.

As dense gas clouds do not have uniform vertical profiles, some type of depth averaging has to be used to represent the cloud as a function of ground position and time. There are a number of ways of doing this and chapter 3 presents one method that allows definition of four depth averaged quantities: cloud concentration, two cloud velocities, and cloud depth. These quantities may be defined for an arbitrary cloud: no assumptions are necessary for their definition.

If the pressure distribution is then assumed to be hydrostatic in the vertical, the four depth averaged quantities evolve according to the generalized shallow water equations. The hydrostatic pressure distribution breaks down at the leading edge of a dispersing dense gas cloud, as vertical accelerations are not negligible there.

The leading edge thus requires separate treatment and this is carried out by simulating the effect of the ambient fluid on the dense layer at this point: the shallow water equations are augmented to allow correct simulation of the leading edge.

Dilution of a dense gas cloud is simulated by the incorporation of physically realistic, empirical, entrainment formulæ. The entrainment methodology used is a generalization of that used for integral models.

A computational model has been written in Fortran-77 that simulates the mathematical model discussed above. This computational model relies on the flux corrected transport (FCT) scheme of Zalesak as this is robust, computationally cheap, and guaranteed to eliminate numerical overshoot.

However, FCT requires generalization to handle variable terrain. The generalization developed fits into the structure of FCT. The computational model has been checked against a number of analytical results.

For validation, the model thus developed has to be compared against exper-

imental data. However, this task is not simple due to the large amount of data typically collected in experiments and in this case the model. Several methods of data reduction, allowing meaningful and objective comparison between experiment and code, have been discussed.

The model has a number of free parameters. A set of parameters has been chosen, motivated either by existing dense gas dispersion models, theoretical arguments, or simplicity. The model with this set of parameters is known as the 'base case'.

The base case model has been compared to the Thorney Island Instantaneous series of experiments. No trends were found, except for near-source points to be underpredicted because upwind cloud transport is not well modelled. Simulation of near-source behaviour is not possible with the present model.

The present model was then placed in context: the code comparison exercise of Mercer [132] was used to provide source terms, and predictions from the present model were placed alongside those of about ten established integral models. The present model gave predictions that were within the spread given by Mercer.

The base case model was then used to simulate dense gas dispersion over a slope. The experiments of Schatzmann [167] were used. Although perfect agreement was not obtained, results are generally accurate (in terms of peak concentration comparison) to within a factor of three. A number of systematic mispredictions have been identified and physical explanations, where available, given.

A number of results from a real hazard site have been given in appendix F. The importance of topography at low windspeed was demonstrated in a visually striking manner.

12.1 Future work

This thesis has presented a model for dense gas dispersion over complex terrain which has been used to understand the physics of dense gas releases over flat terrain and slopes. The model developed has been used in a case study using industrially realistic source terms and topography.

The model under development is not complete. Further work under consideration includes:

1. Determination of the effect of complex terrain on the ambient flow. As Britter and Snyder [32] state, the indirect effect of complex terrain on dispersion (via the ambient flow) may be as important as the direct, buoyancy driven, effect. Incorporation of this information into the model should be relatively straightforward from a computational viewpoint.

2. Investigation of the appropriate edge condition to use in the case of oblique leading edges. This work has argued that the edge condition used in

the present model is reasonable from a number of perspectives; Webber *et al.* [191] use a slightly different method and more research is required to determine whether the present model should be changed.

3. Incorporation of thermodynamic effects such as non-ambient temperature releases and the formation of aerosols. Some work has been carried out in this area by the present author [82], and by Webber [185].

4. Comparison of the model against experimental work where dense gas is released over slopes in non-calm surroundings. This work is related to point 1 as the ambient flow field will respond to a slope, possibly modifying the assumed logarithmic profile.

5. Further accounting for ensemble variability in dense gas dispersion. Workers such as Carn *et al.* [35], Puttock and Colenbrander [156], and Chatwin [38] consider ensemble variability in the context of dispersion models and further accounting for these workers' recommendations would form a useful contribution to future work.

Carrying out the work indicated above may yield a computationally accessible model for dense gas dispersion that is capable of accounting for the effects of complex terrain in a risk assessment context.

12.2 Summary

This thesis has presented a shallow layer model for dense gas dispersion over complex terrain. Only inert, single phase problems were considered. A computational model has been written that solves the generalized shallow water equations, with additional terms to represent the leading edge and entrainment.

On flat ground, peak concentrations are generally correctly predicted to within a factor of three for Thorney Island; results for cloud average concentrations agreed with established integral models. For indoor releases on slopes, the same model was used; both mean and peak concentrations were generally correct to within a factor of three.

Appendix A

The advection equation in multiple dimensions: the flux correction scheme of Zalesak

A.1 Outline

Appendix A presents an account of the advection scheme of Zalesak [200]. For simplicity, the one-dimensional case is considered first. The scheme of Zalesak was not designed for shallow water modelling and requires generalization to handle complex terrain. These generalizations are presented in section A.4.

Section A.5 shows the convective flux approximations used in the present model.

A.2 Flux correction in one dimension

For simplicity, the one-dimensional system of equations

$$\frac{\partial w}{\partial t} + \frac{\partial f}{\partial x} = 0 \tag{A.1}$$

is considered first. Here, w and f are vector functions of position and time. The quantity w may be discretized by considering only $w(x_i, t_n) = w_i^n$. Note that, for fixed i and n, w_i^n is a vector. A finite difference approximation to equation A.1 is in conservation form if it may be written in the form

$$w_i^{n+1} = w_i^n - \Delta x_i^{-1} \left[F_{i+(1/2)} - F_{i-(1/2)} \right] \Delta t \tag{A.2}$$

where $\Delta x_i = (x_{i+1} - x_i)$ and $\Delta t = t_{n+1} - t_n$ is the time step. The $F_{i\pm(1/2)}$ are called the transportive fluxes and are functions of the f of equation A.1 at times t_m where $m \leq n$.

Flux correction, or flux corrected transport (FCT), is a very general concept, capable of solving the advection equation in any number of dimensions. However, FCT in one dimension is first presented. Formally, FCT consists of six steps:

1. Compute $F^L_{i+(1/2)}$, the transportive flux as calculated by some low order scheme chosen to give ripple-free results.

2. Compute $F^H_{i+(1/2)}$, the transportive flux as calculated by some high order scheme chosen to be free of numerical diffusion.

3. Define the *antidiffusive flux*:

$$A_{i+(1/2)} = F^H_{i+(1/2)} - F^L_{i+(1/2)}.$$

4. Compute the updated low order ('transported and diffused') solution:

$$w_i^{td} = w_i^n - (\Delta x_i)^{-1}\left[F^L_{i+(1/2)} - F^L_{i-(1/2)}\right]$$

5. Limit the $A_{i+(1/2)}$ in a manner such that w^{n+1} as computed in step 6 below is free of extrema not found in w^{td} or w^n:

$$A^C_{i+(1/2)} = C_{i+(1/2)}A_{i+(1/2)},$$

where $0 \leq C_{i+(1/2)} \leq 1$. Recall that w^{td} is free from artificial extrema, as the low order scheme is monotonic.

6. Apply the limited antidiffusive fluxes:

$$w_i^{n+1} = w_i^{td} - (\Delta x_i)^{-1}\left[A^C_{i+(1/2)} - A^C_{i-(1/2)}\right].$$

The determination of $C_{i+(1/2)}$ is crucial, and is the essence of Zalesak's scheme. The antidiffusive flux $A^C_{i+(1/2)} = C_{i+(1/2)}A_{i+(1/2)}$ is limited so that $0 \leq C_{i+(1/2)} \leq 1$; and also so that the $A^C_{i+(1/2)}$ do not allow

$$w_i^{n+1} = w_i^{td} - (\Delta x_i)^{-1}\left[A^C_{i+(1/2)} - A^C_{i-(1/2)}\right]$$

to exceed some maximum value $w_i^{\max}$ nor to fall below some minimum value $w_i^{\min}$ (to be determined later). The ability of Zalesak's scheme to determine $w_i^{\max}$ and $w_i^{\min}$ gives it great flexibility: these quantities may be set using information that may or may not be available to the low- and high- order schemes. Numerical solution of the shallow water equations requires such customization, which is simple to implement as it requires only a change in definition of $w_i^{\max}$ and $w_i^{\min}$ and this is easily done.

Three quantities are defined:

$$\begin{aligned} P_i^+ &= \text{the sum of all antidiffusive fluxes } \textit{into} \text{ grid point } i \\ &= \max(0, A_{i-(1/2)}) - \min(0, A_{i+(1/2)}) && \text{(A.3)} \\ Q_i^+ &= (w_i^{\max} - w_i^{td})\Delta x_i && \text{(A.4)} \\ R_i^+ &= \begin{cases} \min(1, Q_i^+/P_i^+) & \text{if } P_i^+ > 0 \\ 0 & \text{otherwise} \end{cases} && \text{(A.5)} \end{aligned}$$

As all three above quantities are positive, so the limiting factor multiplying antidiffusive fluxes *into* grid point i must be less than or equal to R_i^+ to ensure no overshoot at grid point i.

In a completely analogous way three corresponding quantities are defined for antidiffusive fluxes flowing out of grid point i:

$$\begin{aligned} P_i^- &= \text{the sum of all antidiffusive fluxes } \textit{out of} \text{ grid point } i \\ &= \max(0, A_{i+(1/2)} - \min(0, A_{i-(1/2)}) && \text{(A.6)} \\ Q_i^- &= (w_i^{td} - w_i^{\min})\Delta x_i && \text{(A.7)} \\ R_i^- &= \begin{cases} \min(1, Q_i^-/P_i^-) & \text{if } P_i^- > 0 \\ 0 & \text{otherwise} \end{cases} && \text{(A.8)} \end{aligned}$$

and similarly the limiting factor multiplying antidiffusive fluxes *into* grid point i must be less than or equal to R_i^+ to ensure no overshoot at grid point i.

Zalesak recommended taking a conservative approach and used the following values for the limiters:

$$C_{i+(1/2)} = \begin{cases} \min(R_{i+1}^+, R_i^-) & \text{if} \quad A_{i+(1/2)} \geq 0 \\ \min(R_i^+, R_{i+1}^-) & \text{if} \quad A_{i+(1/2)} < 0 \end{cases} \qquad \text{(A.9)}$$

There is one remaining lacuna: if antidiffusive fluxes are directed against the gradient of w_i^{td}, then Zalesak recommended[1] that, in this rare case, the antidiffusive flux be set to zero.

The choice for $w_i^{\max}$ and $w_i^{\min}$ given was

$$\begin{aligned} w_i^{\max} &= \max(w_i^n, w_i^{td}, w_{i-1}^n, w_{i-1}^{td}, w_{i+1}^n, w_{i+1}^{td}) && \text{(A.10)} \\ w_i^{\min} &= \min(w_i^n, w_i^{td}, w_{i-1}^n, w_{i-1}^{td}, w_{i+1}^n, w_{i+1}^{td}) && \text{(A.11)} \end{aligned}$$

as this choice eliminates new extrema in the solution that are not 'legitimate'—i.e. not present in either w_i^n or w_i^{td}. The system thus ensures that any extrema that *do* appear in the solution are not an artefact of the high order scheme chosen.

[1]This recommendation was given as a result of extensive numerical trials but no explicit reason was given. It was acknowledged that this recommendation was partly motivated by numerical elegance and partly by the necessity of generalizing Boris and Book's one dimensional scheme to multiple dimensions.

Zalesak also gave a 'safer' choice

$$w_i^{\max} = \max(w_i^{td}, w_{i-1}^{td}, w_{i+1}^{td}) \tag{A.12}$$
$$w_i^{\min} = \min(w_i^{td}, w_{i-1}^{td}, w_{i+1}^{td}) \tag{A.13}$$

which is clearly more restrictive than equations A.10 and A.11.

These intuitively appealing choices were chosen for the rest of this work. Zalesak presented other choices for $w_i^{\max}$ and $w_i^{\min}$ but equations A.10 and A.11 (or A.12 and A.13 for certain cases) were found to be adequate.

A.3 Extension to multiple dimensions

A full description of the flux limiting scheme of Zalesak may now be given; the method given above easily generalizes to multiple dimensions, but here only the case of two dimensional time dependent equations will be considered:

$$\frac{\partial w}{\partial t} + \frac{\partial f}{\partial x} + \frac{\partial g}{\partial y} = 0, \tag{A.14}$$

where w is again a vector function of time and space.

In the following, for example, $F^H_{i+(1/2),j}$ is the high order flux into $w_{i+1,j}$ from $w_{i,j}$ and $F^H_{i,j+(1/2)}$ is the high order flux into $w_{i,j+1}$ from $w_{i,j}$.

First, antidiffusive fluxes are defined as follows:

$$A_{i+(1/2),j} = F^H_{i+(1/2),j} - F^L_{i+(1/2),j} \tag{A.15}$$
$$A_{i,j+(1/2)} = F^H_{i,j+(1/2)} - F^L_{i,j+(1/2)} \tag{A.16}$$

these are limited with flux limiters C:

$$A^C_{i+(1/2),j} = C_{i+(1/2),j} A_{i+(1/2),j} \tag{A.17}$$
$$A^C_{i,j+(1/2)} = C_{i,j+(1/2)} A_{i,j+(1/2)}, \tag{A.18}$$

where the C's are between 0 and 1. The transported and diffused solution $w^{td}_{i,j}$ is given by

$$w^{td}_{i,j} = w^n_{i,j} - (\Delta V_{i,j})^{-1} \left(F^L_{i+(1/2),j} + F^L_{i,j+(1/2)} - F^L_{i-(1/2),j} - F^L_{i,j-(1/2)} \right).$$

The P, Q, and R quantities are defined in an analogous way:

$$\begin{aligned} P^+_{i,j} &= \max(0, A_{i-(1/2),j}) - \min(0, A_{i+(1/2),j}) \\ &\quad + \max(0, A_{i,j-(1/2)}) - \min(0, A_{i,j+(1/2)}) \end{aligned} \tag{A.19}$$
$$Q^+_{i,j} = \left(w^{\max}_{i,j} - w^{td}_{i,j}\right) \Delta V_{i,j} \tag{A.20}$$
$$R^+_{i,j} = \begin{cases} \min(1, Q^+_{i,j}/P^+_{i,j}) & \text{if} \quad P^+_{i,j} > 0 \\ 0 & \text{if} \quad P^+_{i,j} = 0 \end{cases} \tag{A.21}$$

and

$$
\begin{aligned}
P^-_{i,j} &= \max(0, A_{i+(1/2),j}) - \min(0, A_{i-(1/2),j}) \\
&\quad + \max(0, A_{i+(1/2),j}) - \min(0, A_{1,j-(1/2)}) && \text{(A.22)} \\
Q^-_{i,j} &= \left(w^{td}_{i,j} - w^{\min}_{i,j}\right) \Delta V_{i,j} && \text{(A.23)} \\
R^-_{i,j} &= \begin{cases} \min(1, Q^-_{i,j}/P^-_{i,j}) & \text{if} \quad P^-_{i,j} > 0 \\ 0 & \text{if} \quad P^-_{i,j} = 0. \end{cases} && \text{(A.24)}
\end{aligned}
$$

Equation A.9 is now

$$
C_{i+(1/2),j} = \begin{cases} \min(R^+_{i+1,j}, R^-_{i,j}) & \text{if} \quad A_{i+(1/2),j} \geq 0 \\ \min(R^+_{i,j}, R^-_{i+1,j}) & \text{if} \quad A_{i+(1/2),j} = 0 \end{cases} \tag{A.25}
$$

$$
C_{i,j+(1/2)} = \begin{cases} \min(R^+_{i,j+1}, R^-_{i,j}) & \text{if} \quad A_{i,j+(1/2)} \geq 0 \\ \min(R^+_{i,j}, R^-_{i,j+1}) & \text{if} \quad A_{i,j+(1/2)} = 0. \end{cases} \tag{A.26}
$$

Zalesak then introduced a generalized scheme to cancel antidiffusive fluxes if they were against the direction of increasing w^{td}. The final result was:

$$
w^{n+1}_i = w^{td}_i - (\Delta x_i)^{-1} \left[A^C_{i+(1/2),j} - A^C_{i-(1/2),j} + A^C_{i,j+(1/2)} - A^C_{i,j-(1/2)} \right]. \tag{A.27}
$$

The above numerical routine is now guaranteed to give ripple-free results, if the low order scheme is chosen appropriately. It nevertheless preserves the high order behaviour of the high order scheme away from large gradients in the components of w.

The present author again draws attention to the fact that the above definitions are closely modelled on [200] and acknowledges his debt to Zalesak.

A.4 Varying ground elevation and flux correction

Flux correction was originally used for solving the advection equation in a plasma physics problem; the method is easily changed to solve the Euler equations or the shallow water equations on level ground. However, the shallow water equations over non-level ground require a generalization to FCT and this is considered below.

The effects of ground slope require a change to the choice of $w^{\max}_i$ and $w^{\min}_i$. It is clear that any discretization of space will result in a situation similar to that shown schematically in figure A.1; the situation depicted in figure A.2 is also possible and $w^{\max}_i$ and $w^{\min}_i$ need to be carefully chosen close to such regions. For example, in figure A.1, $w^{\min}_i$ as estimated by equation A.12 could result in h_i being as low as h_{i+1}, clearly an unrealistic value.

Consideration of this situation is necessary (and may not be ignored as pathological) when simulating, for example, a release of dense gas flowing down a slope. At the trailing edge of the cloud, where the cloud depth is very small compared to the vertical displacement between adjacent ground elements, the ground will appear as in figures A.1 and A.2. For simplicity the first case is referred to as a 'slope' and the second as a 'cliff'.

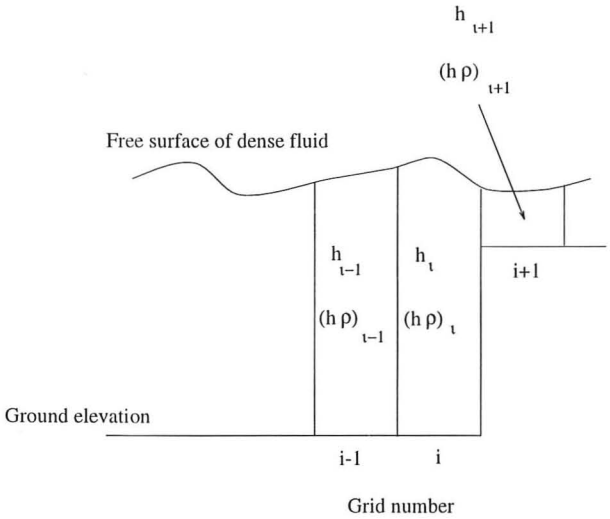

Figure A.1: Numerical solution of the shallow water equations near a large change in ground elevation

A.4.1 Generalizations to the flux correction scheme for flow near sudden changes in ground elevation

For convenience the original suggested values for $w_i^{\max}$ and $w_i^{\min}$ given in equations A.10 and A.11 are restated, and because the generalization is independent of dimension, attention is limited to the one dimensional case:

$$\begin{aligned} w_i^{\max} &= \max(w_i^n, w_i^{td}, w_{i-1}^n, w_{i-1}^{td}, w_{i+1}^n, w_{i+1}^{td}) \\ w_i^{\min} &= \min(w_i^n, w_i^{td}, w_{i-1}^n, w_{i-1}^{td}, w_{i+1}^n, w_{i+1}^{td}) \end{aligned}$$

These equations cover each element of the vector w, and they require modification to account for sudden changes in ground elevation. Two different methods are required: one for the first element of w (the fluid depth h) and a slightly different method for the other elements.

These equations are clearly unsuitable for flow near a situation as shown in figure A.1. If the first element of w (the depth h of the dense fluid) is considered,

then the first element of equations A.28 suggests that $w_i^{\min}$ (that is, the minimum allowed depth of fluid at position i) be as low as h_{i+1}. This is unacceptable as it can lead to gross errors such as negative fluid depths.

Similar difficulties (though not so crucial) occur when calculating the maximum fluid depth at position $i+1$.

If the second element of w which is $h(\rho - \rho_a)$ is considered, a problem of a different type occurs because flux correction limits w and not $\rho - \rho_a$. It is the case that the excess density $\rho - \rho_a$ (and therefore the density ρ) must also be limited as it is free to vary and the computational scheme places no constraint upon it. On level ground the old limiters A.28 and A.28 function completely accurately. However, when ground elevation varied the 'safe' choice for $w_i^{\max}$ and $w_i^{\min}$ (given in equations A.12 and A.13) was found to be needed for all elements of w except the first.

For simplicity, only $w_i^{\max}$ will be considered, as the expression for $w_i^{\min}$ is analogous. Here, equations A.12 and A.13 are used.

The second element of w_i, with $w_i = h_i(\rho_i - \rho_a) = h_i \Delta\rho_i$ is considered. As discussed above, $\Delta\rho$ should be limited rather than w_i. Thus

$$\begin{aligned} \Delta\rho_i^{\max} &= \max(\Delta\rho_{i-1}, \Delta\rho_i, \Delta\rho_{i+1}) \\ &= \max\left(\frac{w_{i-1}}{h_{i-1}}, \frac{w_i}{h_i}, \frac{w_{i+1}}{h_{i+1}}\right) \end{aligned} \tag{A.28}$$

therefore

$$\begin{aligned} w_i^{\max} &= \max\left(\frac{w_{i-1}}{h_{i-1}}.h_i, \frac{w_i}{h_i}.h_i, \frac{w_{i+1}}{h_{i+1}}.h_i\right) \\ &= \max\left(\frac{w_{i-1}}{h_{i-1}}.(h_{i-1} + \Delta e_{i-1}), w_i, \frac{w_{i+1}}{h_{i+1}}.(h_{i+1} + \Delta e_{i+1})\right) \\ &= \max\left(w_{i-1}\left[1 + \frac{\Delta e_{i-1}}{h_{i-1}}\right], w_i, w_{i+1}\left[1 + \frac{\Delta e_{i+1}}{h_{i+1}}\right]\right) \end{aligned} \tag{A.29}$$

with a corresponding expression for $w_i^{\min}$. Here $\Delta e_{i+1} = e_i - e_{i+1}$ is the difference in ground elevation between grid points i and $i+1$. The expression given in equation A.29 is easily generalized to multiple dimensions, and solves a problem not encountered when considering the Euler equations.

Identical expressions are used for the remaining elements of the vector w.

A.4.2 Generalizations to the flux correction scheme for flow near extreme changes in ground elevation

Attention must now be given to cases like those shown in figure A.2. Now, the flux from left to right must be less than zero as the fluid may only flow down the

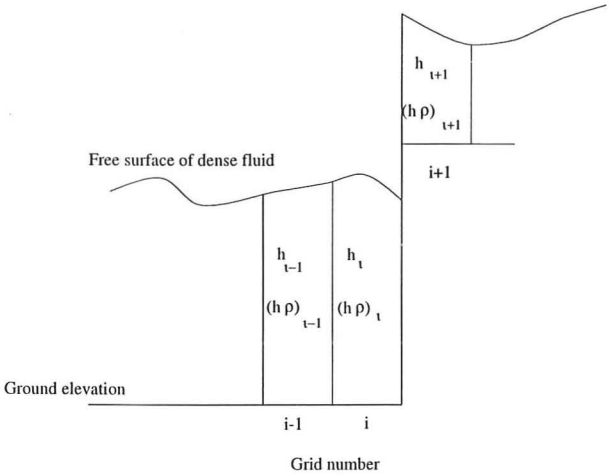

Figure A.2: Numerical solution of the shallow water equations near an extreme change in ground elevation sufficient to halt fluid flow from left to right

cliff.[2] Any numerical routine will need to test for the presence of such cliffs and limit the fluxes (both the high order and the low order) accordingly.

It remains to set the values of $w_i^{\max}$ and $w_i^{\min}$ in the presence of such extreme terrain features. The extension to Zalesak's original scheme given in equation A.29 is clearly of little use, as the height of the cliff Δe appears explicitly. This is incorrect as the height of the cliff is immaterial provided that it is greater than the depth of fluid at the base of the cliff.

This problem may be solved by calculating $w_i^{\max}$ and $w_i^{\min}$ as above, but taking the maximum or minimum *over the adjacent fluid elements which are not separated from element* 'i' *by a cliff.* This simple device assures consistent behaviour close to cliffs and was used to simulate dense fluid flow in a channel for the results shown on pages 91 to 94 in chapter 7; the sides of the channel were cliffs. This method is readily extended to multiple dimensions.

[2]This is not true if the quantity being transported is negative, as may happen if the third element of w is considered; this is the momentum (per unit area) in the $x-$ direction. If this quantity is negative on the upper side of the cliff, then a negative flux will make the value of w *more* negative, which corresponds to a 'leakage' of advected quantity up the cliff, in the sense that the fluid element on the lower side of the cliff affects the fluid element on the upper side of the cliff.

A.5 The convective fluxes used in the computational model

The high- and low- order convective fluxes F^H and F^L are now presented. The precise choice of these fluxes is not central to the numerical method, except insofar as they exhibit the properties discussed in section A.2.

A.5.1 The low order convective flux F^L

The low order flux used is simply a donor cell scheme plus a zeroth order diffusive flux with coefficient D:

$$F^L_{i+(1/2)} = \tfrac{1}{2}(u_i + u_{i+1})w^{\mathrm{DC}}_{i+(1/2)} - D\Delta x_i(w^n_{i+1} - w^n_i)(\Delta t)^{-1} \tag{A.30}$$

where

$$w^{\mathrm{DC}}_{i+(1/2)} = \begin{cases} w^n_i & \text{if } u_i + u_{i+1} \geq 0 \\ w^n_{i+1} & \text{if } u_i + u_{i+1} < 0 \end{cases} \tag{A.31}$$

is read "w donor cell" and u_i is the fluid speed in cell i. The quantity D is required to be the same order of magnitude as the Courant number C because the zeroth order diffusive flux must be comparable to the other flux terms in the equation. This work will specify that $C = D$.

A.5.2 The high order convective flux F^H

The high order convective flux used here is taken from a later work by Zalesak [201]. A series of expressions, to varying degrees of accuracy, for convective flux was given in [201]. Zalesak called these expressions 'high order ZIP fluxes', following the terminology of Hirt [100]. Zalesak presented a number of theoretical advantages of ZIP fluxes and pointed out that a given order of accuracy was more simply achieved using this scheme. To fourth order accuracy:

$$F^H_{i+(1/2)} = \tfrac{2}{3}[w_{i+1}u_i + w_iu_{i+1}] - \tfrac{1}{12}[w_{i+2}u_i + w_iu_{i+2} + w_{i+1}u_{i-1} + w_{i-1}u_{i+1}]. \tag{A.32}$$

Equation A.32 shows an important feature of this high order flux scheme, namely that the high order flux across the leading and trailing edges of the test shown in chapter 7 is zero. This desirable property motivated this choice for the high order flux in the present model.

Appendix B

Concentration profiles and S_1

B.1 Outline

This appendix derives the ground level concentration as a function of depth averaged values and S_1. Two methods are presented: a simple one that neglects the coupling between fluid at altitudes $< h$ and that above; and a more involved method that includes this. These methods give results that agree closely when $1 - \alpha$ is small.

B.2 Introduction

There follows a derivation of certain relationships between depth averaged quantities as defined in chapter 4. Three natural choices of profiles are examined in turn below. The shape parameter S_1 will be shown to be involved in the relationship between ground level- and depth averaged- densities.

Two slightly different definitions for S_1 exist: the definition used by Ellison and Turner [52], and that used here in equation 3.32. The two definitions are approximately equal for values of α close to one. The main results of this appendix (equations B.29) pertain to Ellison and Turner's definition; they change in a slight, but complex, manner when the alternative definition of S_1 is used. The motivation for presenting these results in this way is clear on inspection of equations B.31.

B.3 Results: Ellison and Turner's definition of S_1

In the following derivations, S_1 will be defined slightly differently from equation 3.32 in the interests of simplicity:

$$\frac{1}{2}S_1(\overline{\rho} - \rho_1)h^2 = \int_{z=0}^{\infty}(\rho(z) - \rho_a)z\,dz \tag{B.1}$$

which is identical to that used in Ellison and Turner. The difference between S_1 as defined above and S_1 as defined in equation 3.32 is small for values of α close to one; the full case is tractable but involved and the salient results are given at the end of this appendix.

B.3.1 Gaussian concentration profiles

If the relation

$$\rho(z) - \rho_a = \rho_0 \exp[-(z/h_0)^2] \tag{B.2}$$

holds, where $\rho(z)$ is the concentration at height z, ρ_0 is the density excess at the ground $\rho(0) - \rho_a$, and h_0 is a depth scale of the layer, then the concentration distribution is Gaussian. A pictorial representation is given in figure B.1. The

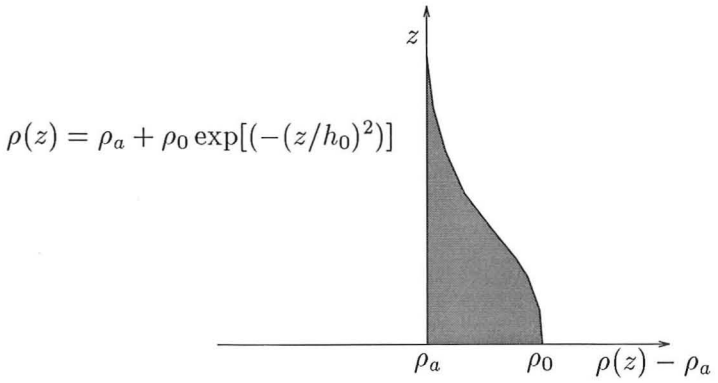

Figure B.1: Gaussian concentration profile: $\rho(z) = \rho_a + \rho_0 \exp[(-(z/h_0)^2)]$

integral relations 3.21 and 3.26 on pages 30 to 31 of chapter 2 define h and $\overline{\rho}$. Equation 3.21 is:

$$\begin{aligned} h(\overline{\rho} - \rho_a) &= \int_{z=0}^{\infty} (\rho(z) - \rho_a)\, dz \\ &= \int_{z=0}^{\infty} \rho_0 \exp[-(z/h_0)^2]\, dz. \end{aligned} \tag{B.3}$$

This integral evaluates to $\rho_0 h_0 \sqrt{\pi}/2$, and thus

$$h(\overline{\rho} - \rho_a) = \frac{1}{2}\rho_0 h_0 \sqrt{\pi}. \tag{B.4}$$

The definition of h (equation 3.26) is

$$\begin{aligned} \int_{z=0}^{h} (\rho(z) - \rho_a)\, dz &= \alpha \int_{z=0}^{\infty} (\rho(z) - \rho_a)\, dz \\ &= \alpha \left[\frac{1}{2}\sqrt{\pi}\rho_0 h_0\right]. \end{aligned} \tag{B.5}$$

The integral on the left hand side of equation B.5 is commonly evaluated in statistical contexts and implies that

$$\frac{h\sqrt{2}}{h_0} = P(\alpha) \tag{B.6}$$

where $P(\cdot)$ is the inverse normal distribution: $(2\pi)^{-1/2}\int_{t=0}^{P(\alpha)} \exp[t^2/2]\,dt = \alpha/2$ (so, for example, $P(0.95) = 1.96$). It is now possible to determine ρ_0 in terms of $\overline{\rho}$ and S_1:

$$\begin{aligned} h(\overline{\rho} - \rho_a) &= \int_{z=0}^{\infty} [\rho(z) - \rho_a]\,dz \\ &= \int_{z=0}^{\infty} \rho_0 \exp[-(z/h_0)^2]\,dz \end{aligned} \tag{B.7}$$

And again, algebra gives

$$\rho_0 = (\overline{\rho} - \rho_a)\sqrt{\frac{2}{\pi}}.P(\alpha) \tag{B.8}$$

Now that h and $\overline{\rho}$ are known in terms of ρ_0 and h_0, determination of S_1 is straightforward:

$$S_1.\frac{1}{2}g(\overline{\rho} - \rho_a)h^2 = g\int_{z=0}^{\infty} (\rho(z) - \rho_a)z\,dz, \tag{B.9}$$

by definition. Thus

$$\frac{1}{2}S_1.h.h(\overline{\rho} - \rho_a) = \int_{z=0}^{\infty} \rho_0 \exp[-(z/h_0)^2].z\,dz, \tag{B.10}$$

giving

$$S_1 = \frac{\rho_0 h_0^2}{(\overline{\rho} - \rho_a)h^2}. \tag{B.11}$$

Using equations B.6 and B.4 gives

$$S_1 = \frac{\sqrt{8/\pi}}{P(\alpha)} \tag{B.12}$$

Combining equations B.4, B.6, and B.11 gives

$$\rho_0 = (\overline{\rho} - \rho_a).\left(\frac{4}{\pi}\right).(S_1)^{-1}. \tag{B.13}$$

and so

$$\rho(z) = \rho_a + (\overline{\rho} - \rho_a).\frac{4}{\pi S_1}.\exp\left[-\left(\frac{z^2}{h^2}.\frac{4}{\pi S_1^2}\right)\right] \tag{B.14}$$

expresses the vertical concentration distribution solely in terms of the depth averaged variables used in the present model.

B.3.2 Exponential concentration profiles

A similar methodology as for the Gaussian concentration profile is appropriate; here

$$\rho(z) - \rho_a = \rho_0 \exp[-z/h_0]. \tag{B.15}$$

The defining equations are thus

$$\begin{aligned} h(\overline{\rho} - \rho_a) &= \rho_0 \int_{z=0}^{\infty} \exp[-z/h_0]\, dz \\ &= \rho_0 h_0 \end{aligned} \tag{B.16}$$

and

$$\int_{z=0}^{h} (\rho(z) - \rho_a)\, dz = \alpha \int_{z=0}^{\infty} (\rho(z) - \rho_a)\, dz \tag{B.17}$$

giving

$$\frac{h}{h_0} = -\ln(1-\alpha) \tag{B.18}$$

and

$$\rho_0 = -(\overline{\rho} - \rho_a)\ln(1-\alpha). \tag{B.19}$$

Determination of S_1 is straightforward:

$$\int_{z=0}^{\infty} (\rho(z) - \rho_a) z\, dz = S_1 . \frac{1}{2} g(\overline{\rho} - \rho_a) h^2 \tag{B.20}$$

giving

$$S_1 = 2[-\ln(1-\alpha)]^{-1} \tag{B.21}$$

Combining equations B.19 and B.21 gives

$$\rho_0 = 2(\overline{\rho} - \rho_a).(S_1)^{-1}; \tag{B.22}$$

the vertical density profile is therefore

$$\rho(z) = \rho_a + (\overline{\rho} - \rho_a).\frac{2}{S_1} \exp\left[-\left(\frac{z}{h}.\frac{2}{S_1}\right)\right]. \tag{B.23}$$

B.3.3 Polynomial concentration profiles

There are two natural vertical concentration profiles that may be considered, class 'A' and class 'B'. These classes will be considered separately.

Class 'A' polynomial concentration profiles

If the profile is of the form

$$\rho(z) = \begin{cases} \rho_a + \rho_0(1 - z/h_0)^n & \text{for } z < h_0 \\ \rho_a & \text{otherwise} \end{cases} \tag{B.24}$$

where $n \geq 0$ is a constant, it can be shown that

- $h(\overline{\rho} - \rho_a) = \rho_0 h_0/(n+1)$
- $\rho_0 = (\overline{\rho} - \rho_a).2(n+1)/(n+2).(S_1)^{-1}$
- $h/h_0 = 1 - (1-\alpha)^{1/(n+1)}$
- $S_1 = 2\left[(n+1)\left(1 - (1-\alpha)^{1/(n+1)}\right)\right]^{-1}$

which give

$$\rho(z) = \rho_a + (\overline{\rho} - \rho_a).\frac{2}{S_1}.\frac{n+1}{n+2}.\left[1 - \frac{z}{h}\left(1 - (1-\alpha)^{1/(n+1)}\right)\right]^n. \tag{B.25}$$

A uniform distribution may be recovered by setting $n = 0$.

Class 'B' polynomial concentration profiles

If the profile is of the form

$$\rho(z) = \rho_a + \frac{\rho_0}{[1 + (z/h_0)]^n} \tag{B.26}$$

where $n > 2$ is a constant, the corresponding results are:

- $h(\overline{\rho} - \rho_a) = \rho_0 h_0/(n-1)$
- $\rho_0 = (\overline{\rho} - \rho_a)2(n-1)/(n-2)(S_1)^{-1}$
- $h/h_0 = (1-\alpha)^{1/(1-n)} - 1$
- $S_1 = 2\left[(n-2)\left((1-\alpha)^{1/(1-n)} - 1\right)\right]^{-1}$

which give

$$\rho(z) = \rho_a + (\overline{\rho} - \rho_a).\frac{2}{S_1}.\frac{n-1}{n-2}.\left[1 + \frac{z}{h}\left((1-\alpha)^{1/(1-n)} - 1\right)\right]^{-n}. \tag{B.27}$$

B.3.4 General concentration profiles

Although only three forms for the vertical concentration profile have been investigated, these are the most natural to consider; profiles of the form

$$\rho(z) - \rho_a = \frac{\rho_0}{1 + (z/h_0)^2},$$

for example, admit values for h and $\overline{\rho}$, but can not specify S_1 because the integral diverges. Higher powers of z/h_0 than the second allow definition of S_1, but the expressions become very complex.

The two sections above have determined relationships between certain constants that appear in the development of the present model. Note that no specific vertical concentration profile is assumed and there is no fitting of a real profile to those considered here. The profiles given here are examples only and the methods given here and in chapter 3 are applicable to any profile. Combining equations B.22, B.13, B.25, and B.27 gives

$$\rho_0 = \Lambda(\overline{\rho} - \rho_a)(S_1)^{-1}, \tag{B.28}$$

where

$$\Lambda = \begin{cases} 2 & \text{for exponential distributions} \\ 4/\pi & \text{for Gaussian distributions} \\ 2\frac{n+1}{n+2} & \text{for } n\text{-th order polynomial distributions (class A)} \\ 2\frac{n-1}{n-2} & \text{for } n\text{-th order polynomial distributions (class B).} \end{cases} \tag{B.29}$$

As may be seen, the choice of an exponential, Gaussian, or uniform concentration profile has little effect on the prediction of the ground concentration ρ_0. Equation B.28 is independent of the choice of α.

B.4 Alternate definition of S_1

Equation 3.32 is restated for convenience:

$$\begin{aligned} &\int_{z=0}^{h} g[\rho(z) - \rho_a] z \, dz \\ &\quad + h \int_{z=h}^{\infty} g(\rho(z) - \rho_a) \, dz \quad = \quad S_1 . \frac{1}{2} g h^2 (\overline{\rho} - \rho_a) \end{aligned} \tag{B.30}$$

and it clear that this definition of S_1, although necessary for the work presented here, is considerably more complex than equation B.1 although the two definitions

are nearly equal for values of α close to one. Equation B.29 may, however, be recast for this more complex definition and becomes

$$\Lambda = \begin{cases} 2\alpha & \text{for exponential distributions} \\ \left(\frac{4}{\pi}\right)\left[1 - e^{-P(\alpha)^2/2} + \frac{P(\alpha)(1-\alpha)}{2}\right] & \text{for Gaussian distributions} \\ 2\left(\frac{n+1}{n+2}\right)\left[1 - (1-\alpha)^{(n+2)/(n+1)}\right] & \text{for } n\text{-th order polynomial distributions (class A)} \\ 2\left(\frac{n-1}{n-2}\right)\left[1 - (1-\alpha)^{(n-2)/(n-1)}\right] & \text{for } n\text{-th order polynomial distributions (class B).} \end{cases} \tag{B.31}$$

which is seen by inspection to approach the coefficients in equation B.31 when α is close to one. However, this formulation is not used here due to its complexity; and equation B.28 no longer having the desirable property that Λ is independent of α.

Appendix C

Further processes occurring in dense gas releases considered in risk assessment

C.1 Outline

This thesis has considered the dispersion of inert, monophase contaminant at ambient temperature. Releases typically considered in risk assessment may depart from this idealisation and a discussion of the importance these approximations is discussed.

C.2 Introduction

One of the aims of this thesis is to have a physically realistic model of dense gas dispersion over complex terrain to be used in risk assessment. Ambient flow will be treated as given, and a depth-averaged approach has been chosen for further study. Several phenomena occur in accidental dense gas releases that the present model ignores; each of these caveats will be discussed in turn. It will be assumed that the effects of the Earth's rotation are negligible as the Rossby radius [64] for dense gas clouds typically considered in risk assessments is of the order of 500 km—far greater than the range usually considered.

C.3 Aerosol effects

A scenario commonly considered in risk assessment is a container of liquified gas undergoing catastrophic failure, leading to an immediate loss of the majority of the vessel's contents.

Such an event may lead to the formation of a cloud which consists, at least partially, of an aerosol of suspended droplets. Water may be condensed from the surrounding atmosphere to form droplets and this process will increase the density of the cloud.

Although this type of behaviour has been modelled [71, 87, 157, 181], extension of these models to a shallow layer formulation is difficult. The assumption of homogeneous equilibrium, discussed by Nikmo *et al.* [146] and Vesala and Kukkonen [181], was designed for integral models of dense gas dispersion, but is less suitable for use in a depth averaged approach because vertical variations in aerosol properties may not be negligible. Such clouds require a large number of vertical profiles for their description and it is not clear that they are related in a simple way. The many thermodynamic phenomena (especially vertical enthalpy fluxes) occurring in such a cloud clearly alter these vertical profiles in a complex and possibly important manner. Work in this field has been carried out [84], suggesting that homogeneous equilibrium may not be an appropriate approximation in moist air.

The approach adopted here is to simulate a gas cloud only after droplet effects become negligible. This caveat renders the model unable to handle materials such as ammonia. This is positively buoyant by virtue of its molecular mass but a real release of ammonia may form a dense layer due to the formation of an aerosol and the condensation of atmospheric water.

C.4 Chemical reactions

Some gases, such as NO_2 and HF, undergo chemical changes when released into the atmosphere. Such complex processes are not considered here and it is not clear that cases where these processes are important can be modelled at all using a depth averaged approach.

Some chemical changes can exert a powerful influence on the gross behaviour of a cloud; for example, accidentally released HF can form a buoyancy reversing flow due to the formation and destruction of oligomers.

However, there exist a large class of industrially important (and hazardous) gases which do not undergo appreciable chemical change when released and attention will be confined to these substances. Examples include Cl_2 and SO_2.

C.5 Thermal effects

Hazardous clouds are often released at a lower than ambient temperature: the gas may be stored under refrigeration, or the substance may undergo flash vaporization; the resulting phase change will cool the mixture [25]. As the density of an ideal gas is inversely proportional to its thermodynamic temperature, thermal

effects are potentially important.

A dispersing cold dense gas cloud will be dense partly because it is cold. If no source of heat apart from entrained air exists, the system conserves buoyancy if the molar specific heats are identical [185]. However, thermal conduction from the ground is often important [187, 188], and the small heat capacity of the cloud compared with that of the ground, coupled with the thermal properties of common flooring materials implies that the heat flow from ground to cloud will be significant. The creation of positive buoyancy at the ground, due to heat transfer, will affect the vertical density profile significantly [67].

These processes all act to reduce the temperature deficit of a dispersing cold gas cloud and the approach adopted here, as for aerosol effects, is to model the cloud only after thermal effects become negligible. However, incorporation of thermal effects into the present model should be straightforward [185].

C.6 Concentration fluctuations

The final output of a risk estimation activity is a statement of human harm. At present, although toxicity information is scarce, the 'probit' relationship [4, 127] is currently used to link concentration exposure to probability of death.

Although concentration traces using instruments of response frequency of the order of one kilohertz are becoming more widely available [42], the 'measuring instrument' (i.e., the human lung) of interest to the risk assessment community has a response time of about one second and (in view of the lack of reliable toxicity data) fluctuations on much shorter timescales are unlikely to be relevant.[1]

There is the possibility of atmospheric motions causing concentration fluctuations on timescale much greater than one second (such as plume meandering); the approach adopted in this thesis is deterministic and apparently unable to account for such behaviour. However, a sufficiently sophisticated simulation of the ambient flow could interact with the depth averaged model to reproduce this effect by passing to the model a time-varying ambient wind field. The validity of the results of this type simulation rest with assessment of the accuracy of the depth averaged model under time-varying boundary conditions; such an approach may or may not be possible.

The presence of Eulerian concentration fluctuations is linked to the instantaneous inhomogeneity of a cloud. As the overpressure generated by the ignition of such a cloud depends on the amount of gas between the upper- and lower-flammability limits, the homogeneity of a cloud has a direct bearing upon risk assessment. However, direct simulation of this is not possible with the present approach as the timescales are less than $(h/g')^{1/2}$ and thus inaccessible.

[1]This is not true when considering the effects of certain toxins that attack mucous membranes; Jones [107] speculates that concentration fluctuations on millisecond timescales can affect toxicity.

C.7 The effect of the cloud on the ambient flow

It is hard to imagine a situation in which an accidentally released dense gas cloud exerts a substantial effect on the ambient flow field at distances large from the cloud. The effect of the cloud on the large-scale motion of the atmosphere will thus be neglected.

Flow visualisation studies of gravity currents [171] show that ambient fluid at heights lower than the front is scarcely perturbed before the front is closer than about two front heights away.

Also, some results [136] indicate that flow properties of the ambient fluid are affected only where gas is present.

The approximation of unchanged atmospheric flow outside the cloud is very advantageous, both from the point of view of computational expense and because existing atmospheric predictors may be used.

Appendix D

The shallow water equations and energy conservation

D.1 Outline

The shallow water equations are known to conserve energy [97, 171]. However, if they are generalized to include entrainment of ambient fluid, the energetics become more complex and an account is given here. The following is a generalization of that found in Wheatley and Webber [194].

D.2 Review

The shallow water equations with all dimensionless coefficients set to unity are:

$$\frac{\partial h}{\partial t} + \frac{\partial hu}{\partial x} + \frac{\partial hv}{\partial y} = u_{\text{ent}} \tag{D.1}$$

$$\frac{\partial h(\rho - \rho_a)}{\partial t} + \frac{\partial h(\rho - \rho_a)u}{\partial x} + \frac{\partial h(\rho - \rho_a)v}{\partial y} = 0 \tag{D.2}$$

$$\frac{\partial h\rho u}{\partial t} + \frac{\partial h\rho u^2}{\partial x} + \frac{\partial h\rho uv}{\partial y} + \frac{\partial}{\partial x}\left[\frac{1}{2}g(\rho - \rho_a)h^2\right] = u_{\text{ent}}\rho_a u_a \tag{D.3}$$

$$\frac{\partial h\rho v}{\partial t} + \frac{\partial h\rho uv}{\partial x} + \frac{\partial h\rho v^2}{\partial y} + \frac{\partial}{\partial y}\left[\frac{1}{2}g(\rho - \rho_a)h^2\right] = u_{\text{ent}}\rho_a v_a \tag{D.4}$$

where (u_a, v_a) is the ambient fluid speed and u_{ent} the entrainment rate. Equations D.1 and D.3 may be combined to give

$$\frac{\partial h\rho}{\partial t} + \frac{\partial h\rho u}{\partial x} + \frac{\partial h\rho v}{\partial y} = u_{\text{ent}}\rho_a. \tag{D.5}$$

Equation D.3 gives

$$u\frac{\partial h\rho}{\partial y} + h\rho\frac{\partial u}{\partial t} + u\frac{\partial h\rho u}{\partial x} + h\rho u\frac{\partial u}{\partial x} + u\frac{\partial h\rho v}{\partial y} + h\rho v\frac{\partial u}{\partial y} + \frac{\partial P}{\partial x} = u_{\text{ent}}\rho_a u_a \tag{D.6}$$

where $P = \frac{1}{2}g(\rho - \rho_a)h^2$. Equation D.6 may be rearranged:

$$h\rho\left(\frac{\partial u}{\partial t} + u\frac{\partial u}{\partial x} + v\frac{\partial u}{\partial y}\right) + u\left(\frac{\partial h\rho}{\partial t} + \frac{\partial h\rho u}{\partial x} + \frac{\partial h\rho v}{\partial y}\right) + \frac{\partial P}{\partial x} = u_{\text{ent}}\rho_a u_a \quad \text{(D.7)}$$

and equation D.5 shows

$$h\rho\left(\frac{\partial u}{\partial t} + u\frac{\partial u}{\partial x} + v\frac{\partial u}{\partial y}\right) + u(u_{\text{ent}}\rho_a) + \frac{\partial P}{\partial x} = u_{\text{ent}}\rho_a u_a. \quad \text{(D.8)}$$

D.3 Potential energy

Noting that $P = \frac{1}{2}g(\rho - \rho_a)h^2$ is the potential energy per unit area,

$$L = \frac{\partial P}{\partial t} + \nabla \cdot (\mathbf{u}P) \quad \text{(D.9)}$$

is the rate of creation of potential energy per unit time and unit area in an infinitesimal control volume.

$$\begin{aligned}
L &= \frac{\partial P}{\partial t} + \frac{\partial uP}{\partial x} + \frac{\partial vP}{\partial y} && \text{(D.10)}\\
&= \frac{\partial}{\partial t}\left[\frac{1}{2}g(\rho - \rho_a)h^2\right] + \frac{\partial}{\partial x}\left[u\frac{1}{2}g(\rho - \rho_a)h^2\right]\\
&\quad + \frac{\partial}{\partial y}\left[v\frac{1}{2}g(\rho - \rho_a)h^2\right] && \text{(D.11)}\\
&= \frac{1}{2}g\left[h\frac{\partial h(\rho - \rho_a)}{\partial t} + h(\rho - \rho_a)\frac{\partial h}{\partial t}\right. && \text{(D.12)}\\
&\quad + h\frac{\partial h(\rho - \rho_a)u}{\partial x} + h(\rho - \rho_a)u\frac{\partial h}{\partial x} && \text{(D.13)}\\
&\quad \left. + h\frac{\partial h(\rho - \rho_a)v}{\partial y} + h(\rho - \rho_a)v\frac{\partial h}{\partial y}\right] && \text{(D.14)}\\
&= \frac{1}{2}g\left[h.0 + h(\rho - \rho_a)\left\{\frac{\partial h}{\partial t} + u\frac{\partial h}{\partial x} + v\frac{\partial h}{\partial y}\right\}\right] && \text{(D.15)}\\
&= \frac{1}{2}gh(\rho - \rho_a)\left\{\frac{\partial h}{\partial t} + \frac{\partial hu}{\partial x} + \frac{\partial hv}{\partial y} - h\frac{\partial u}{\partial x} - h\frac{\partial v}{\partial y}\right\} && \text{(D.16)}\\
&= \frac{1}{2}gh(\rho - \rho_a)\left(u_{\text{ent}} - h\frac{\partial u}{\partial x} - h\frac{\partial v}{\partial y}\right) && \text{(D.17)}\\
&= \frac{u_{\text{ent}}P}{h} - P\nabla \cdot \mathbf{u} && \text{(D.18)}
\end{aligned}$$

Note that the derivation of equation D.18 requires only the volume and buoyancy conservation equations D.1 and D.3 (and not the momentum equations).

D.4 Kinetic energy

Defining $K = K_x + K_y = \frac{1}{2}\rho h u^2 + \frac{1}{2}\rho h v^2$ as the kinetic energy per unit area of a shallow water flow, then

$$
\begin{aligned}
M_x &= \frac{\partial K_x}{\partial t} + \nabla \cdot (\mathbf{u} K_x) && \text{(D.19)}\\
&= \frac{\partial}{\partial t}\left(\frac{1}{2}h\rho u^2\right) + \frac{\partial}{\partial x}\left(\frac{1}{2}h\rho u^3\right) + \frac{\partial}{\partial y}\left(\frac{1}{2}h\rho u^2 v\right) && \text{(D.20)}\\
&= \frac{1}{2}\left[u\frac{\partial h\rho u}{\partial t} + h\rho u\frac{\partial u}{\partial t} + u\frac{\partial h\rho u^2}{\partial x} + h\rho u^2\frac{\partial u}{\partial x}\right.\\
&\quad \left. + u\frac{\partial h\rho u v}{\partial y} + h\rho u v\frac{\partial u}{\partial y}\right] && \text{(D.21)}\\
&= \frac{1}{2}\left[u\left\{\frac{\partial h\rho u}{\partial t} + \frac{\partial h\rho u^2}{\partial x} + \frac{\partial h\rho u v}{\partial y}\right\}\right.\\
&\quad \left. + h\rho u\left\{\frac{\partial u}{\partial t} + u\frac{\partial u}{\partial x} + v\frac{\partial u}{\partial y}\right\}\right] && \text{(D.22)}\\
&= \frac{1}{2}u(u_{\text{ent}}\rho_a u_a - \frac{\partial P}{\partial x}) + \frac{1}{2}u\left(u_{\text{ent}}\rho_a u_a - \frac{\partial P}{\partial x} - u u_{\text{ent}}\rho_a\right) && \text{(D.23)}\\
&= u_{\text{ent}}\rho_a u u_a - u\frac{\partial P}{\partial x} - \frac{1}{2}u_{\text{ent}}\rho_a u^2. && \text{(D.24)}
\end{aligned}
$$

Similarly,

$$M_y = u_{\text{ent}}\rho_a v v_a - v\frac{\partial P}{\partial y} - \frac{1}{2}u_{\text{ent}}\rho_a v^2 \qquad \text{(D.25)}$$

and so

$$
\begin{aligned}
M_x + M_y &= -u\frac{\partial P}{\partial x} - v\frac{\partial P}{\partial y}\\
&\quad + \frac{1}{2}u_{\text{ent}}\rho_a\left(u_a^2 + v_a^2 - (u-u_a)^2 - (v-v_a)^2\right) && \text{(D.26)}\\
&= -\mathbf{u}\cdot\nabla P + \frac{1}{2}u_{\text{ent}}\rho_a|\mathbf{u}_a|^2 - \frac{1}{2}u_{\text{ent}}\rho_a|\mathbf{u}-\mathbf{u}_a|^2. && \text{(D.27)}
\end{aligned}
$$

Combination of equations D.18 and D.27 gives

$$\frac{\partial E}{\partial t} + \nabla\cdot(\mathbf{u}E) + \nabla\cdot(\mathbf{u}P) = \frac{1}{2}g\Delta\rho h u_{\text{ent}} + \frac{1}{2}u_{\text{ent}}\rho_a|\mathbf{u}_a|^2 - \frac{1}{2}u_{\text{ent}}\rho_a|\mathbf{u}-\mathbf{u}_a|^2. \qquad \text{(D.28)}$$

Physical interpretation of equation D.28 is straightforward. If equation D.28 is integrated over a control volume and Gauss' theorem applied, then the first and second terms on the left hand side correspond to the rate of change of energy within the volume, and the flux into the volume respectively. The third term corresponds

to the work done by adjacent fluid on the control volume ($\int_{\partial V} p\mathbf{v} \cdot d\mathbf{S}$, where p is the pressure and $d\mathbf{S}$ is normal to the surface of V).

The first term on the right hand side is the potential energy gained per unit time by virtue of raising the center of gravity of the layer; the second term is the kinetic energy of the entrained air; and the third term is the energy that is dissipated on entrainment, as in an inelastic collision.

Equation D.28 has some interesting consequences. Setting $\mathbf{u}_a = 0$ and writing $u = |\mathbf{u}|$, we see that

$$\frac{\partial E}{\partial t} + \nabla \cdot (\mathbf{u}E) + \nabla \cdot (\mathbf{u}P) = \frac{1}{2} g \Delta\rho h u_{\text{ent}} - \frac{1}{2} u_{\text{ent}} \rho_a |u|^2 \tag{D.29}$$

$$= \frac{u_{\text{ent}}}{2} \rho_a u^2 \left(\frac{g'h}{u^2} - 1 \right). \tag{D.30}$$

As the term on the right hand side may not be greater than zero, it is the case that $g'h > u^2$ implies $u_{\text{ent}} = 0$. Thus entrainment is energetically forbidden if $Fr = u/\sqrt{g'h} < 1$.

Appendix E

Steady solutions to the shallow water equations

E.1 Outline

A discussion of properties of solutions to the shallow water equations in one dimension follows. It is shown that uniform motion solutions to the resisted shallow water equations are unstable to certain small perturbations at Froude numbers greater than unity. A study of the steady state shallow water equations is also presented, and it is shown that no (nontrivial) stable steady solution exists for shallow water motion over a slope. The relationship between this solution and Helmholtz instability is discussed.

E.2 Stability analysis for uniform motion solutions to the resisted shallow water equations

The resisted shallow water equations considered in chapter 4 of the present thesis allow a simple solution over a horizontal boundary: that of uniform motion. The depth of the current may be denoted h_0 and the speed u_0. The density ρ is also a constant. Such a solution is amenable to a simple stability analysis. Here, it is carried out in a frame of reference such that the current is at rest and the ambient fluid moves at speed $u_a(= -u_0)$.

If the perturbation is such that the buoyancy per unit length is unaltered (caused by, for example, the entrainment of a small amount of ambient fluid) then the state of the fluid at $t = 0$ may be described as follows:

$$\begin{aligned} h(x,0) &= h_0 + \eta(x) \\ \rho(x,0) &= \rho - \frac{\eta}{h_0}(\rho - \rho_a) \end{aligned}$$

$$u(x,0) = 0$$

It is convenient to consider perturbations of the form $\eta(x) = (h\delta).H(x)$, where $H(x)$ is the Heaviside step function ($H(x) = 0$ for $x < 0$ and 1 otherwise). Here, $\delta > 0$.

If the resisted shallow water equations are applied in integrated form to a small region surrounding $x = 0$, it is seen that a net restoring force (that is, to the left) of magnitude $\frac{1}{2}h\delta\rho_a u_a^2(R-1)$ is generated. Here, $R = g\Delta\rho h/\rho_a u_a^2$ is a Richardson number. It is clear from this that Froude numbers higher than unity imply instability to small disturbances of the form indicated. The Froude number used in this analysis is most useful in the context of the Boussinesq approximation.

If the speed of the ambient fluid is allowed to vary with height (such as a logarithmic velocity profile seen in the atmospheric boundary layer), then the instability indicated above becomes more acute: as x increases, so does u_a.

It is clear that uniform shallow water solutions with $Fr > 1$ are unstable to small perturbations, which will grow with time.

E.3 Stable solutions to the shallow water equations on slopes

It has been shown in chapter 4 that a steady hydraulic jump is not a solution to the shallow water equations: a hydraulic jump dissipates energy, and the shallow water equations conserve energy.

The argument above is here extended to motion on a slope. It will be assumed that $F < 1$; for, as shown above, $F > 1$ implies instability to small perturbations and stable solutions are investigated here. The restriction to $F < 1$ forces the entrainment to be zero, as shown in appendix C.

The interaction between dense current and ambient fluid is zero because the ambient fluid is stationary and the flow steady.

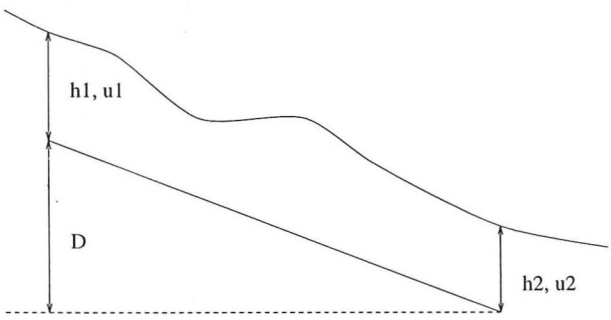

Figure E.1: Shallow water flow over a slope

With the terminology shown on figure E.1, the equations representing volume, momentum, and energy change in the volume shown are

$$h_1 u_1 = h_2 u_2 \tag{E.1}$$

$$h_1 \rho u_1^2 + \frac{1}{2} g \Delta\rho((h_1 + D)^2 - h_2^2) = h_2 \rho u_2^2 \tag{E.2}$$

$$g\Delta\rho(h_2^2 u_2 - h_1^2 u_1) + \frac{1}{2}\rho(h_2 u_2^3 - h_1 u_1^3) = Dg\Delta\rho h u \tag{E.3}$$

Here, the first term in equation E.2 is simplified by the constant density of the current. These equations are inconsistent[1] except for $Du_1 = 0$. If $D = 0$, then $u_1 = u_2$ (uniform flow over horizontal ground); and if $u_1 = 0$ the system is at rest.

It is therefore the case that steady shallow water flow over a slope (positive or negative) is not possible with $F < 1$; and $F > 1$ implies instability to small perturbations.

If a widening current is considered (uniform in cross section), then the right hand sides of equations E.1 to E.3 will be multiplied by a width factor w and the same arguments apply.

It has been shown here that the shallow water equations have no steady, stable solutions except for the special cases of uniform motion over horizontal ground with $F < 1$, and zero speed flow (with a horizontal free surface). No non-stationary flows over a slope are steady and stable.

E.4 Helmholtz instability

Helmholtz, or Kelvin-Helmholtz, instabilities occur at the interface of two fluids in relative motion of different densities [199]. Capillary terms are discarded here.

Two dimensional motion is considered, the effects of viscosity are neglected, and small oscillations about a state of steady motion are considered. The speeds and densities of the lower and upper surface being U and U', and ρ and ρ', respectively.

Lamb [118] considered waves of frequency σ and wavenumber k, and identified complex values of σ with an unstable boundary; the condition for instability was $k\rho\rho'(U - U')^2 > g(\rho^2 - \rho'^2)$.

The difference between the shallow water analysis above and Helmholtz instabilities is that the length scale is the reciprocal of wavenumber in Helmholtz' analysis, and depth of fluid in the shallow water analysis.

[1] Equations E.1 and E.3 are over-specified: three equations specify two unknowns (h_2 and u_2). One of the implications of this set of equations is that $h_2 = h_1 + D$ (that is, a horizontal free surface). But equation E.2 and E.1 then imply $Du_1 = 0$.

Appendix F

Case study

F.1 Outline

The model developed in this thesis is used here to simulate a hypothetical release of chlorine from a real chemical installation surrounded by complex terrain. The results are taken from an investigation carried out by the present author [84]. This case study gives some indication of the effect of the terrain at the site.

F.2 Source terms and meteorology

The release scenarios used were determined using a 'cautious best estimate' philosophy: the releases considered represented a pessimistic view of those possible. The wind bearings considered (225° and 300°) are worst-case: population centres exist that would be directly downwind under these conditions.

Here, instantaneous releases are considered: a full 80 te tank undergoes catastrophic failure, releasing its contents immediately. Two weather categories were simulated, $\mathcal{D}5$ and $\mathcal{F}2$ (these are the weather categories considered by default in the QRA tool RISKAT as used by HSE [150]).

Figure F.1 shows a perspective view of the terrain used.[1] This terrain is not easily decomposed into elementary features such as slopes or valleys, and the only reasonable representation available appears to be a Cartesian array of altitudes.

F.3 Results

The results presented are in the form of perspective views of the terrain, with regions experiencing the HSE dangerous dose of 108 000 ppm^2min or above shown in dark (figures F.2 to F.5).

[1]The work used Ordnance Survey digital terrain data for which the OS hold the copyright.

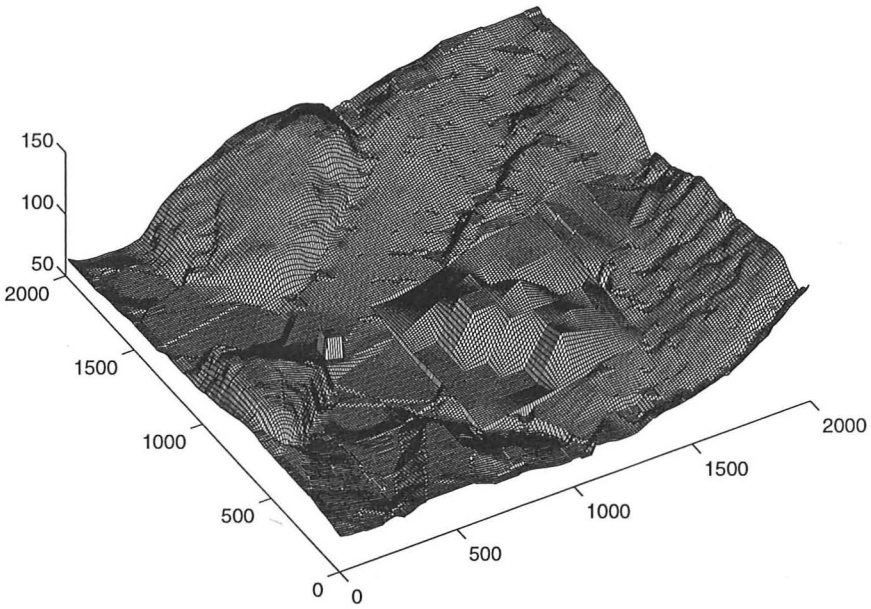

Figure F.1: Perspective map of terrain surrounding source; altitude and horizontal coordinates shown in metres, closest point is the south west corner of the domain. Source is visible as a small square at $(500, 1000)$

Overall, it was found that the effect of terrain is more pronounced in the lower wind conditions of $\mathcal{F}2$ weather. This is because less energy is available in the boundary layer to lift the cloud over terrain features.

F.3.1 Results: $\mathcal{F}2$ weather

In $\mathcal{F}2$ weather, both wind directions gave cloud paths that were strongly affected by the terrain:

- In the case of a wind bearing of 225°, the HSE dangerous dose is strongly correlated with terrain features such as drainage routes and shallow valley-type depressions (figure F.2).
- In the case of a wind bearing of 300°, the large terrain feature immediately downwind of the release point clearly exerts an effect on the behaviour of the cloud, which becomes bifurcated (figure F.3). The HSE dangerous dose contour becomes annular in shape with the high ground being relatively safer.

F.3.2 Results: $\mathcal{D}5$ weather

In the case of $\mathcal{D}5$ weather, the effect of the terrain is much less severe.

- In the case of a wind bearing of 225°, the HSE dangerous dose is not experienced on the high ground to the north of the release (figure F.4). The cloud appears to be channelled by the shallow valley leading to the northeast and is narrower than in the flat ground case.
- In the case of a wind bearing of 300°, the terrain feature immediately downwind of the release point becomes of less importance and the cloud appears to travel over it with no deflection (figure F.5).

F.4 Discussion

Differences between the figures are hard to quantify, but qualitative observations include:

- In $\mathcal{F}2$ conditions, the terrain exerts a far more significant effect on the cloud than in $\mathcal{D}5$. This is because the increase in potential energy required for the cloud to ascend a slope is more readily available in high windspeeds.
- There is a large region of high ground around which the cloud flows in $\mathcal{F}2$ conditions (Britter, writing in 1982 [22] explicitly anticipated this type of behaviour).

- The lateral spread of the cloud is increased at the low windspeed; the outline is apparently affected by the valley-type terrain feature leading to the Northeast of the release point.

F.5 Conclusions

This appendix has shown that the present model may be applied to a real case study. The main conclusions were not unexpected: terrain effects are much more important in low windspeeds; and, in low wind conditions, dense gas is channelled into low-lying areas, with high ground being relatively protected.

Figures F.2 to F.5 show that terrain may exert a significant effect on risk assessment.

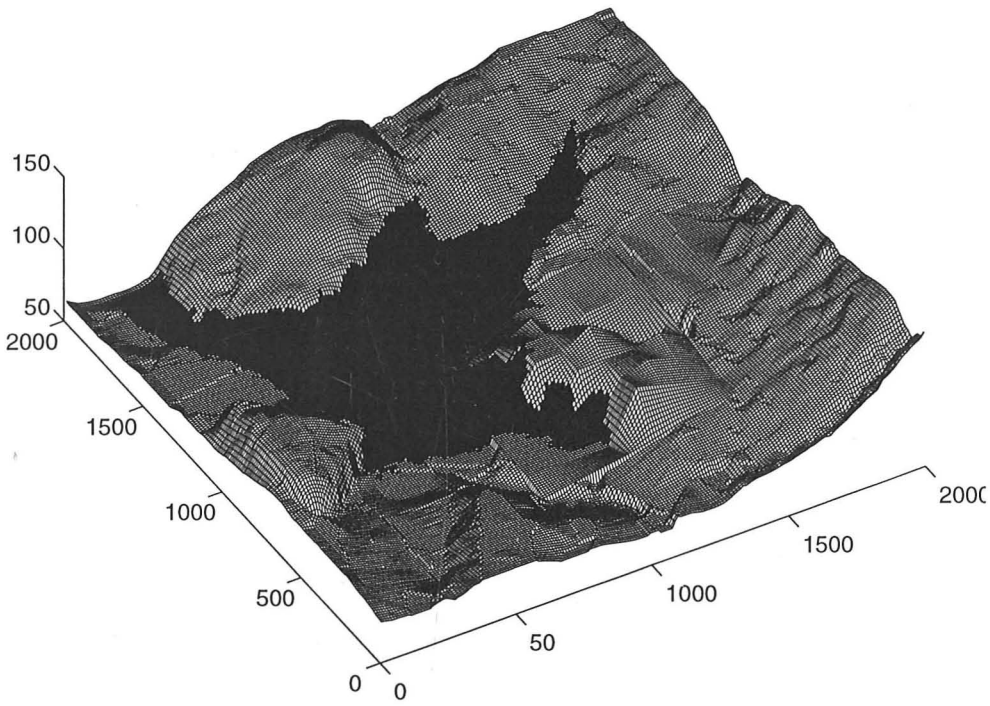

Figure F.2: Perspective view of hazard site; regions experiencing the HSE dangerous dose 108000 ppm^{2}min (or above) shown in dark; $\mathcal{F}2$ weather, wind bearing 225°

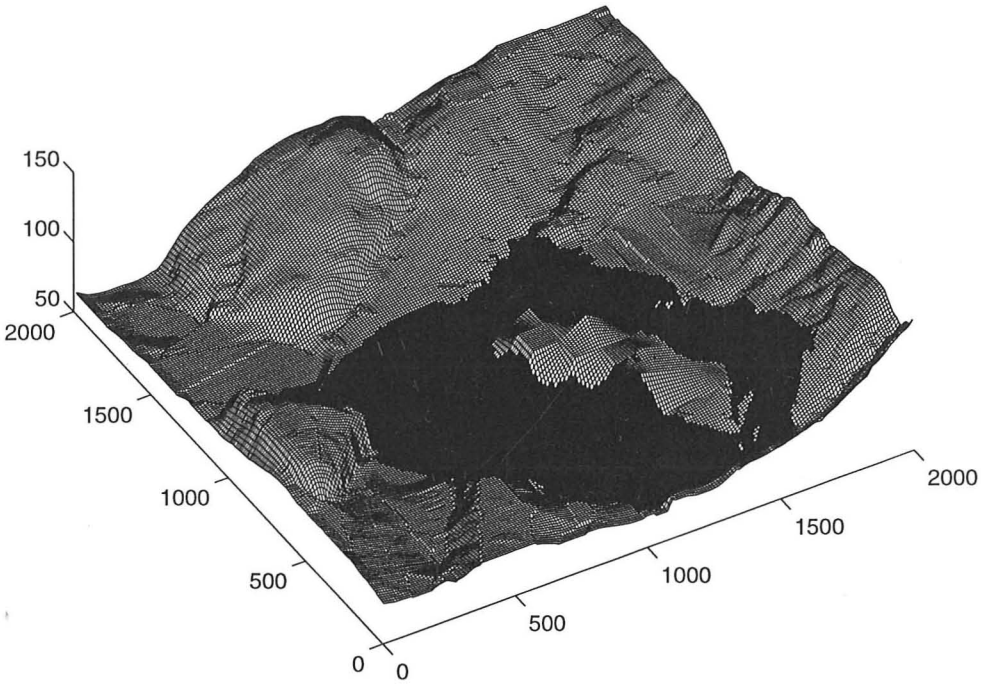

Figure F.3: Perspective view of hazard site; regions experiencing the HSE dangerous dose 108000 $\mathrm{ppm}^2\mathrm{min}$ (or above) shown in dark; $\mathcal{F}2$ weather, wind bearing 300°

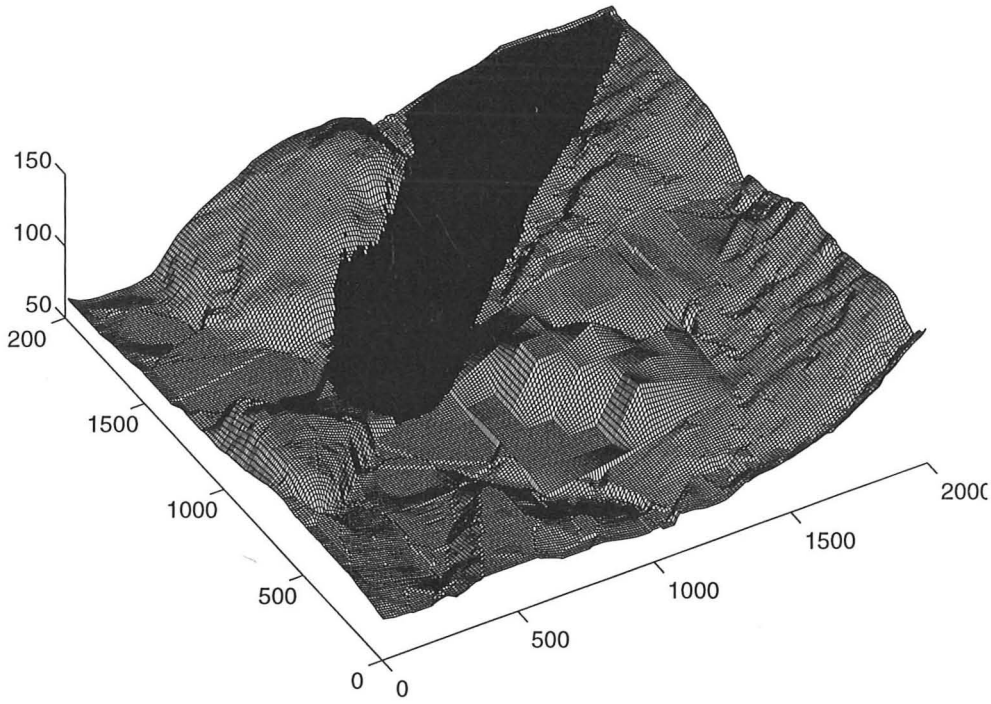

Figure F.4: Perspective view of hazard site; regions experiencing the HSE dangerous dose 108000 ppm^{2}min (or above) shown in dark; $\mathcal{D}5$ weather, wind bearing 225°

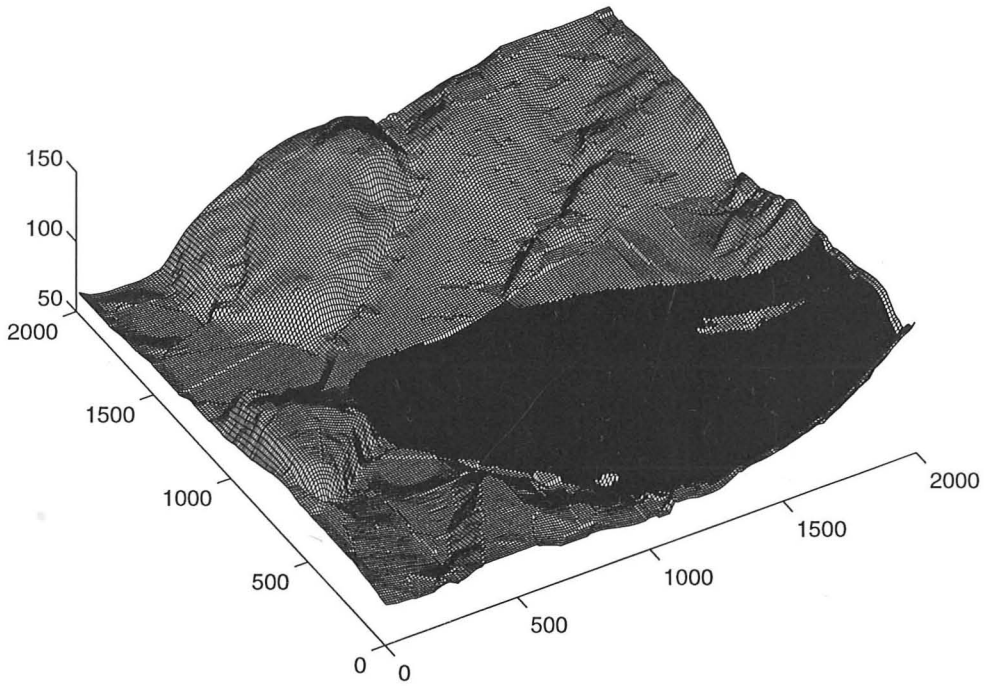

Figure F.5: Perspective view of hazard site; regions experiencing the HSE dangerous dose 108000 ppm^{2}min (or above) shown in dark; $\mathcal{D}5$ weather, wind bearing 300°

Bibliography

[1] M. Abramowitz and I. A. Stegun. *Handbook of mathematical functions with formulas, graphs and mathematical tables (AMS-55).* National Bureau of Standards, 1965.

[2] H. J. Adshead. Avalanche flows: an investigation of the lateral spread of a gravity current moving down an inclined plane, March 1988. Cambridge University Engineering Tripos Part two project report. Supervisor: R. E. Britter.

[3] V. Alavian. Behaviour of density currents on an incline. *Journal of Hydraulic Engineering*, 112(1):27–43, 1986.

[4] G. Alexeeff, D. Lewis, and M. Lipsett. Use of toxicity information in risk assessment for accidental releases of toxic gases. *Journal of Hazardous Materials*, 29:387–403, 1992.

[5] J. M. R. Apraiz. Topics on dense gas dispersion turbulent density interfaces; final report to the Health and Safety Executive, 1990.

[6] P. G. Baines. *Topographic effects in stratified flows.* Cambridge University Press, 1996.

[7] G. K. Batchelor. *An Introduction to Fluid Dynamics.* Cambridge University Press, 1990.

[8] P. J. Baxter and M. Kapila. Acute health impact of the gas release at Lake Nyos, Cameroon, 1986. *Journal of Volcanology and Geothermal Research*, 39:265–275, 1989.

[9] P. J. Baxter, M. Kapila, and D. Mfondu. Lake Nyos disaster, Cameroon, 1986: the medical effects of large scale emission of carbon dioxide? *British Medical Journal*, 298:1437–1441, May 1989.

[10] T. B. Benjamin. Gravity currents and related phenomena. *Journal of Fluid Mechanics*, 31(2):209–248, 1968.

[11] D. N. Blewitt et al. Conduct of anhydrous hydrofluoric acid spill experiments. In J. Woodward, editor, *Proceedings of the International Conference on Vapour Cloud Modelling*, pages 1–38, 1987.

[12] F. Bo Pedersen. *A Monograph on Turbulent Entrainment and Friction in Two- Layer Stratified Flow: Series Paper 25.* Institute of Hydrodynamics and Hydraulic Engineering, Technical University of Denmark, April 1980.

[13] P. Bordeau and G. Green, editors. *Methods for Assessing and Reducing Injury from Chemical Accidents.* John Wiley and Sons Ltd, 1989.

[14] J. P. Boris and D. L. Book. Flux-corrected transport 1. SHASTA, a fluid transport algorithm that works. *Journal of Computational Physics*, 11:38–69, 1973.

[15] J. P. Boris and D. L. Book. Flux-corrected transport 3. Minimal-error FCT algorithms. *Journal of Computational Physics*, 20:297 et seq, 1976.

[16] J. P. Boris, D. L. Book, and K. Hain. Flux-corrected transport 2. Generalisations of the method. *Journal of Computational Physics*, 18:248–283, 1975.

[17] J. Brandeis and D. L. Ermak. Numerical simulation of liquefied fuel spills 2. Instantaneous and continuous LNG spills on an unconfined water surface. Technical Report UCRL-87205-2, Lawrence Livermore National Laboratory, P. O. Box 808, L-451, Livermore, California 94550, 1982.

[18] J. Brandeis and E. J. Kansa. Numerical simulation of liquified fuel spills: 1. instantaneous release into a confined area. Technical Report UCRL-87205-1, Lawrence Livermore National Laboratory, P.O. Box 808, L-451, Livermore, California 94550, February 1982.

[19] P. W. M. Brighton, S. J. Jones, D. Martin, D. M. Webber, and T. Wren. The effects of natural and man-made obstacles on heavy gas dispersion. Report summary. Technical Report SRD/CEC/22938/00, AEA Technology, Wigshaw Lane, Culcheth, Cheshire, WA3 4NE, June 1991.

[20] P. W. M. Brighton, S. J. Jones, and T. Wren. The effects of natural and man-made obstacles on heavy gas dispersion. Part one: Review of earlier data. Technical Report SRD/CEC/22938/01, AEA Technology, Wigshaw Lane, Culcheth, Cheshire, WA3 4NE, June 1991.

[21] R. E. Britter. The spread of a negatively buoyant plume in a calm environment. *Atmospheric Environment*, 13:1241–1247, 1979.

[22] R. E. Britter. Special topics on dispersion of dense gases. report on contract. Technical Report 1200/01.01, Research and Laboratory Services Division, Health and Safety Executive, Broad Lane, Sheffield S3 7HQ, 1982.

[23] R. E. Britter. A review of some mixing experiments relevant to dense gas dispersion. In J. S. Puttock, editor, *Stably stratified flow and dense gas dispersion*, pages 1–38. Oxford, 1988.

[24] R. E. Britter. *Air Pollution and its Application VII*, chapter Modelling dispersion from accidental releases, pages 39–52. Plenum Press, 1989.

[25] R. E. Britter. Atmospheric dispersion of dense gases. *Annual Review of Fluid Mechanics*, 21:317–344, 1989.

[26] R. E. Britter. The evaluation of technical models used for major-accident hazard installations; report to Commision of the European Communities Directorate General XII. Technical report, Department of Engineering, University of Cambridge, Trumpington Street, Cambridge CB2 1PZ, United Kingdom, 1991.

[27] R. E. Britter. The evaluation of technical models used for major-accident hazard installations. Technical Report EUR 1477EN, Commission of the European Communities Directorate-General XII Science, Research and Development, January 1993.

[28] R. E. Britter, R. P. Cleaver, and M. G. Cooper. Development of a simple model for the dispersion of denser-than-air vapour clouds over real terrain. Technical Report MRS E 622, British Gas, Research and Technology, Midlands Research Station, Wharf Lane, Solihull, B91 2JW, May 1991.

[29] R. E. Britter and P. F. Linden. The motion of the front of a gravity current travelling down an incline. *Journal of Fluid Mechanics*, 99(3):531–543, 1980.

[30] R. E. Britter and J. McQuaid. *Workbook on the Dispersion of Dense Gases.* HMSO, 1988.

[31] R. E. Britter and J. E. Simpson. Experiments on the dynamics of a gravity current head. *Journal of Fluid Mechanics*, 88(2):223–240, 1978.

[32] R. E. Britter and W. H. Snyder. Fluid modelling of dense gas dispersion over a ramp. *Journal of Hazardous Materials*, 18:37–67, 1988.

[33] M. A. Brown. The effect of uphill slopes on mixing in turbulent gravity currents. In *Mixing and dispersion in stably stratified flows—Proceedings of the 5th IMA conference on stably stratified flows, Dundee.* Oxford, September 1966.

[34] Cambridge Environmental Research Consultants. GASTAR users' manual, 1994.

[35] K. K. Carn et al. Analysis of Thorney Island data: variability and box models. In J. S. Puttock, editor, *Stably stratified flow and dense gas dispersion*, pages 205–231. Oxford, 1988.

[36] S. T. Chan and D. L. Ermak. Recent progress in modeling the atmospheric dispersion of heavy gases over variable terrain using the three-dimensional conservation equations. Technical Report UCRL-88495, Lawrence Livermore Laboratory, University of California, Livermore, California, 94550, USA, August 1983.

[37] S. T. Chan, H. C. Rodean, and D. L. Ermak. Numerical simulations of atmospheric releases of heavy gases over variable terrain. Technical Report UCRL-87256, Lawrence Livermore Laboratory, University of California, Livermore, California, 94550, USA, August 1982.

[38] P. C. Chatwin. The use of statistics in describing and predicting the effects of dispersing dense gas clouds. *Journal of Hazardous Materials*, 6:213–230, July 1982.

[39] D. P. Chock. A comparison of numerical methods for solving the advection equation, part 2. *Atmospheric Environment*, 19(4):571–586, 1985.

[40] D. P. Chock and A. M. Dunker. A comparison of numerical methods for solving the advection equation. *Atmospheric Environment*, 17(1):11–24, 1983.

[41] R. P. Cleaver et al. Further development of a model for dense gas dispersion over real terrain. *Journal of Hazardous Materials*, 40:85–108, 1995.

[42] N. Collings and M. Peckham. FID capillary flow theory. In *Fast response flame ionization detector—measuring hydrocarbon emissions from IC engines*. Institution of Mechanical Engineers,1 Birdcage Walk, London SW1H 9JJ, March 1994. Organized by the Energy Transfer and Thermofluid Mechanics Group; Seminar S245.

[43] R. Courant and K. O. Friedrichs. *Supersonic Flow and Shock Waves*. New York: Interscience, 1948.

[44] P. F. Crapper and P. F. Linden. The structure of turbulent density interfaces. *Journal of Fluid Mechanics*, 65:45–63, 1974.

[45] J. K. W. Davies. Discussion: hazardous gas model evaulation with field observations [86]. *Atmospheric Environment*, 29(3):456–458, 1995.

[46] J. K. W. Davies. Personal communication, 1996.

[47] J. W. Deardoff. A multi-limit mixed-layer entrainment formulation. *Journal of Physical Oceanography*, 13:988–1002, 1983.

[48] D. M. Deaves. Development and application of heavy gas dispersion models of varying complexity. *Journal of Hazardous Materials*, 16:427–438, 1987.

[49] D. A. Edwards et al. On experimental reflected density currents and the interpretation of certain turbidites. *Sedimentology*, 41:437–461, 1994.

[50] B. Efron. *The jackknife, the bootstrap and other resampling plans.* J. W. Arrowsmith, 1982.

[51] K. J. Eidsvik. A model for heavy gas dispersion in the atmosphere. *Atmospheric Environment*, 14:769–777, 1980.

[52] T. H. Ellison and J. S. Turner. Turbulent entrainment in stratified flows. *Journal of Fluid Mechanics*, 6(3), October 1959.

[53] D. L. Ermak et al. Heavy gas dispersion test summary report. Technical Report UCRL-21210; ESL-TR-88-22, Lawrence Livermore Laboratory, University of California, Livermore, California, 94550, USA, October 1988.

[54] R. A. Falconer. A mathematical model study of the flushing characteristics of a shallow tidal bay. *Proceedings of the Institution of Civil Engineers*, 77(2):311–332, September 1984.

[55] R. A. Falconer. Residual currents in Port Talbot Harbour: a mathematical model study. *Proceedings of the Institution of Civil Engineers*, 79(2):33–53, March 1985.

[56] H. J. Fernando. Turbulent mixing in stratified fluids. *Annual Review of Fluid Mechanics*, 23:455–493, 1991.

[57] C. Flokstra. The closure problem for depth-averaged two-dimensional flow, paper A106. In *17th Congress of the International Association for Hydraulic Research, Baden-Baden, Germany*, volume 2, pages 247–256, 1977.

[58] M. G. G. Foreman. A two-dimensional dispersion analysis of selected methods for solving the linearized shallow water equations. *Journal of Computational Physics*, 56:287–323, 1984.

[59] S. J. Freeth. The deadly cloud hanging over Cameroon. *New Scientist*, pages 23–27, 15 August 1992.

[60] S. J. Freeth and R. L. F. Kay. The Lake Nyos gas disaster. *Nature*, 325:104–105, January 1987.

[61] L. S. Fryer and G. D. Kaiser. DENZ—a computer program for the calculation of the dispersion of dense toxic or explosive gases in the atmosphere. Technical Report SRD R 152, Safety and Reliability Directorate, 1979.

[62] J. R. Garrat. *The atmospheric boundary layer.* Cambridge University Press, 1992.

[63] B. V. Georgiev. Some experimental investigation on turbulent characteristics of stratified flow. In *International Symposium on Stratified Flows, Novosibirsk*, pages 507–514, 1972.

[64] A. E. Gill. *Atmosphere - Ocean Dynamics.* Academic Press, 1982.

[65] D. Gillespie. *Calc manual: GNU Emacs Calc version 2.02*, 1992. Copyright Free Software Foundation.

[66] F. R. Gilmore, M. S. Plessey, and H. E. Crossley, Jr. The analogy between hydraulic jumps in liquids and shock waves in gases. *Journal of Applied Physics*, 21:243–249, March 1950.

[67] H. P. Gröbelbauer. *Experimental study on the dispersion of instantaneously released dense gas clouds.* PhD thesis, Swiss Federal Institute of Technology, Zurich, 1995.

[68] H. P. Gröbelbauer, T. K. Fanneløp, and R. E. Britter. The propagation of intrusion fronts of high density ratios. *Journal of Fluid Mechanics*, 250:669–687, 1993.

[69] R. E. Grundy and J. W. Rottman. The approach to self-similarity of the solutions of the shallow-water equations representing gravity-current releases. *Journal of Fluid Mechanics*, 156:39–53, 1985.

[70] R. E. Grundy and J. W. Rottman. Self-similar solutions of the shallow-water equations representing gravity currents with variable inflow. *Journal of Fluid Mechanics*, 169:337–351, 1986.

[71] C. P. Guldemond. The behaviour of denser than air ammonia in the presence of obstacles—wind tunnel experiments. *Plant/Operations Progress*, 5(2):93–96, April 1986.

[72] M. Habashi. Thermodynamics and fluid mechanics of volcanic plumes, April 1990. Engineering Tripos Part Two project report. Supervisor: R. E. Britter.

[73] D. J. Hall, C. F. Barret, and M. O. Ralph. Experiments on a model of an escape of heavy gas. Technical Report LR 217 (AP), Warren Spring Laboratory, Gunnels Wood Road, Stevenage, Hertfordshire SG1 2BX, November 1975.

[74] D. J. Hall et al. Repeat variability in instantaneously released heavy gas clouds—some wind tunnel model experiments. Technical Report LR 804 (PA), Warren Spring Laboratory, Gunnels Wood Road, Stevenage, Hertfordshire SG1 2BX, 1991(?).

[75] D. J. Hall, E. J. Hollis, and H. Ishak. A wind tunnel model of the Porton dense gas spill field trials. Technical Report LR 394(AP), Warren Spring Laboratory, Department of Industry, PO Box 20, Gunnels Wood Road, Stevenage, Hertfordshire SG1 2BX, 1982.

[76] D. J. Hall, E. J. Hollis, and H. Ishaq. A wind tunnel report of the Porton Down dense gas spill field trials. Technical Report LR 394 (AP), Warren Spring Laboratory, Department of Industry, PO Box 20, Gunnels Wood Road, Stevenage, Hertfordshire SG1 2BX, 1980(?).

[77] D. J. Hall and R. A. Waters. Investigation of two features of continuously released heavy gas plumes. Technical Report LR 707 (PA)M, Warren Spring Laboratory, Gunnels Wood Road, Stevenage, Hertfordshire SG1 2BX, January 1989.

[78] M. A. Hallworth et al. Entrainment into two-dimensional and axisymmetric turbulent gravity currents. *Journal of Fluid Mechanics*, 308:289–311, 1996.

[79] R. K. S. Hankin. A literature review of generic failure rates and a comparison with the failure rates used in RISKAT. Technical Report IR/L/HA/91/4, Health and Safety Executive, Broad Lane, Sheffield S3 7HQ, September 1991.

[80] R. K. S. Hankin. Comparison of the TWODEE model against the Mercer et al heavy gas dispersion code comparison exercise. Technical Report RAS/96/19, Health and Safety Laboratory, Broad Lane, Sheffield S3 7HQ, 1996.

[81] R. K. S. Hankin. Further TWODEE validation: the Thorney Island instantaneous release series. Technical Report RAS/96/16, Health and Safety Laboratory, Broad Lane Sheffield S3 7HQ, 1996.

[82] R. K. S. Hankin. Thermal effects in TWODEE: a feasibility study. Technical Report TBA, Health and Safety Laboratory, Broad Lane Sheffield S3 7HQ, 1996.

[83] R. K. S. Hankin and R. E. Britter. The shallow water approximations in dense gas dispersion over complex terrain. In I. P. Castro and N. J. Rockliff, editors, *Proceedings of the 4th IMA Conference on stably stratifed flows: flow and dispersion over topography*, pages 223–245. Clarendon Press, Oxford, 1994.

[84] R. K. S. Hankin and P. Sims. Dense gas dispersion over complex terrain.... Technical Report RAS/96/02, Health and Safety Laboratory, Broad Lane, Sheffield S3 7HQ, 1966.

[85] S. R. Hanna. Confidence limits for air quality model evaluations, as estimated by bootstrap and kackknife resampling methods. *Atmospheric Environment*, 23(6):1385–1398, 1989.

[86] S. R. Hanna, J. C. Chang, and D. G. Strimatis. Hazardous gas model evaluation with field observations. *Atmospheric Environment*, 27A(15):2265–2285, 1993.

[87] S. R. Hanna, D. G. Strimaitis, and J. C. Chang. Evaluation of fourteen hazardous gas models with ammonia and hydrogen fluoride field data. *Journal of Hazardous Materials*, 26(2):127–158, 1991.

[88] S. R. Hanna, D. G. Strimaitis, and J. C. Chang. Hazard response modeling uncertainty (a quantitative method) volume 1: user's guide to software for evaluating hazardous gas dispersion models. Technical Report F08653-89-C-0136, Sigma Research Corporation, 234 Littleton Road, Suite 2E, Westford MA 01886, U. S. A., September 1991.

[89] S. Hartwig. *Heavy gas and risk assessment–II.* D. Reidel, 1982.

[90] A. E. Hay. On the frontal speeds of internal gravity surges on sloping boundaries. *Journal of Geophysical Research*, 88(C1):751–754, January 1983.

[91] Health and Safety Executive. *Canvey: A Second Report.* HMSO, 1981. ISBN 0-11-883618-8.

[92] Health and Safety Executive. Heavy Gas Dispersion Trials: Thorney Island 1982-3, 1983. Databooks for Trials 5-20 (instantaneous); and 45-47 (continuous).

[93] Health and Safety Executive. *Control of industrial major accident hazards regulations.* HMSO, 1984. ISBN 0-11-047902-5.

[94] Health and Safety Executive. *Risk criteria for land-use planning in the vicinity of major industrial hazards.* HMSO, 1988. ISBN 0-11-885491-7.

[95] Health and Safety Executive. *The tolerability of risk from nuclear power stations.* HMSO, 1988. ISBN 0-11-883982-9.

[96] Health and Safety Executive. *Quantified risk assessment: its input to decision making.* HMSO, 1989. ISBN 0-11-885499-2.

[97] F. M. Henderson. *Open Channel Flow.* Macmillan, 1970.

[98] G. F. Hepner and M. V. Finco. Modeling dense gaseous contaminant pathways over complex terrain using a geographic information system. *Journal of Hazardous Materials*, 42:187–199, 1995.

[99] W. H. H. van Heugten and N. J. Duijm. Some findings based on wind tunnel simulation and model calculations of Thorney Island Trial No. 008. *Journal of Hazardous Materials*, 11:409–416, 1985.

[100] C. W. Hirt. Heuristic stability for finite-difference equations. *Journal of Computational Physics*, 2:339–355, 1968.

[101] E. J. Hopfinger. Snow avalanche motion and related phenomena. *Annual Review of Fluid Mechanics*, 15:47–76, 1983.

[102] E. J. Hopfinger and J. C. Tochon-Danguy. A model study of powder-snow avalanches. *Journal of Glaciology*, 19(81):434–356, 1977.

[103] D. P. Hoult. Oil spreading on the sea. *Annual Review of Fluid Mechanics*, 4:341–368, 1972.

[104] N. W. Hurst, R. K. S. Hankin, L. J. Bellamy, and M. J. Wright. Auditing—a European perspective. *Journal of Loss Prevention in the Process Industries*, 7(2):197–200, 1994.

[105] S. F. Jagger. Development of Crunch: a dispersion model for continuous releases of denser-than-air vapour into the atmosphere. Technical Report SRD R 229, Safety and Reliability Directorate, Wigshaw Lane, Culcheth, Warrington WA4 4NE, January 1983.

[106] G. H. Jirka and M. Arita. Density currents or density wedges: boundary-layer influence and control methods. *Journal of Fluid Mechanics*, 177:187–206, 1987.

[107] C. Jones. Personal communication, 1995.

[108] L. H. Kantha. Turbulent entrainment at the density interface of a two-layer stably stratified fluid system. Technical Report GFDL TR 75-1, Department of Earth and Planetary Science, John Hopkins University, 1975.

[109] L. H. Kantha, O. M. Phillips, and R. S. Azad. On turbulent entrainment at a stable density interface. *Journal of Fluid Mechanics*, 79(4):753–768, 1977.

[110] H. Kato and O. M. Phillips. On the penetration of a turbulent layer into a stratified fluid. *Journal of Fluid Mechanics*, 37, 1969.

[111] G. H. Keulegan. Twelfth progress report on model laws for density currents. The motion of saline fronts in still water. Technical Report NBS 0603-11-3519; 5831, National Bureau of Standards, Washington 25, D.C., April 1958.

[112] B. Kneller et al. Oblique reflection of turbidity currents. *Geology*, 14/19:250–252, March 1991.

[113] S. Komori et al. Turbulence structure in stably stratified open-channel flow. *Journal of Fluid Mechanics*, 130:13–26, 1983.

[114] G. König, M. Schatzmann, and A. Lohmeyer. Measurements of gas concentration fluctuations in wind tunnel simulations. In *Proceedings of the 7th International Conference on Wind Engineering, Aachen, FRG*. International Association for Wind Engineering, July 1987.

[115] C. G. Koop and F. K. Broward. Instability and turbulence in a stratified fluid with shear. *Journal of Fluid Mechanics*, 93(1):135–159, 1979.

[116] R. P. Koopman et al. Analysis of Burro series of 40 m^3 LNG spill experiments. *Journal of Hazardous Materials*, 6:43–83, July 1982.

[117] J. Kukkonen and J. Nikmo. Modelling heavy gas cloud transport in sloping terrain. *Journal of Hazardous Materials*, 31:155–176, 1992.

[118] H. Lamb. *Hydrodynamics*. Cambridge University Press, 1932.

[119] J. T. Lee and R. N. Meroney. *Proceedings of the 8th Symposium on Turbulence Diffusion, San Diego*. San Diego, 1988.

[120] B. P. Leonard. A survey of finite differences of opinion on numerical muddling of the incomprehensible defective confusion equation. In *ASME, amd. Finite elements method for convection dominated flows, symposium at the Winter annual meeting of ASME, New York, December 2nd, 1979*, volume 34, pages 1–17, 1979.

[121] P. F. Linden. Mixing across a density interface produced by grid turbulence. *Journal of Fluid Mechanics*, 100(4):691–703, 1980.

[122] P. F. Linden. Personal communication; Ph.D. research proposal, 1996.

[123] P. F. Linden and J. E. Simpson. Buoyancy driven flow through an open door. *Air Infiltration Review*, 6(4):4–5, 1985.

[124] P. F. Linden and J. E. Simpson. Continuous two-dimensional releases from an elevated source. *Journal of loss prevention in the process industries*, 3(1):82–87, 1990.

[125] Q. Liu, D. Schläper, and J. Bühler. Motion of dense thermals on incline. *Journal of Hydraulic Engineering*, 117(12):1588–1599, December 1991.

[126] P. E. Mansell. An investigation of the lateral spread of a gravity current moving down an inclined plane, April 1984. Cambridge University Engineering Tripos Part Two project report. Supervisor: R. E. Britter.

[127] V. C. Marshall. The predictions of human mortality from chemical accidents with especial reference to the lethal toxicity of chlorine. *Journal of Hazardous Materials*, 22(1):13–56, 1989.

[128] J. McQuaid. Objectives and design of the Phase I Heavy Gas Dispersion Trials. *Journal of Hazardous Materials*, 11:1–33, 1985.

[129] J. McQuaid. Design of the Thorney Island continuous release trials. *Journal of Hazardous Materials*, 16:1–8, 1987.

[130] J. McQuaid and B. Roebuck. The dispersion of heavier-than-air gas from a fenced enclosure. Final report to the U.S. Coast Guard on contract with the Health and Safety Executive. Technical Report RPG 1185, Safety Engineering Laboratory, Research and Laboratory Services Division, Broad Lane, Sheffield S3 7HQ, UK, 1985.

[131] E. J. Melia. *The dispersion of dense fluids through arrays of obstacles.* PhD thesis, Cambridge University Engineering Department, Trumpington Street, Cambridge CB2 1PZ, June 1991.

[132] A. Mercer. CEA/AEA Exchange Agreement on external event. Comparison of heavy gas dispersion models for instantaneous releases: final report. Technical Report IR/L/HA/91/6, Health and Safety Executive Research and Laboratory Services Division, Broad Lane, Sheffield S3 7HQ, June 1991.

[133] A. Mercer. A study of the effect of complex terrain on dispersion using GASTAR. 1. Results for Cefn-Mawr. Technical Report IR/RAMS/96/06, Health and Safety Laboratory, Broad Lane, Sheffield S10 1TB, 1996.

[134] A. Mercer. A study of the effect of complex terrain on dispersion using GASTAR, part 2. Results for Castner Kellner. Technical Report IR/RAMS/96/07, Health and Safety Laboratory, Broad Lane, Sheffield S10 1TB, 1996.

[135] A. Mercer. A study of the effect of complex terrain on dispersion using GASTAR, part 3. Results for Stavely. Technical Report IR/RAMS/96/08, Health and Safety Laboratory, Broad Lane, Sheffield S10 1TB, 1996.

[136] A. Mercer and J. K. W. Davies. An analysis of the turbulence records from the Thorney Island continuous release trials. *Journal of Hazardous Materials*, 16:21–42, 1987.

[137] A. Mercer et al. Comparison of heavy gas dispersion models for instantaneous releases. *Journal of Hazardous Materials*, 36:193–208, 1994.

[138] A. Mercer and C. Nussey. The Thorney Island continuous trials: mass and flux balances. *Journal of Hazardous Materials*, 16:9–20, 1987.

[139] R. N. Meroney. Transient characteristics of dense gas dispersion. Part 2: numerical experiments on dense cloud physics. *Journal of Hazardous Materials*, 9:159–170, 1984.

[140] R. N. Meroney. Guidelines for fluid modeling of dense gas cloud dispersion. *Journal of Hazardous Materials*, 17:23–46, 1987.

[141] G. V. Middleton. Experiments on density and turbidity current, part two: uniform flow of density currents. *Canadian Journal of Earth Sciences*, 3:627–637, 1966.

[142] G. V. Middleton. Experiments on density and turbidity currents, part one: motion of the head. *Canadian Journal of Earth Sciences*, 3:5236, 1966.

[143] H. P. Miller. A comparison of high resolution schemes for the two dimensional linear advection equation. *Computers and Fluids*, 14(4):411–422, 1986.

[144] L. M. Milne-Thomson. *Theoretical Hydrodynamics.* Macmillan Education Limited, fifth edition, 1986.

[145] D. L. Morgan Jr., L. K. Morris, and D. L. Ermak. SLAB: a time-dependent computer model for the dispersion of heavy gases released in the atmosphere. Technical Report UCRL-53383, Lawrence Livermore National Laboratory, University of California, Livermore, California 94550, January 1983.

[146] J. Nikmo et al. A model for mass and heat transfer in an aerosol cloud. *Journal of Hazardous Materials*, 38:293–311, 1994.

[147] J. Nikmo and J. Kukkonen. *Modelling Heavy Gas Cloud Transport in Sloping Terrain.* Technical Inspection Centre, Helsinki, Finland, 1991.

[148] C. Nussey. Research to improve the quality of hazard and risk assessment for major chemical hazards. *Journal of Loss Prevention in the Process Industries*, 7(2):175–196, 1994.

[149] C. Nussey, J. K. W. Davies, and A. Mercer. The effect of averaging time on the statistical properties of sensor records. *Journal of Hazardous Materials*, 11:125–153, 1985.

[150] C. Nussey, M. Pantony, and R. Smallwood. HSE's risk assessment tool, RISKAT. In *Major Hazards: Onshore and Offshore*, October 1992.

[151] H. A. Panofsky and J. A. Dutton. *Atmospheric turbulence: models and methods for engineering applications.* J. Wiley, 1984.

[152] F. Pasquill and F. B. Smith. *Atmospheric Diffusion.* Ellis Horwood, 1983.

[153] D. W. Pepper, C. D. Kern, and P. E. Long. Modelling the dispersion of atmospheric pollution using cubic splines and chapeau functions. *Atmospheric Environment*, 13:223–259, 1979.

[154] W. H. Press et al. *Numerical recipes: the art of scientific computing.* Cambridge University Press, 1989.

[155] J. S. Puttock, D. R. Blackmore, and G. W. Colenbrander. Field experiments on dense gas dispersion. *Journal of Hazardous Materials*, 6:13–41, July 1982.

[156] J. S. Puttock and G. W. Colenbrander. Thorney Island data and dispersion modelling. *Journal of Hazardous Materials*, 11:381–397, 1985.

[157] J. S. Puttock et al. Dispersion models and hydrogen fluoride predictions. *Journal of Loss Prevention in the Process Industries*, 4:16–28, January 1991.

[158] P. J. Roache. *Computational Fluid Dynamics.* Hermosa, 1982.

[159] P. T. Roberts et al. Wind-tunnel studies of roughness effects in gas dispersion. *Atmospheric Environment*, 8(11):1861–1870, 1994.

[160] W. Rodi. Turbulence models and their applications in hydraulics—a state of the art review. Technical Report SFB 80/T/127, Universität Karlsruhe, May 1978.

[161] J. J. Rosenzweig. *A theoretical model for the dispersion of negatively buoyant vapor clouds.* PhD thesis, Massachusetts Institute of Technology, September 1980.

[162] J. W. Rottman. The spreading of dense gas clouds. Technical Report 1918/01/01, Health and Safety Executive, Broad Lane, Sheffield S3 7HQ, August 1984.

[163] J. W. Rottman, J. C. R. Hunt, and A. Mercer. The initial and gravity-spreading phases of heavy gas dispersion: comparison of models with phase one data. *Journal of Hazardous Materials*, 11:261–279, 1985.

[164] J. W. Rottman and J. E. Simpson. Gravity currents produced by instantaneous releases of a heavy fluid in a rectangular channel. *Journal of Fluid Mechanics*, 135:95–110, 1983.

[165] J. W. Rottman, J. E. Simpson, and P. K. Stansby. The motion of a cylinder of fluid released from rest in a cross flow. *Journal of Fluid Mechanics*, 177:307–337, 1987.

[166] M. Schatzmann. Accidental releases of heavy gases in urban areas. In J. E. Cermak et al., editors, *Wind Climate in Cities*, pages 555–574. Kluwer Academic Publishers, 1995.

[167] M. Schatzmann, K. Marotzke, and J. Donat. Research on continuous and instantaneous heavy gas clouds. Contribution of sub-project EV 4T–0021-D to the final report of the joint CEC project. Technical report, Meteorological Institute, University of Hamburg, February 1991.

[168] W. Schmidt. Zur Mechanik der Böen. *Meteorologische Zeitschrift*, 28(8):355–362, August 1911.

[169] L. I. Sedov. *Similarity and dimensional methods in mechanics.* Academic Press, Inc., 1959.

[170] F. S. Sherman, J. Imberger, and G. M. Corcos. Turbulence and mixing in stably stratified waters. *Annual Review of Fluid Mechanics*, 10:267–288, 1978.

[171] J. E. Simpson. *Gravity Currents in the Environment and the Laboratory.* Ellis Horwood, 1987.

[172] J. E. Simpson and R. E. Britter. The dynamics of the head of a gravity current advancing over a horizontal surface. *Journal of Fluid Mechanics*, 94(3):477–495, 1979.

[173] J. E. Simpson and P. F. Linden. Frontogenesis in a fluid with horizontal density gradients. *Journal of Fluid Mechanics*, 202:1–16, 1989.

[174] G. A. Sod. *Numerical Methods in Fluid Dynamics: Initial- and Initial Boundary- Value Problems.* Cambridge University Press, 1985.

[175] T. O. Spicer and J. A. Havens. Modelling the phase one Thorney Island experiments. *Journal of Hazardous Materials*, 11:237–260, 1985.

[176] D. D. Stretch. *The dispersion of slightly dense contaminants in a turbulent boundary layer.* PhD thesis, Cambridge University Engineering Department, Trumpington Street, Cambridge CB2 1PZ, 1986.

[177] R. A. Tapia and J. R. Thompson. *Nonparametric probability density estimation.* John Hopkins University Press, 1978.

[178] H. Tennekes and J. L. Lumley. *A first course in turbulence.* MIT Press, 1972.

[179] J. S. Turner. *Buoyancy Effects in Fluids.* Cambridge University Press, 1979.

[180] J. S. Turner. Turbulent entrainment: the development of the entrainment assumption, and its application to geophysical flows. *Journal of Fluid Mechanics*, 173:431–371, 1986.

[181] T. Vesala and J. Kukkonen. A model for binary droplet evaporation and condensation, and its application for ammonia droplets in air. *Atmospheric Environment*, 26A(9):1573–1581, 1992.

[182] D.-P. Wang. Numerical study of gravity currents in a channel. *Journal of Physical Oceanography*, 15:299–305, March 1985.

[183] D. M. Webber. On the stability of spreading pool solutions of the shallow-water equations. Technical Report SRD/HSE R479, AEA Technology, Wigshaw Lane, Culcheth, Cheshire, WA3 4NE, January 1992.

[184] D. M. Webber. Personal communication, 1994.

[185] D. M. Webber. A review of "Thermal effects in dense gas dispersion: a feasibility study...". Technical Report ISAS/HSE/96/002/01, Integral Science and Software, 1996.

[186] D. M. Webber and P. W. M. Brighton. Similarity solutions for the spreading of liquid pools. Technical Report SRD/HSE/R371, Safety and Reliability Directorate, Wigshaw Lande, Culcheth, Warrington WA4 4NE, July 1986.

[187] D. M. Webber et al. A model of a dispersing dense gas cloud and the computer implementation, DRIFT. Part I, near-instantaneous releases. Technical Report HSE/SRD/090/00010/91, Safety and Reliability Directorate, 1991.

[188] D. M. Webber et al. A model of a dispersing dense gas cloud and the computer implementation, DRIFT. Part II, steady continuous releases. Technical Report HSE/SRD/090/00011/91, Safety and Reliability Directorate, 1991.

[189] D. M. Webber et al. Complex features in dense gas dispersion modelling. Volume 1. Technical Report AEA/CD/FLADIS/1994, AEA Technology, Consultancy Services, December 1994.

[190] D. M. Webber, S. J. Jones, and D. Martin. A model of the motion of a heavy gas cloud released on a slope. Technical Report FLADIS/00020/91 B, AEA Technology, Wigshaw Lane, Culcheth, Cheshire, WA3 4NE, November 1991.

[191] D. M. Webber, S. J. Jones, and D. Martin. A model of the motion of a heavy gas cloud released on a uniform slope. *Journal of Hazardous Materials*, 33:101–122, 1993.

[192] D. M. Webber and C. J. Wheatley. The effect of initial potential energy on the dilution of a heavy gas cloud. *Journal of Hazardous Materials*, 16:357–380, 1987.

[193] C. J. Wheatley, A. J. Prince, and P. W. M. Brighton. Comparison between data from the Thorney Island Trials and predictions of simple dispersion models. Technical Report SRD R 355, Safety and Reliability Directorate, United Kingdom Atomic Energy Authority, Wigshaw Lane, Culcheth, Warrington WA4 4NE, February 1986.

[194] C. J. Wheatley and D. M. Webber. Aspects of the dispersion of denser-than-air vapours relevant to gas cloud explosions. Technical Report SR/007/80/UK/H; XII/829/84-EN, Safety and Reliability Directorate, Wigshaw Lane, Culcheth, Warrington WA3 4NE, 1984.

[195] D. J. Wilson. *Concentration fluctuations and averaging time in vapor clouds.* American Institute of Chemical Engineers, 1995.

[196] I. R. Wood and J. E. Simpson. Jumps in layered miscible fluids. *Journal of Fluid Mechanics*, 140:329–342, 1984.

[197] P. Woodward and P. Colella. The numerical simulation of two-dimensional fluid flow with strong shocks (review article). *Journal of Computational Physics*, 54:115–173, 1984.

[198] J. Würtz. A transient one-dimensional shallow layer model for dispersion of denser-than-air gases in obstructed terrains under non-isothermal conditions. Technical Report EUR 15343 EN, Joint Research Centre, Safety Technology Institute, Process Engineering Unit, I-21020 Ispra (VA), Italy, 1993.

[199] C-S. Yih. *Stratified Flows.* Academic Press, 2nd edition, 1980.

[200] S. T. Zalesak. Fully multidimensional flux-corrected transport algorithms for fluids. *Journal of Computational Physics*, 31:335–362, 1979.

[201] S. T. Zalesak. High order "ZIP" differencing of convective terms. *Journal of Computational Physics*, 40:497–508, 1981.

[202] O. Zeman and H. Tennekes. Parametrization of the turbulent energy budget at the top of the daytime atmospheric boundary layer. *Journal of the Atmospheric Sciences*, 34(1):111–123, January 1977.

[203] M. J. Zucrow and J. D. Hoffman. *Gas Dynamics*, volume 1. John Wily, 1976.